A Soil Temperature and Energy Balance Model for Integrated Assessment of Global Change Impacts at the regional scale

Dissertation der Fakultät für Geowissenschaften der
Ludwig-Maximilians-Universität München

eingereicht von
Markus J. Muerth

im Juni 2008

"When it is not in our power to determine what is true,
we ought to follow what is most probable."

- RENÉ DESCARTES

PREFACE

Within the scope of the increasing demand for assessment tools to understand the future impacts of Global Change on the water cycle and other natural resources, environmental scientists try to bridge the gap between the small scale of well understood physical process models and the regional scale of resource management decisions. In this context, the aim of the integrative project GLOWA-Danube (www.glowa-danube.de) is to develop and apply a regional scale modelling tool to assist future water and resource management in the 77,000 km^2 Upper Danube catchment.

A necessary part of any land surface model implemented in such a predictive, mesoscale modelling tool is the integration of physically based algorithms that couple the energy transfer and storage processes with the water cycle at the soil-vegetation-atmosphere boundary. As a part of my master thesis, I already had the chance to gain insight into the complex world of simulating soil water processes together with the difficulties one encounters trying to provide spatially distributed parameters for such models. Therefore, I was glad to join the "*Hydrology and Remote Sensing*" working group of GLOWA-Danube, led by Prof. Dr. Wolfram Mauser, soon after my graduation. This gave me the chance to further my knowledge about the soilscape as the main storage of water, energy and nutrients at the land surface, as well as its spatial heterogenity. For this reason, special thanks go to Prof. Mauser for giving me the chance to work for an integrative, application oriented project, for having confidence in my work and for the encouragement he always provided. Moreover, he constantly supported the progress of this thesis and simultaneously granted a high degree of personal freedom to develop my own ideas and methods.

The project GLOWA-Danube, as a part of the national GLOWA (Global Change of the Water Cycle) programme is mainly funded by the Federal Ministry of Education and Research (*Bundesministerium für Bildung und Forschung*, BMBF). Additional funding is provided by the Free State of Bavaria and the federal state of Baden-Würtemberg. Best thanks go to these governmental bodies for supporting the project and, as a consequence, making this thesis possible.

This work could not have been compiled without the help and support of the members of the Chair of Geography and Geographical Remote Sensing of the Ludwig-Maximilians University, Munich (Germany). Therefore, many thanks go to all former and current members of this section for the great working atmosphere and the many solutions they provided on various scientific and technical problems I enountered during my time as a PhD student.

A special thank goes to Prof. Dr. Ralf Ludwig for introducing me into the field of numerical models of the land surface, especially hydrological models, during his time as an assistant professor at the Chair of Geography and Geographical Remote Sensing and member of our GLOWA-Danube working group.

TABLE OF CONTENTS

LIST OF FIGURES

LIST OF TABLES

LIST OF ACRONYMS

AgMet	AgroMeteorological Network
AVHRR	Advanced Very High Resolution Radiometer
BEKLIMA	*BEstandesKLIMA* model
BoKA5	*Bodenkundliche KartierAnleitung* (German soil mapping manual)
BT	Brightness Temperature
BÜK	*Bodenübersichtskarte* (Soil Overview Map)
CET	Central European Time
CLC	CORINE Land Cover
CLM	Climate Local Model
CME	Coefficient of Model Efficiency
CV	Coarse material
dBT	difference in Brightness Temperatures
DOY	Day Of Year
DSS	Decision Support System
DWD	*Deutscher Wetter Dienst* (German Weather Service)
EEB	Explicit Energy Balance (algorithm)
EF	Eddy-Flux
EmpGHF	Empirical Ground Heat Flux model
ESCIMO	Energy balance Snow Cover Integrated MOdel
FPV	Fine Soil Pore Volume
GCMs	Global Climate Models
GHF	Ground Heat Flux
GLOWA	*GLObaler WAndel des Wasserkreislaufs* (Global Change of the Water Cycle)
GPV	Gross Pore Volume
HRU	Hydrological Response Unit
HYPRES	HYdrologial PRoperties of European Soils database
inh.	Inhabitants
LAI	Leaf Area Index
LfL	Bay. Landesanstalt für Landwirtschaft (Bavarian State Office of Agriculture)
LHF	Latent Heat Flux
LST	Land Surface Temperature
MBD	Mean Bias Deviation

MM5	Mesoscale Model
MODTRAN	MODerate resolution atmospheric TRANsmission (model)
NDVI	Normalized Difference Vegetation Index
NOAA	North American Oceanic and Atmospheric Administration
NS	Numerical Simulation (model)
NWP	Numerical Weather Prediction
PAI	Plant Area Index
PME	Penman-Monteith Energy balance (algorithm)
PROMET	PROcesses of Mass and Energy Transfer
Proxel	Process pixel
PTFs	PedoTransfer Funktions
QPF	Quadratic Parallel Function
RCMs	Regional Climate Models
REMO	RegionalMOdell
RMSD	Root Mean Square Deviation
RMSE	Root Mean Square Error
SCALMET	SCAling tool for METeorological fluxes
SHF	Sensible Heat Flux
SHTM	Soil Heat Transfer Module
SOHE	SOil HEat model
SNT	Soil Nitrogen Transformation (model)
SST	Soil Surface Temperature
SVAT	Soil-Vegetation-Atmosphere Transfer
SWT	Split Window Technique
TDR	Time Domain Reflectometry
Thermal-TDR	Thermal Time Domain Reflectometry
UML	Unified Modeling Language
UNSODA	UNsaturated SOil hydraulic DAtabase

1. Introduction

1.1. Integrated Global Change Assessment

Over the past several years, the public awareness for climate change, driven by anthropogenic emissions of CO2, methane and other trace gases, has steeply increased. However, global warming is already happening and the immediate reductions in greenhouse gas emissions necessary to stop further atmospheric temperature increase, are not economically and politically feasible. Humans have also altered a significant fraction of the Earth's surface via changing the original land cover to agricultural and built-up areas. Both climate and land use changes are strongly connected to rapidly changing global economics and to a strong increase in the world's population. These socio-economic and environmental transformations are considered in the term "Global Change". Despite recent efforts to reduce the threatening trend in these human-induced changes, especially climate warming will likely carry on for another 100 years or more (IPCC, 2007). For this reason, research on the expected impacts of Global Change on natural and managed environments is needed because knowledge about these impacts is the basis for future mitigation and adaptation strategies.

The objective of the project GLOWA-Danube (www.glowa-danube.de) is to investigate the impact of change in climate, population and land use on the water resources of the Upper Danube basin and to develop and evaluate regional adaptation strategies. Therefore, the integrative Global Change decision support system (DSS) DANUBIA is developed by a team of researchers from different natural and socio-economic science disciplines (MAUSER 2003, LUDWIG et al 2003a). To assist future water management, DANUBIA can simulate the water and energy fluxes and their related matter fluxes in the natural environment, as well as the water use in energy production, farming, tourism, industry and households. For the first time a water-related, predictive modelling framework (Fig. 1-1) is set up, which includes all necessary interactions between natural science process models and social science *deep actors* models. The modular framework is designed within the Unified Modelling Language (UML), which serves as a common language between the disciplines and helps with the integration and sound coupling of the disciplinary models (MAUSER & LUDWIG 2002, MAUSER & MUERTH 2008). The DSS components are implemented in the object-oriented programming language JAVA. The *process pixel* ("proxel") is the basic spatial unit which enables the coupling of all the models on a common spatial platform and the exchange of variables with a well defined spatial representation. Raster-based simulation models have a long tradition in the natural sciences, but the key to the approval of the proxel concept in the socio-economic sciences is the commitment to agent-based (*deep actors*) modelling. In this approach, human activities are spatially

resolved and represented by describing the varying preferences, decisions and the distinct behaviour of the actors.
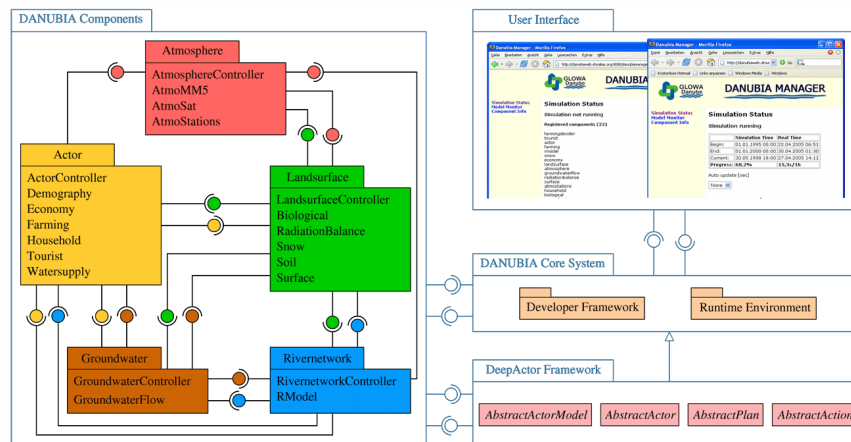
Fig. 1-1: Components of the decision support system DANUBIA.

The main purpose of this DSS is the assessment of the future water cycle in the mesoscale Upper Danube catchment (an area of about 77.000 km^2) under changing boundary conditions, to support knowledge-based water resources and land use management. The concept of scenario based decision support with DANUBIA (Fig. 1-2) regarding Global Change, is based on scientifically sound meteorological input and the dynamic representation of future regional development. This includes political and economical conditions as well as demographic and sociological trends inside and outside the catchment borders. Aside from influencing the scientific projections of regional development, stakeholders can formulate their own strategies to adapt to Global Change or to mitigate its effects. These strategies can be incorporated into the possible decisions of the agents in the *deep actors* models.
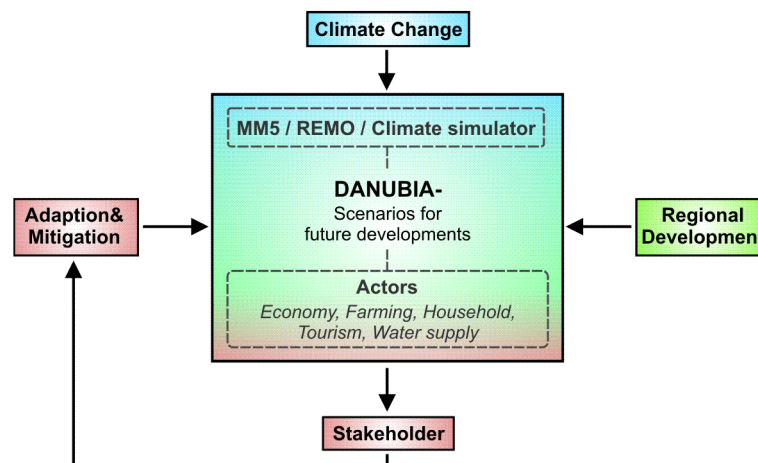
Fig. 1-2: Abstract model of scenario based decision support with DANUBIA.

To realistically assess future impacts of Global Change, especially of climate warming, on the environment and human societies, the exchange and storage of matter and energy on the land surface must be adequately represented by predictive models. These land surface models need to be non-calibrated to landscape characteristics that are under possible change due to the future developments. This includes empirical relationships and lumped model parameters that are connected to pre-defined, lumped parts of the landscape, like Hydrological Response Units (HRUs) (BECKER & BRAUN 1999). It is obvious that future changes in climate and land cover, as well as in the intensity of human activity will have an unknown effect on these relationships and can change the spatial distribution of the predefined representative landscape units. Furthermore, any model specific representation of space hinders direct coupling with other models, of ground water or atmosphere processes for example, and impedes the use of remote sensing data as a major source of spatially distributed data (MAUSER & BACH 2008). Moreover, the closure of matter and energy cycles at the land surface must be explicitly taken into account, to ensure realistic simulations of the expected alteration of water and energy fluxes and their feedbacks from other coupled models. Especially the upcoming (bidirectional) coupling of land surface models and Regional Climate Models (RCMs) needs consistent balances of water, energy and trace gases at the land surface (PITMAN 2003, HAGEMANN & JACOB 2007, MARKE 2008).

The distributed, physical hydrological model PROMET (PROcesses of Mass and Energy Transfer) was further developed during the first and second project stages of GLOWA-Danube, as part of DANUBIA's *Landsurface* component. Its ability to represent the mesoscale water balance of the Upper Danube basin and to reproduce daily runoffs for a number of gauges inside the catchment has recently been proved by MAUSER & BACH (2008).

Besides that, advancements in modules related to the energy and matter cycles at the land surface have been made to include all necessary processes for the assessment of future changes in plant development (LENZ 2007, HANK 2008), soil carbon and nitrogen availability (NEUHAUS & KLAR 2007), storage of water as snow and ice (PRASCH et al 2007) and soil erosion (WALDMANN & MAUSER 2007). Prerequisite for a number of these modules is the realistic simulation of soil physical processes, especially the prediction of spatial and temporal distributed fields of soil moisture and soil temperature on the basis of the available soil physical properties. Even though the better part of mid-latitude catchments is covered with vegetation, fluxes of water vapour, heat and radiation from the soil into the canopy and the atmosphere have to be accounted for in upcoming coupled scenario runs.

1.2.   Scientific Objectives and Outline of the Thesis

The advancement of the DANUBIA *Landsurface* component to predict the soil-vegetation-atmosphere transfer (SVAT) of radiation and heat and to simulate spatially distributed soil temperature patterns were main objectives of the model development during the second GLOWA-Danube project stage from 2004 to 2007. The SVAT of radiation and heat is a prerequisite for the successful coupling of the *Landsurface* component with the RCMs available for scenario simulations (MM5, REMO) (Marke 2008). Hourly prediction of distributed soil temperature fields is a requirement for the successful implementation of biochemical process models that predict the transformation and storage of carbon and nitrogen in soils (Neuhaus & Klar 2007) and an agent-based model of farming decisions (Fig. 1-3).
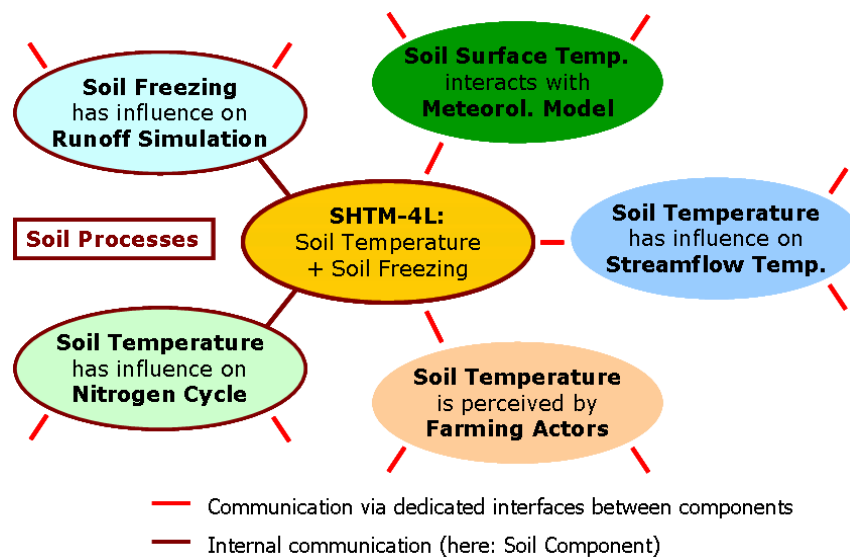
Fig. 1-3: Recipients of output variables computed by SHTM within the DANUBIA framework.

Therefore, it is the objective of this thesis to present the principles and methods of the proposed soil heat transfer and storage module (SHTM) and its sensitivity to different surface energy balance algorithms. This work also investigates the possible mesoscale representation of the interactions between energy and water in soils, especially during times of soil water freezing. During all stages of model development, special consideration was given to the balance between intended temporal and spatial scale of the application in mesoscale river basins and the desired physical accurateness of the proposed algorithms and parameters.

All model components presented in this work were implemented in the raster-based, modular SVAT model PROMET for testing and validation. SHTM was then successfully integrated into the DANUBIA decision support system together with the most promising soil surface energy balance model.

After a brief introduction into the common approaches to model soil energy transfer and storage, Chapter 2 gives a short description of the physical geography and the demographic and economic characteristics of the area under investigation. The present-day water use and water pollution topics in the Upper Danube catchment are outlined and the potential conflicts regarding water use and water resource management are also addressed.

The data necessary to validate simulated time series of soil temperature and the spatial patterns of surface temperature is presented in Chapter 3. The data set includes 43 soil temperature time series from meteorological network stations, two data sets from field campaigns of the Department of Geography, Munich and 12 area-wide remotely sensed surface temperature maps.

Chapter 4 gives a comprehensive exposition of all soil physical processes and parameters related to the simulation and evaluation of soil temperatures. A short summary of the basic principles of the soil water module, implemented in PROMET and the DANUBIA *Landsurface* component, is followed by an in-depth description of the equations, the parameters, the boundary conditions and the chosen model geometry of SHTM. Three surface ground heat flux models of differing complexity for snow-free conditions are presented and rounded off with a snow-soil heat transfer algorithm.

The spatial distribution of the basic soil properties in the Upper Danube basin and the derivation of the associated hydraulic parameters is the subject of Chapter 5.

Output variables of SHTM are validated against point-scale time series and spatially distributed temperature patterns in Chapter 6. First, the influences of different model configurations and boundary conditions on model performance are evaluated by means of an extensive field-campaign data set. Then, the performance of SHTM is assessed via soil temperature time series recorded by meteorological network stations. At the end of this chapter, simulated surface temperature patterns are compared to remote sensing data, with special attention to areas of the catchment with a low degree of vegetation cover.

A summary of the achievements in regional and long-term simulation of the energy household of soils and an outlook on future applications of coupled simulations of soil water and energy conclude the thesis in Chapter 7. Finally, the outlook on possible future advancements suggests a simple, empirical approach for the simulation of mesoscale lateral runoff on frozen soils.

1.3. State of the Art in Soil Temperature Simulation

Temperature variations below the earth's surface have been of scientific interest since the 17th century, when discussion arose about the penetration depth of the solar radiation into the ground (Buntebarth 2002). When Fourier (1822) published the theoretical background for heat conduction problems, different authors started to work on the measurement and the prediction of heat wave propagation into the ground. One of the early works, which includes the collection of soil temperature time series at different sites as well as an analysis of site-specific thermal properties from the annual temperature cycle was compiled by J.D. Forbes (1846). Already at that time, the annual and diurnal variation of soil temperature was described with sine-wave equations, which included the increase in damping and time-lag of the soil temperature amplitude with increasing depth. The modern form of the analytical sine-wave equation was proposed by Carslaw & Jaeger (1959).

Investigations on the influence of landscape properties on measured soil temperatures began in the 19th century with the advent of continuous meteorological measurements and the rising interest in the effect of climate on plant growth and cultivation. Frödin (1913) for example, found that both vegetation and snow cover have a great impact on the amplitude of ground temperatures. Then, in the 1960's, resistance thermometers had led to a multitude of soil temperature surveys. Together with the fundamental works of de Vries (1963) on thermal conductivity and of Geiger (1961) on near-ground climatology, the scientific basis for the understanding of the processes and influencing variables of heat exchange and storage in the soil-vegetation-atmosphere continuum was provided. These works provide all the facts from soil physics and micrometeorology, which are essential for a theoretical model of soil surface heat exchange. In the following years, a number of authors, such as Monteith (1973), Thom (1975), Choudhury et al (1986), Oke (1987) or Campbell & Norman (1998) proposed or compiled different methods, that enabled the numerical quantification of surface energy and matter fluxes at the local scale. Numerical solutions of the differential equations governing the conductive and convective heat transfer in soils were developed in soil physics (Campbell 1985, Huwe 1999, Li & Sun 2008).

From a meteorological or climatological point of view (Liang et al 1999), the calculation of the ground heat flux into the soil can be (a) an empirical relationship between net radiation and ground heat flux (Choudhury et al 1987, Kustas & Daughtry 1990), (b) the "force-restore" method (Deardorff 1978) that assumes a sinusoidal course of the diurnal ground heat flux or (c) the explicit representation of the heat diffusion and storage in soils. The former methods were developed to reduce the computational effort of numerical weather prediction (NWP) and global climate models (GCMs). Increased processing power, the advent of regional climate models (RCMs) and the call for more detailed representations of soil and vegetation processes in atmospheric models, like the carbon cycle in climate models (Pitman 2003), led to the inclusion of explicit multi-layer soil temperature models. However, most of these

models do not incorporate site-specific soil properties nor do they incorporate the influence of soil moisture on soil temperature, mainly due to their large scale application (Ács et al 1990, Hagemann et al 1999, Liang et al 1999, Chen & Dudhia 2001, Best et al 2005 amongst others). These simplifications of the energy and water processes in the soil-vegetation-atmosphere system can lead to significant variations in predicted near-surface temperatures (Peters-Lidard et al 1998, Moberg & Jones 2004, Miao et al 2007).

In the land surface modelling community, a variety of different approaches to soil temperature simulation were developed, which can be roughly divided into empirical-statistical and physical-deterministic models. Many of these models arose out of the need to provide soil moisture and temperature as input data to biochemical process models on the transformation of nitrogen (Ludwig et al 2001) or carbon (Raich & Schlesinger 1992) in soils and their exchange between soil and atmosphere.

The most common empirical approach utilized in ecological models is the sine-wave algorithm of Carslaw & Jaeger (1959), which relates the diurnal or annual course of the soil temperature at a given depth to the mean and extreme values of near-ground air temperature and the average thermal soil properties. A similar methodology was proposed by Kluender et al (1990), which effectively reproduced daily minimum and maximum temperatures at 5 and 10 cm soil depth at different sites in Arkansas, USA. Beltrami (2001) and Thorn et al (1999) analysed the relationship of climate station data and measured soil temperatures in cold climate regions and were able to produce satisfying results with their statistical models, even though snow cover and soil water freezing had a significant impact on the annual soil temperature cycle.

Most Soil-Vegetation-Atmosphere Transfer (SVAT) schemes of energy and matter, primarily designed as predictive tools in agricultural and forest meteorology, hydrology and physical geography, use deterministic representations of the soil heat transfer and storage in soils. But, as opposed to pure soil physical models, their soil temperature algorithms frequently use empirical approximations for some complex parameters, dependencies and boundary conditions. The empirical approximations faciliate the application of these models in areas of local to regional scale if input data from thematic maps, remote sensing or landscape analysis is available. Relevant SVAT models, including physically-based soil temperature schemes are DAISY (van der Keur et al 2001, Hansen 2002), CoupModel (Alvenäs & Jansson 1997) and BEKLIMA (Braden 1995, Welpmann 2003) amongst others. The forest floor model of Ogée & Brunet (2002) combines a typical SVAT approach for water and energy fluxes with the force-restore method of Deardorff (1978).

2. The Upper Danube Watershed

2.1. Hydrology, Climate and Topography

The Danube is the second largest river in Europe with a watershed area of 817.000 km² and a length of 2,888 km (Fig. 2-1). Its source is in the Black Forest in south-western Germany and it flows through the northern foreland of the Alps, the Pannonian and Romanian lowlands, and drains through a delta into the Black Sea.

The project GLOWA-Danube is limited to the analysis of the upper part of the catchment defined by the discharge gauge Achleiten, near Passau in Germany. This Upper Danube discharge basin has an area of 76.653 km² and consists of a southern, mountainous part with altitudes up to 4049 m a.s.l., a large foreland and low mountain ranges along its northern border.
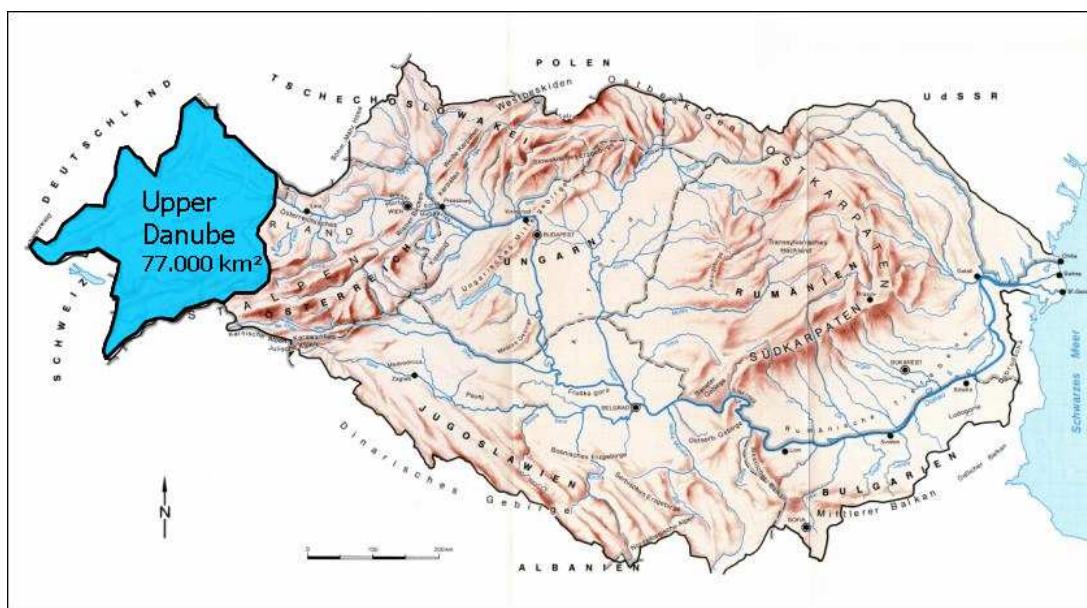
Fig. 2-1: Location of the Upper Danube within the whole Danube catchment.

Following LUDWIG et al (2003) the climate is temperate and humid, but with a strong north-south gradient towards the Alps. The mean annual temperature decreases from +8 °C in the lowlands along the Danube to -5 °C in the partially glaciated Central Alps (Fig. 2-2). Likewise, precipitation ranges from 650 mm in the northern low mountain ranges to over 2000 mm per year in the high mountain ranges of the Northern Alps (Fig. 2-3). The significant difference in precipitation patterns between seasons originates from the stronger and more frequent orographic precipitation events during summer, when moist air from the Atlantic Ocean flows to the Alps by north-western currents and produces frequent convective summer rains.

These heterogeneous physiogeographic characteristics lead to a strong spatial and temporal differentiation of runoff generation. Regional floods occur frequently in the alpine foreland and the Alps, triggered by strong precipitation events in summer. Additionally, characteristic large-scale weather patterns combined with snowmelt activity can trigger floods, which have an impact upon the whole Upper Danube region and its tributaries (e.g. the 200-years *Pentecost Flood* of 1999). For flood protection, energy production and management of water resources, the discharge of all important tributaries of the Upper Danube has been regulated with reservoirs and dams. To a large extent, their management is determined by the dynamics of the snow and ice storage in the Alps. The Inn, the most important alpine tributary, contributes 52% of the average discharge of 1430 m³/s, measured during the period 1901 to 2002. Mean high water during this period was 4110 m³/s and mean low water 615 m³/s. During the most recent flooding of Passau in August 2002, peak discharge of the Danube at Achleiten was 7700 m³/s.
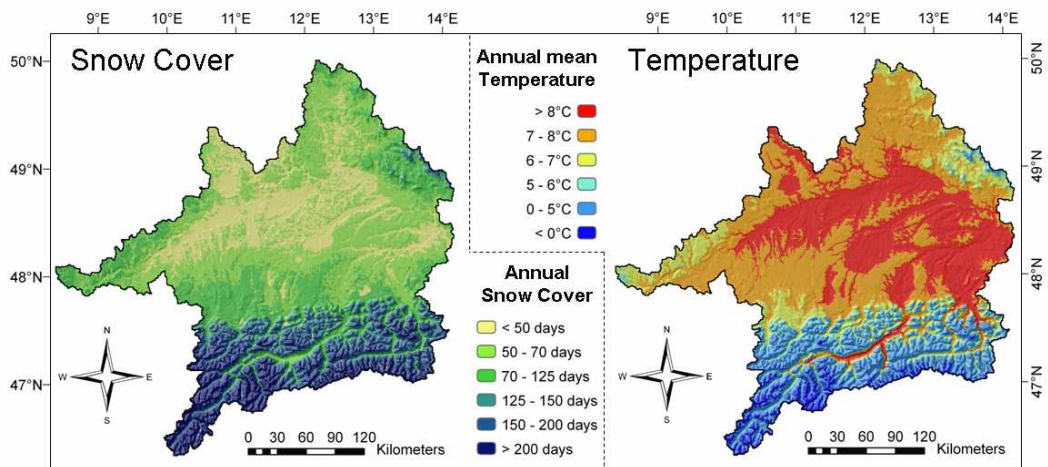
Fig. 2-2: Annual mean snow cover and air temperature simulated with PROMET for the period 1971 to 2000.
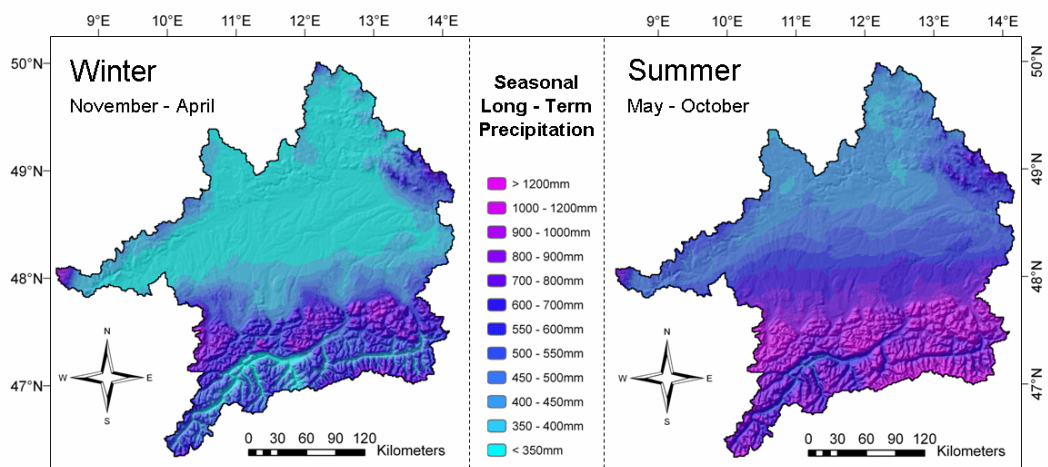
Fig. 2-3: Mean winter and summer precipitation simulated with PROMET for the period 1971 to 2000.

2.2. GEOLOGY, SOILS AND VEGETATION

The geology of the Upper Danube catchment can be divided into 5 major units from north to south: The *Paleaozoic Basement* mountains, the *Karst* low mountain ranges, the *Molasse* lowlands, the alpine foreland dominated by *pleistocene* deposits and the Alps. In the central part of the Upper Danube basin, *Jurassic Karst* is the lowest hydrogeologic layer, covered by two *Molasse* layers. These, again, are covered by *quartenary* deposits in many areas of the catchment.
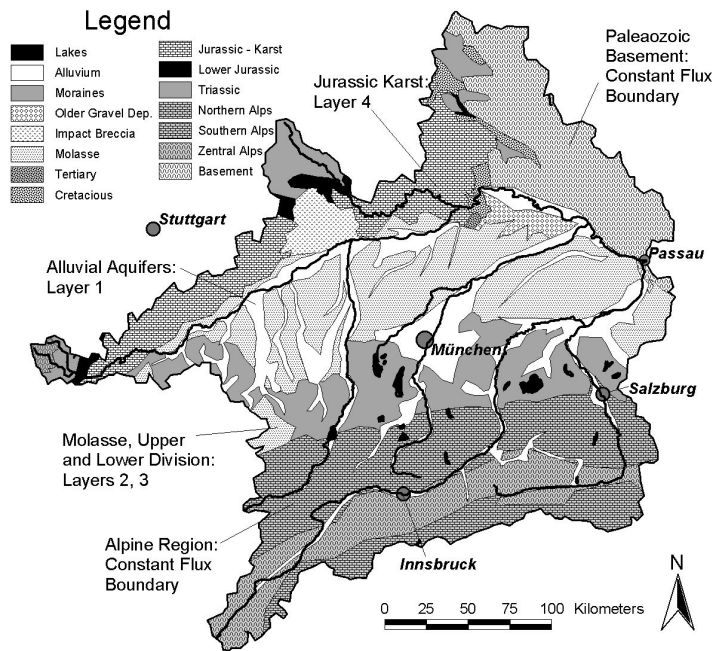
Fig. 2-4: Schematic geologic map of the Upper Danube watershed (BARTHEL **et al 2005).**

The soil distribution in the Upper Danube region is closely related to the surface geology, as shown in Fig. 2-5. Most of the soilscape evolved after the last ice age, for this reason most soils do not exceed a depth of 150 to 200 cm. The prevalent soil textures found on *quartenary* deposits are loamy sand and sandy loam, with gravelly lower horizons in areas of alluvial deposits. Typical soils on tertiary deposits are silt loam and clay silt where *Loess* settled on the periglacial landscape during the glacial periods. In the mountainous regions, the mesoscale soil maps display mainly *Leptosols*, whose textures are determined by the weathering products of the respective bedrock.

The highly fragmented land cover and land use are mostly determined by human activity. Forestry and agricultural use (grassland, farmland) of different intensities dominate, whereas the present agricultural potential is limited in various parts of the catchment by climatic and pedogenic disfavours in terms of high precipitation, low temperatures and shallow soils with a high fraction of coarse material. Natural vegetation is mostly found in inaccessible, mountainous regions, but still often

influenced by tourism and forestry. This includes the once sizeable wetlands that have been drained and cultivated in the past. These wetlands appear as clay loam areas in the soil map (together with the areas covered by water). The land cover map presented in Fig. 2-6 is derived from the 1:100,000 data set of the pan-European CORINE Land Cover project CLC-2000 (2004).
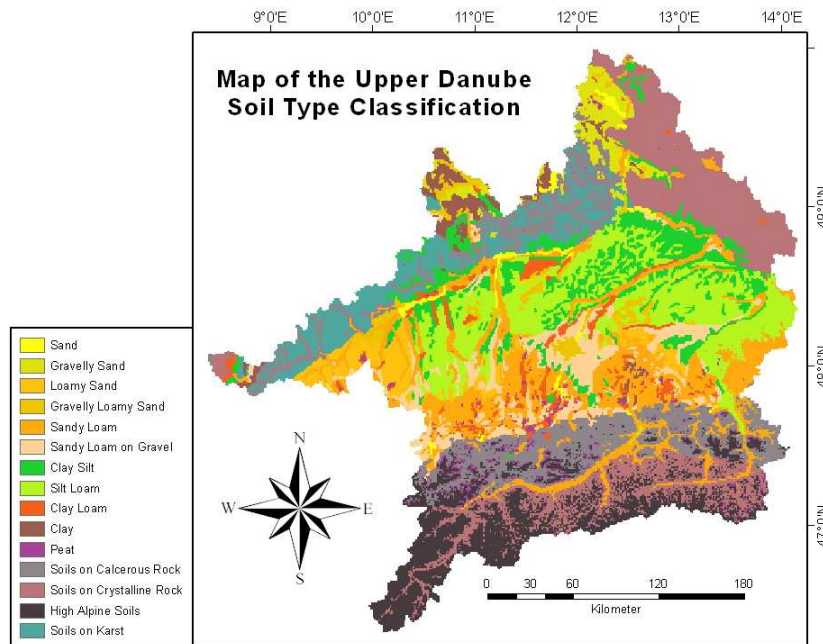
Fig. 2-5: Soil type map of the Upper Danube catchment derived from the 1:1,000,000 soil overview map of Germany (BÜK1000, BGR 1998).
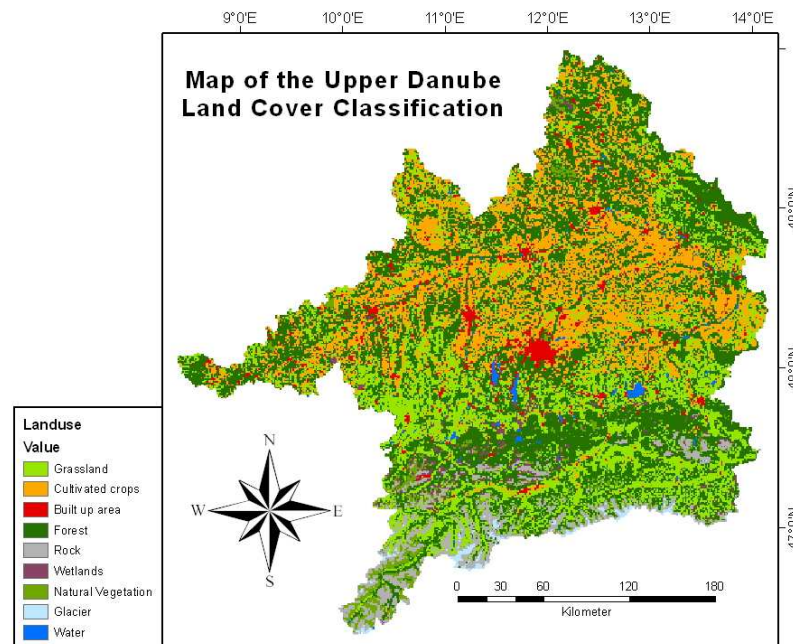
Fig. 2-6: Land cover map of the Upper Danube catchment based on the 1:100,000 data of the European CORINE Land Cover project (2004).

2.3. Water Use and Resource Management

The Upper Danube catchment is home to approximately 10 million people, which comes down to an average population density of about 130 people per km^2. Yet, the majority of the inhabitants (inh.) are located in the central and northern part of the region, in and around the most important agglomerations Munich (1,350,000 inh.), Augsburg (260,000 inh.), Ingolstadt (120,000 inh.) and Ulm (120,000 inh.). While the central part of the region, around Munich, has economical significance on the European level (industry and services), there is a strong socio-economic gradient, especially towards the southern and eastern parts, where agriculture and tourism play a more important role. The diverse physiographic and socio-economic situation in the Upper Danube leads to specific local water use and water pollution topics. Intensive agriculture and stock farming releases large amounts of fertilizers and pesticides, which conflicts with quality issues of the mainly decentralized public water supply from ground- and spring water. Furthermore, the possibly decreasing quantity of river runoff in a changing climate will lead to future struggles regarding surface water use. All important tributaries of the Upper Danube have been regulated for flood protection, water resource management, and energy production through reservoirs and dams. Then again, the lower part of the Upper Danube is part of the European waterway that connects the North Sea to the Black Sea and therefore needs certain water levels. An increasing amount of winter runoff is used for the production of artificial snow in the skiing regions of the Alps and reduces the winter runoff levels of some smaller tributaries. All of this conflicts with environmental sound river levels that are needed to protect the riparian and wetland ecological reserves.

Despite these possible future conflicts, the water resource management of this region is complex and largely uncoordinated between the different administrative entities. 73% of the Upper Danube basin is controlled by the German states Bavaria and Baden-Württemberg, most of the alpine part (24%), including the important tributary Inn, belongs to Austria and some minor areas to Switzerland, Italy and the Czech Republic. On one hand, the water supply structures are split between hundreds of communal water suppliers. On the other hand, the ongoing implementation of the European Water Framework Directive demands for an integrated, ecological sound water resource management on the catchment scale. Combined with the ongoing changes in climate, land use, touristic activity and agricultural production goals, the future of water in the Upper Danube basin is largely unclear. GLOWA-Danube aims at supporting knowledge-based decisions regarding these issues, by providing a decision support system that takes into account most of these natural and socio-economic processes on the catchment scale.

3. THE DATA

This chapter describes the data sets used for the validation of the soil temperature and soil ice simulations presented in chapter 6. Aside from numerous point data sets of climate stations and ground measurements, a limited data set of remotely sensed land surface temperatures derived from NOAA-AVHRR is presented.

3.1. EDDY CORRELATION SYSTEM MEASUREMENTS

To validate simulated soil temperature series against scientifically collected data, time series of two micrometeorological systems of the Department of Geography (University of Munich) were used. Both were situated near Munich, Germany, and measured all necessary variables (Table 3-1) to determine turbulent vapour and energy fluxes between the land surface and the atmosphere, via the *eddy–correlation* method (DABBERDT et al 1993, TWINE et al 2000). Data from these Eddy-Flux (EF) stations, was used in three different ways in this work: First of all, the basic structure of the heat transfer module was tested with measured soil heat flux G_0 and soil moisture data and those simulated temperatures were compared to the measured soil temperatures $T_{meas}(z)$. Secondly, the measurements of R_{net} and G_0 were used to derive an empirical ratio of ground heat flux to radiation, which can be used in PROMET, if no surface energy balance algorithm is run. Finally, the time series of $T_{meas}(z)$ were used to validate the simulated temperatures of the fully coupled land surface model.

Table 3-1: Variables measured at the Eddy-Flux sites.

VARIABLE	DEVICE	COMMENT
wind	sonic anemometer	in 3 dimensions
CO2, H20	infrared gas analyzer	
air temperature	meteorological station	
air humidity	meteorological station	
incident radiation	pyranometer	above canopy
net radiation	net radiometer	above canopy
precipitation	rain collector	
ground heat flux	self-calibrating sensor	at 5 cm depth
soil temperature	electrical sensor	at 6.5, 15 and 25 cm
soil moisture	forked TDR probe	at 6.5, 15 and 25 cm

One station was situated on a rape field at *Gut Hüll*, west of Munich (48.09°N, 11.33°E, 587m a.s.l.) in the summer of 2003. The soil texture at this site was surveyed as clay silt in the upper 0.45 m (about 70% silt and 20% clay), followed by a small silty clay horizon (~3 cm) on loamy gravel deposited during the *Riss* glacial. The EF station was set up during spring and was operational for the main vegetation period of the rapeseed field, which was harvested on July 15, 2003. An agrometeorological

station of the Bavarian State Office of Agriculture is located nearby, that was also used for validation of the annual temperature course. The collected data was used for a diploma thesis that investigated the rapeseed parameters used in the biological module of PROMET (MARKE 2004).

The other station at *Wielenbach*, south-west of Munich (47.89°N, 11.16°E, 550 m a.s.l.), is operational since 2003 on an floodplain meadow. The soil texture of the upper horizon is loamy sand (about 40% silt and 15% clay) with high organic material content on the alluvial deposits (sandy gravel) of the river *Ammer*. Unfortunately, soil moisture and soil temperature are heavily influenced by the shallow groundwater level most of the year. Interestingly, a soil temperature station of the German meteorological network was put into operation in April 2007 nearby, so soon comparisons of the measurements of both stations can be conducted. For this work the data of this new station is not used, because the meteorological time series for the year 2007 was not available for the summer of 2007.
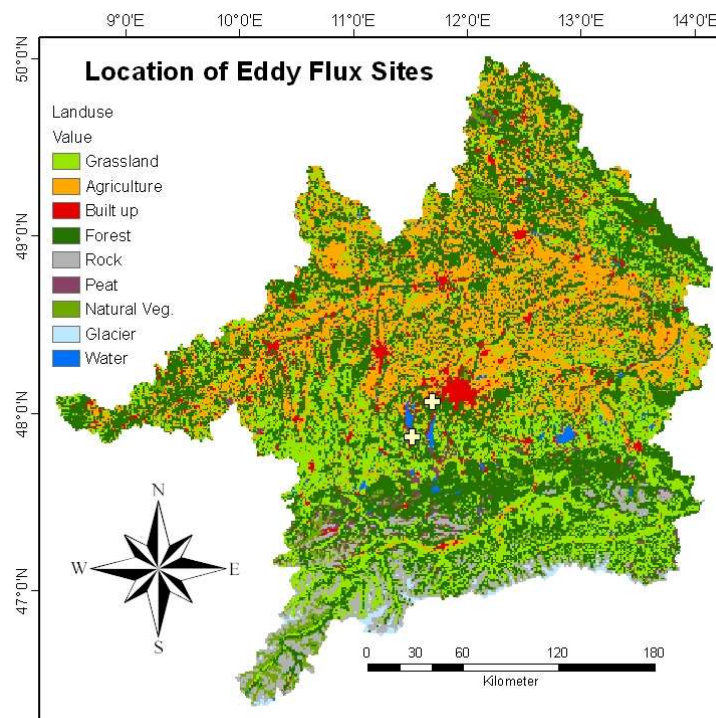
Fig. 3-1: Locations of the Eddy-Flux stations inside the Upper Danube catchment.

3.2. Data from Meteorological Networks

To validate SHTM on a variety of catchment proxels (*process pixels*), time series from a number of meteorological stations were used. However, the two available datasets both have their own limitations, as described below. Consequently we compared simulated temperature time series with data from both networks, in order to get an overall evaluation of the performance of PROMET regarding soil heat flux simulations.

3.2.1. Network of the German Weather Service

At some of the meteorological and climatological stations of the German Weather Service (*Deutscher Wetter Dienst*, DWD), soil temperature and the basic meteorological variables are measured simultaneously three times a day. Synoptic stations not only detect soil temperature continuously, but also provide data three times a day for the climatological data set. The advantage of this dataset is that the thermometers are maintained regularly and errors or gaps in the data are identified automatically and evaluated by professionals. Yet, the data set has a limited temporal resolution, that does not always capture the true daily amplitude of the near surface soil temperature fluctuations. For that reason, the daily mean values and daily amplitudes of soil temperature provided by the DWD are used. Most of the continuous measurements of soil temperature are conducted at 5, 10, 20 and 50 cm depth and at 7:30h, 14:30h and 21:30h CET, the so-called *Mannheimer Stunden*.
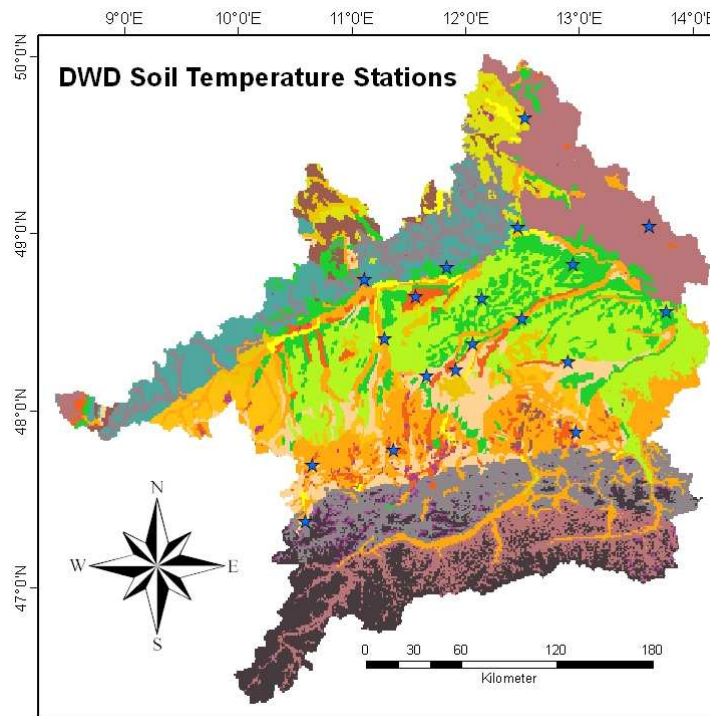
Fig. 3-2: Locations of the DWD soil temperature stations inside the catchment.

About 70 soil temperature stations have been operational inside the catchment from 1951 to 2007. The validation dataset from 15 stations was selected based on two conditions: The chosen stations had to represent different regions of the investigation area and recorded soil temperature during the years 2001 to 2005.

Table 3-2: DWD soil temperature stations used for validation.

Station	Name	Northing [°]	Easting [°]	Elevation [m a.s.l.]	Start	End	Gaps
4144	Oberstdorf (WST)	47.400	10.283	810	01.01.1961	30.06.2007	0
4161	Hohenpeissenberg (OBS)	47.800	11.017	977	01.01.1980	30.06.2007	0
4890	Fürstenzell (WST)	48.550	13.350	476	30.12.1996	30.06.2007	0
4481	Weiden a.Off. (WST)	49.667	12.183	438	01.01.1972	30.06.2007	1
4187	Oberschleißheim	48.250	11.550	484	01.01.1987	31.05.2006	62
4131	Maisach-Gernlinden	48.217	11.300	509	01.01.1987	30.11.2004	63
4137	Kempten (WST)	47.717	10.333	705	01.01.1986	30.06.2007	73
4499	Regensburg (WST)	49.050	12.100	371	01.01.1986	30.06.2007	75
4505	Straubing (WST)	48.833	12.567	350	05.04.1994	30.06.2007	77
4109	Kösching	48.833	11.483	415	01.01.1987	30.06.2007	93
4503	Landshut	48.533	12.117	393	01.09.1992	30.06.2007	229
4362	Königsmoos-Untermaxfeld	48.667	11.217	378	01.04.1994	30.06.2007	279
4185	Mainburg	48.650	11.783	431	01.06.1990	31.01.2005	367
4497	Zwiesel (AWST)	49.033	13.233	612	17.05.1990	31.03.2007	475
4528	Mühldorf a. Inn (WST)	48.283	12.500	405	01.01.1953	30.06.2007	5114

3.2.2. AGROMETEOROLOGICAL NETWORK OF BAVARIA

The second source of continuous time series of soil temperature for validation is the Agrometeorological Network (AgMet, http://www.lfl.bayern.de/agm/) of the Bavarian State Office of Agriculture (*Bayerische Landesanstalt für Landwirtschaft*, LfL). The 128 meteorological stations operated by the LfL are distributed over the agricultural regions of Bavaria, but are mainly supervised by farmers. Thus, the quality of the measurements varies from station to station. Measurements are provided as hourly values and can easily be downloaded via the internet. Additionally, basic information about each location is supplied, including mean annual temperature and precipiation, as well as a short description of the landscape. The data recorded at every site includes precipitation, air temperature at 20 and 200 cm height, wind speed and soil temperature at 5 and 20 cm depth. The temperature sensors used for air and soil measurements are resistance thermometers of the type *Pt 100 A* that have an effective range of -30 to +40 °C and an accepted tolerance of ±0.15 °C. Some stations also measure incident radiation, humidity, leaf wetness and/or soil temperature at 50 cm depth.

The network was founded in 1989 to support environmentally friendly crop production in Bavaria. Climate, beneath soil and vegetation type, is an important criterion for successful crop development and influences many aspects of agriculture. As the spatial density of the DWD meteorological network was insufficient for field specific adaption of cultivation techniques, the first AgMet stations were put into operation in the early 1990s. To encourage use of knowledge based cultivation management, a public web-based data server was set up, to allow unlimited access to

the AgMet data for public and scientific users (FRÖHLICH 2001). Mean and extreme values from the station's sensors are logged every 10 minutes and put into the network's database. Users can download mean and extreme values on an hourly or daily basis from the internet site of the Bavarian agrometeorological network.

The validation dataset used in this work consists of 28 stations chosen to represent the different agricultural areas of Bavaria and two purposely chosen ones. *Freising* (Nr. 008) was chosen because it is operated by the University of Applied Sciences Weihenstephan and the DWD and *Gut Hüll* (Nr. 072) because it is situated near the EF site mentioned above. Unfortunately, the 2003 soil temperature dataset from *Gut Hüll* was obviously flawed when compared to recorded air temperatures, so the validation dataset used in this work includes only the 2004 soil temperature time series.

The names and numbers of all stations used in this work are found in Appendix B, their distribution in the catchment is depicted in Fig. 3-3.
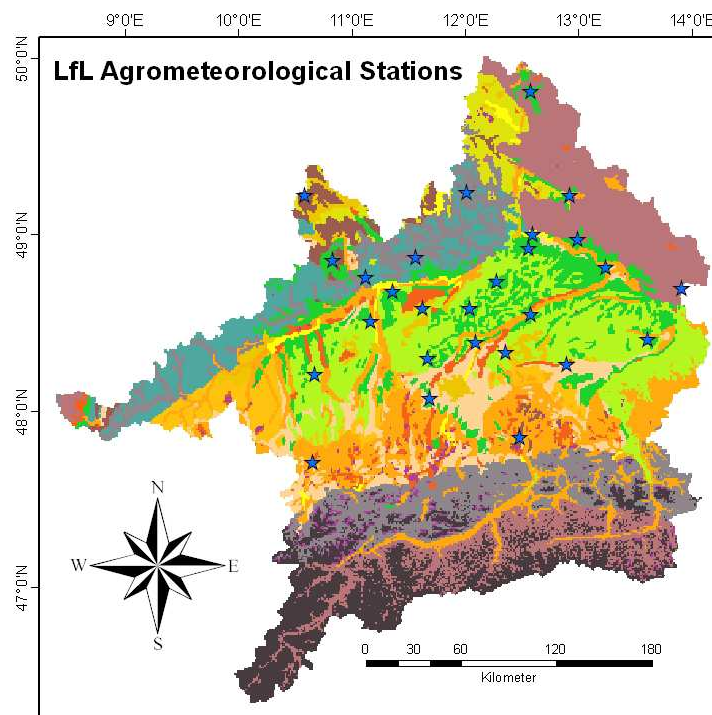
Fig. 3-3: Location of the agrometeorological stations inside the Upper Danube catchment.

3.3. NOAA-AVHRR Land Surface Temperature

The only feasible way to measure surface temperature over regional or continental scales is to use remote sensing by satellites. Many studies have been devoted to establish a methodology to retrieve land surface temperatures from sensor data of the Advanced Very High Resolution Radiometer (AVHRR) of the US National Oceanic and Atmospheric Administration (NOAA). It measures the radiance of earth's surface in five spectral channels, of which channels 4 and 5 are within the range of earth's thermal emission bands. In this study, data from the NOAA-17 AVHRR/3 sensor is used because it has a repetition rate of one day, scanning the Upper Danube region at approximately 11:00 CET, and a spatial resolution of about 1km.

The sensor data from NOAA-17 is recorded by a ground station operated at the Department of Geography in Munich and is automatically processed and georeferenced for use in the Upper Danube catchment at the company VISTA, including an automatic cloud and snow cover classification. The land surface temperature (LST) of each scene is retrieved from AVHRR brightness temperatures (BTs) in channels 4 and 5 by the application of three different Split Window Techniques (SWT). Because there are numerous SWT algorithms published in literature (see DASH et al 2002), this chapter shall examine the possible differences in using different techniques for LST retrieval.
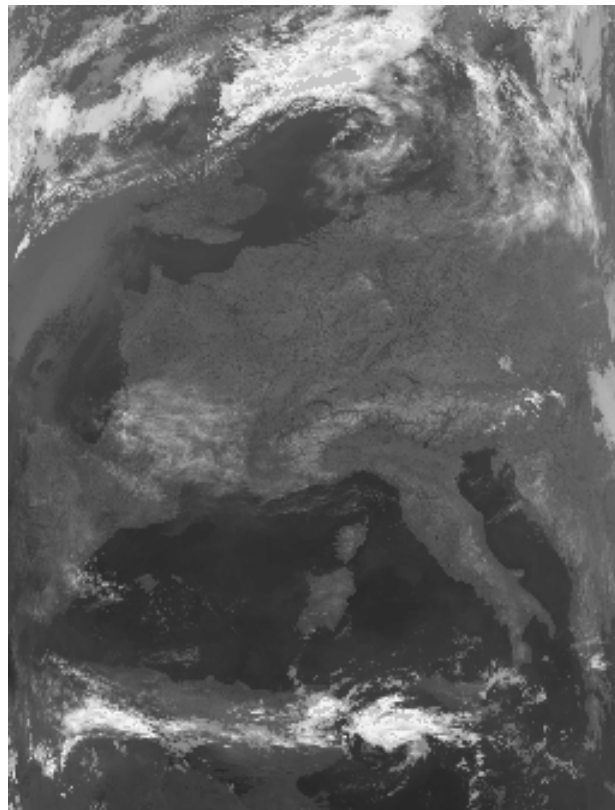
Fig. 3-4: Part of a NOAA-AVHRR strip map over Europe (17.09.2003).

3.3.1. THE AVHRR/3 SENSOR

The AVHRR/3 is a six channel scanning radiometer providing three solar channels in the visible-near infrared region and three thermal infrared channels. Of these channels only five can be transmitted to Earth at any given time, including channels 4 and 5, which work at the spectral ranges of 10.3 – 11.3 and 11.5 – 12.5 µm respectively. The detectable temperature range of the thermal channels is 180 to 350 K and the spatial resolution at nadir is 1.09 km. The orbital spacecraft NOAA-17 travels at an altitude of 833 km and retrieves complete strip maps of the earth's surface from pole to pole approximately once a day. The satellite orbits around the earth every 101 minutes, passing the area of interest, the Upper Danube basin, between 10:30 and 12:00 CET heading south.

3.3.2. THE DETERMINATION OF LAND SURFACE TEMPERATURES

Satellite sensors measure the surface-leaving radiance of the land surface, modified by the atmosphere, in different spectral channels (DASH et al 2002). For this reason, LST retrieval has to solve three different problems:

1) To estimate the thermal emissivity ϵ_T of a land surface as a heterogeneous, non-flat reference face, that is characterized by the type of land cover and underlying soil, and the moisture on the surface and in the soil.

2) To determine the amount of atmospheric absorption of radiation transmitted from the surface to the sensor, especially due to water vapour.

3) And to compute the true LST from the brightness temperature (BT) of the available infrared channels. BT is defined as the temperature of a hypothetical black body emitting an identical amount of radiation at the channel's mean wavelength.

True emissivities of heterogeneous surfaces are hard to come by, but their values lie within the range of 0.90 and 0.99 for most natural land covers. Only the extensive use of remote sensing techniques is able to determine the true emissivity of a land surface pixel (DASH et al 2002). Therefore most SWTs distinguish ϵ by the type of land cover, namely water ($\epsilon_T \approx 0.98$), bare soil ($\epsilon_T \approx 0.90\text{-}0.96$) and vegetation ($\epsilon_T \approx 0.94\text{-}0.99$), with values given for the 8 to 14 µm thermal waveband. A summary of experimentally determined emissivities and their implication on LST retrieval can be found in QIN & KARNIELI (1999), SNYDER et al (1998) and SOBRINO et al (2000).

Regarding atmospheric effects, the AVHRR sensor was built to make measurements in one of the "atmospheric windows" (10.3-12.5 µm wavelength), where the influence of atmospheric absorption, especially due to water vapour, is as small as possible. If the atmosphere is dry and visibility is good, then, as several authors assume, there is no atmospheric contribution to the thermal sensor's signal (e.g. KERR et al 1992). Some of the more sophisticated LST retrieval methods make use of atmospheric transmittance and radiance models, like MODTRAN, to quantify the atmospheric effect on a physical basis (e.g. YANG & YANG 2006). Preparations for global scale

monitoring of LST, where detailed information on atmospheric temperature and water vapour content are hardly available, distinguish SWT parameters for cold and warm, as well as dry and wet atmospheric conditions (YU et al 2008).

The brightness temperatures BT_4 and BT_5 of both channels of the AVHRR determined by the sensor algorithm then are fed into the basic split window equation:

$$T_0 = BT_4 + a \cdot (BT_4 - BT_5) + b \tag{3.1}$$

Where coefficients a and b account for atmospheric conditions and surface emissivity, respectively. Some SWT methods determine these coefficients solely depending on ϵ_T of channels 4 and 5, while others also incorporate the water vapour dependence in non-linear equations (DASH et al 2002).

In this study three different techniques were chosen, in order to quantify the difference between using a simple SWT and using a more complex one. The first SWT algorithm was chosen because of its simple structure and semi-empirical consideration of vegetation cover, although it was developed for semi-arid regions (KERR et al 1992). Additionally, it is based on the basic algorithm for SWT and is designed to work without the need for atmospheric correction and emissivity estimation, as most other algorithms. The coefficients of equation (3.1) only vary as a result of land cover and were determined during a case study in southern France (Table 3-3). Actual surface temperature is determined by a weighting coefficient C_{NDVI} depending on the *Normalized Difference Vegetation Index* (NDVI)

$$C_{NDVI} = \frac{(NDVI - NDVI_{min})}{(NDVI_{max} - NDVI)} \tag{3.2}$$

The final surface temperature is determined from the weighted mean between the potential soil and vegetation temperatures (T_{veg} and T_{soil}) which are calculated by using equation (3.1) and the coefficients of KERR et al (1992)

$$T_0 = C_{NDVI} \cdot T_{veg} + (1 - C_{NDVI}) \cdot T_{soil} \tag{3.3}$$

The second method presented here is a modification of the widely used SWT equation of BECKER & LI (1990) for use with NOAA-16 and -17 sensors

$$T_0 = c + d \cdot \frac{BT_4 + BT_5}{2} + e \cdot \frac{BT_4 - BT_5}{2} \tag{3.4}$$

The coefficients used in this equation have to be calibrated according to atmospheric conditions, emissivity values and sensor specifications. The offset of this equation is constant, but the other two coefficients are related to mean thermal emissivity (ϵ_T) and the emissivity difference ($\Delta \epsilon_T$) between channel 4 and 5, if sensor characteristics and typical atmospheric conditions are known (BECKER & LI 1990). YANG & YANG (2006) used the MODTRAN atmospheric transmittance and radiance algorithm, to simulate 4 different model atmospheres for the main land of China and found for NOAA-17, that c = 0.89 and d and e are related to emissivity by

$$d = 1 + 0.1549 \frac{1 - \varepsilon_T}{\varepsilon_T} - 0.03959 \frac{\Delta \varepsilon_T}{\varepsilon_T{}^2} \tag{3.5}$$

$$e = 4.0578 + 11.7207 \frac{1 - \varepsilon_T}{\varepsilon_T} + 1.55951 \frac{\Delta \varepsilon_T}{\varepsilon_T{}^2} \tag{3.6}$$

The third SWT algorithm used in this study was developed by ULIVIERI et al (1994) and is a variant of the basic SWT equation that incorporates thermal emissivity. If atmospheric water vapour content is less than 3.0 g/cm^3, LST is defined as

$$T_0 = BT_4 + 1.8(BT_4 - BT_5) + 48(1 - \varepsilon_T) - 75 \Delta \varepsilon_T \tag{3.7}$$

This simple technique was found to correlate well with ground measurements by VASQUEZ et al (1997) and is recommended by YU et al (2008) for application in heterogeous, large scale investigations, because of its low sensitivity to emissivity errors, but acceptable precision performance under different conditions. VASQUEZ et al (1997) report, that the typical temperature deviation due to a 1% error in estimated emissivity is about 0.8 K for the ULIVIERI et al (1994) algorithm, while the BECKER & LI (1990) type algorithm shows a deviation of about 1.4 K due to this emissivity error.

To determine the actual emissivities of the different land surface types without any additional information about the true NDVI, it is assumed that, if vegetation cover is present in humid climates, then the NDVI is greater than 0.5. After SOBRINO et al (2000), the mean emissivity of both thermal bands is therefore set to 0.985 for vegetated pixels, but following VASQUEZ et al (1997) and the investigations on emissivities cited in SOBRINO et al (2000), $\Delta \varepsilon$ is assumed to be 0.010. In the case of built up areas or in regions of intensive agricultural use after harvest, where only a small number of trees and meadows remain, we suppose the NDVI to be smaller than 0.2. Again, following SOBRINO et al (2000) and their analysis of typical land surface emissivities, the mean thermal emissivity ε_T is set to 0.970 and $\Delta \varepsilon_T = 0.010$. This relates to a reflectivity of the AVHRR channel 1 of 0.25 in the equations derived by SOBRINO et al (2000). Solving the above equations leads to the parameters c/d/e in Table 3-3.

Table 3-3: Coefficients a & b (KERR et al 1992) and c, d & e (YANG & YANG 2006).

	a	b	c	d	e
Vegetation	2.6	-2.4	0.89	1.002	4.2524
Bare Soil	2.1	-3.1	0.89	1.0044	4.4369

In case of vegetation cover, the ULIVIERI et al (1994) algorithm then reduces to

$$T_0 = BT_4 + 1.8(BT_4 - BT_5) + 0.03 \, K \tag{3.8}$$

and for bare soil surfaces to

$$T_0 = BT_4 + 1.8(BT_4 - BT_5) + 0.69 \, K \tag{3.9}$$

Applying these three methods on theoretical brightness temperatures reveals remarkable differences in estimated land surface temperatures. For comparison only, graphs showing the original parameterisation of equation (3.4) by BECKER & LI (1990) are also presented in the following figures.

If the difference in brightness temperatures of channel 4 and 5 (dBT) is fixed to a typical value (for example 1.3 K), then the difference of these SWTs in derived LST is nearly constant for a broad range of brightness temperatures (Fig. 3-5). This arises from the fact that in both basic SWT equations, the relationship between mean brightness temperature and LST is nearly 1:1. Only the offset varies significantly.

Moreover, the influence of dBT on the calculated LST is expressed differently, when comparing the different SWT parameterisations. Typically, BT_4 is between 1 and 2 K higher than BT_5. For that reason, Fig. 3-6 shows the relationship of LST to BT_5, with a fixed BT_4 of 290.0 K. Apparently, two SWT methods developed for the second generation of AVHRR sensors (BECKER & LI 1990 and KERR et al 1992) show a nearly parallel slope in Fig. 3-6, but about 4.5 K difference in absolute LST. The YANG & YANG (2006) parameterisation of the BECKER & LI (1990) equation, on the other hand, displays a different dependency of LST to dBT, especially in the case of a vegetated surface. The ULIVIERI et al (1994) model has a similar slope than the YANG & YANG (2006) equations and represents a moderate relationship of LST to brightness temperature difference.

Still the expected difference in LST, in the typical dBT range of the AVHRR channels, is 2 to 3 K for vegetated surfaces between the algorithms used in this study. In case of bare soil, the computed LST is in the range of about 1 K for all algorithms beside the KERR et al (1992) equation, which seems to underestimate soil surface temperatures by 4 to 5 K.

Given the evaluations in literature (QUADRIARI et al 2002, VASQUEZ et al 1997, YU et al 2008), the ULIVIERI et al (1994) algorithm is supposed to be the most reliable SWT for heterogeneous landscapes like the Upper Danube catchment. Based on this analysis, the effort to validate simulated land surface temperatures, presented in the following chapter will concentrate on correlations between remotely sensed and simulated land surface temperatures. Only in regions with intensive agricultural land use, soil surface temperature can be estimated from NOAA-AVHRR in late autumn. Here, the bare soil parameterisations are applied depending on simulated vegetation cover, even if the real heterogeneous land cover could have a NDVI greater than 0.2.
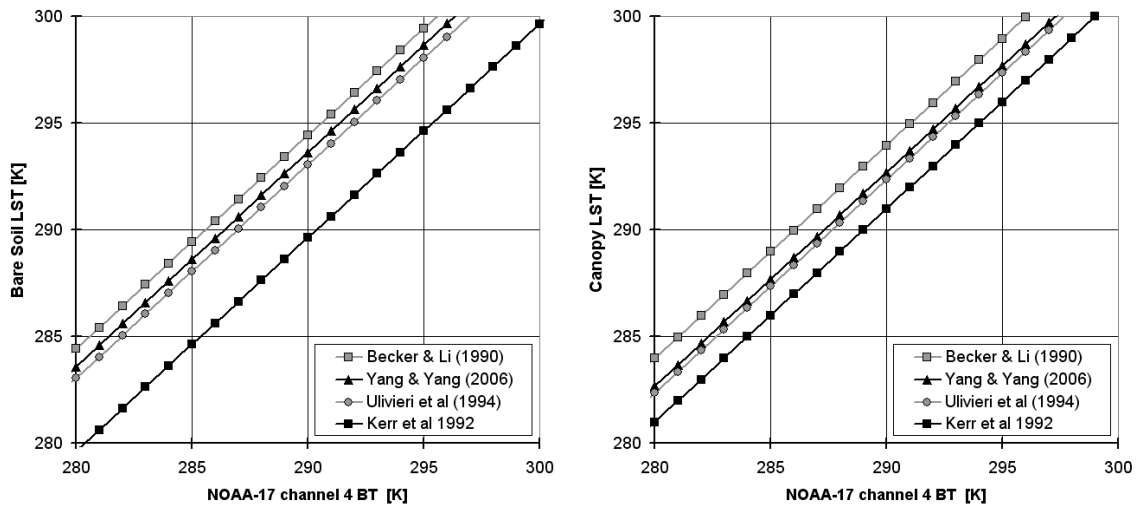
Fig. 3-5: Relationship of LST to channel 4 BT with dBT = 1.3 K.
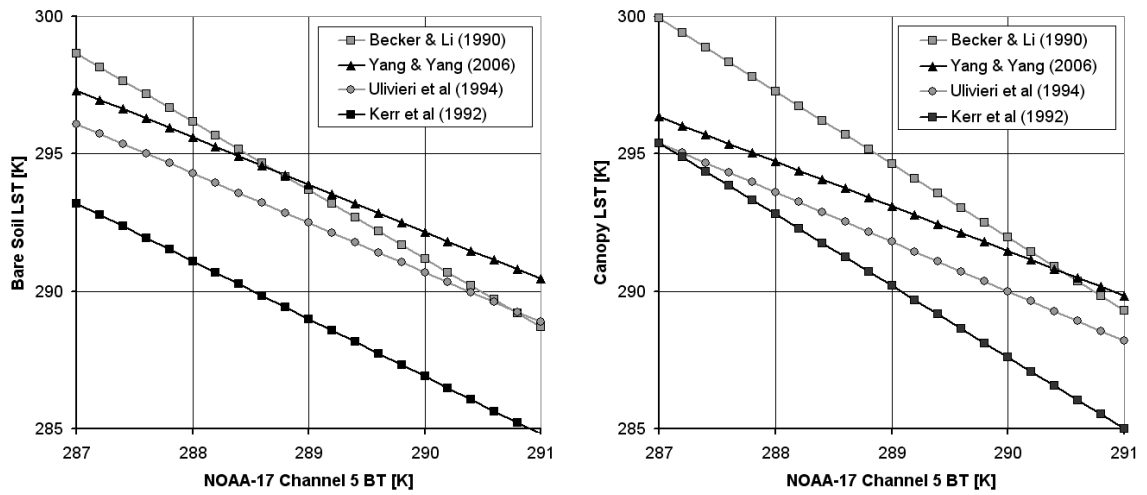
Fig. 3-6: Relationship of LST to channel 5 BT (with channel 4 BT of 290.0 K).

4. Description of Soil Processes

4.1. The Modular Land Surface Model PROMET

The Soil-Vegetation-Atmosphere-Transfer (SVAT) model PROMET (PROcesses of Mass and Energy Transfer) is a raster-based, modular framework consisting of several interdependent but coupled modules to simulate water, energy and matter fluxes on the catchment scale. The original model for the computation of land cover-dependent evapotranspiration with the *Penman-Monteith* equation (as in MAUSER & SCHÄDLICH 1997) includes the following modules:

(a) The radiation module calculates the radiation balance according to its geographical location, sun angle and cloud cover.

(b) The soil hydraulic module calculates the soil water content as a function of infiltration, exfiltration, percolation and capillary rise (EAGLESON 1978).

(c) The plant physiological module calculates the water transport in plants as a function of the specific stomatal resistance, determined by absorbed photosynthetic active radiation, temperature, humidity and soil moisture (BALDOCCHI et al. 1987).

(d) The aerodynamic module calculates the removal of transpired water vapour into the atmosphere (MONTEITH & UNSWORTH 2008).

(e) The snow module ESCIMO, which was recently updated by PRASCH et al (2008) after STRASSER et al (2007), calculates the surface processes in case of snow cover.

Recent developments in PROMET account for the processes needed to close the energy and matter cycles at the land surface and the coupling of transpiration to the biophysical processes of a dynamic vegetation (Fig. 4-1). The advancements include:

(f) An alternative two-layer dynamical biophysical canopy module (HANK 2008) based on the work of FARQUHAR et al (1980) that calculates the transpiration, biomass production and energy balance of the canopy,

(g) improvements of the radiation module to calculate incoming radiation for both vegetation layers and the ground surface (HANK 2008, MAUSER & BACH 2008),

(h) a multi-layer soil hydraulics module that extends the original EAGLESON (1978) approach to calculate surface and interflow runoff (MAUSER & BACH 2008)

(i) an energy balance algorithm for non-vegetated surfaces and the soil surface below canopies,

(k) and the Soil Heat Transfer Module (SHTM) that calculates soil energy fluxes and storage (including soil freezing) for the soil layer stack, both presented in this work.

Therefore, PROMET, in its latest version (MAUSER & BACH 2008), extends the classical SVAT scheme by coupling energy and water fluxes at the land surface with biophysical processes (Fig. 4-1). The main driving meteorological variables (precipitation, air temperature, wind speed, air moisture and cloud cover) needed for simulation can be obtained from measured time series, for example from German Weather Service (*Deutscher Wetter Dienst*, DWD) climate stations data. For the simulation of future Climate Change scenarios, possible future weather trends based on DWD data from 1960 to 2006 can be generated with the stochastic weather generator (MAUSER et al 2007). Additionally, PROMET has the ability to use output variables of regional climate models (RCM) for scenario modelling. As RCMs like REMO, MM5 or CLM work on different temporal and spatial scales not compatible with PROMET, the meteorological scaling tool SCALMET (MARKE 2008) was developed, which conserves energy and mass flux densities between land surface and atmosphere even in alpine terrain.
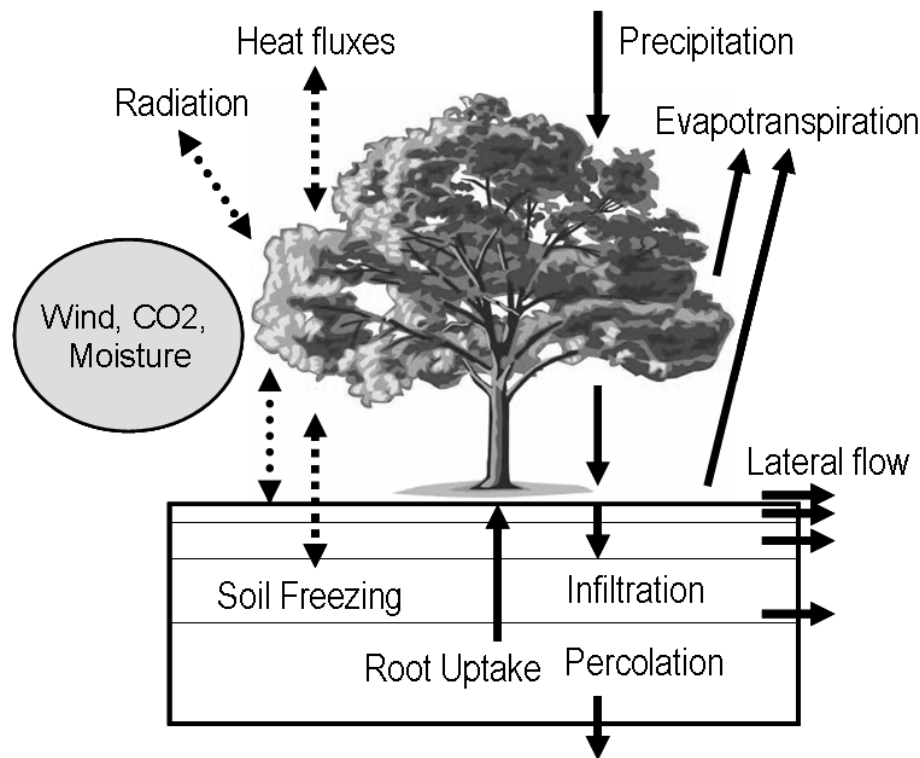
Fig. 4-1: PROMET energy and mass transfer at the land surface without snow cover.

Like most SVAT models, PROMET describes the processes at the land surface as vertical, one-dimensional fluxes, aside from lateral runoff. For the adequate representation of future changes in fluxes and storage variables, the submodels of PROMET are not calibrated to any site-specific characteristics. All static vegetation and soil parameters are predefined on the basis of field measurements, literature values or transfer functions. The basic, spatially distributed input data needed for simulation runs are raster maps of elevation, slope and exposition, as well as raster maps of vegetation and soil type classes.

To close the water cycle at the catchment scale, additional modules describing the ground water retention and the flow through channels, lakes and man-made reservoirs are available within the PROMET framework. For a climatological study period of 33 years, the water balance, daily discharges and significant return periods at several gauges in the Upper Danube basin were reproduced with good accuracy and without calibration against measured discharge (MAUSER & BACH 2008).

The processes of water and heat transfer in soils represented in PROMET are depicted in Fig. 4-2, together with their main influences on root zone processes. The vertical distribution of soil temperatures is driven by an interannual lower boundary condition and the ground heat flux provided by an energy balance algorithm at the soil surface. Soil temperature influences the biochemical activity in the root zone and can affect the soil water distribution via soil water freezing. The energy fluxes computed by SHTM in return are impacted by the actual water content supplied by the soil water model of PROMET. Additionally, both the soil water and the soil energy cycles are connected by the evaporation of water at the soil surface.
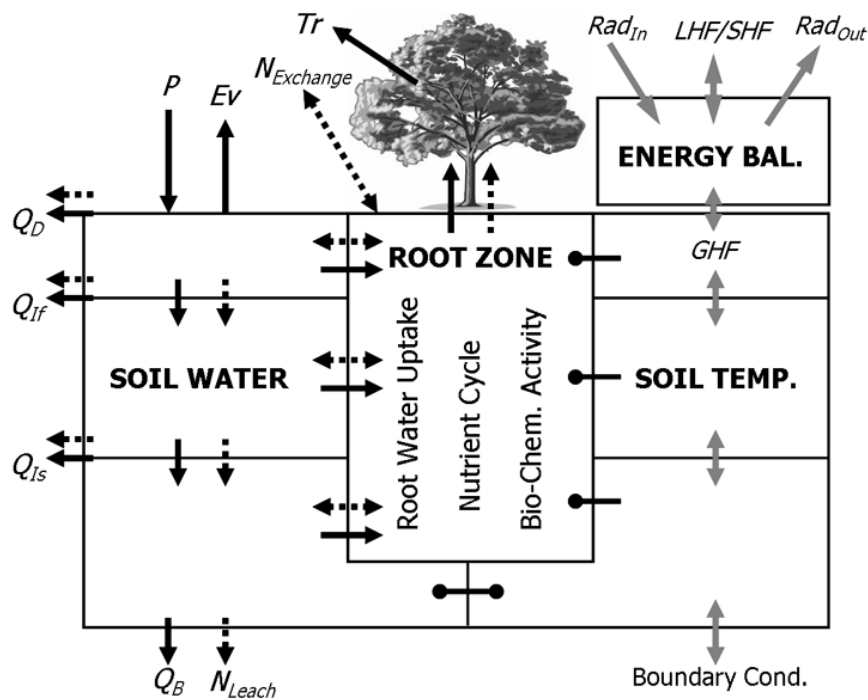
Fig. 4-2: Energy and mass transfer on and inside the soil layer stack of PROMET.

In the following, a detailed description of all soil physical processes and parameters related to the simulation of soil temperatures with SHTM are presented. After a short summary of the basic principles of the soil water module, an in-depth description of the equations, the parameters, the boundary conditions and the chosen model geometry of SHTM is given. Three surface ground heat flux models of differing complexity for snow-free conditions are presented and complemented with a soil surface heat transfer algorithm in case of snow cover.

4.2. The Soil Moisture Module

To simulate water fluxes in the soil column, PROMET uses a modified version of the *Eagleson* model (Eagleson 1978, Mauser & Schädlich 1997) that predicts the infiltration and exfiltration of the soil column. In recent years, the soil layer stack of the model was extended to compute up to 4 layers (Mauser & Bach 2008) and implemented in the decision support system DANUBIA (Ludwig et al 2003) along with other new modules for PROMET. The algorithm basically distinguishes between "wet" and "dry" time steps. Water sources for a soil layer are infiltration from above (effective precipitation or percolation from upper soil layer) and capillary rise from the groundwater table or the lower soil layer. Water sinks can be evaporation from the top soil layer, root water uptake (all layers with roots) and gravitational drain (which is summed up with capillary rise for the net percolation of a soil layer). Actual infiltration into a soil layer is handled by the *Philip* equation Philip (1957), excess water is added to lateral flow. If surface infiltration into the top soil layer exceeds the infiltration capacity, the remaining water is added to the simulated overland flow. If the net percolation of a soil layer exceeds the infiltration capacity of the soil layer below, the remaining water is added to the model output "interflow". All computations in the soil layer stack are run "top down", which means that the most active upper layer is run first and the lowest, least dynamic layer is run last.

4.2.1. Derivation of Hydraulic Parameters

The following section describes the derivation of the static parameters used to compute an analytic solution of the *Philip* equation based on the concepts of Eagleson (1978) and Brooks & Corey (1964). The classification of soils and the derivation of the hydraulic parameters for these classes are found in Chapter 5.

The variability of the volumetric water content Θ of a homogenous soil column is described by the one-dimensional concentration dependent diffusion equation of Philip (1957):

$$\frac{\partial \Theta}{\partial t} = \frac{\partial}{\partial z}\left[D(\Theta)\frac{\partial \Theta}{\partial z}\right] - \frac{\partial k(\Theta)}{\partial z} \qquad (4.1)$$

where t is the time in [s], z is the depth in [cm], $k(\Theta)$ is the effective hydraulic conductivity in [cm/s].

Herein the hydraulic diffusivity $D(\Theta)$ in [cm^2/s] is defined as

$$D(\Theta) = k(\Theta)\frac{\partial \Psi(\Theta)}{\partial \Theta} \qquad (4.2)$$

with $\Psi(\Theta)$ being the soil matrix potential in [cm].

To find an analytic solution of the *Philip* equation, an approximation of $\Psi(\Theta)$ and $k(\Theta)$ based on measurable, static soil parameters must be found. Eagleson (1978) applied

the equation proposed by Brooks & Corey (1964) to describe the relationship between soil moisture and matrix potential

$$\Psi(s) = \Psi(1) \cdot S^{-\frac{1}{m}} \tag{4.3}$$

where $\Psi(1)$ is the air entry tension in [cm], also called *bubbling pressure head* (bph), S is the saturation of the effective pore space n with water ($S = \Theta/n$) and m is the *pore-size distribution index* (psdi).

"The *bubbling pressure head* represents the value of the suction head at which, during dewatering of a sample, gas is first drawn through the soil sample." (Eagleson 1978) The psdi is the slope of the retention curve, where the soil suction increases exponentially with decreasing soil water content Θ.

The hydraulic conductivity $k(\Theta)$ for the unsaturated soil matrix after Brooks & Corey (1964) is

$$k(\Theta) = k_f \cdot S^c = k_f \cdot S^{(2+3m)/m} \tag{4.4}$$

where k_s is the saturated hydraulic conductivity and

$$c = (2 + 3m) / m \tag{4.5}$$

Because n is constant for a simulation time step, the approximative equation of the diffusivity $D(\Theta)$ is

$$D(\Theta) = k_s \cdot s^c \cdot \frac{\partial}{\partial \Theta}\left(\Psi(1) \cdot s^{-\frac{1}{m}}\right) = \frac{|\Psi(1)| \cdot k_s}{n \cdot m} s^{c-\left(\frac{1}{m}\right)-1} \tag{4.6}$$

$$\rightarrow \quad D(\Theta) = \frac{|\Psi(1)| \cdot k_s}{n \cdot m} \cdot s^d \tag{4.7}$$

$$\text{with} \quad d = c - (1/m) - 1 \tag{4.8}$$

and can be solved if the following static parameters are known:

- saturated hydraulic conductivity k_s
- bubbling pressure head $\Psi(1)$
- pore-size distribution index m
- effective porosity n

4.2.2. The Eagleson-type Model of Soil Water Dynamics

The soil water algorithm implemented in PROMET is based on the model proposed by EAGLESON (1978) for homogenous soil columns, but was enhanced by MAUSER & BACH (2008) for simulating soil moisture movement in a multi-layer soil model. Instead of applying the *Eagleson* equations to a single homogenous root zone layer, each layer of the soil model is assumed to be one *Eagleson*-type homogenous soil column. The following initial and boundary conditions were set by EAGLESON (1978) to assure the soundness of his analytical solution of the *Philip* equation and were accounted for in the PROMET soil water model.

The ground water table is much deeper than the bottom of the simulated soil layer, so the medium is considered to be effectively semi-infinite. Sensitivity analysis has shown that the minimum distance between the simulated soil compartment and the groundwater table has to be greater than the *bubbling pressure head* of the lowest soil layer, because the bph describes the theoretical height of the capillary fringe.

The soil moisture is spatially uniform throughout the soil column. This is not true for the multi-layer soil module, but water transfers into and out of a soil layer are modelled assuming that the surrounding soil matrix has the same characteristics as the computed layer.

Even heterogeneous vegetation cover has its roots distributed evenly throughout the soil column in the single layer model. The multi-layer model root density is definable for each individual soil layer, but is homogenous throughout a soil layer.

Based on these basic assumptions, EAGLESON (1978) defined the following conditions for the ratios of exfiltration and infiltration:

$i_p < f_i^*$: If the precipitation intensity i_p is lower than infiltration capacity f_i^*, the precipitated water can infiltrate and the soil (layer) surface is unsaturated ($S_i \leq 1$), because the soil moisture is transferred to the soil matrix below.

$Ep < f_e^*$: If the evaporation demand Ep is lower than the exfiltration capacity f_e^*, actual evaporation is not inhibited and the soil (layer) surface does not run dry ($S_i \geq 0$), because the soil (layer) provides enough water for surface evaporation.

$i_p \geq f_i^*$: If the precipitation intensity exceeds the infiltration capacity, the soil (layer) surface can be saturated ($S_i = 1$) and water runs off laterally at the soil (layer) surface.

$Ep \geq f_e^*$: If the evaporation demand exceeds the exfiltration capacity, the soil (layer) surface dries up ($S_i = 0$) and the actual evaporation equals the exfiltration capacity of the soil (layer).

This simple concept was extended by MAUSER & BACH (2008) to incorporate the simulation of lateral runoff and vertically explicit soil moisture contents. Validation runs showed a better correlation of simulated surface soil moisture patterns with remote sensing (LÖW et al 2007) and more realistic time series of soil layer moisture compared with field measurements (see LÖW 2008).
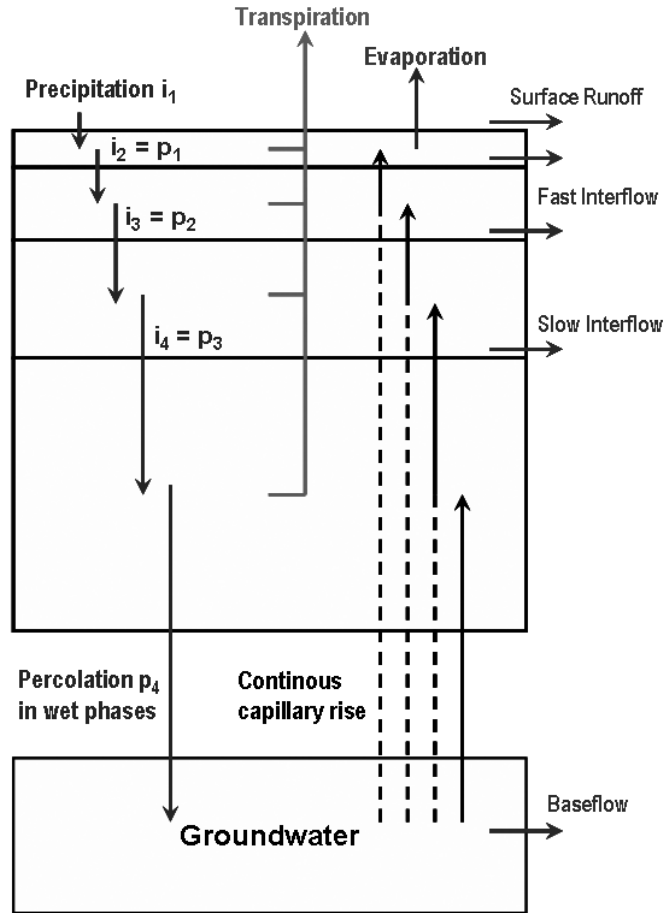
Fig. 4-3: Soil water fluxes simulated by the modified 4-layer Eagleson model.

The infiltration and exfiltration capacity of a soil column is defined by the equations provided by PHILIP (1969). The increase in soil moisture during infiltration into a semiinfinite soil with an initial soil moisture content $\Theta_0 = n \cdot S_0$ is defined as

$$\int_0^\infty (\Theta - \Theta_0)\, dz = \int_{\Theta_0}^{\Theta_1} z\, d\Theta = F_i(t) - K(\Theta_0)t \qquad (4.9)$$

with Θ_1: effective water content at the soil surface, $F_i(t)$: sum of infiltrated water [cm], $K(\Theta_0)$: unsaturated hydraulic conductivity at water content Θ_0.

The reduction in soil water content between precipitation events (with the transpiration rate E_V of the vegetation cover) is obtained by the formula

$$\int_0^\infty (\Theta_0 - \Theta)\, dz = \int_{\Theta_1}^{\Theta_0} z\, d\Theta = F_e(t) + [K(\Theta_0) + E_V]t \qquad (4.10)$$

with $F_e(t)$: sum of exfiltrated water [cm].

At the same time, an amount of water equal to $K(\Theta_0) \cdot t$ percolates out of the considered soil compartment.
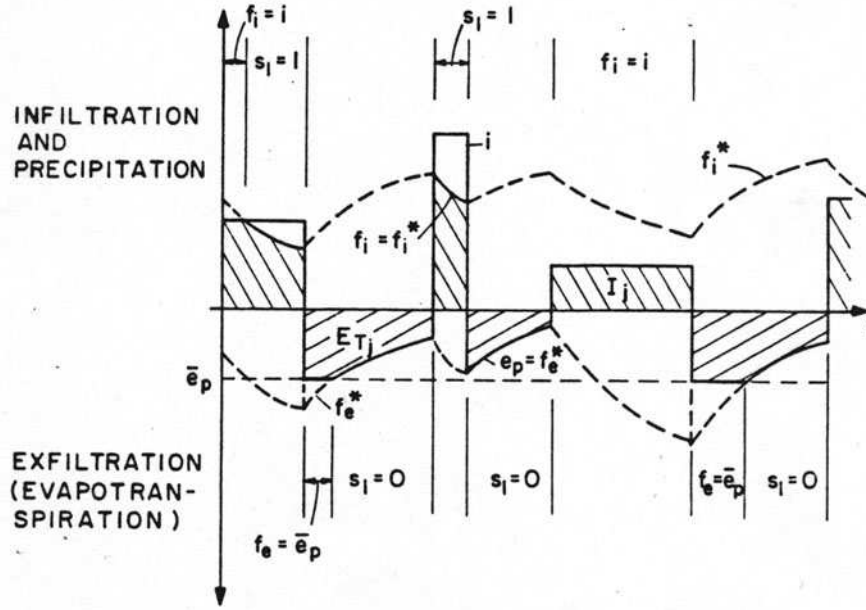
Fig. 4-4: Boundary conditions at the soil surface during wet and dry periods (EAGLESON 1978).

By series expansion and transformation of the original *Philip* equation (4.1) and by use of the approximations (4.3) and (4.4) of BROOKS & COREY (1964), the **infiltration capacity f_i*** after EAGLESON (1978) is defined as

$$\frac{f_i^*(t,s_0)}{K(1)} = (1-s_0)\left[\frac{5n\Psi(1)\varphi_i(d,s_0)}{3\pi mtK(1)}\right]^{\frac{1}{2}} + \frac{1}{2}\left[1+s_0^{\,c}\right] \tag{4.11}$$

with the nondimensional **infiltration diffusivity φ_i**, which CRANK (1956) determined for even-numbered d.

$$\varphi_i(d,s_0) = (1-s_0)^d * \left[\frac{1}{d+\frac{5}{3}} + \sum_{n=1}^{d}\frac{1}{d+[\frac{5}{3}-n]}\binom{d}{n}\left(\frac{s_0}{1-s_0}\right)^n\right] \tag{4.12}$$

The analogous exfiltration capacity f_e* is

$$\frac{f_e^*(t,s_0)}{K(1)} = s_0^{\,1+d/2}\left[\frac{n\Psi(1)\varphi_e(d)}{\pi mtK(1)}\right]^{\frac{1}{2}} - \frac{Me_v}{K(1)} \tag{4.13}$$

with the **exfiltration diffusivity φ_e** for even-numbered d.

$$\varphi_e(d) = \left[1+1,85\sum_{n=1}^{d}(-1)^n\binom{d}{n}\frac{1}{1,85+n}\right] \tag{4.14}$$

Equations (11) and (13) are the simulation equations for infiltration and exfiltration.

As mentioned before, the percolation is only a function of the hydraulic conductivity $K(S_0)$ of the soil matrix with the initial saturation S_0. Therefore, the percolation velocity v is

$$v = K(S_0) \tag{4.15}$$

After GARDNER (1958) the soil hydraulic conductivity for capillary rise is related to the soil suction Θ by the power function

$$K(\Theta) = a * \Psi(\Theta)^b \tag{4.16}$$

If the surface of the soil compartment is dry and the matrix potential above the groundwater table (depth Z) is equal to the *bubbling pressure head* $\Psi(1)$, the velocity ω of the capillary rise is defined as

$$\frac{\omega}{K(1)} = B * \left[\frac{\Psi(1)}{Z} \right]^{mc} \tag{4.17}$$

The relation of the empirical parameter B to the pore-size distribution index is

$$B = 1 + \left[\frac{1,5}{m \cdot c - 1} \right] \tag{4.18}$$

As a result, the equation for the capillary rise in the E*agleson*-model with the constraint $\omega / e_p < 1$ is

$$\frac{\omega}{K(1)} = \left[1 + \frac{1,5}{mc - 1} \right] \left[\frac{\Psi(1)}{Z} \right]^{mc} \tag{4.19}$$

So the effective netto percolation p of the computed soil compartment is

$$p = (v - \omega) * t \tag{4.20}$$

Equations (4.11), (4.13) and (4.20) now provide descriptions of the three relevant processes for the vertical movement of soil moisture on the basis of the parameters described in the previous section. The regionalization of these parameters is presented in Chapter 5.

4.3. THE SOIL HEAT TRANSFER MODULE SHTM

4.3.1. BASIC CONCEPTS OF SOIL HEAT TRANSFER

Basis for the computation of soil temperature are the one-dimensional, conductive heat transfer equations

$$G(z) = -\lambda \frac{\partial T}{\partial z} \tag{4.21}$$

$$C_s \frac{\partial T}{\partial t} = \frac{\partial}{\partial z}\left(\lambda \frac{\partial T}{\partial z}\right) \Rightarrow \frac{\partial T}{\partial t} = \frac{\lambda}{C_s}\left(\frac{\partial^2 T}{\partial z^2}\right) \tag{4.22}$$

where $G(z)$ is the heat flux [W/m^2] at depth z, C_s is the heat capacity [J/kgK] and λ is the heat conductivity [W/mK].

For large enough, homogenous layers and a fixed time step, it is possible to reduce the heat flow $G_{1,2}$ from the mean depth of layer 1 (z_1) to the mean depth of layer 2 (z_2) to

$$G_{1,2} = -\lambda \cdot \frac{T_1 - T_2}{z_2 - z_1} \tag{4.23}$$

where λ is the heat conductivity between these two points. In SHTM λ is the heat conductivity of the lower (in this case thicker) soil layer and fluxes are positive if upward towards the soil surface.

The Newman criterion defines the minimum distance between two layer means (points) if heat flux parameters and the simulation time step are known, so there is no oscillation between those two points

$$\Delta z = \sqrt{\Delta t \cdot 2\lambda / C_v} \tag{4.24}$$

with C_v: volumetric heat capacity [J/m^{3}K]. For example, if λ = 2,0 W/mK, C_v = 1.7*10^6 J/m^{3}K and the typical time step is 3600 seconds, the minimum distance between to layer means has to be 0.09 m. Because this would lead to heat flux oscillations with the geometry applied to the upper soil layers, a sufficient overclocking is done.

The driving variable of any soil temperature model is the surface ground heat flux G_0, which can significantly change the temperature of the upper soil layer during a time step of one hour. This upper boundary condition can be an empirical surface ground heat flux G_0 or the soil surface temperature T_0 generated by a surface energy balance model (see 4.5). If the upper boundary is forced by a soil surface temperature T_0, the resulting surface ground heat flux is computed by

$$G_0 = -\lambda \cdot \frac{T_0(t) - T_1(t_0)}{z_1} \tag{4.25}$$

Like in the modified *Eagleson*-model, the forcing at the upper boundary is transfered from top down to the next soil layer. Therefore, the temperature $T_1'(t)$ is used to compute the heat flux from the upper layer downwards. This method was tested with measured ground heat flux data and provided the best results for SHTM:

$$T_1'(t) = \frac{-G_0 \cdot \Delta t}{z_1 \cdot C_{v,1}} + T_1(t_0) \tag{4.26}$$

$$G_{1,2} = -\lambda \cdot \frac{(T_1'(t) - T_2(t_0))}{\Delta z_{1,2}} \tag{4.27}$$

After computing all the heat fluxes, the new mean temperature of each layer of the soil layer stack with thickness d_j at time step $t = t_0 + \Delta t$ is calculated by

$$T(t) = \frac{-(G_{upper} - G_{lower}) \cdot \Delta t}{d_j \cdot C_{v,j}} + T(t_0) \tag{4.28}$$

The heat flux commences downwards as described by equations (4.26) to (4.28) with the downward heat flux becoming the upper one of the next lower layer. For the lowest layer n of the soil layer stack (here: n = 4) the lower heat flux $G_{n,n+1}$ is influenced by lower boundary condition T_V, which is computed by an analytical solution (CARSLAW & JAEGER 1959):

$$T_v(z_v, t) = T_{av} + A_y \cdot e^{-z_v/z_D} \cdot \cos\left(\omega(t - t_{max}) - \frac{z_v}{z_D}\right) \tag{4.29}$$

with T_{av}: mean annual air temperature, A_y: annual amplitude of air temperature, z_v: mean depth of virtual layer, t_{max}: time of maximum air temperature and $\omega = 2\pi/\tau$: angular velocity of cosine function, while the damping depth z_D is a function of thermal conductivity λ and volumetric heat capacity C_V. The damping depth z_D, represents the reduction in amplitude of the temperature variation with depth, and is the depth at which the amplitude is e^{-1} (0.37) times its value at the surface

$$z_D = \sqrt{2\lambda/C_V\omega} \tag{4.30}$$

Depending on the chosen angular velocity ω, the damping depth can be calculated for the annual or daily amplitude of the soil temperature. As the daily damping depth A_d for a soil with a relatively high λ (2.0 W/mK) and low C_V (1,700,000 J/m^{3}K) is about 0.18 m, the daily amplitude A_d(2.5 m) at a depth of 2.5 m is negligible

$$A_d(2.5m) = A_d \cdot e^{-2.5/0.18} = A_d \cdot e^{-13.89} = 9.3 \cdot 10^{-7} \cdot A_d \tag{4.31}$$

Therefore, the algorithm applied for the analytical temperature T_v (4.29) does not consider a daily amplitude, but shows a considerable lag of the annual maximum temperature at 2.5 m depth (Fig. 4-5).
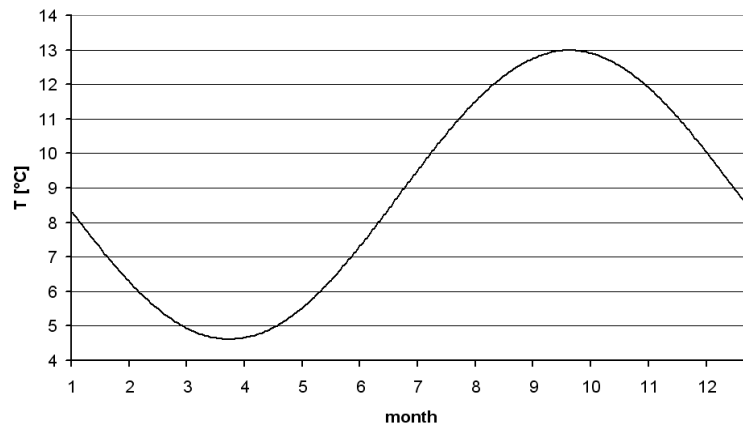
Fig. 4-5: Typical analytical temperature curve at 2.5 m virtual layer depth.

The required air temperature dependent parameters were prepared for the whole Upper Danube watershed from meteorological data for each year from 1970 to 2004. In multiple year simulations T_{av} is updated at the end of the hydrological year to account for annual differences in air temperature. As the deeper soil "remembers" the annual temperature cycle, any simulation run should be started with the mean annual temperature of the previous year.

The convective transport of energy by liquids or vapor is neglected, but the thermal parameters λ and C_v are computed each time step with regard to the material composition of each soil layer (solids, liquid and frozen water, air). The assumption is that slow moving soil water passing a small temperature gradient has only a small temperature difference to the surrounding soil matrix. On the other hand the volumetric water content is raised, so the volumetric heat capacity increases while temperature stays the same. This equates to an effective increase in stored energy per soil layer when the soil moisture increases, and vice versa. Furthermore, the biggest impact of convective heat transfer on simulated temperature is in times of high infiltration. However, estimating precipitation temperature of rainstorms is difficult and has a high rate of uncertainty. Simple models equal precipitation temperature to near ground air temperature, but this is critized by authors from other disciplines too (e.g. JANSSEN et al 2007) or simply not true for some regions of the world (ANDERSON et al 1998). More complex algorithms assume it to be equal to the dew point temperature for rain (e.g. MARKS et al 1999), but still the atmospheric processes are not easily parameterized.

Point scale evaluation showed only a minor impact of convective heat transport on predicted soil temperatures for mesoscale simulations with SHTM. When comparing time series simulated with convective transport against time series simulated without it, less then 10% of the simulated hourly soil temperatures differed by more than 0.1 K, while only less then 1% differed by more than 1.0 K. Furthermore, including convective heat transport could not improve the model results in any statistically significant way. Therefore, for the time being we abstained from adding another algorithm with high uncertainty and show in Chapter 6 that conductive heat transfer characterizes long term soil temperature time series soundly.

4.3.2. The Significance of Freezing Water

To include a realistic simulation of winter temperatures and soil freezing, the potential releasable latent energy $LE_{pot,j}$ [J] of the soil water in each layer is computed as soon as the layer temperature drops below the freezing point. $LE_{pot,j}$ of a given layer j acts as a buffer before the soil layer temperature T_j further diminishes. Because some of the water in a soil matrix is influenced by freezing point depression, we included an empirical relationship between liquid and frozen water against the soil temperature $\breve{T}_j$ in °C. The empirical relationship is derived from the laboratory findings of WATANABE & MIZOGUCHI (2002). Because the logarithmic curve is extremely steep for temperatures near the freezing point, we assume soil freezing starts at $\breve{T}_j = -0.1$ °C. Using this empirical approximation, about 70% of the water is frozen at $\breve{T}_j = -1$ °C and about 90% at $\breve{T}_j = -6$ °C. This algorithm agrees well with the findings of NYBERG et al (2001), who measured a reduction in liquid soil water content of about 2/3 for mineral soils below −1 °C.
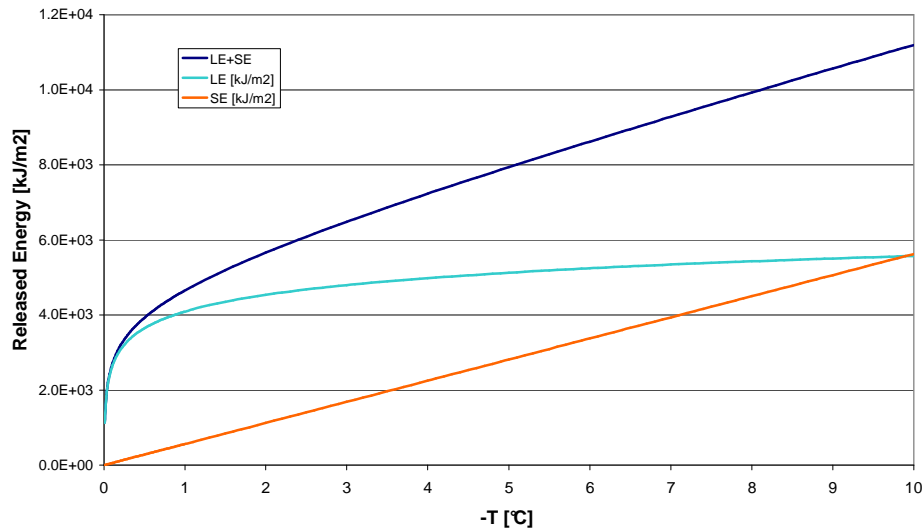
Fig. 4-6: Release of latent (LE) and sensible energy (SE) of soil water during freezing.

Based on this work of WATANABE & MIZOGUCHI (2002), we relate the volumetric content of frozen water in a soil layer to the soil layer temperature by

a)   if $\breve{T}_j < -0.1$ °C then

$$\Theta_{ice,j}(\breve{T}_j) = 0.0 \tag{4.32}$$

b)   if $\breve{T}_j \leq -0.1$ °C then

$$\Theta_{ice,j}(\breve{T}_j) = \left(0.7 + 0.11 \cdot \ln(-\breve{T}_j)\right) \cdot \Theta_j \tag{4.33}$$

So the potential releasable latent energy due to freezing $LE_{pot,j}$ is dependent on the current temperature T_j of the soil layer j

$$LE_{pot,j}(T_j) = -\Theta_{ice,j}(\breve{T}_j) \cdot d_j \cdot 1m^2 \cdot 334000 \frac{J}{kg} \cdot 1000 \frac{kg}{m^3} \tag{4.34}$$

The actual released latent energy due to freezing $\Delta LE_{act,j}$ is the sum of the upper and low heat flux $G_{net,j}$ and the sensible heat change of a soil layer ΔSE_j , which is dependent on the temperature change of the soil layer.

$$\Delta SE_j = (T(t) - T(t_0)) \cdot d_j \cdot C_V \tag{4.35}$$

$$G_{net,j} = G_{upper} + G_{lower} \tag{4.36}$$

$$-G_{net,j} \cdot \Delta t = \Delta LE_{act,j}(t) + \Delta SE_j \tag{4.37}$$

In reality the total released latent energy due to freezing $LE_{act,j}$ is equal to $LE_{pot,j}$. But as $\Delta LE_{act,j}$ is very large compared to the change in sensible energy just below freezing point, the frozen soil procedure in PROMET calculates $LE_{pot,j}$ and T_j in 0.1 K temperature steps for soil temperatures below 273.15 K.

If the net heat flux into a soil layer is negative and $\breve{T}_j > 0$, the algorithm checks if the (negative) potential releasable latent energy of the last time step is greater than the possible change in actual freezing energy due to $G_{net,j}$

$$LE_{pot,j}(T_j(t_0)) > LE_{act,j}(t_0) + G_{net,j} \cdot \Delta t \tag{4.38}$$

If this is true, the temperature of the soil layer is reduced in 0.1 K steps until

$$G_{net,j} \cdot \Delta t \leq \Delta LE_{pot,j}(T_j(t_0) + \Delta T) - \Delta SE_j(\Delta T) \tag{4.39}$$

Then the new soil layer temperature $T_j(t)$ is

$$T_j(t) = T_j(t_0) + C_{V,j} \cdot \Delta SE_j(\Delta T) \tag{4.40}$$

and the new actual released latent energy due to freezing is

$$LE_{act,j}(t) = LE_{act,j}(t_0) + G_{net,j} \cdot \Delta t + \Delta SE_j(\Delta T) \tag{4.41}$$

If the change in energy is positive during a time step, the procedure checks if the energy input would raise the latent energy content above the threshold of the next warmer temperature step (+ 0.1 K)

$$LE_{pot,j}(T_j(t_0) + 0.1\ K) < LE_{act,j}(t_0) + G_{net,j} \cdot \Delta t \tag{4.42}$$

If equation (4.42) is true, T_j and $LE_{act,j}$ are again computed by Eq. (4.40) and (4.41), otherwise the temperature is raised by another step and (4.42) is checked again.

If the soil layer temperature rises above 273.05 K in this way, the procedure is repeated until the released latent energy is filled up again ($LE_{act,j} = 0$).

4.3.3. Influence of Soil Layer Geometry on Heat Flux Simulations

The layer structure of the soil model in PROMET is flexible, but for most applications it is run with four layers of 0.05, 0.15, 0.45 and 1.35 m thickness in descending order. A fifth "virtual" layer acts as the lower boundary condition of the SHTM, describing the temperature in a depth of 2.5 m with an analytical function. This stacking was used for all temperature simulations presented in this work.

The thickness of the individual soil layers was uniformly determined for all soil types, to achieve an identical impact of the model geometry on runoff generation and energy fluxes for all soil type classes. The influence of soil layer geometry on simulated water and energy fluxes has to be considered in any catchment scale model with a low vertical resolution of the soil column. To achieve the best solution for the computation of soil temperatures with four layers, we followed the work of Best et al (2005). Their paper describes the analysis of the errors in amplitude and phase of simulated time series of soil surface temperature for numerical heat transfer models in comparison to the analytical, exact solution of the one-dimensional heat transfer equations (4.21) and (4.22). On the other hand, soil layer depths were constrained by the soil horizon database and the maximum depth of the root zone normally considered by the soil water model. Therefore, the maximum depth was set to 2.0 m and the thickness of the top layer set to 0.05 m. To employ a geometric progression, as recommended by Best et al (2005), we used a multiplier of 3.0, which resulted in a total soil depth of 2.0 meters.
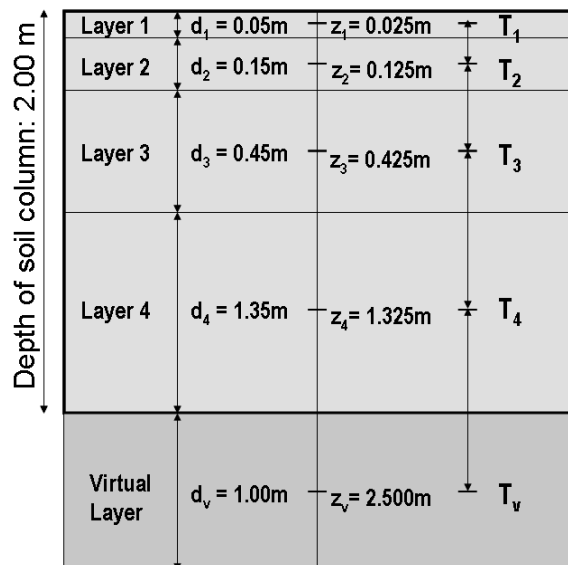
Fig. 4-7: Structure of the SHTM soil layer stack.

To quantify the damping of the daily temperature amplitude A_d of the upper two modelled soil layers, the soil temperature series of a simulation run with fixed thermal parameters was analyzed. λ was set to 2.0 W/mK and C_v to $2.0 \cdot 10^6$ J/m^{3}K, while all other parameters and variables were left unchanged. The presented daily amplitudes of hourly temperatures were simulated at a maize site with clay loam soil in the

central part of the catchment. Fig. 4-8 clearly shows the typical damping of the temperature amplitude at the soil surface $A_d(z_0)$ with increasing depth in conjunction with a good coefficient of determination. Not surprisingly R^2 gets worse with increasing depth, due to the fact that the heat flux pulse gets weaker with depth. The amplitude in the second layer already is less controlled by hourly extreme values at the surface, more by the average surface temperatures around noon and before sunrise.
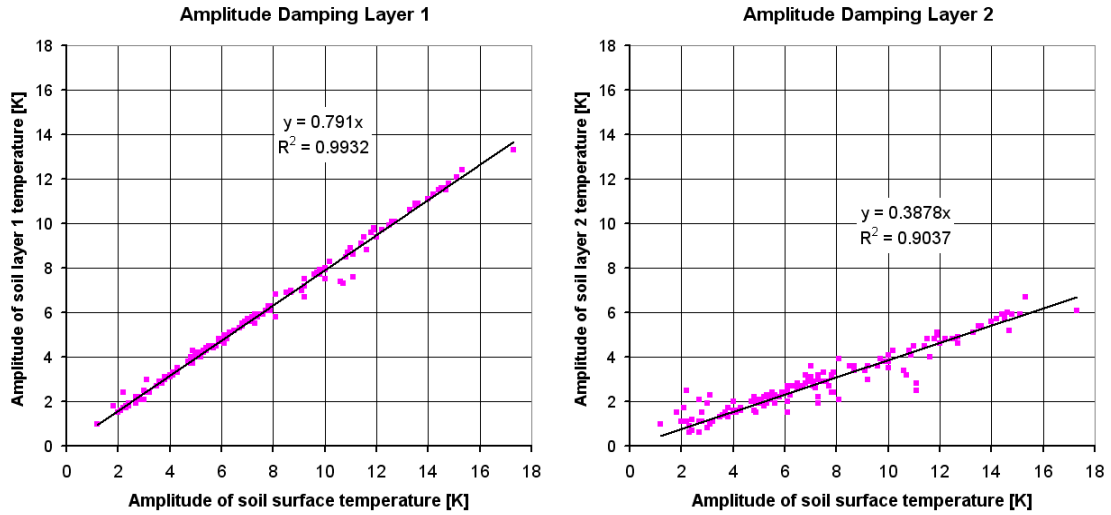
Fig. 4-8: Comparison of the simulated daily temperature amplitude at the soil surface with the simulated daily temperature amplitude in the upper soil layers.

Even more interesting is the comparison of the simulated damping with the theoretical damping. The daily damping depth d_D (4.30) of the test configuration is 0.166 m and the actual damping of the temperature variation at a given depth is

$$\frac{A_d(z)}{A_d(z_0)} = e^{-z/d_D} \qquad (4.43)$$

Dissolving this equation for z leads to

$$z = -d_D \cdot \ln\left(\frac{A_d(z)}{A_d(z_0)}\right) \qquad (4.44)$$

The relationships of $A_d(z)$ to $A_d(z_0)$ are provided by the slopes of the linear regressions shown in Fig. 4-8 for the upper two soil layers. Solving (4.44) leads to the finding that the numerically simulated amplitude of the first layer represents the analytic temperature amplitude at 0.04 m depth and the simulated second layer amplitude is related to the analytical temperature amplitude at 0.16 m. This implies that the daily amplitude of simulated layer-average temperatures should be validated against measurements at these depths and this insight can be used for the determination of soil parameters from measured time series of soil temperature in the future. A similar analysis regarding the annual amplitude over 20 years revealed that the simulated amplitude of the first layer resembles the analytical amplitude at 0.05 to 0.10 m and

the second layer amplitude resembles the one at about 0.25 to 0.30 m. This would mean that the geometry of the soil layer stack and the algorithms used in SHTM underestimate the annual amplitudes of soil temperature compared to the analytical sine-wave solution of heat transfer in soils. But as shown in section 6.4.2, SHTM does not underestimate the annual amplitude when compared to measured data. In fact, the analysis of the annual temperature damping with depth is flawed by an overestimation of the amplitude at the soil surface, as a single hot day can increase it significantly. Still this does not flaw the daily analysis, as on most days of a year the surface temperature amplitude is not influenced by single, hourly peaks.

4.4. The Computation of Thermal Soil Parameters

4.4.1. The Volumetric Heat Capacity

The actual volumetric heat capacity C_v of each soil layer is computed at the beginning of every simulation time step as the sum of the volumetric heat capacities of its constituents C_{vi} and their volumetric fraction x_i

$$C_v = \sum_{i=1}^{n} x_i C_{vi}$$ (4.45)

Liquid and frozen soil water are separately accounted for, hence the heat capacity of a soil layer decreases (see Table 4-1) when freezing. Yet, the volumetric fraction of water increases by 8.9% for soil ice during the phase change, raising the C_V by a small amount. The heat capacity of air is negligible ($0.065 \cdot 10^6$ J/m^{3}K) and is not taken into account.

Table 4-1: Volumetric heat capacity C_V [J/m^{3}K] of soil components.

Minerals	Org. Mat.	Water, liquid	Water, frozen
$2{,}0 \cdot 10^6$	$2{,}5 \cdot 10^6$	$4{,}2 \cdot 10^6$	$1{,}9 \cdot 10^6$

4.4.2. Theory on the Thermal Conductivity of Soils

The calculation of the thermal conductivity λ of a highly complex mixture of solids, liquids and gases like soil is much more problematic. The typical range of λ is between 0.5 and 2.5 W/mK for natural soils. A possible method to measure thermal conductivity is the *Thermal Time Domain Reflectometry*, also called Thermal-TDR, which uses heat pulses and their time lag at different depths (e.g. OCHSNER et al 2001). But as these field techniques are expensive and time-consuming, most non-point simulation models use physical or empirical models to estimate this thermal property. The most commonly used model for n soil components is the physical one from DE VRIES (1963), which characterizes λ in relation to the shape and volumetric fraction x_i of the main constituents of the soil:

$$\lambda = \frac{\sum_{i=1}^{n} k_i \lambda_i x_i}{\sum_{i=1}^{n} k_i x_i}$$ (4.46)

with λ_i being the conductivities of the individual soil components and k_i a coefficient related to the conductivity λ_0 of the main surrounding medium ($\lambda_0 = \lambda_w$ for water or $\lambda_0 = \lambda_a$ for air), the shape-factor $g_d(\alpha)$ and the dimensions of space m

$$k_i = \sum_{m=1}^{3} \left[1 + \left(\frac{\lambda_i}{\lambda_0} - 1 \right) * g_d(\alpha) \right]^{-1}$$
(4.47)

The form-factor α describes the deviation of a soil particle from the spherical shape (α = 1). Oblate spheroids are flattened spheres (α < 1), while prolate spheroids are bulging spheres (α > 1). Flat particles are extremely prolate (α→∞).

Again the shape-factor $g_d(\alpha)$ depends on the form-factor α and is the absolute measure of describing the shape of the rotational ellipsoid in one dimension of space. Dimensions 1 and 2 are perpendicular to the axis of the ellipsoid, dimension 3 is parallel to it.

$$g_1(\alpha) = g_2(\alpha)$$
(4.48)

$$g_3(\alpha) = 1 - 2* g_1(\alpha)$$
(4.49)

For oblate spheroids (α < 1) $g_1(\alpha)$ is

$$g_1(\alpha) = \frac{1}{2} \frac{\alpha^2}{1-\alpha^2} \left[\frac{1}{\alpha^2} + \frac{1}{2\sqrt{1-\alpha^2}} \ln\left(\frac{1-\sqrt{1-\alpha^2}}{1+\sqrt{1+\alpha^2}} \right) \right]$$
(4.50)

In the case of prolate spheroids (α > 1)

$$g_1(\alpha) = \frac{1}{2} \frac{\alpha^2}{\alpha^2-1} \left[-\frac{1}{\alpha^2} + \frac{\pi}{2\sqrt{\alpha^2-1}} - \frac{\arctan\left(\sqrt{\alpha^2-1}\right)}{\sqrt{\alpha^2-1}} \right]$$
(4.51)

The mineral components of the soil are often regarded as one medium, but to distinguish the fraction of clay minerals $x_{claymin}$ from quarts and other minerals, Møberg (1988) empirically found a relation to soil texture

$$x_{claymin} = 0.3 \cdot x_{sand} + 0.4 \cdot x_{silt} + 0.85 \cdot x_{clay}$$
(4.52)

Given the typical form-factors α (after Møberg 1988), one can calculate the coefficients k_i for wet and dry conditions (Table 4-2) with equations (4.47) and (4.51) and solve de Vries' equation (4.46). This parameterisation technique was validated against data by Ochsner et al (2001), Abu-Hamdeh (2003), Cosenza et al (2003) and others.

Table 4-2: Heat conductivity of soil constituents after de Vries (1963), form-factor α (* = if condition is dry) after Møberg (1988) and calculated coefficients k_i.

	Quarts	Clay minerals	Organic material	Liquid water	Frozen water	Moist air
λ [W/mK]	8,8	2,9	0,25	0,57	2,2	0,065
α [-]	2,0	4,0	>10	1 – 7(*)	1 – 7(*)	1
$k_{i\ (wet)}$	0,17	0,52	1,36	1,00	1,00	1,42
$k_{i\ (dry)}$	0,022	0,113	0,676	0,883	0,883	1,000

4.4.3. NUMERICAL APPROXIMATION OF THE SOIL THERMAL CONDUCTIVITY

As DE VRIES stated in 1963, it is assumed that water rests on soil particles as a thin film, dominating as the connecting continuum well below field capacity while air forms bubbles. Not until soil moisture reaches the permanent wilting point (Θ_{PWP}), air becomes the connecting continuum between soil particles. Because of that we follow HANSEN (2002), who suggests using the wet condition k_i up to a soil suction of 1000 hPa (moisture content Θ_{pF3}). To simplify the numerical computation, the *Quadratic Parallel Function* (QPF) of WOODSIDE & MESSMER (1961) is used for moist soil layers instead of the DE VRIES (1963) equation.

$$\lambda = \left[\sqrt{\lambda_s}\left(1-\Phi\right) + \sqrt{\lambda_w}\,\Theta + \sqrt{\lambda_a}\left(\Phi-\Theta\right)\right]^2 \qquad (4.53)$$

with Φ: total porosity of the soil, λ_w: thermal conductivity of water and λ_a: thermal conductivity of air. The thermal conductivity of the solid particles λ_s with the respective $k_{i(wet)}$ values is

$$\lambda_s = \frac{(k \cdot \lambda \cdot x)_{Clay} + (k \cdot \lambda \cdot x)_{Quarts} + (k \cdot \lambda \cdot x)_{OrgMat}}{k_{Clay} \cdot x_{Clay} + k_{Quarts} \cdot x_{Quarts} + k_{OrgMat} \cdot x_{OrgMat}} \qquad (4.54)$$

For larger soil moisture deficits, the actual heat conductivity is interpolated in relation to soil moisture content Θ between λ_{pF3} (conductivity at 1000 hPa, wet condition) computed with the QPF and λ_{pwp} (conductivity at 16000 hPa, dry condition). The thermal conductivity λ_{pwp} of a soil at the wilting point (where x_w: the fraction of water equals the simulated water content Θ_{pwp}) is calculated using DE VRIES' (1963) equation and the k_i coefficients for dry soils ($\lambda_0 = \lambda_a$)

$$\lambda_{pwp} = \frac{\sum_{i=1}^{n} k_i \lambda_i x_i}{\sum_{i=1}^{n} k_i x_i} \qquad (4.55)$$

The interpolation procedure utilizes the following weighting function

$$\lambda = \frac{\Theta - \Theta_{pwp}}{\Theta_{pF3} - \Theta_{pwp}} \cdot \lambda_{pF3} + \left(1 - \frac{\Theta - \Theta_{pwp}}{\Theta_{pF3} - \Theta_{pwp}}\right) \cdot \lambda_{pwp} \qquad (4.56)$$

A validation of the simplified QPF model with different sets of measured data by COSENZA et al (2003) showed that it is in good agreement with the *de Vries* model and has a similar accuracy when predicting the thermal conductivity of soils. It also outperformed the transfer function based on multiple regression developed by COSENZA et al (2003). Their Numerical Simulation (NS) model is also shown in Fig. 4-9, but was not adopted in SHTM.
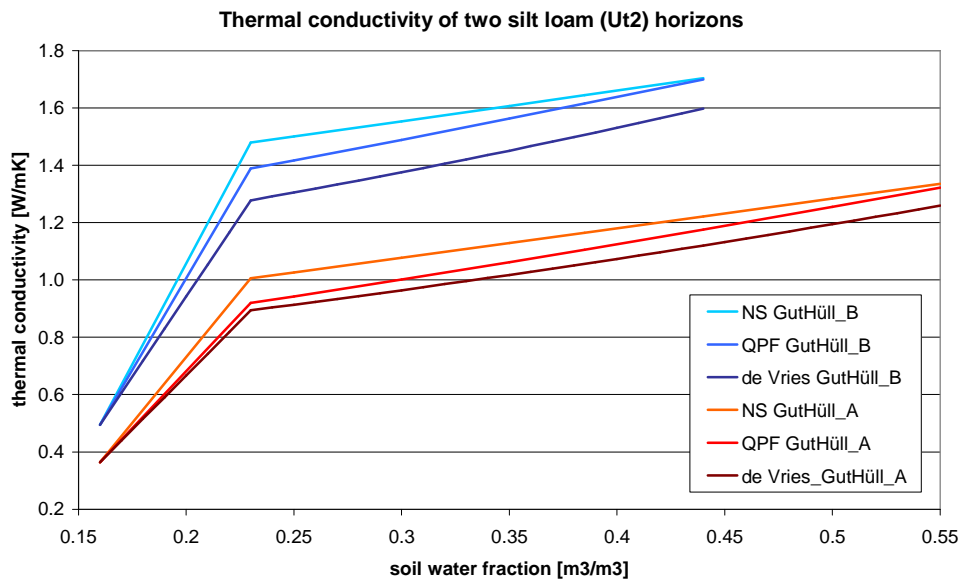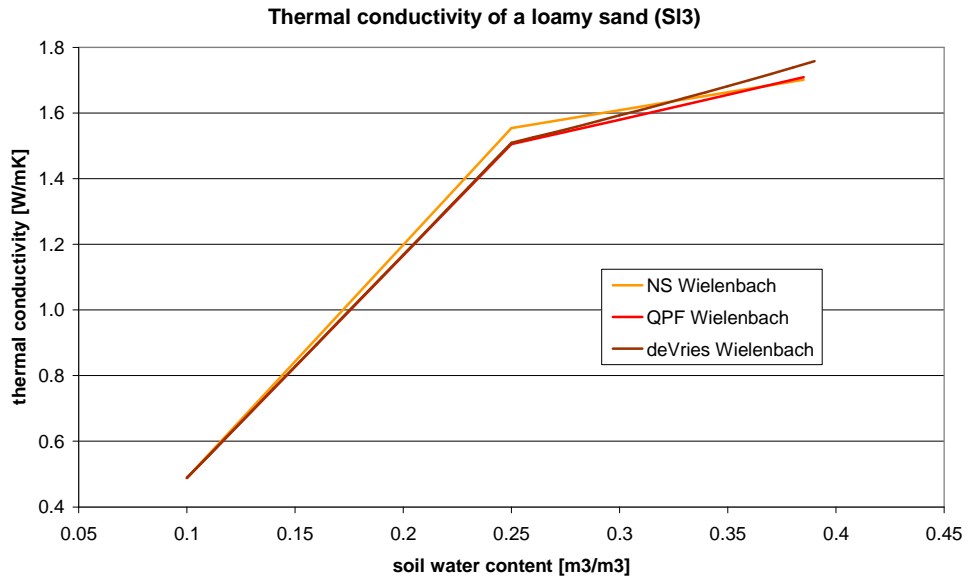
Fig. 4-9: Comparison of thermal conductivity of two soils computed with a) the DE VRIES (1963) equation, b) the QPF of WOODSIDE & MESSMER (1961) and c) the transfer function (NS) of COSENZA et al (2003).

4.4.4. Sensitivity of Thermal Parameters on Soil Properties

For large scale simulations, where few or no soil properties are measurable spatially, it is important to determine the sensitivity of model parameters to spatially distributed input data like soil texture, which have a large inherent uncertainty due to their spatial heterogenity. This analysis can be a guideline for more sophisticated geostatistical techniques to predict soil properties, such as soil-landscape models. Summaries of digital soil mapping and geostatistical techniques used in quantitative soil science are found in MCBRATNEY et al (2003) or SCULL et al (2003).

Obviously, the heat capacity C_V of a soil is most sensitive to the static parameter porosity and the variable soil moisture content (Table 4-1). The sensitivity of C_V to soil moisture changes (~ 4.2 MJ/m^{3}K) is twice as high as the sensitivity to porosity (~ 2.0 MJ/m^{3}K), but as the simulation of soil moisture is even more sensitive to the input parameter porosity, this is the most important spatially variable soil parameter for calculating C_V.

The examination of the sensitivity of the *de Vries* model on its input parameters is definitely more complex. The sensitivity of λ, relative to the soil's solid composition (sand, silt, clay) has two aspects. On one hand, different soil textures have a large impact on the conductivity for a given soil moisture in the lower moisture range, because of the assumption of DE VRIES (1963) that the continuous medium changes below a soil suction of about 1000 hPa. On the other hand, soil suction characterizes the relative state of the soil in terms of water availability, biochemical processes etc. better than the absolute soil water content. Fig. 4-10 shows that soil textural composition has only minimal impact on thermal conductivity related to soil suction. The impacts of more clay minerals (increase of λ) and therefore higher soil moisture (decrease of λ) seem to negate each other when using the *de Vries* model.
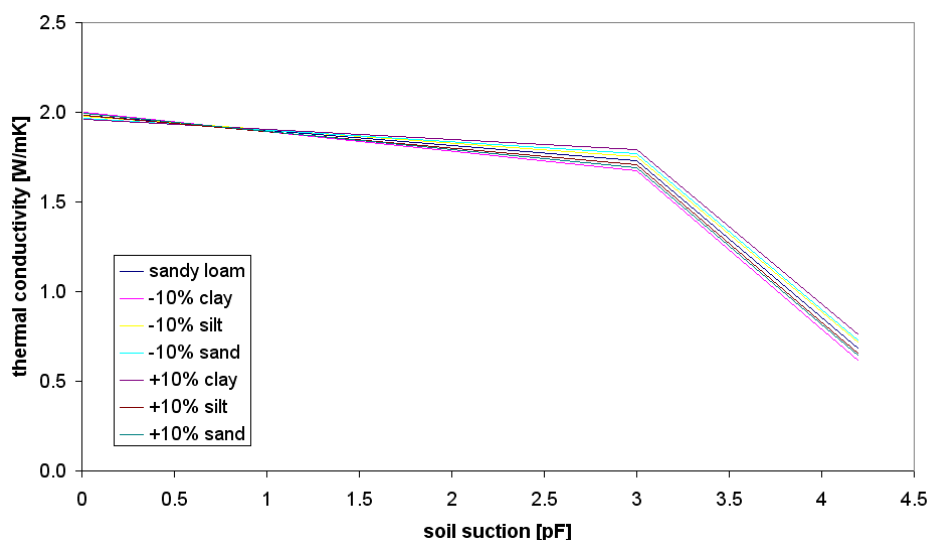
Fig. 4-10: Sensitivity of thermal conductivity to changes in soil texture for a sandy
loam, simulated with the numerical approximation algorithm (see 4.4.3).

The crucial input parameters for the calculation of soil heat conductivity are the total porosity and the organic matter content of a soil layer. The high k_i values and low conductivities of organic matter and air (Table 4-2) have a significant impact on λ when using the *de Vries* model. For this short sensitivity analysis, a typical sandy loam soil is chosen, with a soil matrix consisting of 25% clay, 35% sand and 5% organic matter and having a total porosity of 45%. Fig. 4-11 and Fig. 4-12 clearly show that λ is inversely related to these parameters and both have a similar impact within their typical limits. In contrast to soil hydraulic properties, where soil texture (and porosity) have the strongest influence on soil water balance, the parameterisation of a soil temperature model needs better spatially distributed, vertically heterogeneous organic matter content values. The use of a soil-landscape model, which also utilizes high resolution land use data, seems to be the appropriate tool for this, because organic matter content is strongly related to vegetation type.
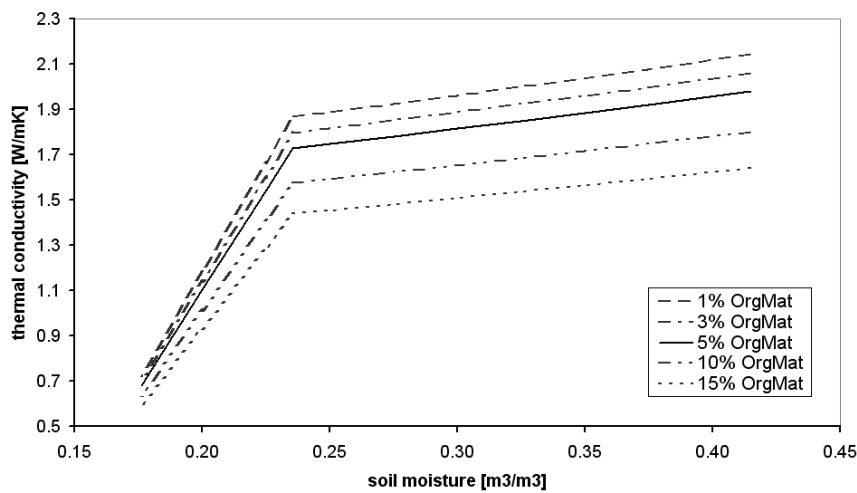
Fig. 4-11: Sensitivity of thermal conductivity to organic matter content of a sandy loam.
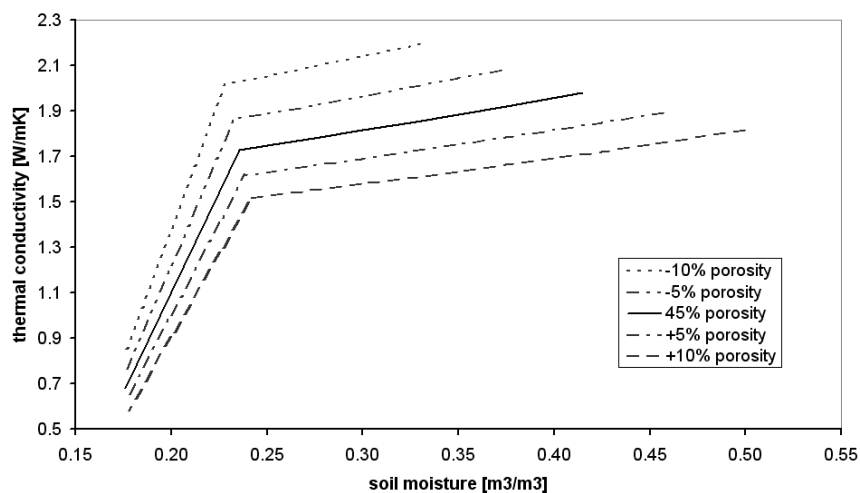
Fig. 4-12: Sensitivity of thermal conductivity to total porosity of a sandy loam.

4.5. The Determination of the Surface Ground Heat Flux

Depending on the model configuration, the ground heat flux G_0 at the soil surface is computed by three different methods for snow-free conditions. The first method, also used in the DANUBIA *Landsurface* component, distinguishes between the energy fluxes at the canopy and at the soil surface level to close the energy balance. The second approach calculates the energy fluxes at the land surface depending on the incoming radiation and the evapotranspiration from the *Penman-Monteith* equation (MONTEITH 1965). Then, an empirical approximation of the surface ground heat flux as a fraction of the net radiation is implemented. In the end, a physically based approach is presented, that determines the heat flux between a potential snow cover and the soil.

4.5.1. Explicit Model of Landsurface Energy Fluxes

If PROMET is run with the dynamic vegetation module (HANK 2008) based on the work of FARQUHAR (1980), then the energy transfer between atmosphere, canopy and soil is modelled by two independent energy balance algorithms for vegetation and inanimate surfaces. The transmission of the solar radiation R_{global} through canopies is handled by the light interception algorithm of CAMPBELL & NORMAN (1998). The shortwave incoming radiation ($R_{sw,in}$) minus the reflected shortwave radiation ($R_{sw,out}$), determined by the soil albedo α_s, and the longwave emission ($R_{lw,in}$) of the canopy (if vegetation cover is present) or the near-ground air layer in case of none (derived from measured T_{air} at 2 meter height) equal the incoming radiation (R_{in}) [W/m^2] at the soil-atmosphere interface

$$R_{in} = R_{sw,in} + R_{sw,out} + R_{lw,in} = (1 - \alpha_s)\, R_{sw,in} + R_{lw,in} \qquad (4.57)$$

In this fully coupled land surface algorithm, an iterative procedure to determine the soil surface temperature T_0 is applied (see Fig. 4-13). The incoming radiation flux (R_{in}) is put into an iteration scheme, which seeks for the optimum of T_0 to solve this approximative energy balance equation where all fluxes are positive towards the exchange surface

$$R_{in} = -\left(R_{lw,out} + LE_{soil} + H_{soil} + G_0\right) + \chi \qquad (4.58)$$

with G_0: surface ground heat flux, H_{soil}: sensible heat flux, LE_{soil}: latent heat flux, $R_{lw,out}$: outgoing longwave radiation and χ: error in estimation at the soil surface.

If the state variables of soil and boundary layer are known, then only T_0, as the controlling variable between the outgoing fluxes must be found. Because $R_{lw,out}$, H_{soil} and G_0 are

$$R_{lw,out} = -\varepsilon \cdot \sigma \cdot T_0^4 \qquad (4.59)$$

$$H_{soil} = \rho_{air} C_{air} \cdot \frac{T_{air,soil} - T_0}{R_A} \qquad (4.60)$$

$$G_0 = \lambda \cdot \frac{T_1 - T_0}{z_1} \qquad (4.61)$$

with ε: emissivity of soil surface, σ: Boltzmann constant (= $5.67 \cdot 10^{-8}$ W/m^{2}K^4) , ρ_{air}: density of air [kg/m^3], C_{air}: specific heat capacity of air [J/kgK], $T_{air,soil}$: air temperature above soil surface, T_1: temperature of upper soil layer and z_1: mean depth of upper soil layer [m].

R_A [s/m] is the aerodynamic resistance to diffusive and turbulent transport of heat and vapour from a surface into the atmosphere. It is assessed at each time step by the procedure presented in 4.5.5.
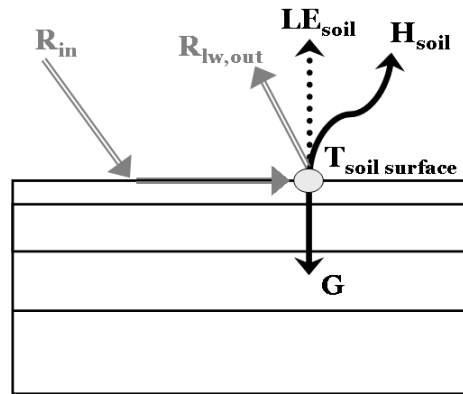
Fig. 4-13: Representation of the surface energy fluxes at the soil surface.

The latent energy flux of evaporation LE$_{soil}$ is solved by the *Penman-Monteith* equation (MONTEITH 1965) for evaporation from non-vegetated surfaces. Though the equation is not dependent on T_0, the net radiation R$_{net}$ available for evaporation is, because

$$-LE_{soil} \leq R_{net}(T_0) = R_{in} - R_{lw,out}(T_0) \qquad (4.62)$$

Additionally, the amount of water evaporated (Ev) in [mm] due to the heat flux (LE$_{soil}$) [W/m^2] is related to surface temperature (T_0), because the latent heat of vaporization C_{LE} [J/g] can be approximated after DINGMAN (2002) with

$$C_{LE} = 2501 - (2.361 \cdot (T_0 - 273.16 K)) \qquad (4.63)$$

$$Ev = -\frac{LE_{soil} \cdot 3.6}{C_{LE}(T_0)} \qquad (4.64)$$

The iteration of T_0 is stopped if the modulus of χ in the approximative energy balance equation (4.58) is smaller than the accepted imprecision, usually 5 W/m^2. A similar procedure without the surface ground heat flux term is used to determine the energy balance of the canopy during the evaporation of intercepted water.

4.5.2. Penman-Monteith Energy Balance Model

If PROMET is run with the plant physiological module of BALDOCCHI et al (1987) to solve the *Penman-Monteith* equation for both vegetated and non-vegetated surfaces, then the energy balance can be closed for the complete land surface, incorporating the ground surface and the canopy (if any).

$$R_{in} = -\left(R_{lw,out} + LE + H + G_0\right) + \chi \qquad (4.65)$$

with H: the total sensible heat flux from the landsurface.

Thus, the incoming radiation (R_{in}) is the total net shortwave radiation on top of the canopy plus the longwave incoming radiation from the atmosphere

$$R_{in} = R_{global}(1-\alpha) + R_{lw,in} \qquad (4.66)$$

As the total evapotranspiration (ET) is determined by the *Penman-Monteith* algorithm in advance, the total latent heat flux (LE) from the land surface to the atmosphere is determined by rearranging equation (4.64) for the latent heat flux LE

$$LE = -0.2778 \cdot ET \cdot C_{LE}(T_0) \qquad (4.67)$$

As $C_{LE}(T_0)$ varies only slightly for small differences in temperature, the terms depending on the surface temperature on the right-hand side of the approximative energy balance can be reduced to

$$(R_{in} - LE) = -\left(G_0 + H + R_{lw,out}\right) + \chi \qquad (4.68)$$

Assuming that the energy fluxes at the land surface are computed with one temperature for canopy and ground surface, then the temperature dependent variables are found with equations (4.59) and (4.61) and the general form of the sensible heat flux equation

$$H = \rho_{air} C_{air} \cdot \frac{T_{air} - T_0}{R_A} \qquad (4.69)$$
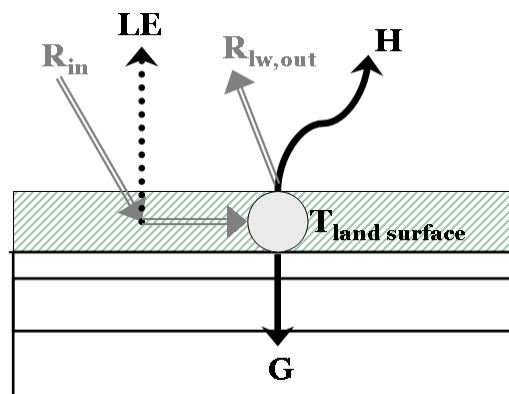
Fig. 4-14: Representation of the energy fluxes at the bulk land surface.

As was the case in the previous model variant, the iteration procedure varies the surface temperature T_0 until the modulus of χ in the approximative energy balance equation (4.65) is smaller than the predefined value 5 W/m^2.

4.5.3. EMPIRICAL MODEL OF SURFACE GROUND HEAT FLUXES

The third approach to determine the energy flux from the landsurface into the soil is based on the empirical analysis of measured ground heat fluxes and the net short and long wave radiation. This enables PROMET to simulate the soil temperature without any surface energy balance algorithm, hence saving computing time.

Analysis of the hourly aggregated time series of surface ground heat flux (G_0) and net radiation (R_{net}) at the two Eddy-Flux measurement sites used in this study gave a first estimate of the ratio C_{GHF} between these two variables. C_{GHF} is often used as an empirical relationship, because areal measurement of G_0 is difficult and its physical based simulation requires some kind of soil temperature model.

$$G_0 = -C_{GHF} \cdot R_{net} \qquad (4.70)$$

Many surface energy models used to simulate mesoscale evapotranspiration or land surface temperatures estimate a daytime C_{GHF} of 5% to 20 % for vegetated surfaces (e.g. CHOUDHURY et al 1986, NIEMEYER 2000, BOEGH et al 2002). More advanced empirical relationships take *Leaf Area Index* (LAI) (CHOUDHURY et al 1987) or the *Normalized Differenced Vegetation Index* (NDVI) (KUSTAS & DAUGHTRY 1990) into account when computing the values of daytime G_0 of vegetated surfaces. Although taking vegetation cover into account, these models have the major drawback that they were developed for semi-arid regions, where G_0 plays an important role in determining energy balance and evapotranspiration, unlike in temperate, humid landscapes like the Upper Danube basin. Furthermore, in most of these simple models, night time C_{GHF} is not calculated, even though empirical analysis shows it to be distinctly different from the day time value.

Therefore, we analysed the hourly relationship between measured R_{net} and G_0 during the vegetation period of a rapeseed field (*Gut Hüll*) in summer 2003 and a marshy meadow (*Wielenbach*) during the summer months of 2004. Apart from the hours around sunrise and sunset the linear regression of G_0 to R_{net} was satisfying to both the Gut Hüll site (Fig. 4-15), as well as the meadow site (Fig. 4-16). For the rapeseed field the mean daytime ratio $C_{GHF(day)}$ was 0.08 and the night time ratio $C_{GHF(night)}$ was 0.35. The corresponding values for the meadow site were 0.10 and 0.40. Consequently, the empirical ground heat flux model distinguishes between day time and night time on the basis of incoming short wave radiation.
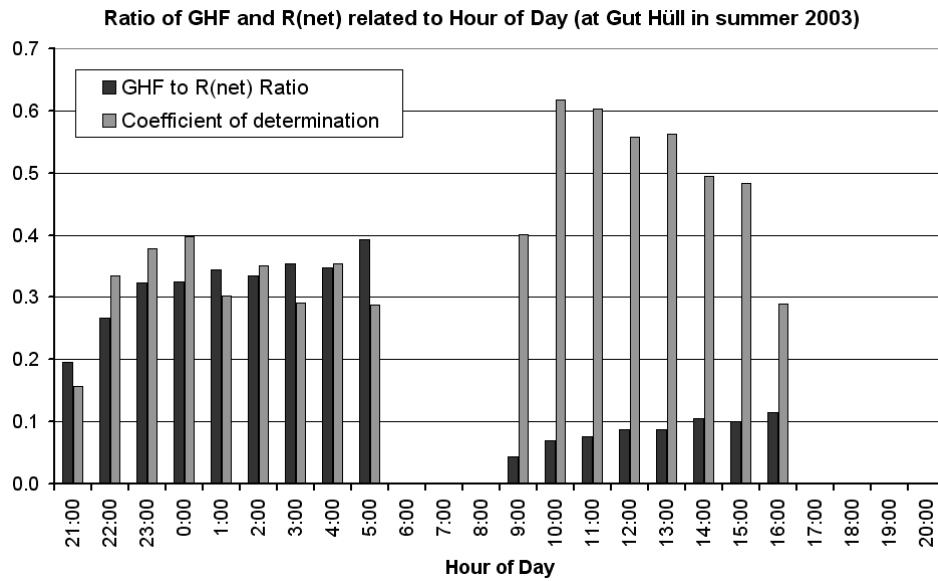
Fig. 4-15: Ratio of ground heat flux to net radiation of a rape field (April-July 2003).
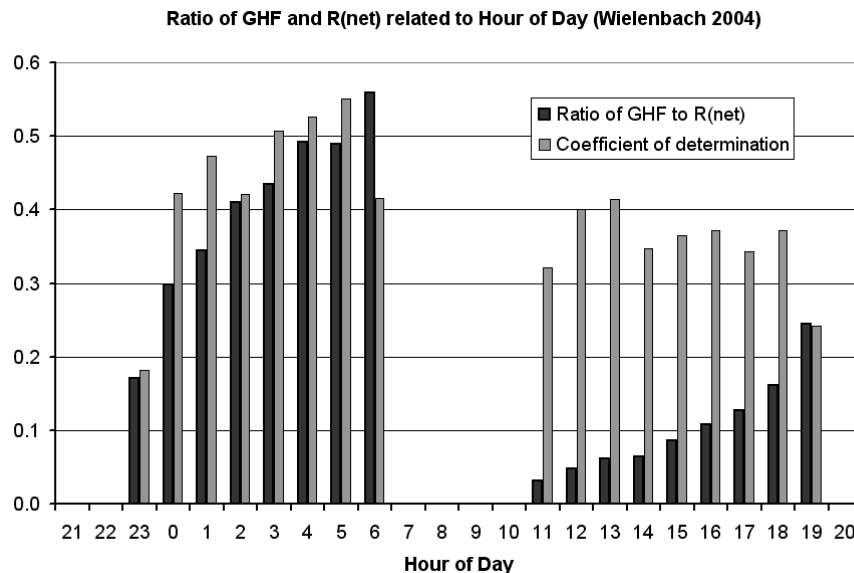
Fig. 4-16: Ratio of ground heat flux to net radiation of a meadow site (May-Sept. 2004).

The results of applying this simple model on the measured hourly net radiation are shown in Fig. 4-17. The model performed better than expected at the rapeseed site, presumably because of the short time series and the stable and dry atmospheric conditions during the summer of 2003. Convective heat transport played no significant role due to the lack of strong precipitation events. At the meadow site, the result was still satisfying despite the unsettled weather conditions during the summer of 2004 and the unpredictable influence of ground water at this site near the river *Ammer*. That is, the applied C_{GHF} is found to be not valid during precipiation events and the true soil moisture was considerably higher most of the year than the one simulated by the *Eagleson* soil water model, due to the shallow ground water table.

OGÉE et al (2001) assessed the daytime soil heat flux below forests as 5 to 10 % of the incident net radiation for south-west France. As we had no measurements at a forest site, we used the lower value for the temperate, denser forests in the Upper Danube basin. From the data presented in OGÉE et al (2001) the estimated $C_{GHF(night)}$ is also about 40% like the ratio applied to grassland sites.

The range of $C_{GHF(day)}$ for non-vegetated surfaces is estimated between 0.2 and 0.5 by CHOUDHURY et al (1987). Other authors assume values between 0.2 and 0.35 (KUSTAS & DAUGHTRY 1990, NORMAN et al 1995, NIEMEYER 2000), mostly for semi-arid regions where evaporation is less dominant than in northern Europe. Hence we assumed, the lower boundary as the effective $C_{GHF(day)}$ for non-vegetated surfaces. The night time value was set to 0.8, based on the assumption that the often stable near ground air layers allow for little latent and sensible heat flux to the soil surface.
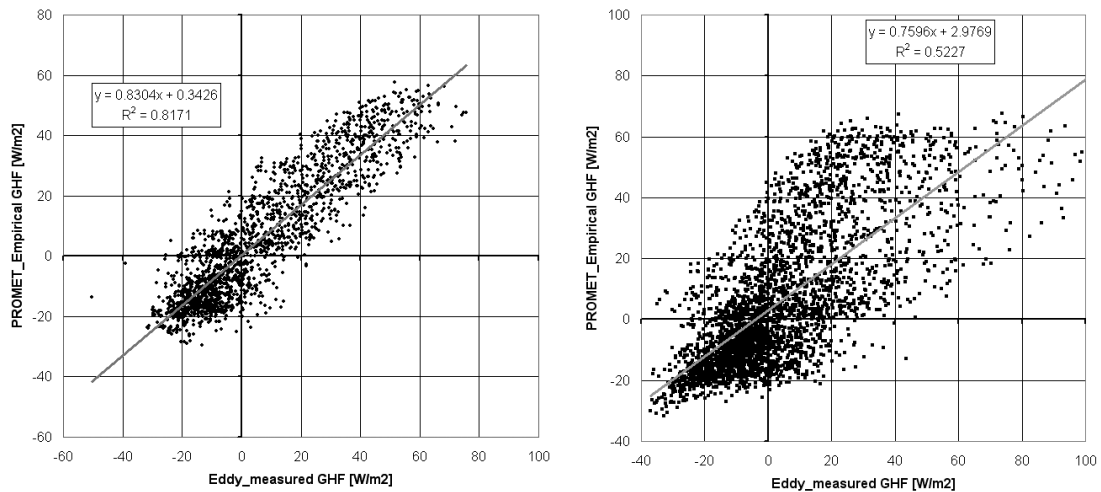
Fig. 4-17: Measured vs. empirical ground heat flux (*Gut Hüll* and *Wielenbach*).

Table 4-3 sums up the parameterisation described here. Solar angle was not incorporated in this simple model (like in KUSTAS & NORMAN 1999), nor was the heat capacity of soil above the heat flux plates taken into account as MAYOCCHI & BRISTOW (1995) demand. The uncertainty in determining the soil heat flux for a mesoscale catchment on the basis of some point measurements was considered too high in contrast to these problems. Unfortunately, a linear relationship between soil wetness and G_0 could not be found in the data, therefore the empirical ground heat flux model is consciously kept very simple, as most soil temperature applications are run with one of the energy balance models implemented in PROMET.

Table 4-3: Empirical landcover-dependent ratios of ground heat flux to net radiation.

	Agriculture	Grassland	Forest	Bare Soil	Built up
$C_{GHF(day)}$	0.08	0.10	0.05	0.20	0.20
$C_{GHF(night)}$	0.35	0.40	0.25	0.80	0.80

4.5.4. The Snow-Soil Heat Transfer Algorithm

If snow cover is present on a process pixel, the soil heat flux is determined based on the temperature difference between the snow pack surface T_{snow} and the first layer of the soil layer stack T_1. The snow module ESCIMO (Strasser et al 2002) implemented in PROMET (Prasch et al 2008) calculates the snow surface temperature on the basis of the snow pack energy balance (Fig. 4-18)

$$R_{net} + LE + H + G_0 + AE + ME = 0 \tag{4.71}$$

with AE: advective energy due to precipitation and ME: potential snow melt energy.
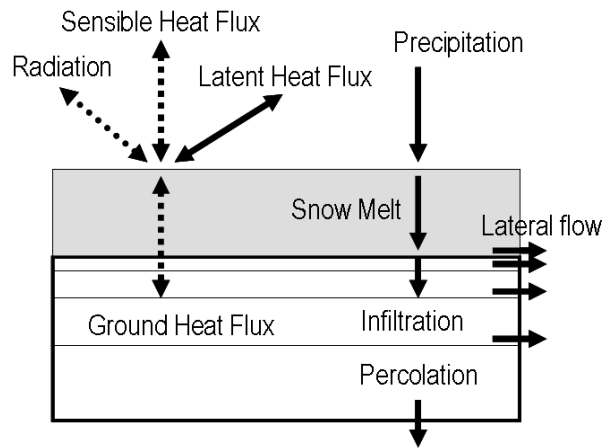
Fig. 4-18: Energy (broken lines) and water/energy fluxes (solid lines) during snow cover.

In many snow process models G_0 is assumed to be constant in space and time, often with a value of 2 W/m^2. To close the energy balance for the whole land surface, a steady-state heat flow equation as proposed by Stähli & Jansson (1998) is modified for the heat transfer from the upper soil to the snow pack surface. As the thermal conductivity of snow λ_{snow} is distinct from the thermal conductivity λ_1 of most soils, the problem is solved by finding the soil surface temperature T_0 with

$$T_0 = \frac{T_1 + f_{SS} T_{snow}}{1 + f_{SS}} \tag{4.72}$$

The weighting factor f_{SS} to determine T_0 in case of steady state heat flux is

$$f_{SS} = \frac{\lambda_{snow} \cdot z_1}{\lambda_1 \cdot z_{snow}} \tag{4.73}$$

where z_{snow}: the snow pack height and z_1: the mean depth of the top soil layer.

The heat flow from the upper soil layer is calculated through equation (4.74)

$$-G_0 = \lambda_1 \cdot \frac{T_0(t) - T_1(t_0)}{z_1} \tag{4.74}$$

and the heat flux into the snow pack could be calculated with

$$G_{0,snow} = \lambda_{snow} \cdot \frac{T_{snow}(t_0) - T_0(t)}{z_{snow}}$$

(4.75)
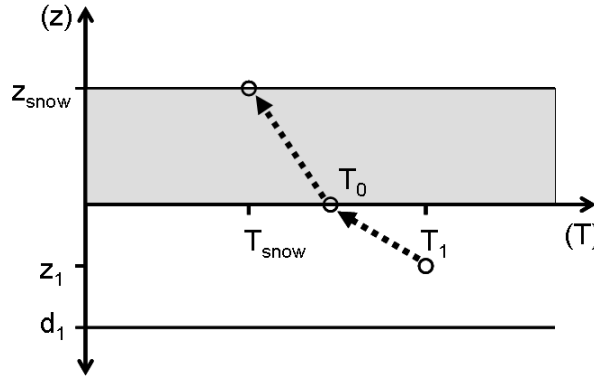
Fig. 4-19: Steady state assumption of heat flow through upper soil layer and snow pack.

Because of the steady state assumption, $G_{0,snow}$ should be equal to $-G_0$ (STÄHLI & JANSSON 1998). But the assumption that the soil surface temperature should be at, or below, the freezing point when it is covered by snow does not allow for a steady state. Snow falling on a non-frozen surface immediately melts, so when a snow pack builds up, the soil surface temperature is set to 273.16 K and G_0 is calculated using equation (4.75). This leads to strong ground heat fluxes toward the surface, as seen in Fig. 4-20, and to melting of freshly fallen snow on relatively warm ground. However, soon the thin top soil layer is cooled down and isolates the snow pack from the warmer soil layers below. Results regarding the snow water equivalent presented by PRASCH et al (2008) and validation of winter soil temperature presented in this work (see section 6.4.2) show a good agreement with natural conditions.
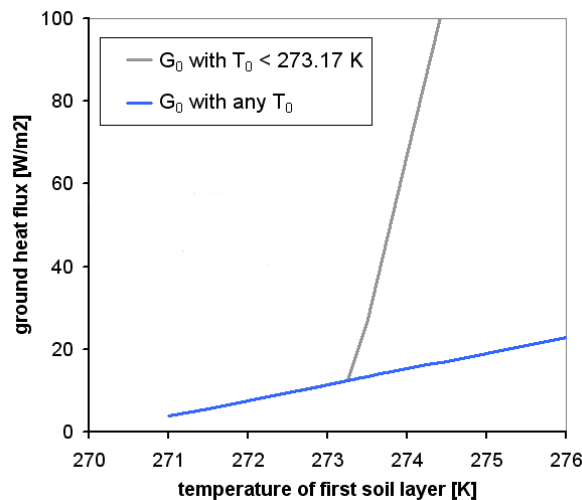
Fig. 4-20: Difference in G_0 with and without the assumption of $T_0 \leq 273.16$ K (with $T_{snow} = 270$ K, $z_{snow} = 0.05$ m and $z_1 = 0.025$ m).

4.5.5. The Atmospheric Resistance above the Soil Surface

The general formulation of the aerodynamic resistance $R_{A,0}$ for turbulent transfer into neutral atmospheric conditions is dependent on the horizontal wind speed (u_z) and the roughness parameters of the surface (e.g. CAMPBELL & NORMAN 1998)

$$R_{A,0} = \frac{1}{k^2 \cdot u_z} \cdot \ln\left(\frac{h_c - h_d}{z_h}\right) \cdot \ln\left(\frac{h_c - h_d}{z_m}\right) \tag{4.76}$$

with h_c: reference height, h_d: displacement height, z_h: roughness length for heat flux, z_m: roughness length for momentum flux, k: *von Karman*'s constant (k = 0.4). This formulation is used for the computation of the atmospheric resistance, where energy fluxes from canopies are computed.

For soil surfaces, one can estimate the roughness parameters $h_c = 0.04$ m, $h_d = 0.0$ m and $z_m = 0.004$ m from values given in literature (CAMPBELL & NORMAN 1998, OKE 1987 and LIU et al 2007) and follow CAMPBELL & NORMAN (1998), who assume that the roughness length for heat flux z_h within canopies is related to z_m by

$$z_h = 0.2 \cdot z_m \tag{4.77}$$

Solving equation (4.76) with these fixed parameters for soil surfaces reduces the aerodynamic resistance $R_{A,0}$ for neutral conditions to

$$R_{A,0} = \frac{56.2}{u_z} \tag{4.78}$$

To assess the influence of atmospheric stability on heat fluxes in the near-ground air layers, one can use the empirical bulk Richardson number Ri_B (MONTEITH & UNSWORTH 2008) instead of more complex physical models, where g is the acceleration due to gravity (9.81 ms^{-2})

$$Ri_B = \frac{g}{T_{air}} \cdot \frac{(T_{air} - T_0) \cdot (h_c - h_d)}{u_z^2} \tag{4.79}$$

The actual atmospheric resistance R_A can then be computed with the well-known stability correction function of CHOUDHURY (1986) with $\beta = 5$

$$R_A = R_{A,0} \cdot \left(1 - \beta \cdot Ri_B\right)^{-3/4} \tag{4.80}$$

This leads to plausible values of atmospheric resistance for soil surfaces, but this algorithm to determine the atmospheric resistance is complex and unstable for very low, but realistic, wind speeds (< 0.2 m/s) and is based on very sensitive surface parameters that are only roughly estimated. Hence, an empirical approach to determine the atmospheric resistance above soil surfaces, especially under canopies, is presented in the following.

KUSTAS & NORMAN (1999) developed a simple model (N95) to predict heat fluxes from soil and vegetation in which they used the results from two empirical studies about the heat transfer from soil surfaces into the atmosphere. Their formulation of the

aerodynamic resistance of a soil surface includes two empirical parameters: C_{FC}, a constant related to free convection, and C_{TC}, related to turbulent convection.

$$R_A = \frac{1}{C_{FC} + C_{TC} \cdot u_z}$$

(4.81)

KONDO & ISHIDA (1997) conducted laboratory and field experiments on the free convection of soils and found R_A of soils without the influence of wind to be approximately 260 s/m, relating to a C_{FC} of 0.0038 m/s. Measurements of heat transfer from bare soils and soils under canopies (SAUER et al 1995 and others) and the analysis of these measurements in comparison with theoretical models by SAUER & NORMAN (1995) led to the universal empirical value of 0.012 m/s for C_{TC} used in the N95 model KUSTAS & NORMAN (1999).

As Fig. 4-21 portrays, this algorithm leads to similar values of R_A for wind speeds > 0.5 m/s as the complex algorithm presented above. But for very low wind speeds, the CHOUDHURY (1986) algorithm becomes unstable, even for this typical case of $(T_{air} - T_0)$ = −3 K. Therefore, this simple, empirical approach is implemented in this version of PROMET, for both bare and vegetated soil surfaces.
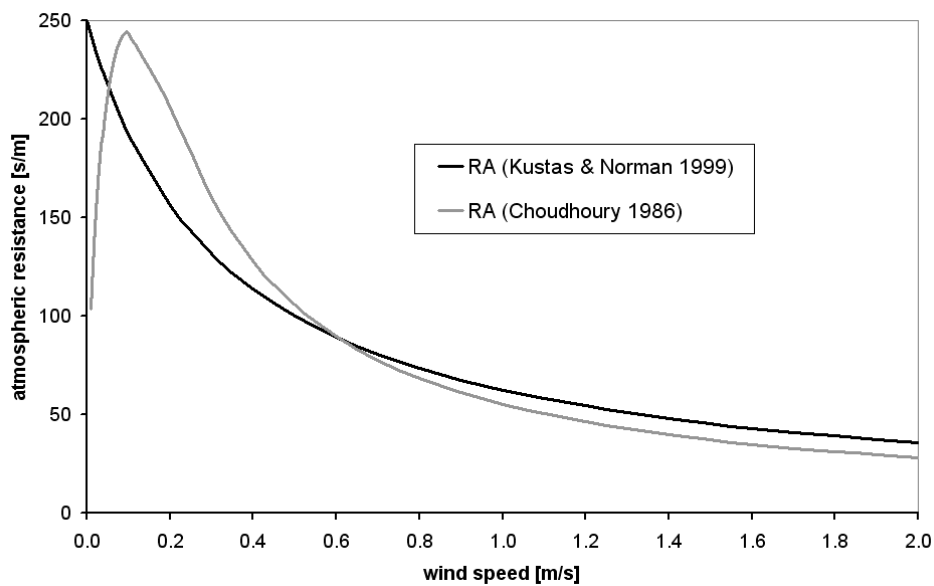
Fig. 4-21: Relationship of atmospheric resistance over a soil surface to wind speed for both algorithms presented, with $(T_{air}-T_0)$ equal to -3 K.

5. THE PARAMETERISATION OF SOILS

5.1. AVAILABLE SOIL MAPS

The only available soil map covering the whole German part of the Upper Danube catchment is the Soil Overview Map of Germany on a scale of 1:1,000,000 (*Bodenübersichtskarte von Deutschland 1:1.000.000*, BÜK1000). It shows 34 soil associations within the Upper Danube catchment with a spatial accuracy of about 1 kilometre. Each primary soil type of the 34 soil associations is described by a typical soil profile with quantitative values of the main soil properties (soil texture, pore volume, water holding capacity, organic material content, coarse material content and others). Because this map has the highest coverage in the Upper Danube basin, it is the spatial reference for all parameterisations of the soil process models.
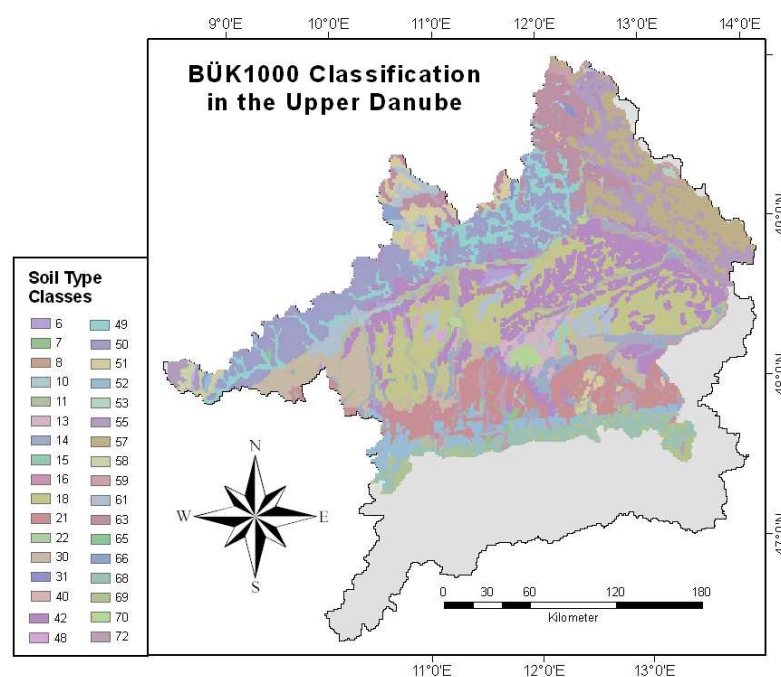
Fig. 5-1: Southern part of the BÜK1000 soil type map of Germany.

The challenge of applying spatially relevant parameters to the soil association classes of the BÜK1000 is to interpret the legend of the soil map in conjunction with the explicitly given soil horizon properties of one typical soil found in a specific class. The soil horizon properties include contents of clay, sand, coarse material and organic matter as well as porosity and volumetric water contents at field capacity and wilting point. Aside from that, data on carbon and nitrogen contents and acidity is tabulated for each soil layer.

Spatially more explicit soil maps, like the German Soil Overview Map on a scale of 1:200,000 (BÜK200), are unfortunately only available for some parts of the catchment. Furthermore, soil maps of this scale were not produced for most of the alpine parts (Austria, Swiss) of the catchment, especially for non-agricultural areas. Yet, a first analysis of the simulated water cycle based on BÜK200 data has shown, that local ground water recharge and lateral runoff rates are significantly different when using this soil map data with higher spatial accuracy, but catchment scale water fluxes are only slightly affected. Therefore, if 1:200,000 soil maps with a greater coverage are available in the future, this analysis should be redone.

5.2. Classification of the BÜK1000 Soil Units

For the establishment in the decision support system DANUBIA, the soil mapping units of the BÜK1000 were standardized to four layers and the soil properties of the layers of each class were determined and tabulated. Soil units with similar vertical soil texture sequences were merged and the properties of the soil units with the highest degree of coverage in the Upper Danube basin were assigned to 15 new soil type classes. For the evaluation of the soil type classes, the retention parameters, *bubbling pressure head* and *pore-size distribution index* after Brooks & Corey (1964), were determined for each class with the equations (5.2) and (5.3) found in chapter 5.3. Then the water contents at field capacity and permanent wilting point were computed with equation (4.3). The resulting plant available water for the soil type classes was compared with the tabulated values of the dominant soil units to assure a good spatial representation of the soil type specific hydraulic properties.

The first step of grouping the 34 soil units of the BÜK1000 (see Appendix A) into 15 soil type classes based on textural information was done manually, because the descriptions of the soil associations in the map legend sometimes did not fit the tabulated properties of these soil units. Especially soil units 11 and 13 were assigned to soil type classes based on their description. The calcareous soils found in low lying floodplains (soil unit 11) were characterized by a great variety of soil textures. Here we found a sandy loam texture to fit the description better than the loamy clay horizons given as an example in the horizon database of the BÜK1000. Secondly, soil unit 13 found on the gravel plain around Munich was assigned to sandy loam soils on gravel, not to the clay loam class, as the horizon database suggested.

For each class the soil profile of the spatially dominant soil unit was standardized to four soil layers and was used as a basis for all further parameterisation and validation steps (Table 5-1). The transformation of the horizon characteristics of the original soil profiles into the 4 model horizons was done in a way that preserved the typical layering of the dominant soil type.

Table 5-1: Basic properties of the DANUBIA soil type classes.

#		Depth	Type	Coarse	OrgMat	GPV	FPV	Clay%	Sand%
1	Sand	5	mS	0%	15.0%	51.5%	51.5%	1	95
1	(dominant soil unit: 10)	20	mS	0%	4.0%	45.5%	45.5%	1	95
1		65	mS	0%	4.0%	45.5%	45.5%	1	95
1		200	mS	0%	0.0%	34.2%	34.2%	1	95
2	Gravelly Sand	5	gS	0%	5.0%	40.4%	40.4%	1	95
2	(dominant soil unit: 63)	20	gS	20%	1.8%	27.8%	34.8%	1	95
2		65	gS	20%	0.5%	26.8%	33.5%	1	95
2		200	gS	20%	0.0%	30.6%	38.3%	1	95
3	Loamy Sand	5	Sl4	0%	3.0%	47.5%	47.5%	15	60
3	(dominant soil unit: 30)	20	Sl3	0%	1.0%	42.3%	42.3%	10	65
3		65	Ls4	20%	0.0%	27.6%	34.5%	20	60
3		200	Ls4	20%	0.0%	27.6%	34.5%	20	60
4	Gravelly Loamy Sand	5	Slu	0%	10.0%	60.0%	60.0%	10	45
4	(dominant soil unit: 61)	20	Sl4	20%	3.0%	42.5%	53.1%	15	60
4		65	Sl4*	40%	0.0%	25.0%	41.7%	15	60
4		200	Sl3*	40%	0.0%	25.0%	41.7%	10	60
5	Sandy Loam	5	Sl4	0%	5.0%	47.5%	47.5%	15	60
5	(dominant soil unit: 21)	20	Sl4	0%	3.0%	47.5%	47.5%	15	60
5		65	Lt2	0%	0.0%	35.2%	35.2%	30	30
5		200	Ls2	0%	0.0%	38.5%	38.5%	20	35
6	Sandy Loam on Gravel	5	Sl4	20%	10.0%	43.8%	54.8%	18	52
6	(dominant soil unit: 14)	20	Sl4	20%	3.0%	43.8%	54.8%	18	52
6		65	Sl4	20%	1.0%	34.0%	42.5%	18	52
6		200	gS*	60%	0.0%	14.4%	36.0%	5	90
7	Clayey Silt	5	Ut3	0%	4.0%	52.5%	52.5%	15	10
7	(dominant soil unit: 42)	20	Ut3	0%	2.0%	52.5%	52.5%	15	10
7		65	Ut4	0%	1.0%	44.5%	44.5%	20	10
7		200	Ut4	0%	0.0%	41.5%	41.5%	24	6
8	Silt Loam	5	Lu	0%	5.0%	46.5%	46.5%	20	20
8	(dominant soil unit: 18)	20	Lu	0%	1.0%	46.5%	46.5%	20	20
8		65	Tu3	0%	0.0%	39.5%	39.5%	35	10
8		200	Lu	10%	0.0%	35.6%	39.6%	20	20
9	Clay Loam	5	Lt2	0%	3.0%	47.0%	47.0%	30	30
9	(dominant soil unit: 58)	20	Lt2	0%	1.0%	47.0%	47.0%	30	30
9		65	Lu	0%	1.0%	45.5%	45.5%	30	15
9		200	Tu3	0%	1.0%	42.0%	42.0%	35	10
10	Clay	5	Tl	0%	10.0%	65.0%	65.0%	60	20
10	(dominant soil unit: 51)	20	Tl	0%	3.0%	54.5%	54.5%	60	20
10		65	Tt	0%	0.0%	51.0%	51.0%	60	20
10		200	Tt	0%	0.0%	51.0%	51.0%	60	20
11	Peat	5	H	0%	35%	77.0%	77.0%	-1	-1
11	(dominant soil unit: 6)	20	H	0%	35%	77.0%	77.0%	-1	-1
11		65	H	0%	35%	77.0%	77.0%	-1	-1
11		200	H	0%	35%	77.0%	77.0%	-1	-1
12	Soils on Calcerous Rock	5	Lts	0%	15.0%	61.8%	61.8%	35	45
12	(dominant soil unit: 68)	20	Lts	0%	6.5%	46.1%	46.1%	40	40
12		65	Tl*	60%	0.0%	18.2%	45.5%	50	30
12		200	Lts*	85%	0.0%	7.1%	47.3%	45	35
13	Soils on Crystalline Rock	5	Ls4	20%	15.0%	45.2%	56.5%	20	60
13	(dominant soil unit: 55)	20	Ls4	30%	8.0%	36.1%	51.5%	20	60
13		65	Ls4*	40%	1.0%	23.7%	39.5%	20	60
13		200	Ls4*	60%	0.0%	15.4%	38.5%	20	60
14	High Alpine Soils	5	Lt2	20%	10.0%	48.1%	60.1%	30	30
14	(dominant soil unit: 69)	20	Slu*	80%	2.5%	10.1%	50.5%	17	38
14		65	Sl3*	85%	0.0%	7.4%	49.3%	10	65
14		200	Sl3*	85%	0.0%	7.4%	49.3%	10	65
15	Soils on Karst	5	Lt3	0%	9.0%	63.5%	63.5%	40	20
15	(dominant soil unit: 50)	20	Tl	20%	4.0%	45.5%	56.9%	50	30
15		65	Tt*	64%	2.0%	21.2%	58.9%	70	15
15		200	Tt*	64%	2.0%	21.2%	58.9%	70	15

Because most simulation algorithms and parameterisation techniques do not incorporate the coarse material fraction of soils, the coarse material classes of the soil horizon data were converted to coarse material volumetric fractions (CV) (Table 5-2) as described in the German Soil Mapping Manual (*BoKA5*, AG BODEN 2005).

Table 5-2: Allocation of CV values for the coarse material classes used in the *BoKA5* (AG BODEN 2005).

Coarse Class	1	2	3	4	5	6
Volumetric Fraction	0%	10%	20%	40%	60%	80%

The pore volumes of the fine textured soil (FPVs) were then computed from gross pore volumes (GPVs) to achieve realistic pore volumes compared to the values given by the *BoKA5* (AG BODEN 2005) for the considered soil type classes using the relation

$$FPV = \frac{GPV}{(1 - CV)}$$

(5.1)

Regarding the nomenclature of the German soil texture classification (AG BODEN 2005), it is important to note that it differs substantially from the US soil taxonomy. All soil texture related class terms were derived from the German soil taxonomy. For comparison the following figure demonstrates these differences (Fig. 5-2).
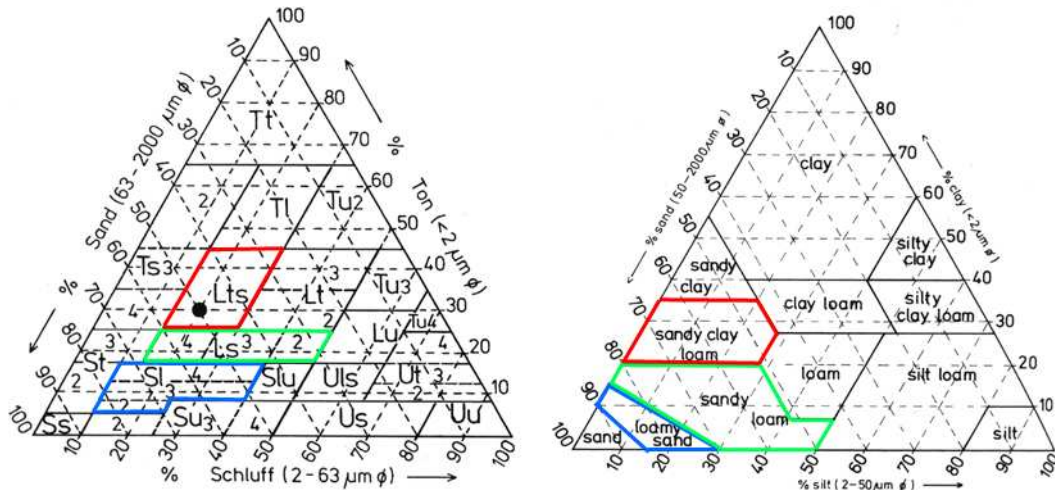
Fig. 5-2: Soil texture triangles of the German and the US soil taxonomy. Coloured areas show the different boundaries of the classes loamy sand, sandy loam and sandy clay loam.

To extrapolate the soil type classes of the BÜK1000 to the non-German parts of the catchment, a simple classification based on elevation and geology was performed. In the first step, the distribution of soil textures in the southern part of the BÜK1000 was analyzed in relation to elevation above sea level. Then, the result was applied to the southern (alpine) part of the basin:

Up to 490 m:	Silt loam
491 - 880 m:	Sandy loam
881 – 1330 m:	Leptosols (on Calcareous / Crystalline Rock)
Above 1330 m:	High Alpine Soils

In a second step the Leptosols were distributed among the *Soils on Calcareous Rock* and *Soils on Crystalline Rock* classes by splitting the alpine part of the basin into the northern *Limestone Alps* and the crystalline *Central Alps*. The small Czech part of the catchment in the north-east (not shown in Fig. 5-3) was classified as *Soils on Crystalline Rock*, like the surrounding area.

Finally, the soil type classes of some map units were reclassified according to the land cover information used in the Upper Danube. Areas with *Peat* soil but non-bog land cover were reclassified as *Clay Loam* and non-peat pixels with bog land cover were reclassified as *Peat*. Additionally, the *High Alpine Soils* with forest land cover were reclassified as *Leptosols*. The soil unit *Water Surface* was given the soil type *Clay Loam*, as spatial information about land cover is governed by the dedicated data layer.
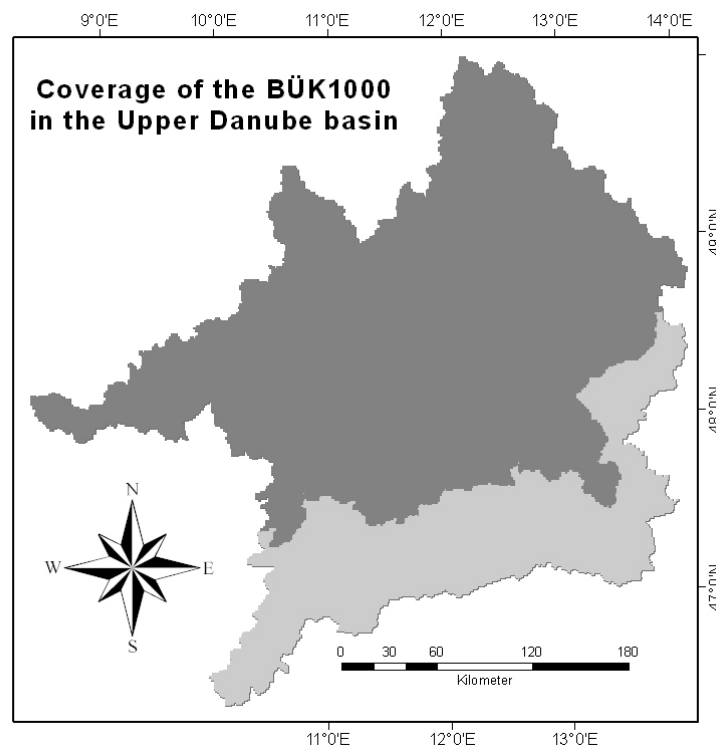
Fig. 5-3: Coverage of the BÜK1000 (dark) in the Upper Danube basin (light).
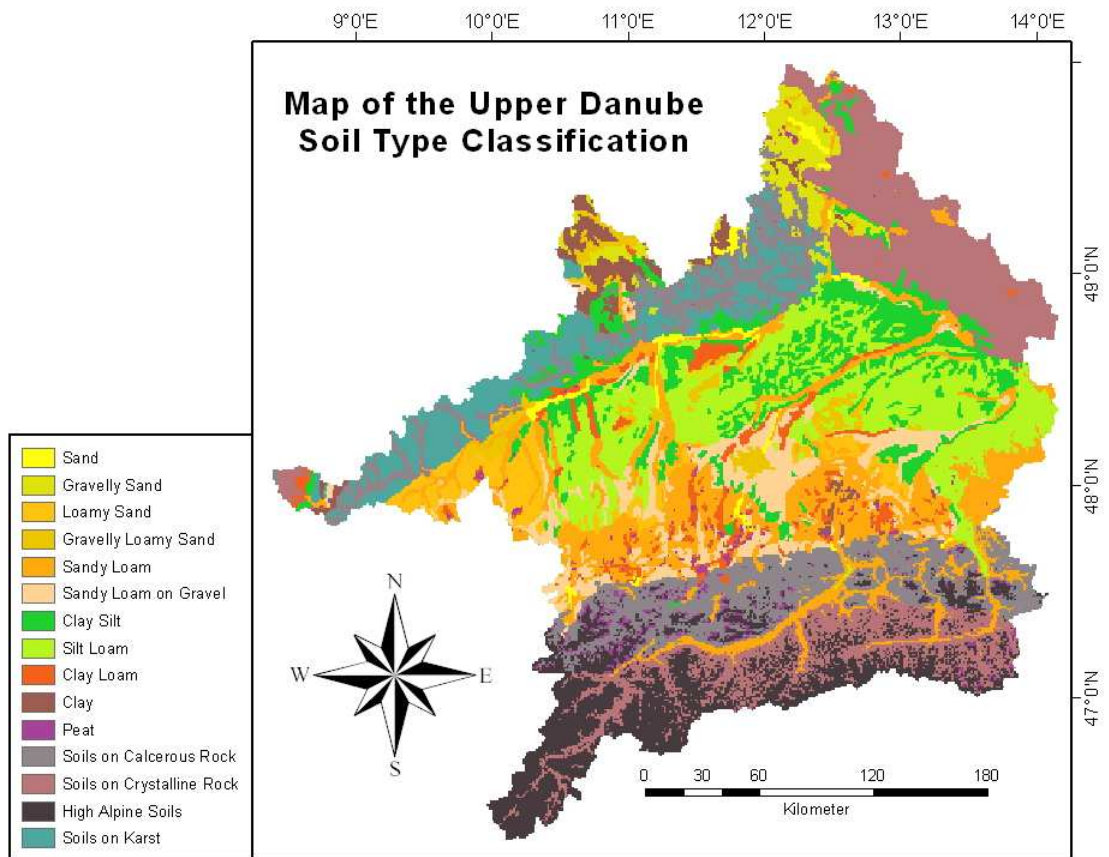
Fig. 5-4: Map of the 15 soil type classes of the Upper Danube catchment assigned to the 1:1,000,000 soil map of Germany and extrapolated to the non-German parts of the catchment.

5.3. Soil Hydraulic Parameterisation

For the application of the *Eagleson*-type soil water model, the easily available soil characteristics specified in the BÜK1000 database are used to derive the soil hydraulic properties of the soil type classes defined for the Upper Danube basin. Good predictions of these hydraulic parameters for regional scale simulations are achieved if well-tested *Pedotransfer Functions* (PTFs) are used (McBratney et al 2002, Wösten et al 2001 and others). The most common types of PTF are the multiple regression equations based on soil hydraulic databases like UNSODA (Nemes et al 2001) or HYPRES (Wösten et al 1999). Because measurements of soil hydraulic characteristics are time-consuming and costly for larger simulation areas, PTFs are the only effective method to generate the parameters needed to model soil water processes on a larger scale. Yet, PTFs show considerable prediction errors due to their simplifying nature and have to be carefully chosen with regard to the available input data, the desired accuracy, the needed hydraulic parameters and the geographical region. Therefore, attempts to evaluate PTFs with different data sets have resulted in inconsistent conclusions regarding the accuracy of these PTFs (Tietje & Tapkenhinrichs 1993, Cornelis et al 2001, Wagner et al 2004). The only set of PTF equations that performed well in all three studies was the one of Vereecken et al (1989) to predict the parameters of the van Genuchten (1980) water retention equation. Still, these authors agree on the fact, that the best PTF are derived from data sets collected in geographically similar regions.

Regarding the Upper Danube basin, the main factors considered were the types of parameters to be predicted and the representation of typical runoff behaviour for the mapped soil units. The available soil characteristics for the typical soil profiles are extensive, but the spatial extent of the mapped soil units and their definition as soil type associations do not allow an accurate parameterisation. Thus, we chose the Pedotransfer Functions of Rawls & Brakensiek (1985), because they provide the water retention parameters *bubbling pressure head* ($\Psi(1)$) and *pore-size distribution index* (m) of the *Brooks & Corey* model (Brooks & Corey 1964). Wagner et al (2004) evaluated different PTFs with data sets from Bavaria and found that the Rawls & Brakensiek (1985) functions for the *Brooks & Corey* model performed poorly for root zone soil measurements compared to other models. This result can be expected due to the fact that the *Brooks & Corey* model describes the soil water retention with a continuous function with one less parameter than does the widely used *van Genuchten* model (Van Genuchten 1980). Then again, the *Brooks & Corey* model showed the best performance for water retention simulations of deeper tertiary sediments due to its low sensitivity on clay content. Actually, the validation of the soil parameterisation at the point scale does not make sense when the modified *Eagleson* model is applied on the mesoscale Upper Danube basin. Therefore the focus for this parameterisation was to achieve a realistic simulation of the regional scale plant available water content and the validation of runoff generation on the sub-catchment scale.

Nevertheless, point scale soil moisture validation with the parameters based on the BÜK1000 showed reasonably good results considering the parameterisation strategy and the simplified nature of the soil water model. The following Pedotransfer functions were used to obtain the hydraulic parameterisation of the soil type classes found for the Upper Danube catchment.

RAWLS & BRAKENSIEK (1985) found the following relationship between $\Psi(1)$ and the basic soil properties clay content C [%], sand content S [%] and total porosity Φ [volumetric fraction].

$$
\begin{aligned}
\Psi(1) = \exp [\ & 5{,}3396738 + 0{,}1845038\ C - 2{,}48394546\ \Phi \\
& - 0{,}00213853\ C^2 - 0{,}04356349\ S\ \Phi - 0{,}61745089\ C\ \Phi \\
& + 0{,}00143598\ S^2\ \Phi^2 - 0{,}00855375\ C^2\ \Phi^2 \\
& - 0{,}00001282\ S^2\ C + 0{,}00895359\ C^2\ \Phi \\
& - 0{,}00072472\ S^2\ \Phi + 0{,}0000054\ C^2\ S \\
& + 0{,}50028060\ \Phi^2\ C]
\end{aligned}
\tag{5.2}
$$

Furthermore the *pore-size distribution index* can be computed with

$$
\begin{aligned}
m = \exp [\ & {-}0{,}7842831 + 0{,}0177544\ S - 1{,}062498\ \Phi \\
& - 0{,}00005304\ S^2 - 0{,}00273493\ C^2 + 1{,}11134946\ \Phi^2 \\
& - 0{,}03088295\ S*\Phi - 0{,}00026587\ S^2\ \Phi^2 \\
& - 0{,}00610522\ C^2\ \Phi^2 - 0{,}00000235\ S^2\ C \\
& + 0{,}00798746\ C^2\ \Phi - 0{,}0067449\ \Phi^2\ C]
\end{aligned}
\tag{5.3}
$$

For the computation of the effective porosity considered by the soil water model, the simple equations of SCHEINOST et al (1997) were favoured because they gave similar good results, compared to other, more complex equations. Organic material (OM) is considered as a weight per weight percentage [w/w%], Θ_s and Θ_r are volumetric fractions.

$$
\Theta_s = 0.85\ \Phi + 0.13\ C
\tag{5.4}
$$

$$
\Theta_r = 0.52\ C + 0.928\ OM
\tag{5.5}
$$

Effective porosity n then is the difference between the saturated water content Θ_s and the residual water content Θ_r

$$
n = \Theta_s - \Theta_r
\tag{5.6}
$$

At last, the saturated hydraulic conductivity of the fine textured soil $k_{s,f}$ is estimated by the regression equation of WÖSTEN et al (1999) (with D: bulk density in [g/cm^3] and topsoil: a parameter that is 1 for upper soil layers and 0 for lower soil layers)

$$
\begin{aligned}
k_s = \exp [\ & 7.755 + 0.0352\ S + 0.93\ topsoil - 0.967\ D^2 \\
& - 0.000484\ C^2 - 0.000322\ S^2 + 0.001\ S^{-1} - 0.0748\ OM^{-1} \\
& - 0.643\ \ln(S) - 0.01398\ D\ C - 0.1673\ D\ OM \\
& + 0.02986\ topsoil\ C - 0.03305\ topsoil\ S]
\end{aligned}
\tag{5.7}
$$

This function performed well in the study of WAGNER et al (2001) and was developed for a wide range of soils based on the HYPRES (HYdraulic PRoperties of European

Soils) database. Furthermore, it considers the organic material content and distinguishes between topsoil and subsoil layers, which relates to the basic soil morphology. By this means, the hydraulic conductivity is differentiated depending on the soil horizon and the layer depth, which led to lower conductivities for the upper horizons in relation to the *BoKA5* values (AG Boden 2005). Many other PTFs, as well as the *BoKA5* tables, do not incorporate these facts when estimating soil physical properties. Nonetheless, the comparison of the $k_{s,f}$ values (Table 5-3 and Fig. 5-5) calculated with Wösten et al (1999) and the values tabulated in the soil mapping manual *BoKA5* (AG Boden 2005) results in a good coefficient of determination.
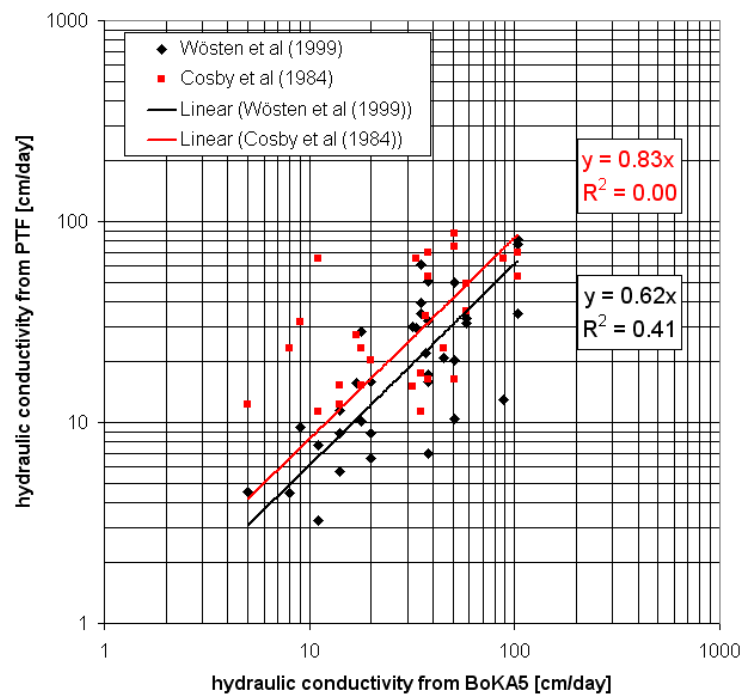
Fig. 5-5: Saturated hydraulic conductivity of two PTFs vs. BoKA5 (AG Boden 2005).

The correlation of other PTFs with the values of the *BoKA5* and their coefficient of determination are given in Table 5-3. Obviously, the PTFs of Wösten (1997), Brakensiek et al (1984) and Saxton et al (1986) correlate badly with very low coefficients of determination. The simple equation of Cosby et al (1984) gave a satisfying correlation with the *BoKA5* data, but a larger scatter. The correlations do not include soil horizons dominated by sand or coarse material.

Table 5-3: Statistical measures of the linear regression (forced through zero) of hydraulic conductivities derived from PTF vs. BoKA5 values

	Wösten (1997)	Wösten et al (1999)	Cosby et al (1984)	Saxton et al (1986)	Brakensiek et al (1984)
Slope of the linear regression with BoKA5 values	1.621	0.616	0.830	0.499	0.350
Coefficient of determination of the linear regression	0.177	0.408	0.000	0.000	0.111

For the final parameterisation of k_s the volumetric fraction of coarse material CV was taken into account. In soil layers with a CV up to 30%, the volume taken up by the coarse material was considered as an inactive region, effectively reducing the cross section for water flow. Therefore a small CV reduces the k_s value by

$$k_s = k_{s,f} \bullet (100\% - CV) \tag{5.8}$$

The hydraulic conductivity of soil layers with a CV above 30% was found by using the weighted average of $k_{s,f}$ and the typical hydraulic conductivity of the bedrock $k_{s,br}$ taken from DINGMAN (2002)

$$k_s = k_{s,f} \bullet (100\% - CV) + k_{s,br} \bullet CV \tag{5.9}$$

Fig. 5-6 shows the final k_s values for the soil types classified in the Upper Danube basin subdivided into the 4 computational soil layers. Since hydraulic conductivity is the key parameter for the simulation of infiltration and lateral runoff generation, validation runs were performed to validate the lateral runoff generated by the model with gauge measurements at the subcatchment scale. Generally, good coefficients of determination for simulated daily river runoff compared to gauge measurements at the catchment outlet *Achleiten* and at subcatchment outlets were achieved by MAUSER & BACH (2008).
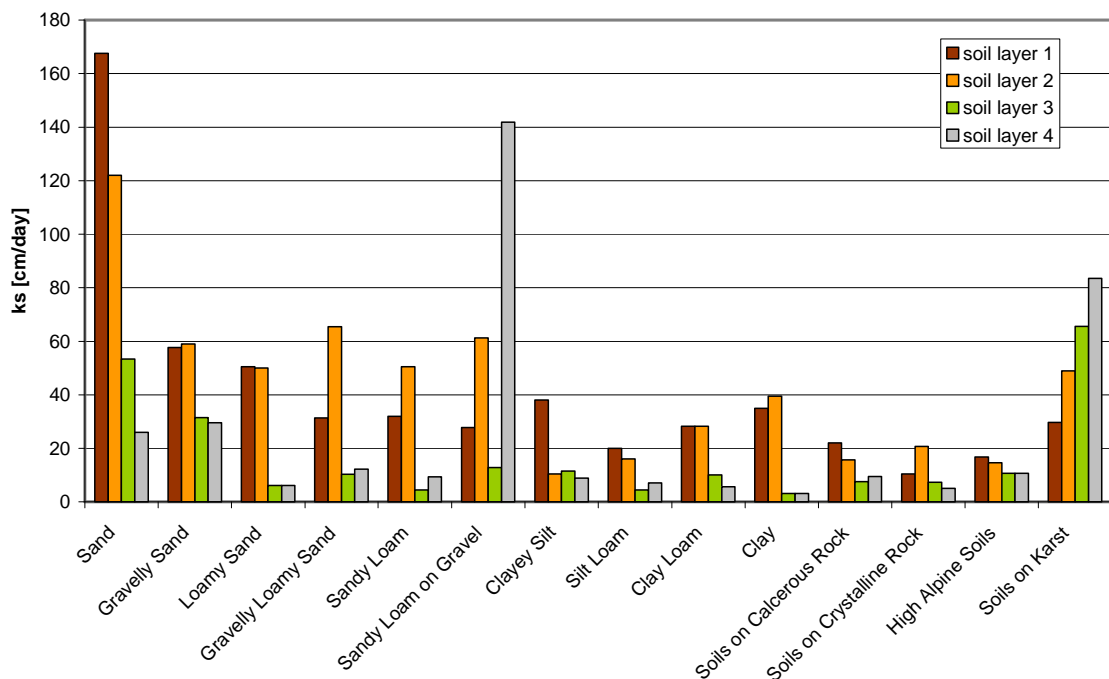
Fig. 5-6: Saturated hydraulic conductivity of the Upper Danube soil type classes.

Like the hydraulic conductivity, the plant available water of the soil type classes on the basis of the parameters n, m and Ψ(1) had to be assessed. Therefore the *Brooks & Corey* soil water retention equation (4.3) was applied for each soil layer for the distinctive soil suctions used in the German soil mapping manual. Soil moisture at *field capacity* Θ_{fc} is defined with pF 1.8 (–64 hPa) in the German soil handbook (AD-

HOC-AG BODEN (2005) and often with pF 2.5 (–330 hPa) in the international literature (DINGMAN 2002). Yet, the true suction of a specific soil horizon at Θ_{fc} is a result of its specific textural and structural composition, as well as the depth to the saturated zone (SCHEFFER & SCHACHTSCHABEL 2002). The water content Θ_{pwp} at *permanent wilting point* is computed for a pF 4.2 (–15,000 hPa), therefore the plant available water content Θ_{pa} of a soil layer is

$$\Theta_{pa} = \Theta_{fc} - \Theta_{pwp} \qquad (5.10)$$

The total plant available water storage in the soil column WS_{pa} for each soil type class is the sum of the volumetric water content times the layer thickness d_i of each layer i and is expressed as a volume per unit area [mm]

$$WS_{pa} = \sum_{i=1}^{4} \Theta_{pa,i} \cdot \Delta d_i \qquad (5.11)$$

Because *field capacity* is defined for a range of soil suctions, Fig. 5-7 displays both the minimum (pF 2.5) and maximum (pF 1.8) values of WS_{pa} computed with the *Brooks & Corey* function against the total plant available soil water storage of the typical BÜK1000 soil profiles. The standard deviation of simulated WS_{pa} at pF1.8 from the one given in the BÜK1000 legend is 42 mm and the parameterisation explains about 91% of the differences between the individual soil type classes (Fig. 5-8). The *Peat* soil type class could not be parameterized with the PTFs, thus the required hydraulic properties had to be taken from the *BoKA5* and the *Brooks & Corey* parameters had to be calibrated to fit the typical water retention of boggy soils.
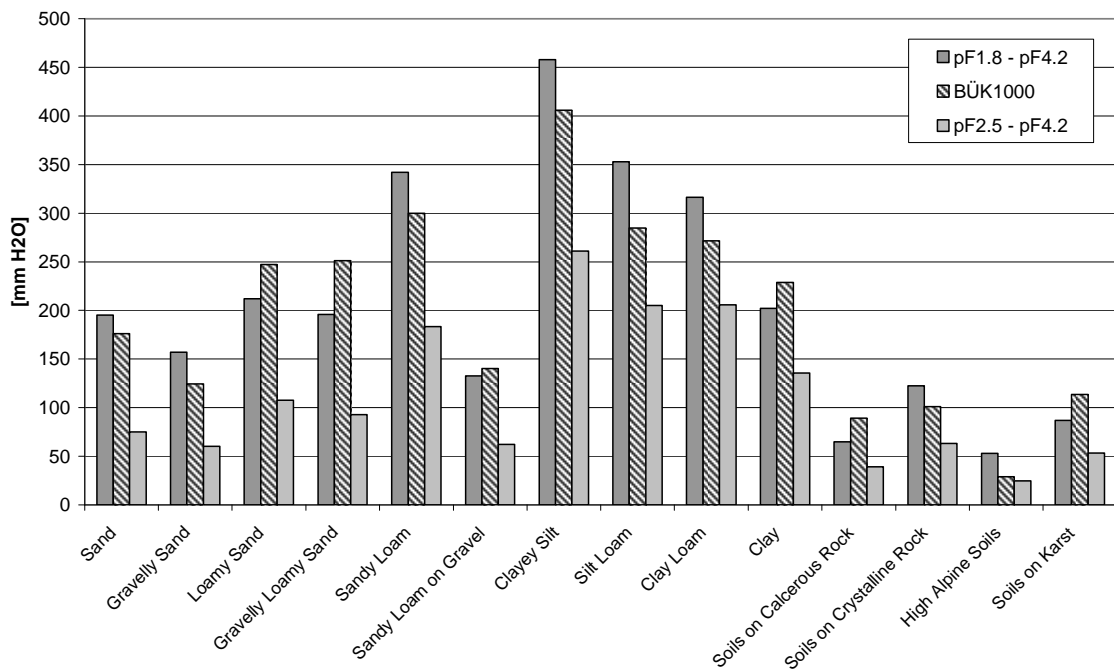
Fig. 5-7: Plant available water WS$_{pa}$ per soil type class (PROMET vs. BÜK1000).

As Bohrmann (2007) could show, the hydraulic parameterisation of soils based on the German soil texture classification (Ad-hoc-AG Boden 2005) seems to be appropriate for regional scale hydrological model applications, because the soil texture classes are relatively small. Together with the above comparison of the WS_{pa} values, it is shown that this parameterisation strategy is able to represent the soil water dynamics of the soil type classes extracted from the BÜK1000 data. As a consequence, the greatest uncertainties of the regional scale hydrological simulations in the Upper Danube basin are a result of the low spatial resolution of the available soil map, resulting in a strong aggregation of different soil types and textures into single landscape scale soil associations.
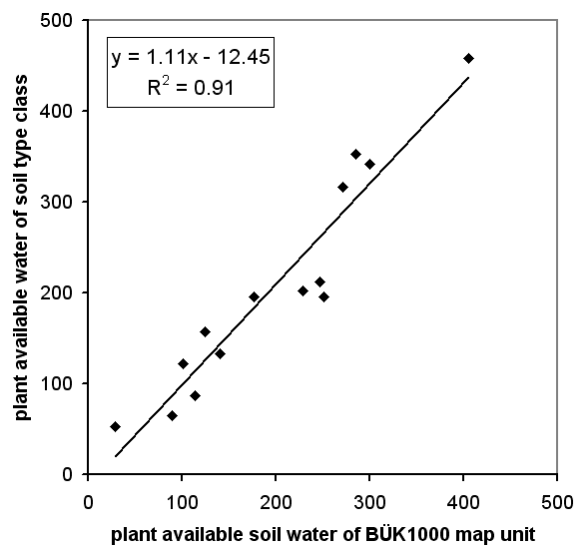
Fig. 5-8: Scatter plot of WS_{pa} per soil type class (PROMET vs. BÜK1000).

6. Evaluation of SHTM Accuracy and Uncertainty

The first part of the validation strategy concentrates on the comparison of point measurements with simulated layer averaged soil temperatures. Furthermore, the influences of interpolated climate data, plant cover and simulated soil moisture on model performance are evaluated by means of the extensive data set recorded during the *Eddy-Flux* campaigns in 2003 and 2004. The performance of PROMET / SHTM in different regions of the Upper Danube catchment is assessed via soil temperature time series recorded by DWD and AgMet network stations. Finally, land surface temperature patterns of the investigated area derived from NOAA-AVHRR scenes are compared to model outputs.

6.1. Statistical Criteria

For the comparison of simulated time series with measured data, quantitative criteria that explain the correlation of mean and extreme values, as well as potential phase shifts between different time series, are needed. The following statistical criteria were found to be significant for the analysis of continuous time series, especially in hydrology (see Nash & Sutcliffe 1970, Legates & McCabe 1999 and Dingman 2002 amongst others), besides the daily and annual means, amplitudes and frequencies of these continuous series.

The linear regression of simulated hourly or daily values with the associated measured values is expressed as a linear function

$$y = a \cdot x + b \tag{6.1}$$

The correlation coefficients a (gain) and b (offset) describe the ability of the model to represent the physical processes that result in the measured variable. The associated coefficient of determination (R^2) is a measure of the implicit scatter involved in reproducing the natural processes due to phase shifts, parameter uncertainty or non-systematic model errors. For comparison of simulated with measured hourly time series, every 5th value was taken as a random sample. This type of random sample was chosen, because analytical statistics like linear regression analysis requires independent samples of the statistical population of data pairs (Bahrenberg et al 1999). As the actual hourly mean value of a temperature time series is dependent on the previous hourly mean value, especially during the diurnal cycle, the systematic random sample taken every 5th hour of a time series tries to reduce this interdependency of the investigated temperature values. At the same time, taking

every 5th value of an hourly time series moves the three chosen hours a day by one hour every day, resulting in randomly chosen hours per day in a longer time series.

A widely used measure is the *Root Mean Square Error* (RMSE), which gives a good measure for overall deviation, but is very sensitive to single large deviations.

$$RMSE = \sqrt{\frac{\sum_{i=1}^{N}(S_i - M_i)^2}{N}} \tag{6.2}$$

with N: number of data pairs, S_i: simulated value and M_i: measured value.

The *Root Mean Square Deviation* (RMSD) used for the comparison of simulated and remotely sensed data is similarly

$$RMSD = \sqrt{\frac{\sum_{i=1}^{N}(S_i - RS_i)^2}{N}} \tag{6.3}$$

with RS_i: remotely sensed value. It is mathematically similar to RMSE, but marks the comparison of a simulated dataset with data derived from remote sensing by techniques that are models themselves.

Another commonly used criterion in hydrology is the *Coefficient of Model Efficiency* (CME) after NASH & SUTCLIFFE (1970) that ranges between one and zero for satisfying agreement between model and measurement and becomes negative for an insufficient correlation of these two.

$$CME = 1 - \frac{\sum_{i=1}^{N}(M_i - S_i)^2}{\sum_{i=1}^{N}(M_i - M_m)^2} \tag{6.4}$$

with M_m: the average value of M_i.

For the assessment of the systematic bias of a predicted variable, the deviation of the simulated arithmetic mean from the measured arithmetic mean (deviation of mean, DM), which is equal to the arithmetic mean of the differences between simulated and measured variables, reads

$$DM = \frac{1}{N}\sum_{1}^{N}(S_i - M_i) = \frac{1}{N}\sum_{1}^{N}S_i - \frac{1}{N}\sum_{1}^{N}M_i \tag{6.5}$$

A mixture of these criteria together with graphical representations of simulated and measured time series of, mostly, soil temperature is used to validate the performance of the heat flux and storage models implemented in PROMET.

6.2. DEPENDENCE OF SHTM ON BOUNDARY CONDITIONS

The following field data was recorded at the two Eddy-Flux sites (see 4.1) south-west of Munich, located in a rapeseed field and a meadow, respectively. Measurements taken on both sites by colleagues of the Department of Geography (University of Munich) included soil temperature at depths of 7.5, 15 and 25 cm, soil moisture by TDR probes at the same depths and ground heat flux (G_0) with a heat flux plate in 5 cm depth. They were used to validate the performance of the Soil Heat Transfer Module as a stand-alone model.

As the G_0 measurements were taken at 5 cm depth, in the following, the model's upper boundary and the depths of the soil thermometers are corrected for this shift when comparing these measurements to simulated data. In this case, validation depths are 2.5, 10 and 20 cm below the level of the heat flux plates, the imaginary "soil surface" and upper boundary condition.
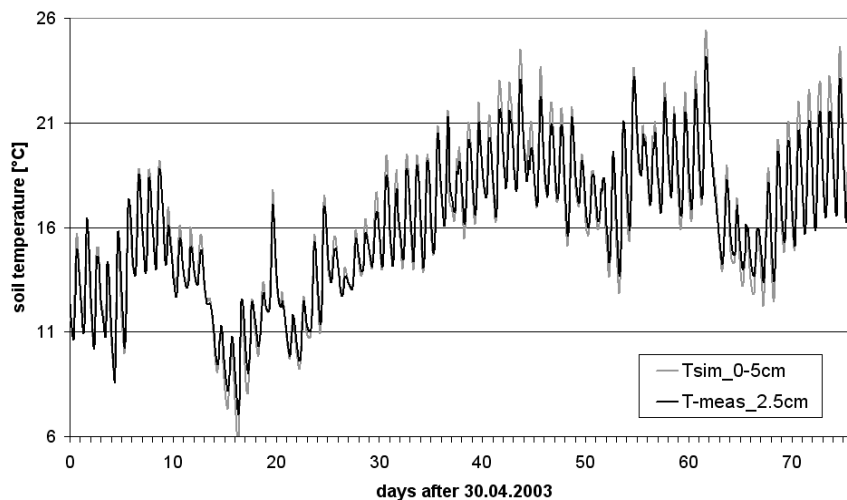
Fig. 6-1: Performance of SHTM with known boundary conditions at the *Gut Hüll* site: Measured vs. simulated hourly values of soil temperature (CME = 0.95).

The simulation for the summer season at *Gut Hüll*, from 30.04.2003 to 15.07.2003, fitted very well with the measured data (see Fig. 6-2) when using measured soil moisture and ground heat flux. Soil texture and soil density were determined as part of the field work during the summer of 2003 and were used as input parameters for this stand-alone simulation with SHTM. However, Fig. 6-2 shows that the daily amplitude is slightly overestimated, which can be ascribed to the coarse layering of the soil layer stack used in SHTM. Models for the exact reproduction of soil temperatures at certain depths, like SOHE (HUWE 1999) or BEKLIMA (BRADEN 1995), divide the soil column into 10 or more layers, with thicknesses as small as 0.005 m. The slight overestimation of daily temperature amplitudes with a 4-layer model is consistent with the analysis of BEST et al (2005) regarding the transmission of heat pulses into the soil.

Fig. 6-2: Performance of SHTM with known boundary conditions at the *Gut Hüll* site: Scatter plots of simulated vs. measured hourly soil temperatures at two depths of the soil column.

The *Wielenbach* data of 2004 could not be reproduced equally well by SHTM. The problems encountered here were missing soil texture data, strong influence of ground water and damaged soil moisture probes. Texture was estimated as loamy sand, with a high, but unknown, organic material content in the upper horizon. But variation of the soil properties did not enhance model performance significantly. Soil water content had to be simulated with the *Eagleson*-type soil water model, but it could not capture the strong influence of the shallow ground water table on soil moisture dynamics due to the model constraint, that the water table has to be deeper than the lower soil boundary. Consequently, in this case not all of the boundary conditions are known and the analysis of this model run shows the possibly strong influence of unknown soil water dynamics on soil temperature simulations. At that site, the high soil water content dampens the temperature amplitude and furthermore, in case of ground water influence, there is an unknown convective heat transport between ground water and soil that is not represented in SHTM simulations.

Nonetheless, the model could reproduce the dynamics of the upper two soil thermometers (Fig. 6-3) quite well, until the start of the winter season. Then, the convective transport of heat from the warmer saturated zone into the upper soil seemed to compensate some of the negative heat flux towards the cold soil surface. This led to a much warmer subsoil at the measurement site, unlike the model output.

Table 6-1: Statistics of simulation runs with SHTM and known boundary conditions.

	Mean_Sim	Mean_Meas	RMSE	CME	Gain	Offset
Gut Hüll Layer 1	15.83 °C	16.11 °C	0.73 °C	0.95	1.07	-1.06
Gut Hüll Layer 2	15.12 °C	15.72 °C	0.73 °C	0.93	1.04	-0.92
Wielenbach Layer 1	12.34 °C	13.22 °C	2.25 °C	0.76	1.39	-5.99
Wielenbach Layer 2	12.37 °C	13.30 °C	2.04 °C	0.76	1.35	-5.48
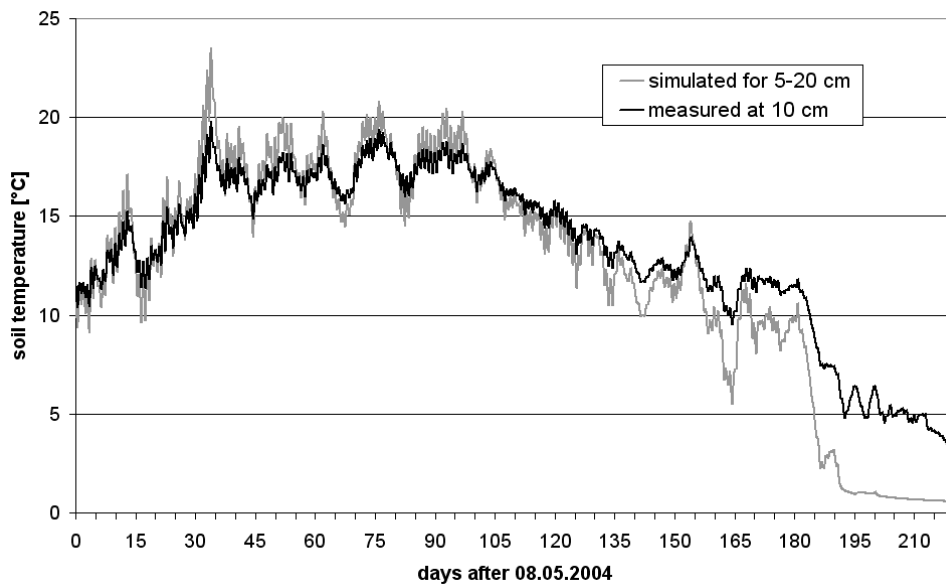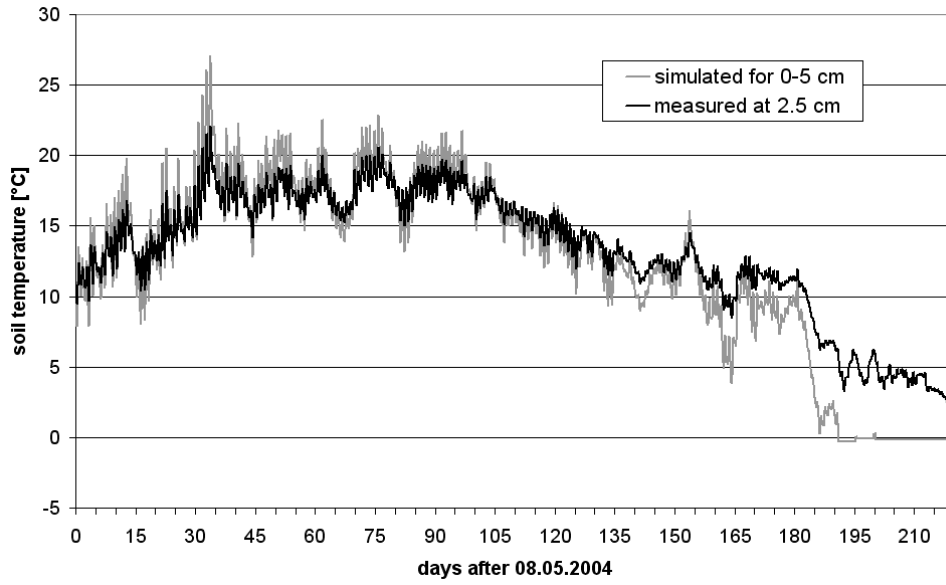
Fig. 6-3: Performance of SHTM with known boundary conditions at the *Wielenbach* site: Measured vs. simulated hourly soil temperature at two depths of the soil column.

6.3.   Influence of Different Model Configurations

In the following, the simulation run of PROMET with SHTM and the explicit energy balance algorithm at the standard 1x1 km^2 resolution is compared to the point scale measurements taken at the *Gut Hüll* site in summer 2003. Then, the influence of other PROMET modules on the performance of SHTM is evaluated by analyzing a modified plant parameterisation and a different meteorological input. Results with both the *Penman-Monteith* energy balance model and the empirical ground heat flux model are also presented.

6.3.1.   Results Based on the Explicit Energy Balance Algorithm

The comparison of simulations with the full PROMET model, including the explicit energy balance algorithm, against temperature series taken at the EF sites, naturally shows larger deviations than the stand-alone SHTM version, because the input variables of SHTM are provided by other modules with inherent uncertainties. The following analysis of model results and measurements aims at showing how mesoscale simulations of soil temperature compare to point scale conditions. All simulations were started at a model time of one year before the validation period, in order to minimize the influence of any arbitrary starting conditions.
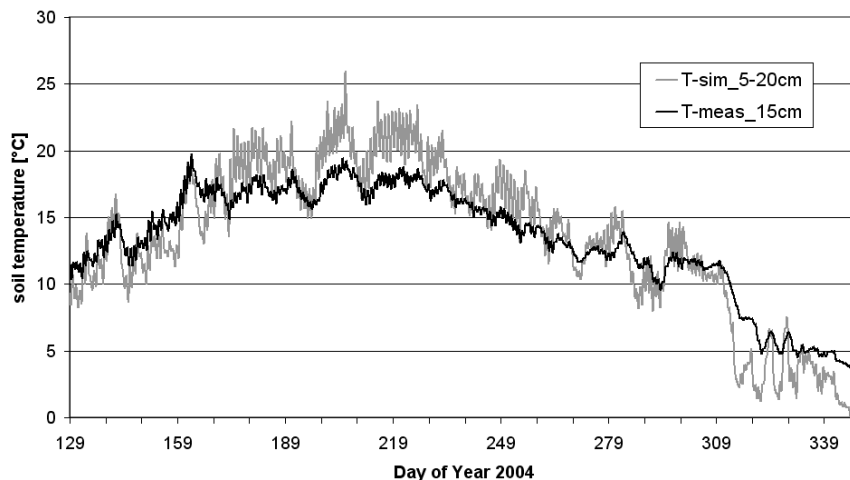
Fig. 6-4: Performance of PROMET w/ SHTM at the *Wielenbach* site: Measured vs. simulated hourly soil layer 2 temperatures.

The proxel (*process pixel*) of the *Wielenbach* site is characterized by intensive grassland on a nearly flat clay loam (Ut2) soil at an altitude of 542 m. Again, the amplitudes of the simulated time series are highly overestimated, due to the problems described in the previous section (see Fig. 6-4). The CME (= 0.72) is relatively high because the *Wielenbach* time series spans from May to December and therefore, the deviation of measured temperatures from the mean is quite high. The RMSE (= 2.2 °C) is acceptable for this type of location, but most importantly, the mean temperatures are reproduced quite well by the model (Table 6-2). It should be noted, the full model

performs better in simulating soil temperatures in late autumn, more so than the stand-alone version with measured ground heat flux.

Because of the ground water related, strong systematic error of the simulated soil temperatures at the *Wielenbach* site, the further validation of PROMET with SHTM concentrates on the *Gut Hüll* site, where the previous validation with known boundary conditions showed that these are well known. Attention should be paid to the fact that in this case, soil layer temperatures are compared with time series taken at the true measurement depths unlike in section 6.2, because the depth of the heat flux plates has not to be considered.

Like the previous site, the measurement site *Gut Hüll* is located on a proxel with matching land cover and soil type conditions. The land use of this proxel is cultivated land, which is set to rapeseed cultivation for all simulation runs, on a clay silt (Ut2) soil at 581 m height above sea level. The model slope is 0.5°, facing north.

A qualitative assessment of the temperature graphs in Fig. 6-5 shows, that the mean daily temperatures of the upper two soil layers are overestimated by the model, but the run of the simulated curves is well related to the measurements. Following the analysis of the amplitude damping in 3.3.3, the hourly top soil layer (0-5 cm) temperature should match a measurement in 4 cm depth and the one of the third layer should be evaluated against measurements taken at 60 cm depth. But because the daily amplitude in the third layer is very small and the annual damping decreases slowly with depth, presumably the layer averaged temperature (20-65 cm) can be validated against the measured temperature at 25 cm depth with some caution. Yet the simulated temperature of the second layer (5-20 cm) can clearly be validated against the time series of the soil thermometer at a depth of 15 cm. This conclusion is supported by the statistical values presented in Table 6-2, especially arithmetic mean, RMSE and CME. Analysis of the linear regressions (see also Fig. 6-6) illustrates some systematic error that is reduced with increasing depth and very good coefficients of determination for layers 2 and 3.

A quantitative assessment of the daily amplitudes produced by the model shows that for both, the top and the second soil layer, the correlation between model and reality (R^2) is low (Fig. 6-7). Still, the data of the second soil layer scatters sufficiently well along the 1:1 graph. All in all, the performance of SHTM with the explicit energy balance module inside the PROMET framework performs well when comparing simulated hourly temperatures with field measurements. Still some unknown factors reduce the potential accuracy of SHTM that it has shown, when run with known boundary conditions. Therefore, the most influential model parameters, inputs and configurations, are assessed in the following section.
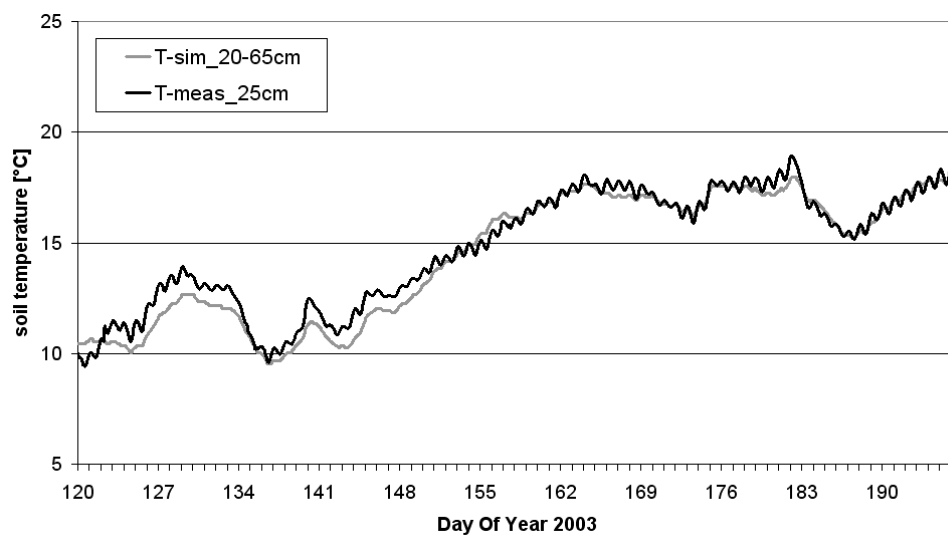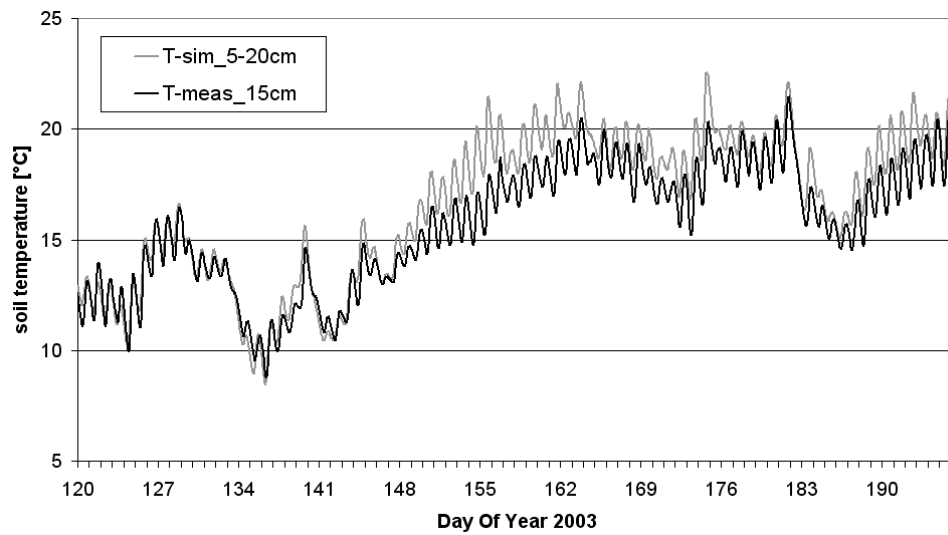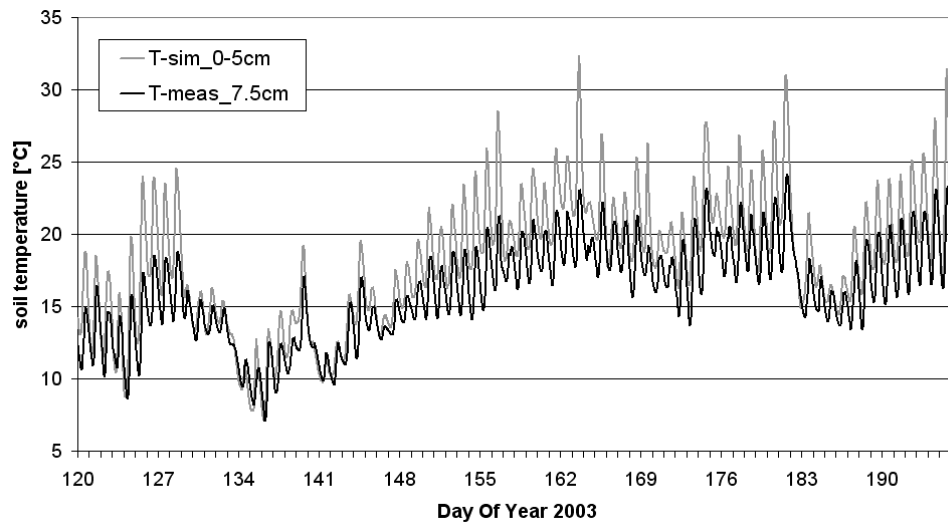
Fig. 6-5: Performance of PROMET w/ SHTM on the *Gut Hüll* proxel: Measured vs. simulated hourly soil temperatures for three modelled soil layers.
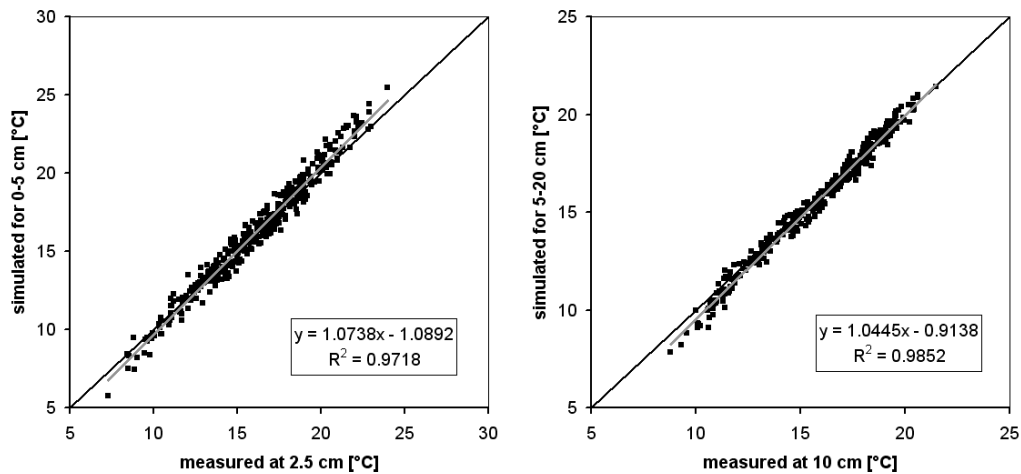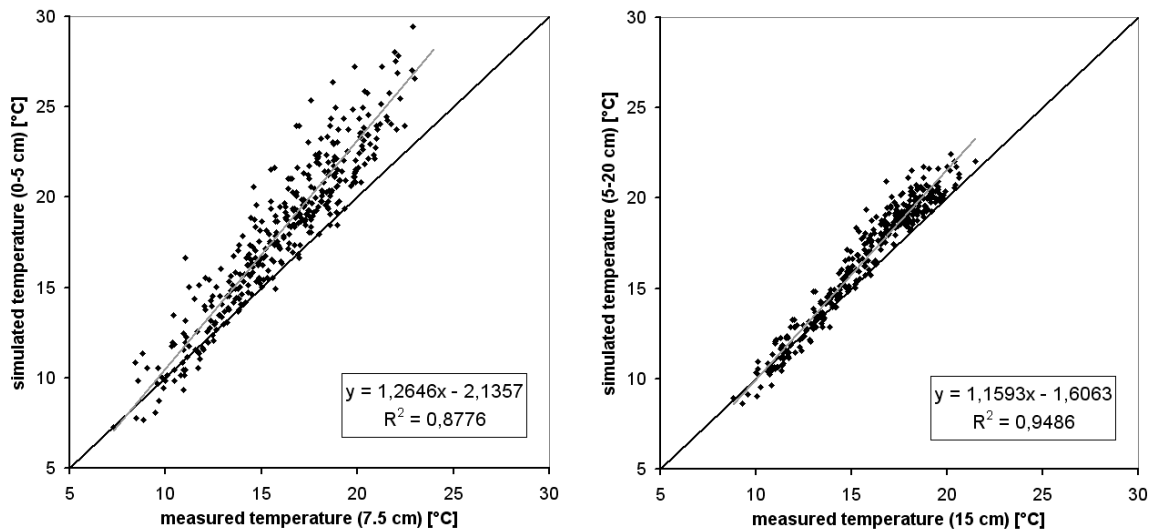
Fig. 6-6: Performance of PROMET w/ SHTM at the *Gut Hüll* site: Scatter plots of simulated vs. measured hourly soil temperatures at two depths of the soil column.
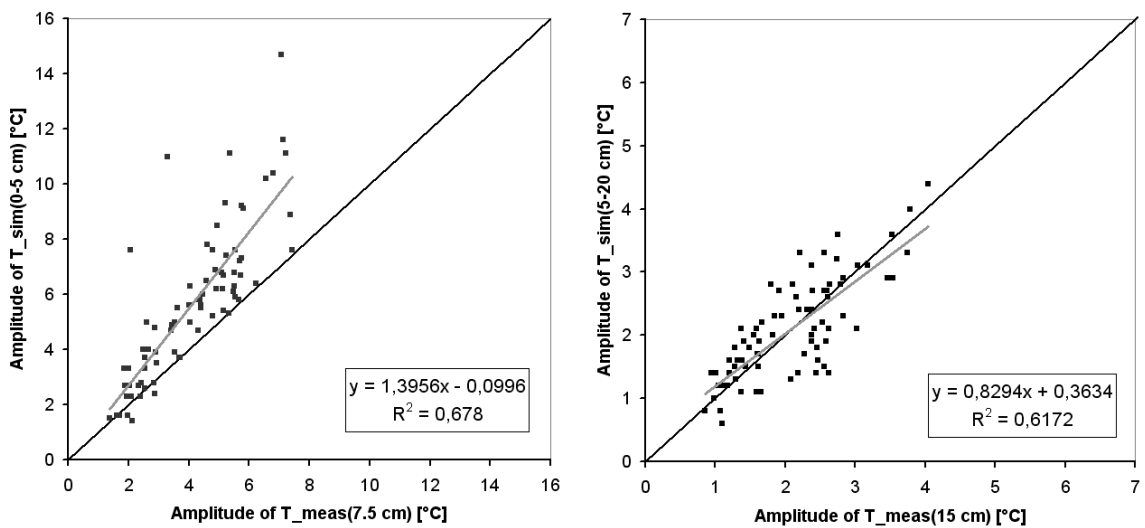
Fig. 6-7: Performance of PROMET w/ SHTM at the *Gut Hüll* site: Scatter plots of daily soil temperature amplitudes at two depths of the soil column.

Table 6-2: Statistical values of the simulations with the PROMET w/ SHTM model.

	Mean_Sim	Mean_Meas	RMSE	CME	Gain	Offset	R2
Gut Hüll Layer 1	18.24 °C	16.11 °C	2.79 °C	0.28	1.26	-2.14	0.88
Gut Hüll Layer 2	16.61 °C	15.72 °C	1.25 °C	0.80	1.16	-1.61	0.95
Gut Hüll Layer 3	14.48 °C	14.79 °C	0.56 °C	0.95	1.06	-1.19	0.98
Wielenbach Layer 1	13.58 °C	13.23 °C	2.85 °C	0.61	1.34	-4.11	0.87
Wielenbach Layer 2	13.45 °C	13.3 °C	2.19 °C	0.72	1.34	-4.41	0.92
Wielenbach Layer 3	13.03 °C	12.57 °C	1.41 °C	0.85	1.19	-1.89	0.94

6.3.2. Influence of Soil and Plant Parameters

The influence of soil properties on thermal conductivity of a soil layer is addressed in 3.4.4, as well as in the linear relationships of volumetric heat capacity with porosity and soil water content. Thermal conductivity λ is mainly influenced by the organic material fraction of a soil layer, its porosity and soil water content. A sensitivity analysis has already been presented, but a variation of porosity or organic material content at the *Gut Hüll* site does not improve the overall performance of SHTM because the differences between simulated and measured soil temperatures vary with time. This leads to the conclusion that the simulated soil moisture differs from the measured one, due to differences in interpolated and measured precipitation. A simulation run with the meteorological time series recorded by the EF station is presented in the next section.

To assess the influence of the canopy on the soil energy balance, the LAI, the most important input variable of the canopy light interception algorithm, was modified. Fig. 6-8 shows the standard LAI simulated by the *Farquar* model, two test parameterisations with reduced and increased LAI trends and an interpolation of *Plant Area Index* (PAI) measurements that were recorded at the *Gut Hüll* site. While PAI is a measure of the surface of the whole crop, including blossoms, stems and fruits, the LAI only relates to the photosynthetically active leaf areas of a crop.
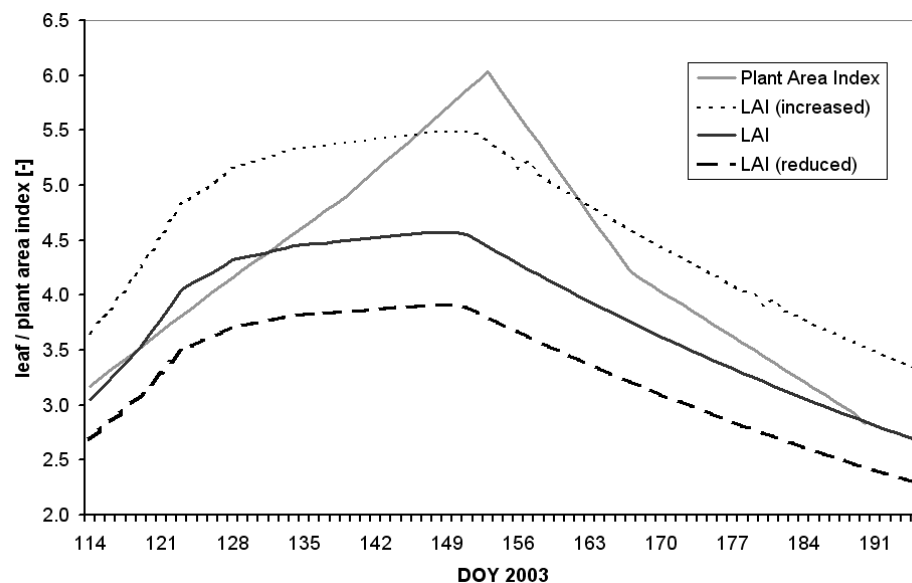
Fig. 6-8: Simulated LAI and interpolated, measured PAI of rapeseed in summer 2003.

As expected, the influence of the LAI variation on the ground heat flux due to the two test parameterisations is clearly visible in the statistical criteria. Even a small reduction (~0.6) in simulated LAI leads to a warmer soil surface and higher simulated soil temperatures, therefore a reduced performance of SHTM (CME = 0.64, RMSE = 1.68, see Table 6-3). Similar to the model used by Thunholm (1990), simulated soil temperatures are sensitive to the LAI and the light interception ratio of the canopy.
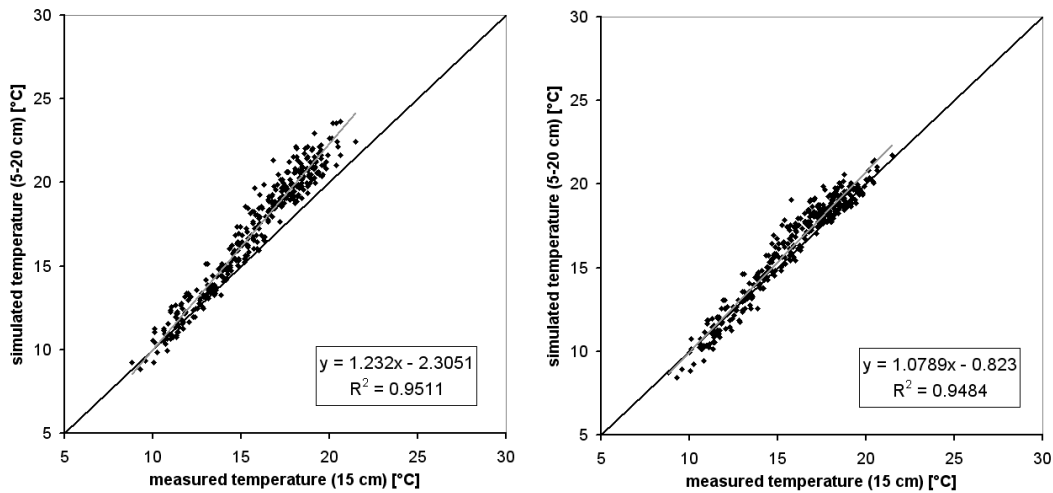
Fig. 6-9: Correlation of simulated with measured soil temperatures based on reduced (left) and increased (right) LAI at *Gut Hüll.*
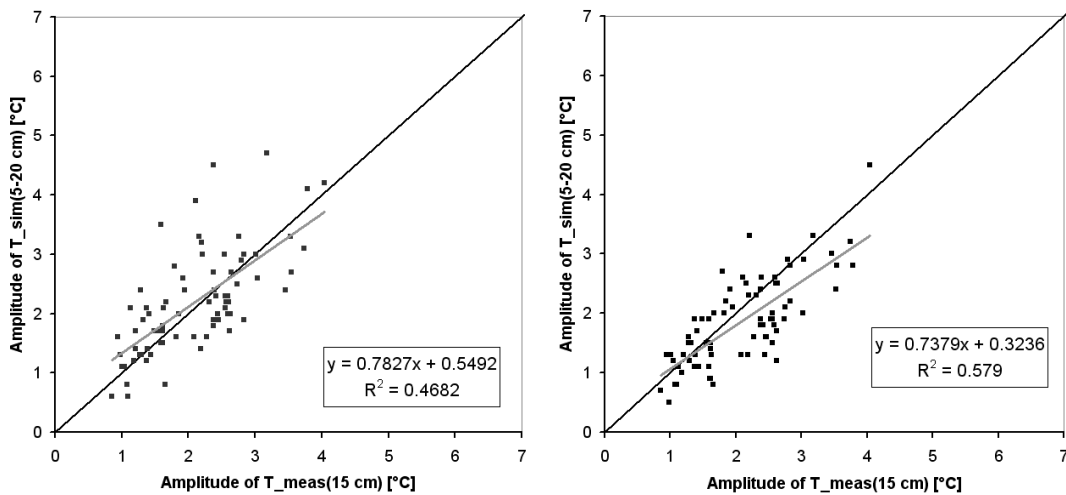
Fig. 6-10: Correlation of simulated with measured temperature amplitudes based on reduced (left) and increased (right) LAI at *Gut Hüll.*

By contrast, a slightly stronger increase (~1.0) in LAI leads to a better representation of mean daily temperatures (CME = 0.91, RMSE = 0.84), as shown in Fig. 6-9 and Table 6-3. But even though the increased LAI leads to a better performance of SHTM in regards to mean daily temperatures, the correlation of the simulated daily amplitudes (Fig. 6-10) with the measured ones decreases. But PROMET is also designed for the simulation of plant growth, when the biophysical canopy module of HANK (2008) is included. On this account, these high LAI values during most of the growth period can not be accepted as realistic, when compared to measurements and literature values. Most likely, the light transmission through canopies algorithm should be improved. And, as the analysis of the stand-alone version showed, a slight overestimation of daily amplitudes is expected, presumably due to the soil layer stack geometry, contrary to the underestimation in the "increased LAI" case.

6.3.3. INFLUENCE OF METEOROLOGICAL INPUT DATA

Meteorological input variables for catchment scale simulations with PROMET are provided by an algorithm that supplies hourly time series by temporal interpolation of climate station records. Subsequently, at each time step, a spatial interpolation scheme prepares the meteorological input for each proxel on the basis of the surrounding climate stations data. As a consequence, the meteorological drivers of the land surface process modules already differ from the true conditions found at the investigated site. To assess the deviation of the most influential inputs, Fig. 6-11 presents scatter plots of air temperature and global radiation. Notably, simulated air temperature has a lower daily amplitude (gain < 1), but is generally higher than the true air temperature at *Gut Hüll* (offset = 2.7), especially at night. Warmer air temperatures that have been mostly recorded at midday are reproduced much better by the interpolation procedure of the model. Overall, the difference between the arithmetic means of the simulated and measured time series for the recorded period (30.04. to 15.07.2003) is +0.52 °C, mainly caused by an overestimation of night time air temperatures by the temporal interpolation of the meteorological module.

Global radiation from the radiation model is actually on average 14 W/m^2 lower than the measured one, but average net radiation above canopy is about 40 W/m^2 higher in the model than measured in the field. Three reasons seem to lead to this overestimation of net radiation: Especially during night time, the long wave net radiation is biased by overestimated air temperatures in the model. Additionally, too high simulated air temperatures reduce the sensible heat flux from the soil surface into the atmosphere and therefore adding a positive bias on simulated soil temperatures.
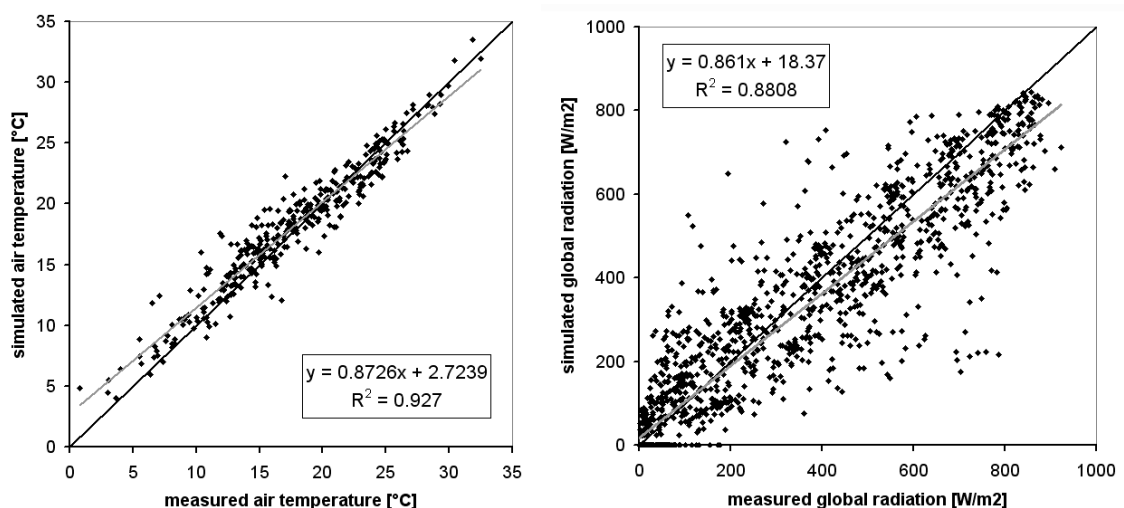
Fig. 6-11: Differences between simulated and measured air temperature (left) and above canopy global radiation (right) at *Gut Hüll*.

Secondly, reflection and absorption of incoming radiation are strongly related to vegetation and soil parameters that can not be exactly known. Finally, standard

measurements of net radiation generally underestimate true net radiation. HODGES & SMITH (1997) found, that at 15 of 21 measuring sites they investigated, net radiation was underestimated by about 5% in the daytime and about 45% at night. TWINE et al (2000) also estimate the daytime accuracy of net radiation measurements to be about 6 %, mainly caused by the heating of their measurement devices by solar radiation.

Spatial interpolation of precipitation introduces even more uncertainty, due to the spatial and temporal non-continuous nature of precipitation. But since SHTM does not consider convective heat transport due to infiltrating water, the main effect of precipitation taken in consideration is the increase in soil moisture during and after rain events. Graphs of simulated and recorded soil moisture time series (Fig. 6-12) reveal that too little precipitation is computed in the beginning and during the second half of the validation period. Substituting the interpolated precipitation with the one recorded at the EF site produces a better fit of simulated and recorded soil moisture in the second layer.
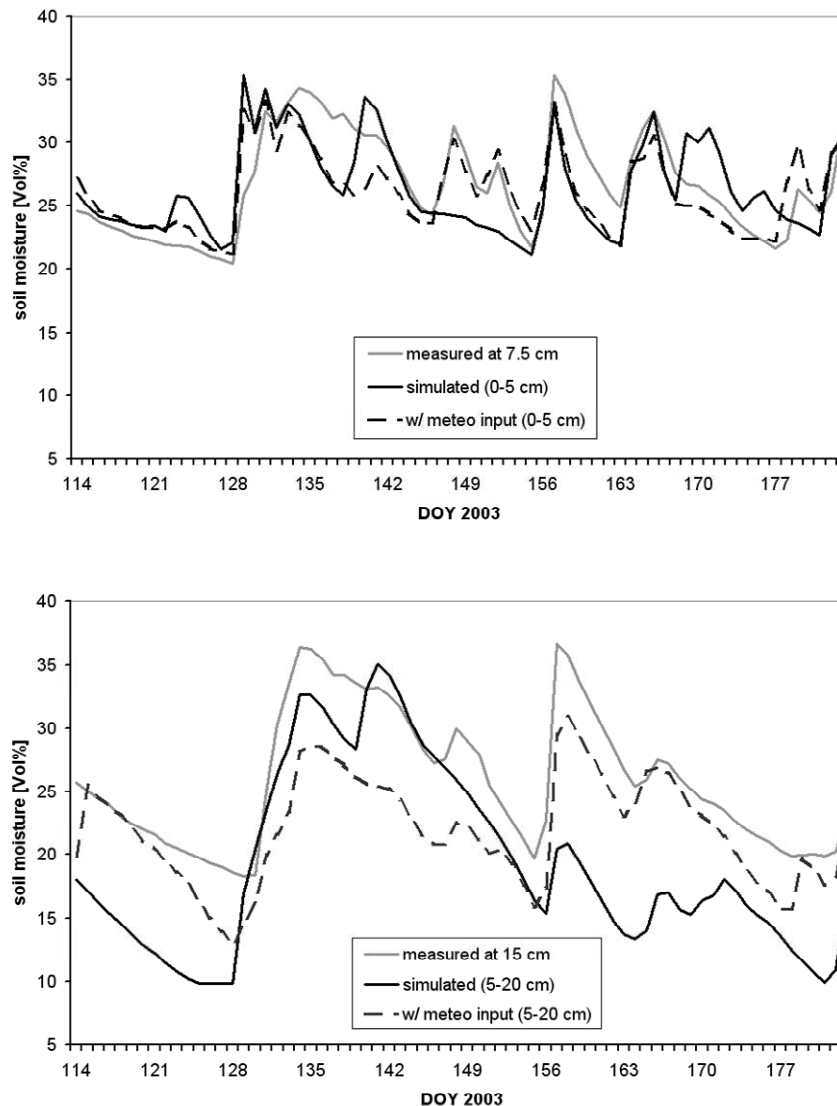
Fig. 6-12: Measured soil moisture at different depths (*Gut Hüll* 2003) vs. simulated soil moisture with interpolated and measured meteorological drivers.

In some way, the performance of the model is improved during the validation period, by using the recorded values of air temperature, global radiation above canopy and precipitation as driving input (Fig. 6-13). The fit of the top layer temperature with the 7.5 cm measurement improves (Table 6-3), but the measures of deviation between the simulated second layer temperature and the associated measurement are not improved. Only the coefficient of determination (R^2) points out, that the non-systematic errors, due to the meteorological inputs, are reduced. As expected, the average simulated daily amplitude is greater than before for both soil layers, as a result of increased input from global radiation, and the coefficients of determination for the regression of daily amplitudes increase too, at both soil depths (Fig. 6-14 and Table 6-4), when using the recorded meteorological inputs.
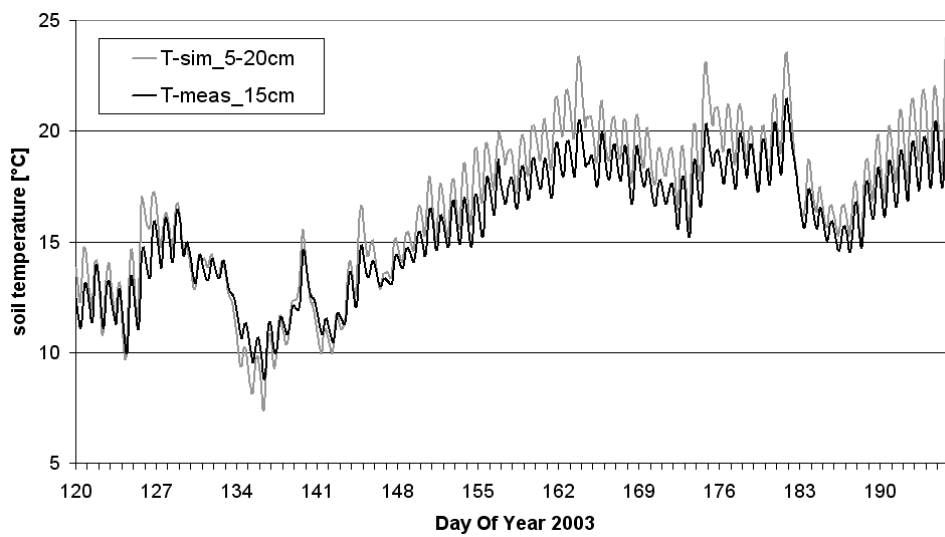
Fig. 6-13: Performance of PROMET with measured meteorological input at *Gut Hüll*:
Measured vs. simulated hourly soil temperature of the second soil layer.
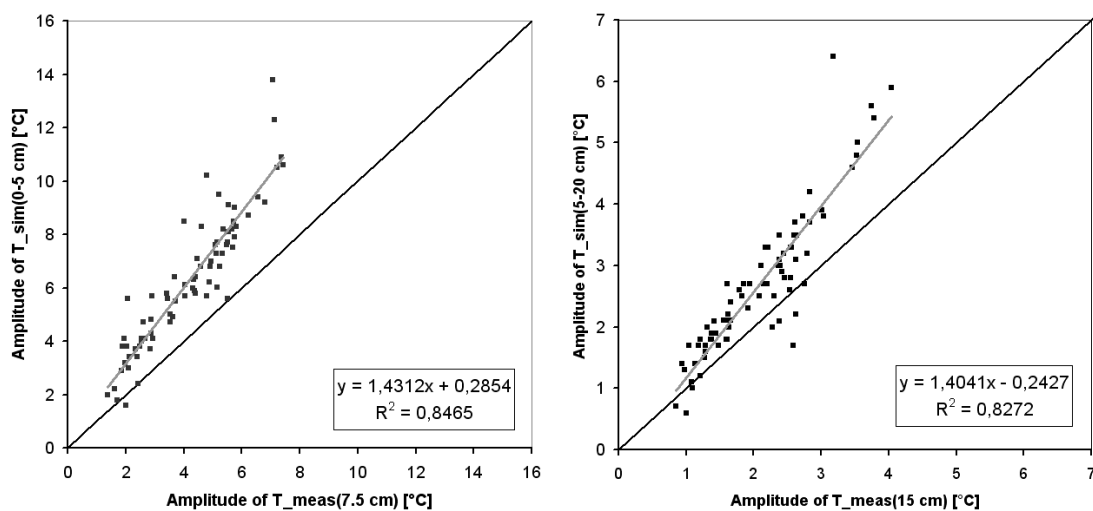
Fig. 6-14: Performance of PROMET with measured meteorological input at *Gut Hüll*:
Scatter plots of measured vs. simulated daily soil temperature amplitudes
of the upper two soil layers.

This investigation shows that interpolated climate data leads to non-systematic errors in soil temperature simulations that can be reduced for point-scale model runs, when using recorded meteorological data. It reveals also, that in this case, the implemented combination of canopy model, explicit energy balance module and SHTM introduces a systematic overestimation of daily and long-term soil temperature amplitudes in the upper layers. Though, the deviation of the modelled temperatures from the measured ones is rated low. This is because a simplified, mesoscale model, run with standard parameterisations, is compared to point scale measurements of a sensitive variable, that is affected by highly complex conditions.

Table 6-3: Summary of statistical criteria related to different model runs (standard = standard model run; meteo input = model run with recorded T_{air}, R_{global} and precipitation).

Gut Hüll	dev. of mean	RMSE	CME	Gain	Offset	R2
Layer 1 standard	2.13 °C	2.79 °C	0.28	1.26	-2.14	0.88
Layer 1 reduced LAI	2.38 °C	2.98 °C	0.18	1.26	-1.79	0.88
Layer 1 increased LAI	1.89 °C	2.59 °C	0.38	1.26	-2.36	0.88
Layer 1 meteo input	1.68 °C	2.34 °C	0.49	1.27	-2.72	0.91
Layer 2 standard	0.91 °C	1.25 °C	0.80	1.16	-1.61	0.95
Layer 2 reduced LAI	1.34 °C	1.68 °C	0.64	1.23	-2.31	0.95
Layer 2 increased LAI	0.41 °C	0.84 °C	0.91	1.08	-0.82	0.95
Layer 2 meteo input	0.90 °C	1.28 °C	0.79	1.22	-2.62	0.97

Table 6-4: Summary of linear regression between measured and different simulated daily amplitudes of soil temperature at the Gut Hüll site.

Gut Hüll	Gain	Offset	R2
Layer 1 standard	1.40	-0.10	0.68
Layer 1 reduced LAI	1.25	0.19	0.62
Layer 1 increased LAI	1.45	-0.44	0.71
Layer 1 meteo input	1.43	0.29	0.85
Layer 2 standard	0.83	0.36	0.62
Layer 2 reduced LAI	0.78	0.55	0.47
Layer 2 increased LAI	0.74	0.32	0.58
Layer 2 meteo input	1.40	-0.24	0.83

6.3.4. RESULTS WITH SIMPLIFIED GROUND HEAT FLUX MODULES

Besides the sensitivity of the simulated soil temperature to input variables and parameters, PROMET provides three different algorithms that compute ground heat fluxes on an hourly time scale. All findings shown so far, were computed with the algorithm presented in 3.6.1, that separates the energy balances for the soil surface and the canopy (if any). In the following, results are shown with the energy balance algorithm for the *Penman-Monteith* evapotranspiration module and the empirical model of surface ground heat flux.

The *Penman-Monteith* Energy balance (PME) module basically uses the same iteration scheme as the Explicit Energy Balance (EEB) model, but calculates the surface energy fluxes for the entire land surface, including soil surface and canopy. Hence, in case of plant cover, no soil surface temperature is computed, only a overall land surface temperature. Thus it is assumed, that for dense canopies the influence of the above canopy radiation flux on soil heat flux is disproportionately strong, leading to exaggerated daily and long-term amplitudes of simulated soil temperatures. Fig. 6-15 illustrates, that the deviation of PME temperature from measured temperature in the second layer is noticeable stronger than with the EEB model (Fig. 6-5) before day of year (DOY) 155 at *Gut Hüll*. During the second half of the validation period, the PME model performs similarly well as the EEB. As a consequence, the correlation of hourly simulated temperatures with measured ones has a similar trend, but a larger scatter (Fig. 6-16), that way the coefficient of determination is reduced when compared to the results with EEB input, as well as the CME (Table 6-5). Interestingly, the deviation of the simulated from the measured mean temperature during the validation period is lower for the PME variant than for the EEB variant. The daily amplitudes are overestimated with PME input for both tabulated soil layers and surprisingly the correlation (R^2) of PME-simulated amplitudes with measured ones in the second soil layer is very low.
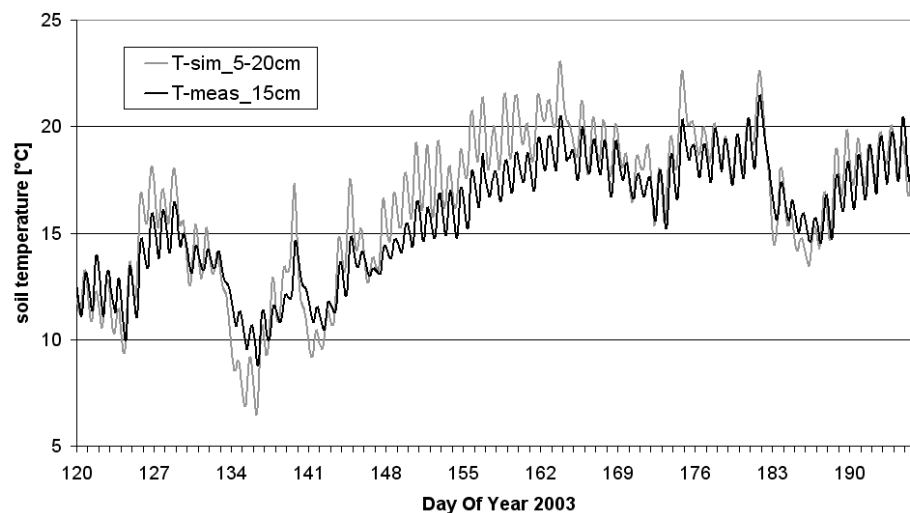
Fig. 6-15: Performance of SHTM w/ PME input at the *Gut Hüll* site: Measured vs. simulated hourly soil temperatures in the second soil layer.
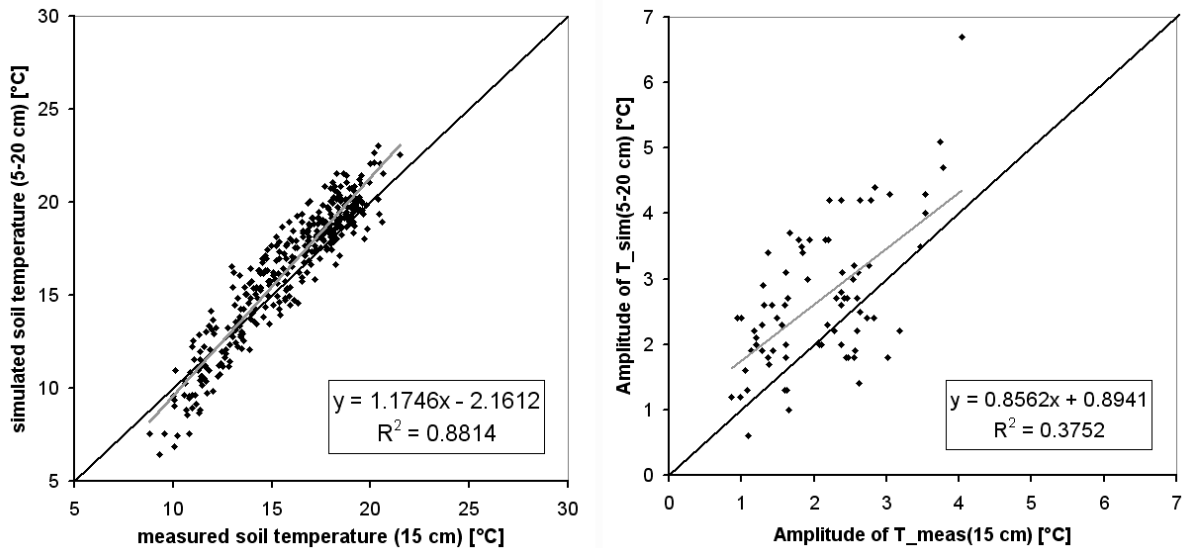
Fig. 6-16: Performance of SHTM w/ PME input at the *Gut Hüll* site: Scatter plots of hourly soil temperatures and daily amplitudes in the second soil layer.

Table 6-5: Summary of statistical criteria related to the three different surface ground heat flux models EEB, PME and EmpGHF.

	dev. of mean	RMSE	CME	Gain	Offset	R2
Layer 1 (EEB)	2.13 °C	2.79 °C	0.28	1.26	-2.14	0.88
→ Amplitude Correlation				1.40	-0.10	0.68
Layer 1 (PME)	1.67 °C	3.11 °C	0.10	1.25	-2.29	0.73
→ Amplitude Correlation				1.47	1.10	0.71
Layer 1 (EmpGHF)	1.62 °C	3.40 °C	-0.07	1.50	-6.42	0.80
→ Amplitude Correlation				1.36	-0.15	0.63
Layer 2 (EEB)	0.91 °C	1.25 °C	0.80	1.16	-1.61	0.95
→ Amplitude Correlation				0.83	0.36	0.62
Layer 2 (PME)	0.58 °C	1.42 °C	0.74	1.17	-2.16	0.88
→ Amplitude Correlation				0.86	0.89	0.38
Layer 2 (EmpGHF)	0.35 °C	2.70 °C	0.18	1.58	-8.73	0.83
→ Amplitude Correlation				0.65	0.39	0.51

If SHTM is run with the Empirical Ground Heat Flux module (EmpGHF), where G_0 is calculated as a fraction of net radiation, the fit of the predicted soil temperatures with the measurements is drastically reduced (Fig. 6-17). The simulated daily amplitudes are of the same order as the ones produced with the EEB module (Table 6-5), but the progression of the daily mean temperature from April to Juli 2003 is too much influenced by the position of the sun and the related global radiation. Despite the low performance of this model configuration, it has advantages over using the purely analytical sine wave approach, implemented in some models. The analytical approach overlays two sine waves based on equation (4.29) for the daily and annual amplitudes of the soil temperature. Even if the model efficiency of the analytical solution for the 15 cm depth (Fig. 6-19) is better in this case (CME = 0.32, RMSE = 2.31 °C), it cannot explain the day to day variation of soil temperature ($R^2 = 0.61$ as opposed to $R^2 = 0.83$

in the EmpGHF case), nor does its amplitude vary with differing atmospheric or soil-related conditions.

In summary, this analysis points out, that some energy balance algorithm has to be implemented in any catchment scale land surface model to compute realistical estimates of hourly soil temperatures. The simple empirical approach that relates ground heat fluxes to computed net radiation, implemented in some models which emphasize on assimilation of remotely sensed data (CHOUDHURY et al 1987, KUSTAS & DAUGHTRY 1990, NIEMEYER 2000, BOEGH et al 2002), should not be used in soil physical or biochemical predictions. It only beats the sine wave approach in terms of sensitivity to local conditions; otherwise its ground heat flux predictions are unreliable. The long term predictive ability of the EEB and PME driven soil temperature simulations, as well as the ability of SHTM to predict soil temperatures below the freezing point are explored in the next section.
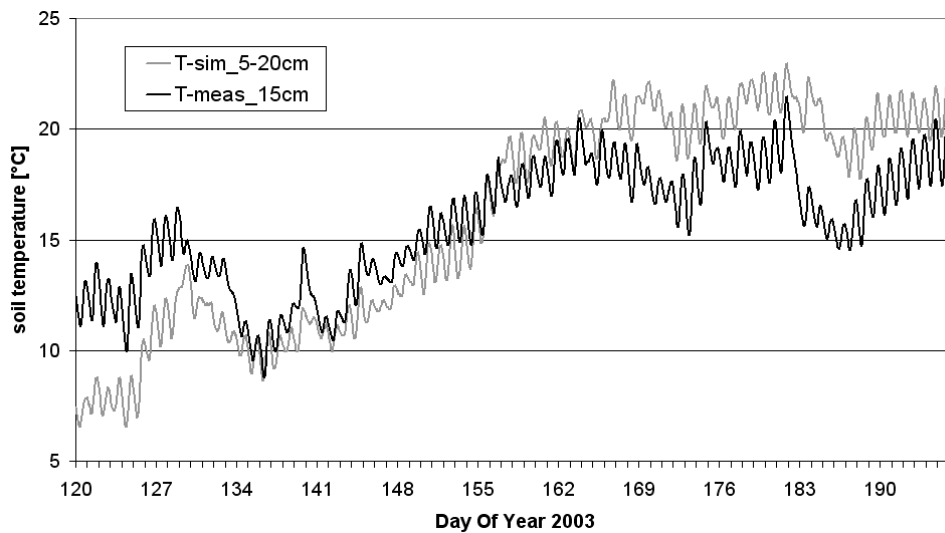
Fig. 6-17: Performance of SHTM w/ EmpGHF at the *Gut Hüll* site: Measured vs. simulated soil temperatures in the second soil layer.
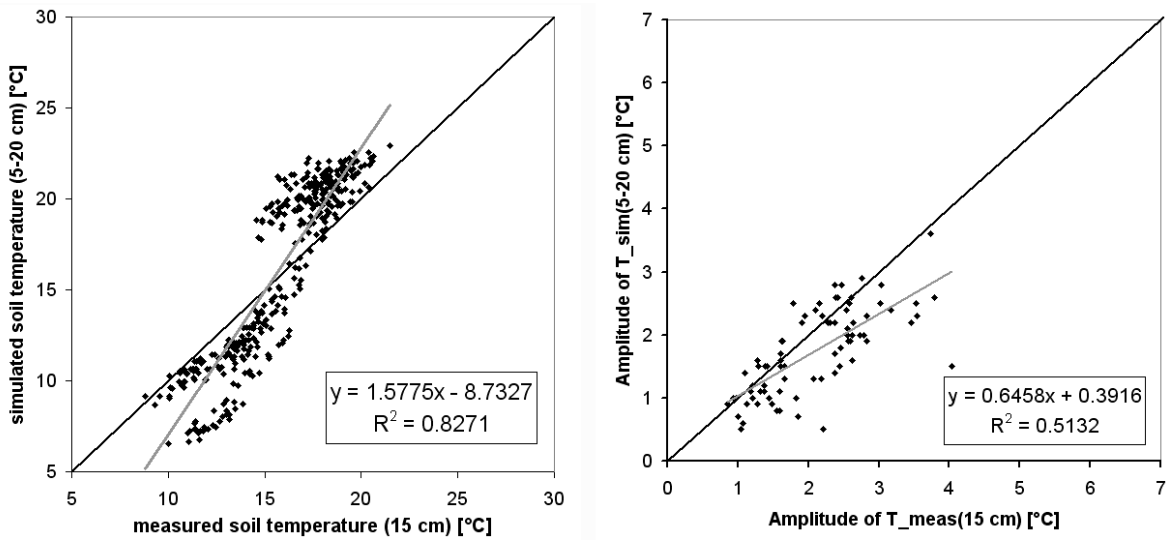
Fig. 6-18: Performance of SHTM w/ EmpGHF at the *Gut Hüll* site: Scatter plots of measured vs. simulated hourly soil temperatures and daily temperature amplitudes in the second soil layer.
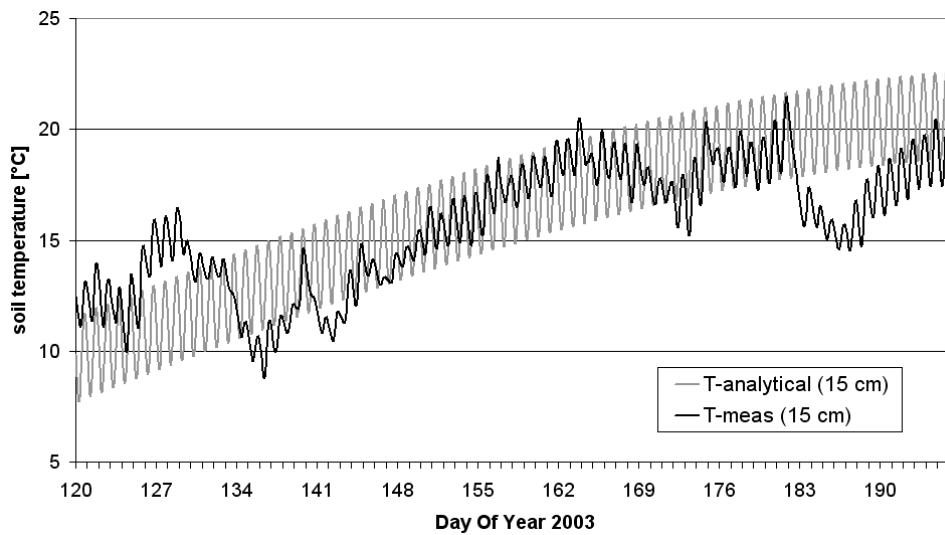
Fig. 6-19: Temperature curve of a possible solution of the sine-wave approach against soil temperature measured at *Gut Hüll* at 15 cm depth.

6.4.   Validation against Meteorological Network Data

6.4.1.   Comparison of SHTM with AgMet Time Series

To assess the performance of SHTM within in the PROMET framework in different regions of the mesoscale Upper Danube catchment, temperature time series, recorded at 5 and 20 cm soil depth at 28 agrometeorological (AgMet) stations (Fig. 4-3) are compared to model outputs of the soil layers for 0-5 cm and 5-20 cm depth, respectively. At three sites only the time series of the year 2004 could be used for validation, because of measurement errors during the extreme summer of 2003.

All PROMET runs for this investigation are carried out with standard input parameters on a 1x1 km^2 raster size. The spatial distribution of soils is not modified, but land use is set to extensive grassland for all investigated proxels, to reflect the usual plant cover of meteorological measurement sites. Output of SHTM is validated for both the EEB and PME surface energy modules, because both configurations are applicable in hydrological studies. The validation of the simulated in comparison to the recorded hourly time series of soil temperature is quantified on the basis of statistical criteria prepared for each simulated year and each investigated site. The coefficient of model efficiency (CME), the root mean of squared error (RMSE) and the deviation of the simulated annual mean from the measured one are tabulated for all AgMet stations and both years (2003 and 2004) in Appendix B. To assess the overall performance of SHTM, frequency distributions of 10 evenly distributed classes of the statistical criteria of the 53 available combinations of the modeled years and the chosen AgMet stations, or "cases", are analysed in the following.

Although the actual soil properties found at some AgMet sites differ considerable from the ones used in the soil parameterisation, the mean RMSE of the second soil layer temperature for all cases is only 1.75 °C and over 61% of the RMSE values are below 1.8 °C (Fig. 6-20), when the EEB variant is used. Compared to the RMSE achieved at the EF sites, at 82% for the AgMet cases the model performance is better than the one achieved for the second soil layer at *Wielenbach*. The RMSE mean values of the more dynamic upper soil layer are greater, but still over 75% of the calculated RMSE are lower than 2.6 °C and therefore better than the one achieved for the top layer of the *Gut Hüll* proxel. As for RMSE, the PME variant performs only slightly worse than PROMET / SHTM with EEB, but extreme deviations, with RMSE values greater than 3.0 °C (Fig. 6-21), increase notably.

Regarding the simulated annual mean of soil temperature at the depths of 5 and 20 cm, most of the simulated annual means with the EEB variant are close to the measured mean annual temperatures (Fig. 6-20). The PME variant on the other hand, underestimates the mean annual soil temperature for nearly all of the investigated sites (Fig. 6-21). Interestingly, the negative deviation is less pronounced in the second than in the top soil layer, leading to the conclusion that average energy input from the PME module is too small.
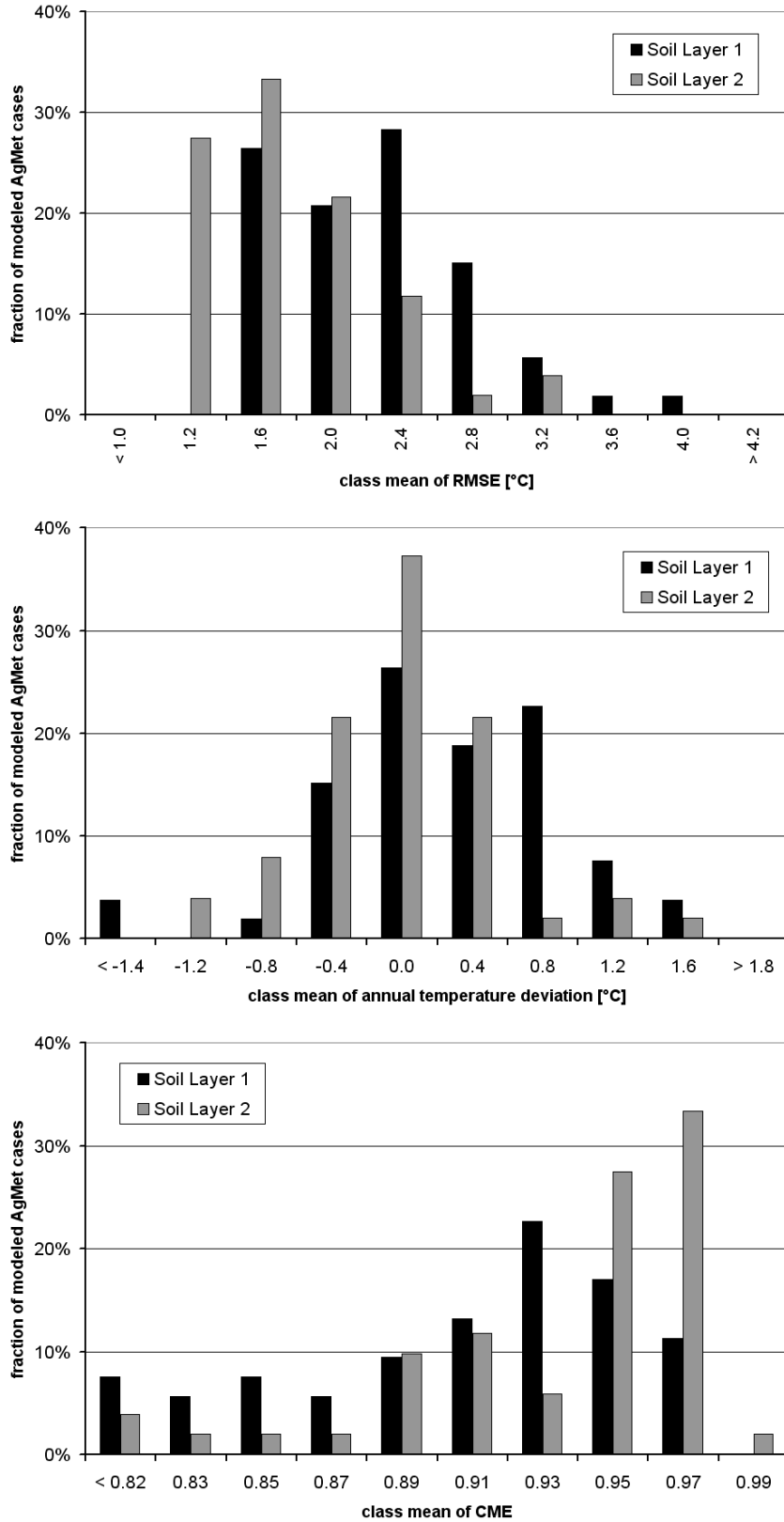
Fig. 6-20: Frequency distribution of annual statistical criteria (RMSE, deviation of annual mean temperature, CME) of the AgMet cases (one case per year and per AgMet station) simulated with PROMET w/ EEB ground heat flux.

Fig. 6-21: Frequency distribution of annual statistical criteria (RMSE, deviation of annual mean temperature, CME) of the AgMet cases (one case per year and per AgMet station) simulated with PROMET w/ PME ground heat flux.

Finally, the frequency distributions of the CME show the greatest discrepancy between both energy balance options. About 62% of the calculated soil layer 2 CME values of the EEB driven simulation are greater than 0.94 (Fig. 6-20), as opposed to only 36% in the case of the PME variant (Fig. 6-21). As the CME after NASH & SUTCLIFFE (1970) is dependent on the variation of the measured variable during the investigated period, a CME ≥ 0.90 is expected for a good fit of near surface soil temperature with an annual amplitude of about 15 °C. Low CME values (< 0.82), due to possible measurement errors or model input and parameterisation problems, show up in the EEB statistics, but are sharply increased in the PME variant. This is due to larger daily temperature amplitudes in the PME simulation, as shown by example at the *Sarching* site in Fig. 6-22. As the PME ground heat flux is related to the energy balance on top of canopy, it is evident, that daily G_0 rates are overestimated and night time G_0 is underestimated in case of plant cover. On the other hand, measured amplitudes vary strongly from site to site, by reason of varying soil properties, differing canopy heights and variations in data quality.

Table 6-6: Comparison of two PROMET configurations validated against time series of the years 2003 and 2004 from 28 agrometeorological sites in Bavaria.

		deviation of mean [°C]		RMSE [°C]		CME	
		mean	mode	mean	mode	mean	mode
EEB	soil layer 1	0.27	0.00	2.27	2.40	0.90	0.93
	soil layer 2	-0.03	0.00	1.75	1.60	0.93	0.97
PME	soil layer 1	-0.44	-0.80	2.60	2.40	0.87	< 0.82
	soil layer 2	-0.72	-0.40	1.96	1.60	0.92	0.93
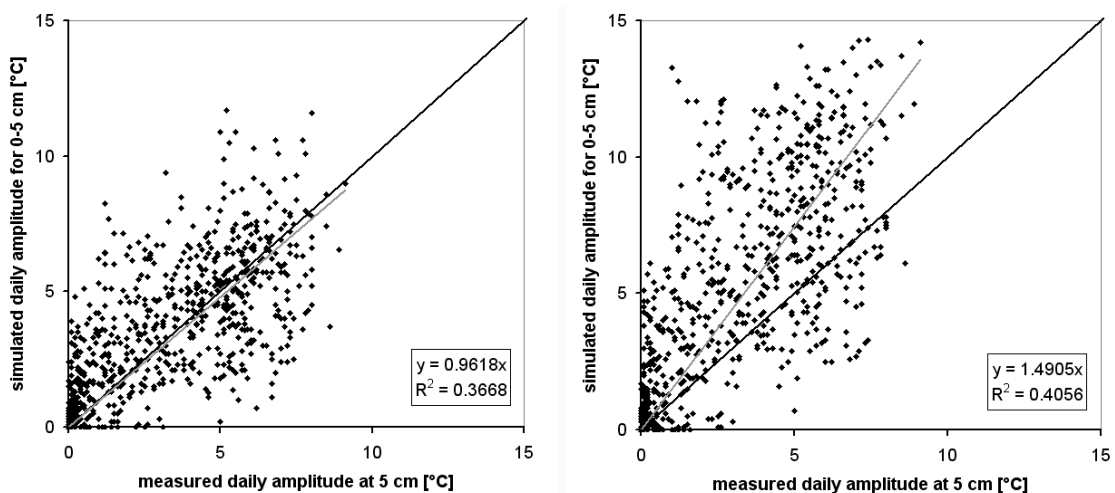
Fig. 6-22: Scatter plots of measured vs. simulated top soil layer temperature amplitudes at the AgMet site *Sarching* during 2004 (left: PROMET w/ EEB; right: PROMET w/ PME).

Nevertheless, some improvement of the PME algorithm should be possible by relating the effective G_0 to land cover properties, especially to vegetation properties. But instead of relating G_0 directly to R_{net} like the EmpGHF algorithm does, the daily amplitude of the land surface temperature could be reduced for the calculation of G_0 depending on vegetation cover. A possible approach could be similar to the method of ZHENG et al (1993) and KANG et al (2000), who related daily soil temperature dynamics to air temperature and LAI derived from Landsat Thematic Mapper data.

6.4.2. COMPARISON OF SHTM WITH DWD TIME SERIES

The German weather service (DWD) data on soil temperature time series, used in the following, are only recorded three times a day, but provide a higher accuracy as a result of regular, professional sensor calibration and post-processing of the data. As the simulated daily amplitudes of soil temperature have already been evaluated in the previous sections, the available DWD time series are used to validate daily SHTM outputs over multiple years, with focus on the performance of the soil freezing model and the resulting winter temperatures of the near surface soil. Again, no soil or vegetation parameters are customized to local conditions and all validation runs are carried out on the standard 1x1 km^2 proxel with extensive grass land cover for the years 2002 to 2005. The model configuration includes the enhanced biophysical canopy module of HANK (2008) and the explicit energy balance (EEB) algorithm.

Table 6-7: Summary of statistical criteria for the validation period 2002 to 2005 of SHTM w/ EEB at 15 DWD stations inside the Upper Danube catchment.

ID	Name	Top Layer (0-5 cm)			Second Layer (5-20 cm)		
		dev. mean [°C]	RMSE [°C]	CME	dev. mean [°C]	RMSE [°C]	CME
4144	OBERSTDORF (WST)	-0.25	1.59	0.96	-0.41	1.63	0.95
4161	HOHENPEISSENBERG (OBS)	0.17	1.43	0.96	0.29	1.52	0.95
4890	FUERSTENZELL (WST)	-0.46	1.36	0.97	-0.94	1.29	0.98
4481	WEIDEN/OFF. (WST)	0.24	1.42	0.96	-0.12	1.03	0.98
4187	OBERSCHLEISSHEIM	-1.39	2.10	0.94	-1.53	2.10	0.94
4131	MAISACH-GERNLINDEN				-0.18	1.32	0.98
4137	KEMPTEN (WST)	-0.37	1.32	0.97	-0.66	1.21	0.98
4499	REGENSBURG (WST)	-0.18	1.35	0.97	-0.40	1.33	0.98
4505	STRAUBING (WST)	0.48	1.35	0.98	0.12	1.08	0.98
4109	KOESCHING	-0.50	1.14	0.98	-0.53	1.31	0.98
4503	LANDSHUT	0.48	1.64	0.94	0.29	1.33	0.96
4362	KOENIGSMOOS-UNTERMAXFELD	0.55	1.75	0.94	0.30	1.55	0.95
4185	MAINBURG				-1.05	1.52	0.98
4497	ZWIESEL (AWST)	-0.13	1.33	0.97	-0.37	1.20	0.97
4528	MUEHLDORF/INN (WST)	-0.44	1.51	0.97	-0.74	1.42	0.97

As the first part of the analysis, the statistical criteria, deviation of annual mean, RMSE and CME, are computed for each year at each validation site. The daily mean of the simulated temperature of the first soil layer is compared to the measured mean soil temperature at 5 cm depth and the second soil layer temperature with the measurement at 20 cm. Table 6-7 shows the statistical values for each DWD site, averaged over the validation period. Due to the less dynamic nature of daily temperature time series, the mean CME values calculated for each site are in the

range of 0.94 to 0.98. Likewise, the RMSE values range from 1.03 °C to 2.10 °C and therefore are significantly lower than in the analysis of hourly soil temperatures at the AgMet sites. The difference in RMSE between the top and the second soil layer is considerable reduced when investigating daily time series, from about 0.5 °C to 0.1 °C, averaged over all data sets. The mean annual deviation of simulated to measured soil temperature is on average close to zero for the top layer (-0.12 °C) and slightly lower in the second layer (-0.39 °C).
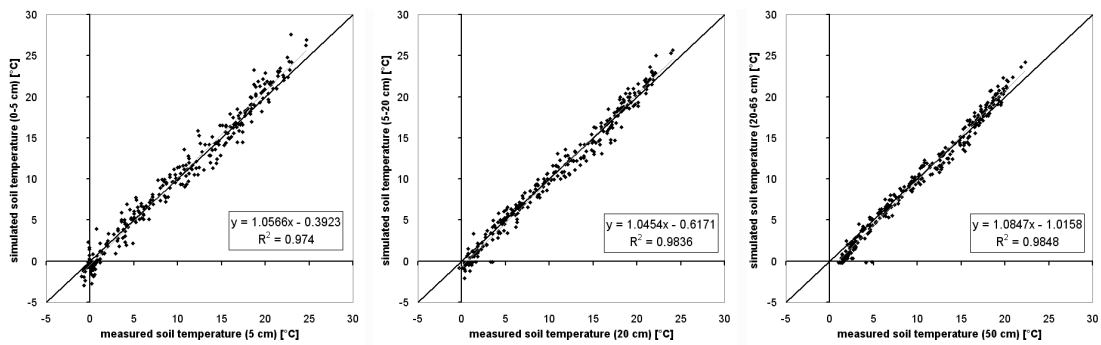
Fig. 6-23: Scatter plots of measured and simulated daily soil temperature at the DWD station *Weiden* for the years 2002 to 2005.
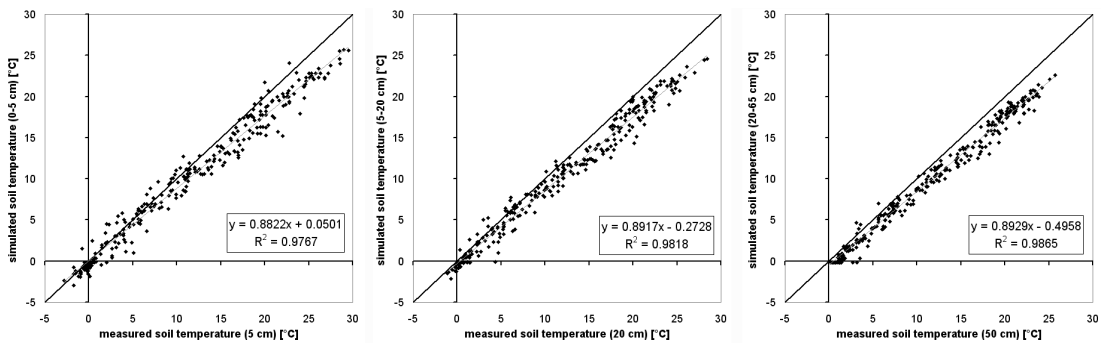
Fig. 6-24: Scatter plots of measured and simulated daily soil temperature at the DWD station *Oberschleissheim* for the years 2002 to 2005.

To further inspect the performance of SHTM compared to the DWD records, scatter plots of simulated temperatures in the upper three model layers against the measurements at 5, 20 and 50 cm at the best and worst performing sites, *Weiden* and *Oberschleissheim*, are depicted in Fig. 6-23 and Fig. 6-24. The linear regressions presented, are based on every 5th value (see section 6.1) of the 4-year time series chosen as a random samples. As the day-to-day variation in temperature decreases with increasing depth, the coefficient of determination increases with soil depth in both cases from about 0.975 to 0.985. The slope of the regression curve in the *Weiden* case (Fig. 6-23), is closer to one at all soil depths, than at the *Oberschleissheim* site (Fig. 6-24). The slight overestimation of the annual amplitude at *Weiden* is compensated by a negative offset that denotes some systematic model error, likely due to differences between the soil parameterisation and the true soil properties. The same holds true for the *Oberschleissheim* site, but with a more drastic reduced annual

amplitude at all depths that leads to a regression curve slope below 0.9. The increase in offset with depth, demonstrates that the 5 to 20 cm model layer does not represent the measurement at 20 cm adequately. This also holds true for the 20 to 65 cm model layer and the 50 cm measurement depth. Contrary to the analysis in section 4.3.3, the representative measurement depths regarding the annual temperature course are closer to the surface for these two soil layers.

To quantify the expected accuracy of SHTM throughout the Upper Danube catchment under different atmospheric conditions, frequency distributions of the main statistical criteria, divided into 10 even classes, for each year and each site (DWD "cases", Fig. 6-25) are discussed in the following. The 84 sets of statistical values computed from the daily soil temperatures for each year and each DWD station used in this study are tabulated in Appendix B.

As the average value of the mean annual deviation of soil temperature suggests (see above), over 80% of the mean deviations of simulated from measured temperature in the top soil layer range between -0.6 and 0.6 °C and in the second layer between -1.0 and 0.6 °C. The mode of the soil layer 1 distribution is -0.4 °C, while the soil layer 2 distribution has no clear mode, but two at -0.4 °C and -0.8 °C. Together with the results of the AgMet analysis, it is evident, that SHTM models the mean annual temperature with an accuracy better than 1.0 °C in 90% of all tested cases.

Over 90% of the daily soil temperature RMSE values computed for the top soil layer are lower than 2.0 °C and even 73% are lower than 1.6 °C. In the AgMet validation 75% of the RMSE values were lower than 2.6 °C, showing that simulating hourly values of soil temperature increases the standard error significantly. Switching from hourly to daily analysis of simulated soil temperatures still decreases the average standard error of the simulated second layer temperature to 1.39 °C for the DWD cases, with over 81% of all calculated RMSE values being lower than 1.6 °C.

When examining the coefficient of model efficiency for mean daily soil temperatures on an annual basis, the frequency distributions show clear modes at 0.97 for the top soil layer and 0.98 for the second soil layer. Over 90% of all computed CME are greater than 0.93 and 0.94, respectively. This leads to the conclusion that PROMET with SHTM and the EEB algorithm performs very well, when simulating daily soil temperatures under grass land cover, even on a mesoscale resolution.
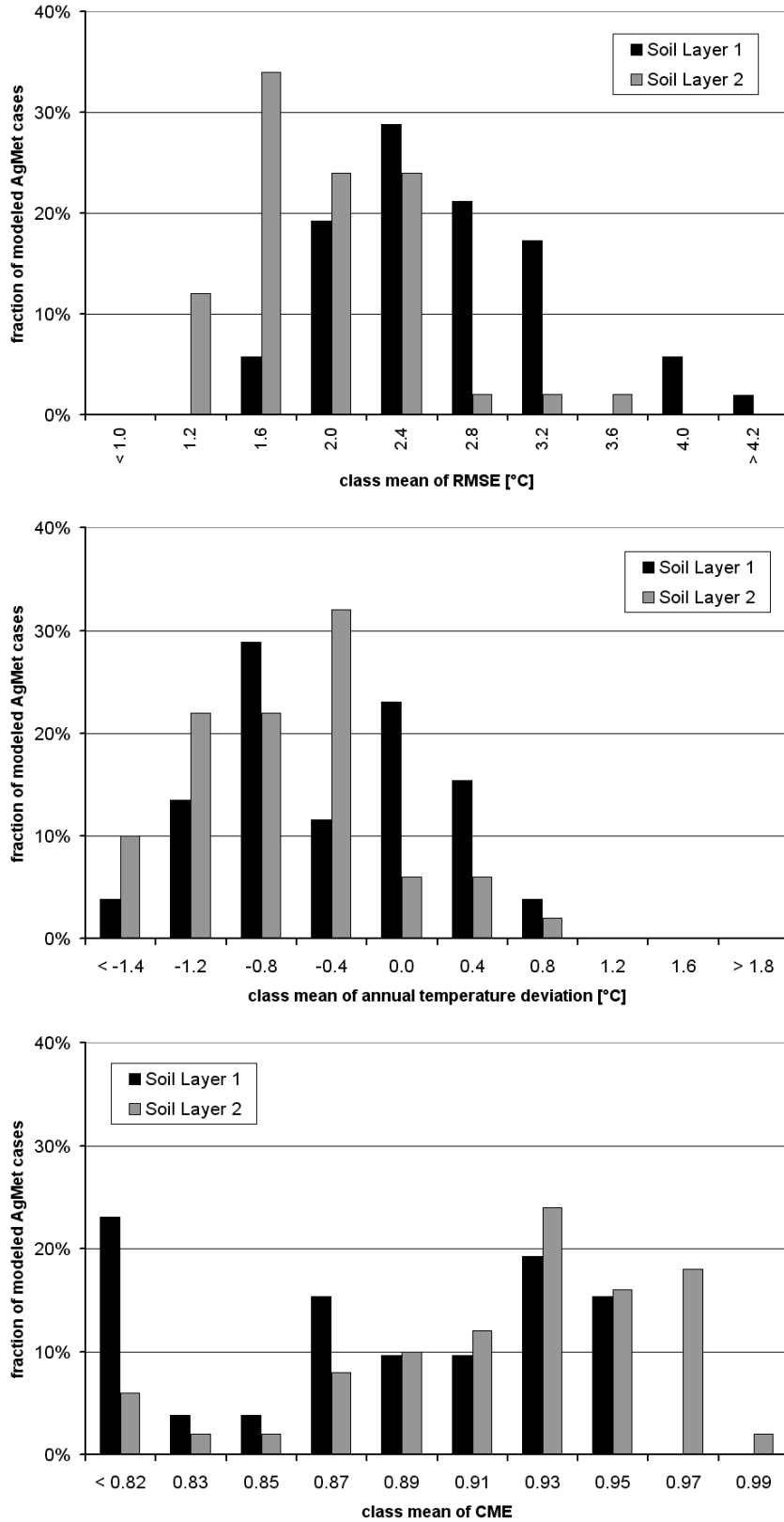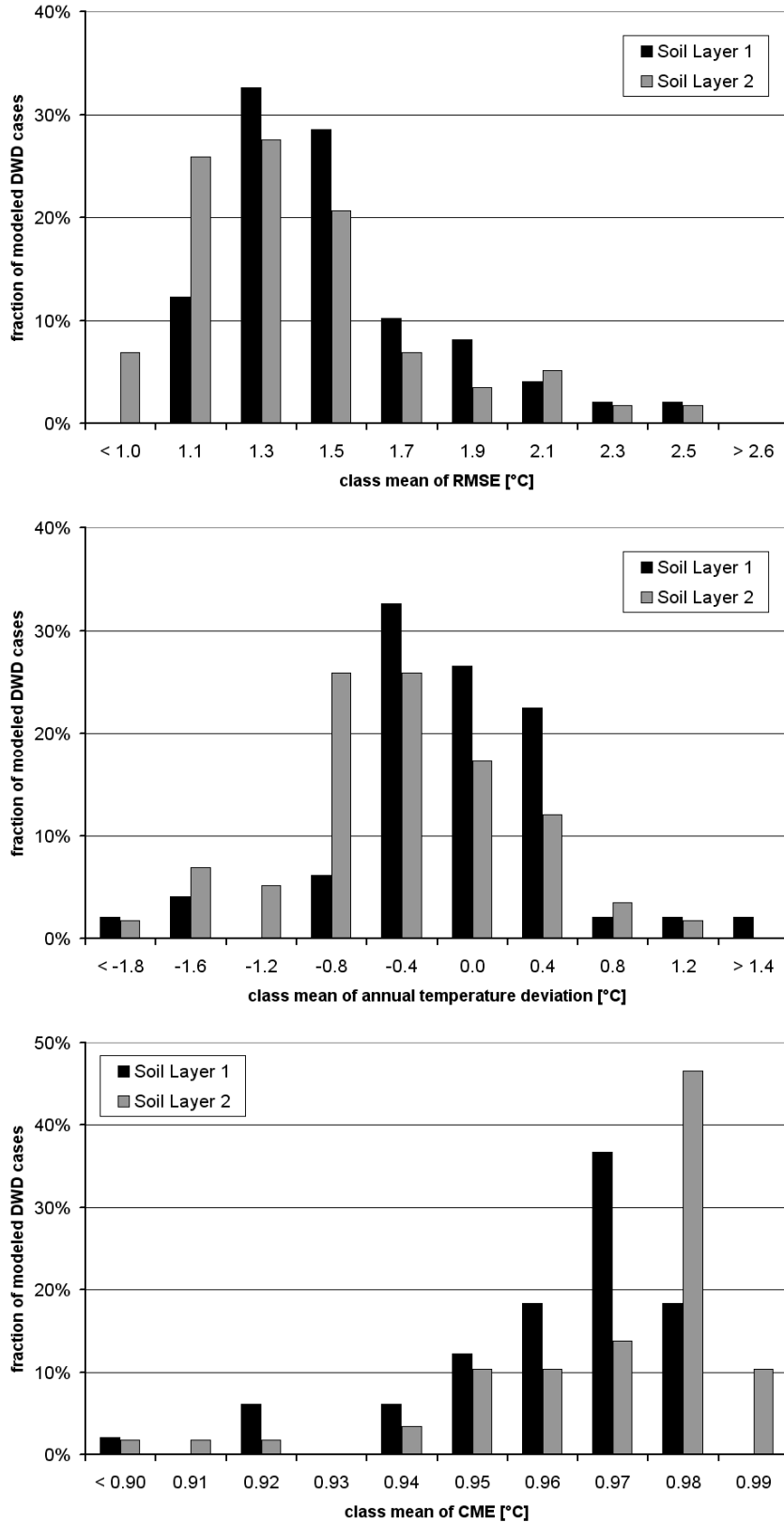
Fig. 6-25: Frequency distribution of annual statistical criteria (RMSE, deviation of annual mean temperature, CME) of the DWD cases (one case per year and per DWD station) simulated with PROMET w/ EEB ground heat flux.

To assess the performance of the soil energy transfer and storage model with respect to freezing of soil water, the correlation of simulated to measured daily soil temperatures during the winter months December, January and February is inspected in detail by means of the DWD ground temperature records. First the scatter plots of measured and simulated soil temperatures during the winter months at the DWD sites *Weiden* and *Oberschleissheim* are discussed. In contrast to the whole year data sets, the simulated winter temperatures correlate better with the recorded data at the *Oberschleissheim* station (Fig. 6-26). The linear regression between the 10 cm temperature record and the second layer simulation (RMSE = 0.75 °C) at this site exhibits the best R^2, the lowest offset and the gain closest to 1:1. The top soil layer temperature also correlates well with the 5 cm record (RMSE = 0.92 °C), only the temperature recorded at 20 cm depth is underestimated by the simulated temperature of the second soil layer (RMSE = 1.02 °C). All scatter plots for the *Weiden* site (Fig. 6-27), show that the simulation seems to overestimate the temperature fluctuations in winter, with gain values greater than one and negative offsets up to 1 °C. Again the linear correlation closest to 1:1 is found when comparing the second layer temperature with the 10 cm temperature record (RMSE = 0.85 °C). Obviously, the freezing of soil water changes the comparability of modelled and recorded temperature time series.
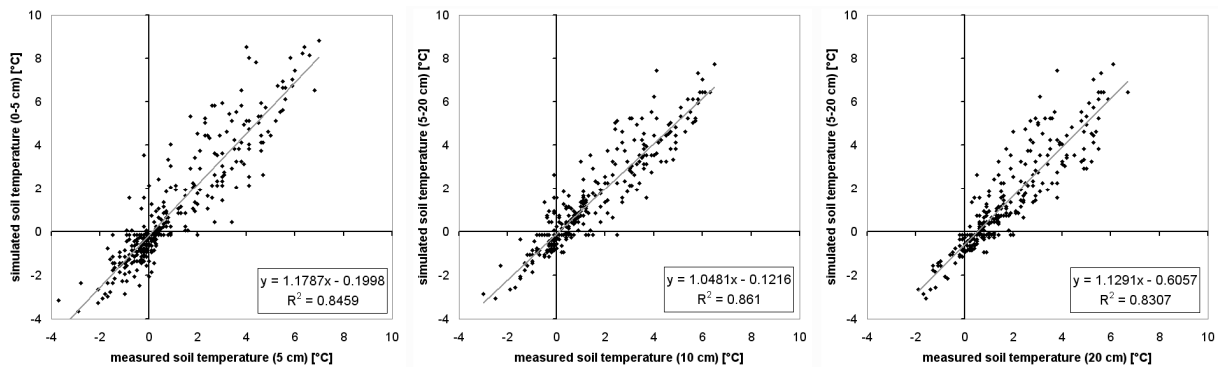
Fig. 6-26: Scatter plots of daily measured vs. simulated winter temperatures (Dec. to Feb.) at the DWD station *Oberschleissheim*.
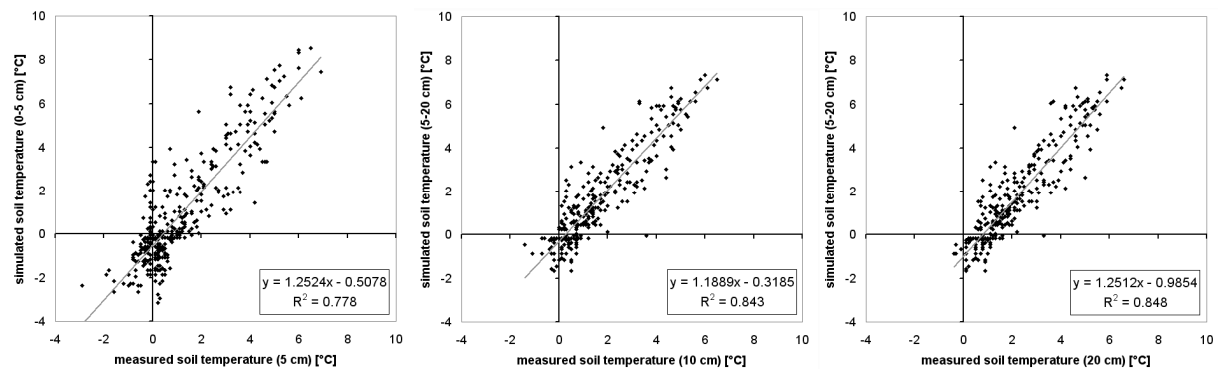
Fig. 6-27: Scatter plots of daily measured vs. simulated winter temperatures (Dec. to Feb.) at the DWD station *Weiden*.

As freezing starts at the soil surface, the soil temperature below is kept above the freezing point as long as there is liquid water available at the surface. The freezing front slowly moves downwards and as the volumetric energy content above the freezing front is drastically reduced, the soil below still has the additional latent energy content of the water trapped in its soil matrix. The soil freezing model, on the other hand, assumes that the amount of frozen water is equally distributed throughout the soil layer. Hence, modelled soil temperatures during soil freezing could fit better with records above the lower soil boundary, like the 5 to 20 cm soil layer temperatures at both sites correlate better with measurements at 10 cm depth, than at 20 cm depth. Additionally, the presumption, that the soil surface temperature is set to 0.0 °C when covered with snow, potentially leads to unrealistic accumulations of simulated top soil temperatures close to the freezing point.
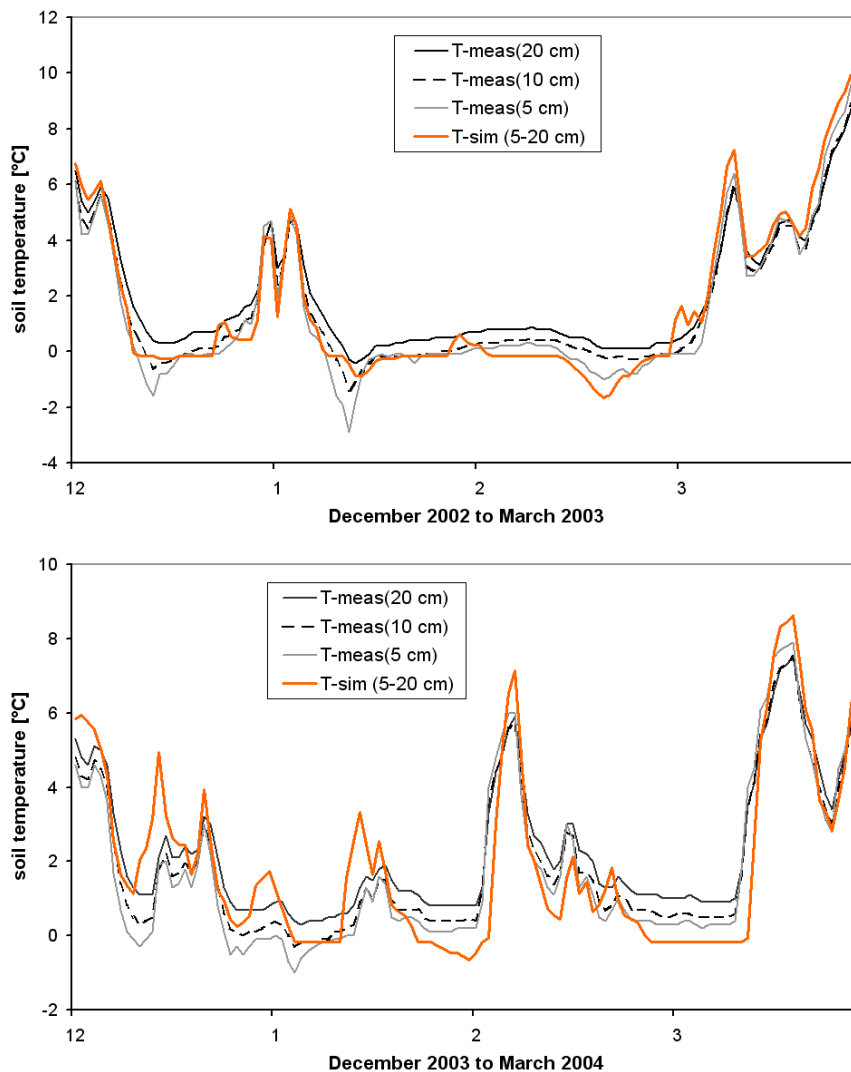
Fig. 6-28: Measured vs. simulated hourly soil temperatures at the *Weiden* site during two winters of the validation period 2002 to 2005.

Fig. 6-28 depicts the simulated temperature of the second soil layer at the *Weiden* site and the three temperature records related to this model layer for the winter 2002/03. One can perceive that until the end of January the model fits well with the dynamics of the three records. The deviation of the simulated from the recorded graphs after that date is likely a result of deviations of modelled from true ground heat flux between the snow cover and soil, or differences in modelled and true liquid water contents. In the following simulated winter SHTM performs not as good as in the previous one. Again in late January, the simulated soil temperature drops below the measurements, which surprisingly do not fall below the freezing point, even at 5 cm depth. This raises the suspicion, that measurements of soil temperatures near 0.0 °C could be disturbed by the measuring setup or other anthropogenic impacts (e.g. nearby buildings).

SHTM performs similar at most of the investigated DWD measurement sites, with the exception of the *Hohenpeissenberg* observatory data set, where only 9 days of top soil freezing were measured in the 4 year validation period (Table 6-8). As DEDECEK et al (2008) report, larger anthropogenic structures, like the one found at *Hohenpeißenberg*, can have a significant impact on the subsurface temperature field. Therefore it is assumed that the freezing point temperature record of this site is modified by the ground heat flux of the nearby building. Similar, but smaller, effects could have also affected other temperature time series used in this work.

But as the main field of application of PROMET is the simulation in mesoscale catchments, a different validation strategy is applied to evaluate the soil freezing algorithm. In Table 6-8, the number of days in the validation period (2002 to 2005) with a temperature at or below the freezing point for each measurement depth and the top two model layers is presented. Comparison of the modelled and recorded soil frost days highlights the ability of the model to reproduce the statistical frequency of occurrence of soil frost. If the typical depth of frost penetration at the investigated sites is seldom greater than 20 cm, the occurrence of non-frozen topsoil above frozen subsoil can be neglected. After LÖPMEIER (2006), the frost penetration in lowland Bavaria is about 35 cm in extreme winters like 1996/97 or 2005/06 and considerably shallower in most other years.

As expected, the top model layer overestimates the occurrence of soil freezing in relation to the 5 cm measurement, because this temperature record disregards any freezing in the soil above. The average frequency of frozen soil water recorded at 5 cm and simulated for 5 to 20 cm soil depth, on the other hand, fits quite well for most of the investigated DWD sites (Fig. 6-29). If the average is calculated without the extreme exception *Hohenpeißenberg* and the three stations with not sufficient records at 5 cm depth during the winter months, the model overestimates days with frozen soil by two per year (Table 6-8). But frozen soil water at 5 cm depth, does not equate to soil freezing at 10 cm depth for most of the DWD sites. Therefore, the occurrence of soil frost at this depth is clearly exaggerated by the second soil model layer and at most sites the freezing front seldom reaches a depth of 20 cm. But this inaccuracy of the model is due to the coarse model geometry in combination with the large amount of energy that is released when soil water freezes.

Table 6-8: Frequency of the occurrence of daily soil temperatures at or below the freezing point during the validation period 2002 to 2005 at three measurement depths (5, 10 and 20 cm) and in the upper two model layers.

	Layer 1 Sim.	5 cm Meas.	Layer 2 Sim.	10 cm Meas.	20 cm Meas.
Hohenpeissenberg (HPB)	124	9	86	0	0
Kempten (KE)	225	76	117	56	11
Landshut (LA)	185	86	156	62	25
Oberstdorf (OB)	124	115	86	45	6
Weiden (WE)	204	117	171	50	4
Fürstenzell (FZ)	246	121	123	67	8
Regensburg (RE)	194	141	101	71	7
Mühldorf (MD)	225	145	165	49	0
Oberschleissheim (OS)	213	153	168	110	53
Straubing (SR)	207	163	166	108	0
Königsmoos (KM)	202	170	136	176	38
Zwiesel (ZW)	265	224	218	129	48
Kösching (KO)			112	110	66
Maisach-Gernlinden (MG)			115	34	22
Mainburg (MB)			107	122	64
Average frequency (KE-ZW)	**208**	**137**	**146**	**84**	**18**
Average frequency	**201**	**127**	**135**	**79**	**23**
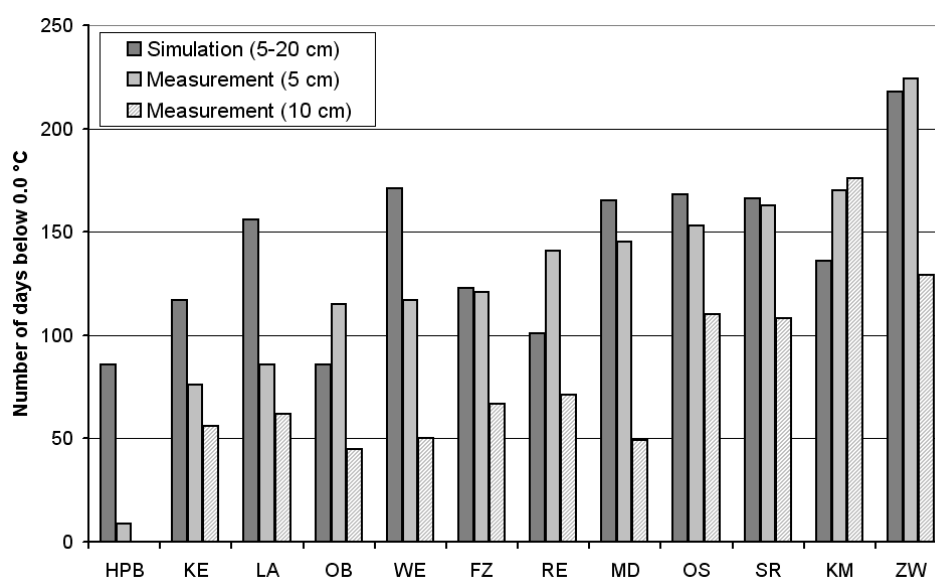
Fig. 6-29: Frequency of daily soil temperatures at or below the freezing point during the validation period 2002 to 2005 at two measurement depths (5, 10 and 20 cm) and in the second model layer.

6.5. Identification of Surface Temperature Patterns

In the previous sections, a systematic analysis of recorded and simulated soil temperatures has proved, that the soil heat transfer module SHTM, implemented in PROMET, driven by an explicit energy balance (EEB) algorithm at the soil surface, provides soil temperature time series with an accuracy of about 1.5 K when compared to daily recordings and with a typical standard deviation of 2.3 K, when compared to hourly recordings. But the most sensitive part of a soil column with regard to the energy balance of the land surface, the few upper most centimetres and with it the soil surface temperature can not be evaluated with meteorological station data. The sole method to validate the spatial distribution of simulated soil surface temperature (SST) is its comparison with land surface temperature (LST) from remote sensing products using thermal infrared wavelengths. For that reason, LST products of the NOAA-AVHRR thermal channels 4 and 5 were derived with the simple Split Window Techniques (SWT) of KERR et al (1992) and ULIVIERI et al (1994), as well as with the more complex SWT of Becker & Li (1990), modified for the NOAA-17 sensor by YANG & YANG (2006). Three SWTs were chosen to quantify the differences of the LST results, when using SWT algorithms of different complexity (see section 3.3 for more details). The analysis of these SWT algorithms showed (see section 3.3.2), that the simple KERR et al (1992) technique produces LSTs close to the channel 4 brightness temperature (BT_4), whereas the SWTs of ULIVIERI et al (1994) and YANG & YANG (2006) compute LSTs about 2-4 K and 3-5 K higher than the BT_4, respectively.

The evaluation of simulated LST, and particularly of simulated SST, is based on 12 AVHRR scenes (Table 6-9), retrieved during March and April of 2003 and September and October of 2005. Scenes taken during early spring and early autumn are preferable for an analysis of SST, because many agricultural crops have not yet developed in early spring and most crops have been harvested in September and October. It should be noted that this study only relatively compares model outputs with remote sensing products, because the average surface temperature of the chosen SWTs algorithms differ by up to 5 K.

Table 6-9: Date and time of the NOAA-17 recordings used in this study.

Date	UTC	CET	Model Time	Date	UTC	CET	Model Time
27.03.2003	10:09	11:09	11h	01.09.2005	10:09	11:09	11h
01.04.2003	09:57	10:57	11h	05.09.2005	10:18	11:18	12h
14.04.2003	10:03	11:03	11h	06.09.2005	09:54	10:54	11h
15.04.2003	09:42	10:42	11h	22.09.2005	10:27	11:27	12h
				24.09.2005	09:42	10:42	11h
				13.10.2005	10:48	11:48	12h
				14.10.2005	10:24	11:24	12h
				17.10.2005	10:57	11:57	12h

As a first qualitative comparison of simulated and remotely sensed temperature patterns, the visual differences of a simulated LST map and the LST maps generated by the various SWTs are compared in the following. The 22nd of September 2005 is

chosen, because the NOAA scene of that day has a very low fraction of snow and cloud cover over most of the Upper Danube basin. Fig. 6-30 depicts the LST pattern derived from the AVHRR scene with the KERR et al (1992) SWT for vegetated surfaces. The simulated LST map (Fig. 6-31) shows similar patterns, especially the warmer regions along the course of the river Danube and the colder regions in the Alps are well defined. The simulated LST map also identifies a colder central western part, as opposed to the warmer central eastern part of the catchment. The YANG & YANG (2006) algorithm surface temperature map (Fig. 6-32) reveals similar patterns, but the mean LST is about 3 K higher, as found in section 3.3. The same can be perceived in the ULIVIERI et al (1994) map (Fig. 6-33) with LSTs on average 1.5 K warmer than the ones derived with the KERR et al (1992) SWT. The main visual difference between remotely sensed and simulated LST is the less pronounced land use pattern in the simulated map, especially the cooler forest areas in the central and western part of the catchment are missing in the simulation. This can be attributed to the dominant land cover "Extensive Grass" (Fig. 2-6) in this area, which has a high simulated LAI in autumn (HANK 2008), and the missing soil temperature signal for high LAI canopies due to the implemented canopy transmittance algorithm (see also below).

The NOAA-derived LST is also more influenced by the relief in the mountainous regions of the Alps than the simulated surface temperature. This could be due to the fact that the intensity of the longwave radiation recorded by the AVHRR sensor is influenced by the slope and exposition of the land surface. This leads to errors in the measurements of the true land surface temperature by remote sensors, because of the reduced radiant intensity obtained by the sensor from sloping surfaces (e.g. MINNIS & KHAIYER 2000). Then again, the smoothed relief of the 1 km^2 digital elevation map used for the simulations in the Upper Danube basin also introduces errors in the calculation of incoming solar radiation, leading to errors in simulated LSTs.

In the next step, the differences between the simulated surface temperatures and the ones derived with the presented SWTs are analyzed visually and with the help of frequency distributions of their differences for two selected AVHRR scenes. All LST maps derived from remote sensing data via SWTs were generated with the respective parameters for a vegetation covered land surface, while the SST maps of the presumed "vegetation-free" proxels were created with the bare soil parameters given in section 3.3.2. At the end of the chapter, the diagrams of mean deviation and RMSD between simulated and remotely sensed surface temperatures for all presented AVHRR scenes show that the presented results are consistent for both the spring 2003, as well as the autumn 2005 NOAA-AVHRR recordings.

Although some parts of the remotely sensed LST maps are influenced by nearby clouds or the steep relief in the high alpine part of the catchment, the following analysis is carried out on all proxels not covered by clouds or snow. Removal of the problematic raster points from two sample scenes did not alter the statistical criteria significantly, since the major part of the investigation area is cloud free in all chosen AVHRR scenes and the fraction of the catchment proxels affected by steep relief (here: slope > 15°) effects is lower than 5 %.
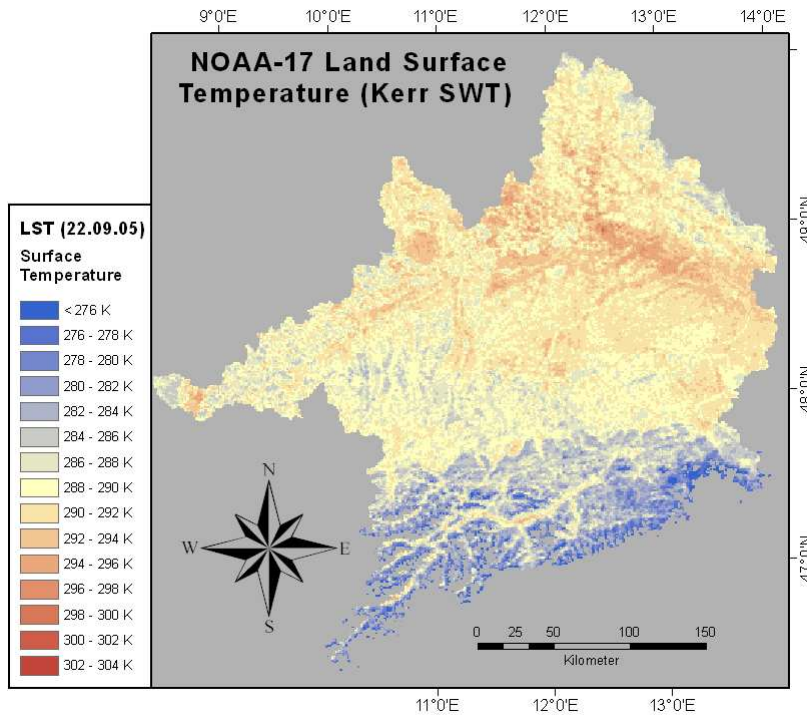
Fig. 6-30: Land surface temperature of the Upper Danube catchment derived from NOAA-AVHRR channels 4 and 5 with the KERR et al (1992) SWT algorithm (DOY 265).
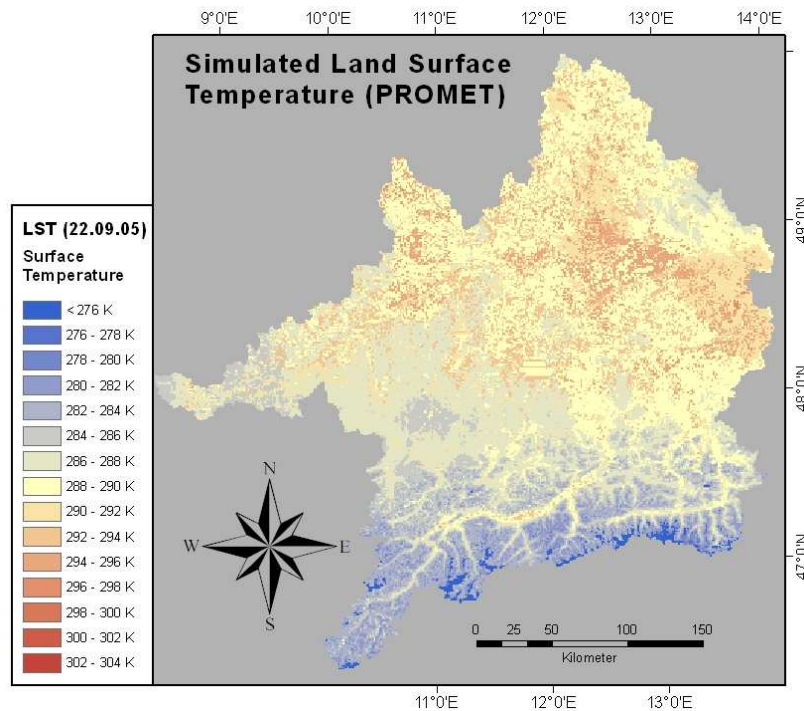
Fig. 6-31: Land surface temperature of the Upper Danube catchment simulated with PROMET (DOY 265).
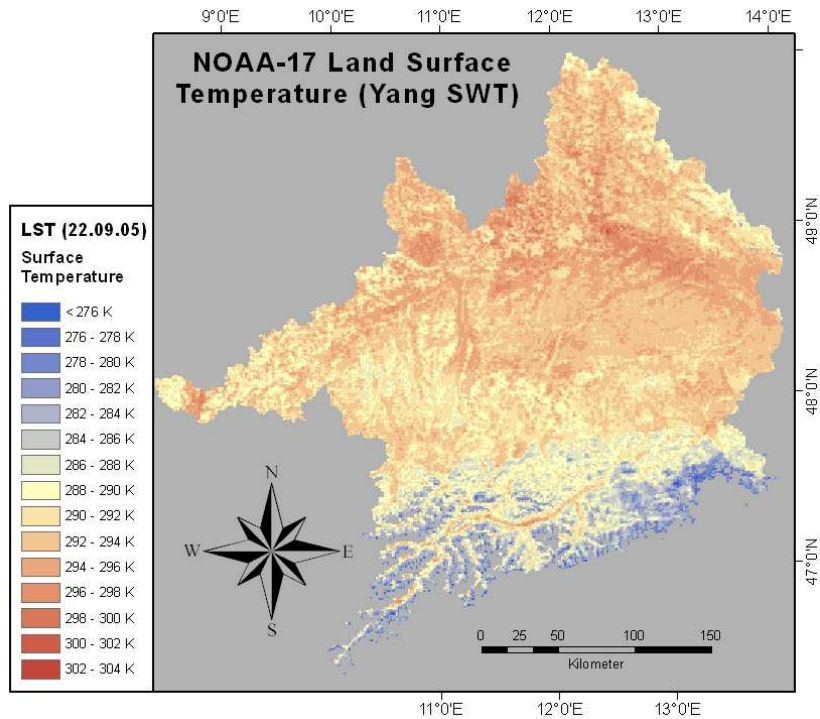
Fig. 6-32: Land surface temperature of the Upper Danube catchment derived from NOAA-AVHRR channels 4 and 5 with the YANG & YANG (2006) SWT algorithm (DOY 265).
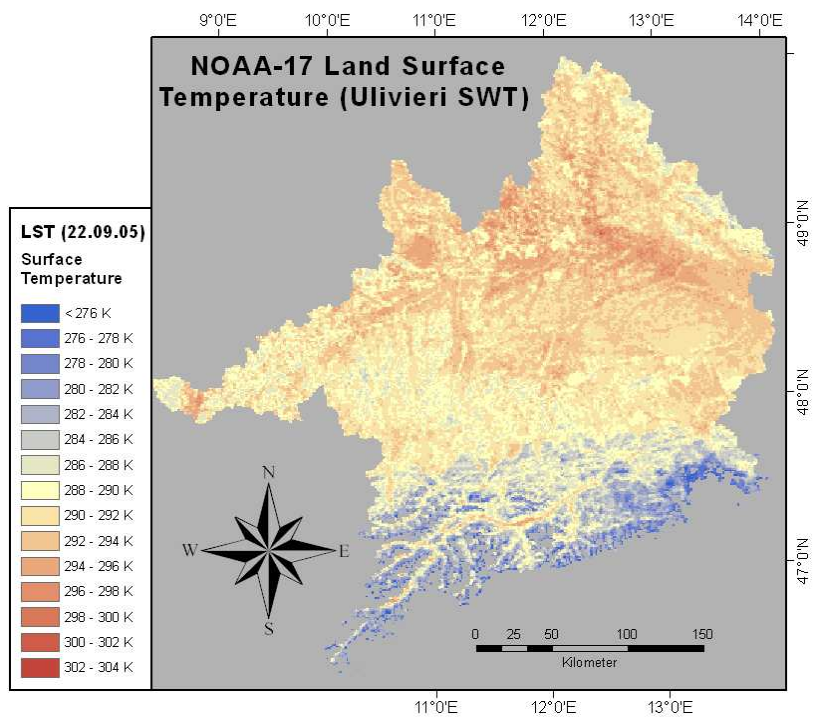
Fig. 6-33: Land surface temperature of the Upper Danube catchment derived from NOAA-AVHRR channels 4 and 5 with the ULIVIERI et al (1994) algorithm (DOY 265).

To assess the correlation of simulated to remotely sensed SSTs, the differences in surface temperature for all proxels with agricultural use but without any plant cover are presented in the following. Even though most proxels assumed to be uniformly covered with agricultural crops in the model have highly heterogeneous land cover in reality, the warm regions in Fig. 6-32 show that the land cover of the main agricultural areas is dominated by open soil and anthropogenic structures with low evapotranspiration rates. Proxels with active vegetation cover and sufficient soil moisture always appear cooler, because of the heat loss caused by transpiration.

The maps depicting the differences between the modelled LST and the LST derived from AVHRR sensor data with three different SWTs (Fig. 6-34) emphasize the observations made above. But even more important, the SST difference maps, showing the differences between simulated bare soil skin temperature and the surface temperature of presumably vegetation-free pixels (Fig. 6-34), are evidence for a good fit of model and remote sensing data, especially when using the *Ulivieri* SWT to derive SST. Bare soil pixels are defined as all proxels with any crop cultivation land use, that are set to "harvested" before the 1st of September by the agricultural management module included in the biophysical canopy module of HANK (2008). About 16 % of the proxels in the catchment meet this requirement in autumn 2005, which is accounted for in the scaling of the diagram axes in Fig. 6-35.

To quantify the differences between simulated and SWT-derived soil surface temperatures, as well as their variation, Fig. 6-35 shows the frequency distributions of the SST differences between land surface model and investigated SWTs for the midday NOAA scene of the 22nd September 2005. The LST differences are presented in the same way and the differences between modeled air temperature (AT) and AVHRR-derived LSTs are also displayed for comparison. The deviation of the areal mean SSTs and the respective root mean square deviations (RMSD) are discussed in the following for the assumed bare field proxels.

The modelled SST has the lowest bias if substracted from the *Ulivieri* SST (0.73 K), while it has a clear negative bias (-1.33 K) when compared to the *Yang&Yang* SSTs and a strong positive one (2.70 K) versus the *Kerr* algorithm results. The root mean square deviation (RMSD) is lowest for the comparison with the *Ulivieri* SWT as well (2.18 K), slightly higher for the *Yang&Yang* SWT (2.45 K) and very high for the *Kerr* SWT (4.03 K). The standard deviations of the SST differences are quite similar for all SWTs, with 2.05 K for the *Ulivieri* and *Yang&Yang* algorithms and 2.07 K for the *Kerr* SWT. These statistical values of this particular date are very close to the average ones for the 8 AVHRR scenes in autumn 2005 (Fig. 6-39) and therefore are presented here.

Regarding the whole catchment LST, the PROMET versus *Kerr* SWT comparison scores best, with a mean deviation of 0.13 K and a RMSD of 2.70 K. The mean bias between the simulated values and the *Ulivieri*-derived LSTs is -1.36 K and the bias is clearly negative when the simulation is compared to the *Yang&Yang* SWT (-2.71 K). The corresponding RMSD values are 3.01 K and 3.83 K, respectively. These results

highlight the difficulties of choosing the appropriate SWT algorithm and parameters for the comparison of simulation results with remotely sensed surface temperatures.
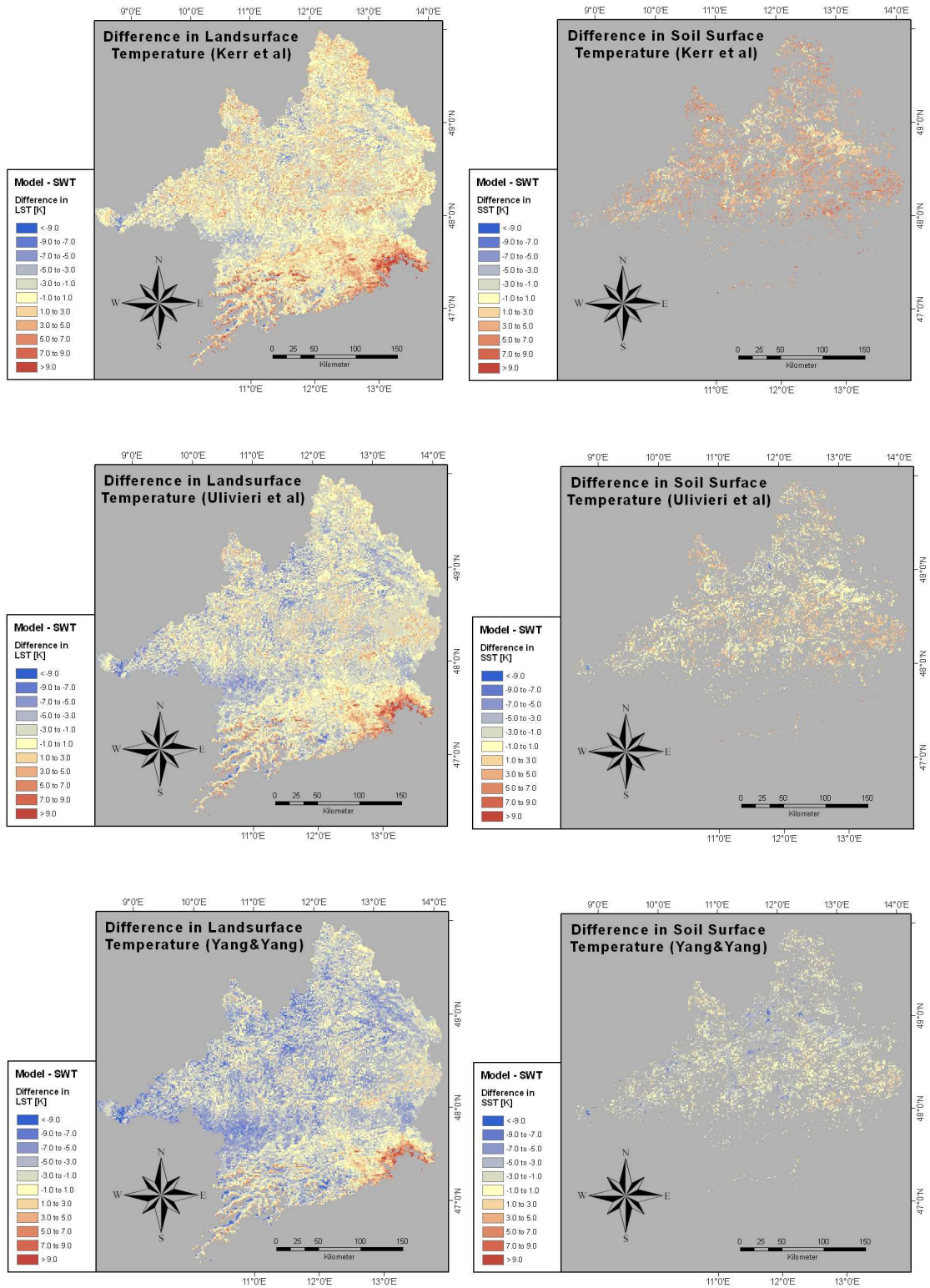
Fig. 6-34: Difference maps of simulated to remotely sensed LSTs (left) and difference maps of simulated to remotely sensed SSTs (proxels with agricultural use, but no vegetation cover) on 22.09.2005 (DOY 265) for the three SWT algorithms used in this study.

Fig. 6-35: Frequency distributions of the differences between simulated surface and air temperatures and the LSTs and SSTs derived from NOAA-AVHRR data with three different SWTs (KERR et al 1992, ULIVIERI et al 1994 and YANG & YANG 2006) for the 22nd of September 2005, 11:27 CET.

Fig. 6-35 also shows that the simulated near-ground air temperatures (AT) are lower than the simulated LSTs as expected for cloud-free, midday conditions. The mean deviation of modeled AT from *Ulivieri*-derived LSTs, for example, is -2.71 K while the deviation of modeled LST from *Ulivieri*-LST is only -1.36 K. At the same time, the standard deviations of the differences between AT and NOAA-LST are slightly lower (2.3 K) than the ones of the differences between PROMET-LST and NOAA-LST (2.7 K) for all utilised SWTs. This points to some irregular errors in the simulation results, most likely related to the spatial distribution and parameterisation of land cover properties. Then again, the clearly pronounced peak of the SST frequency distributions and their relatively low standard deviation (2.1 - 2.2 K) leads to the conclusion that the simulated bare soil fraction represents the true land cover conditions well.
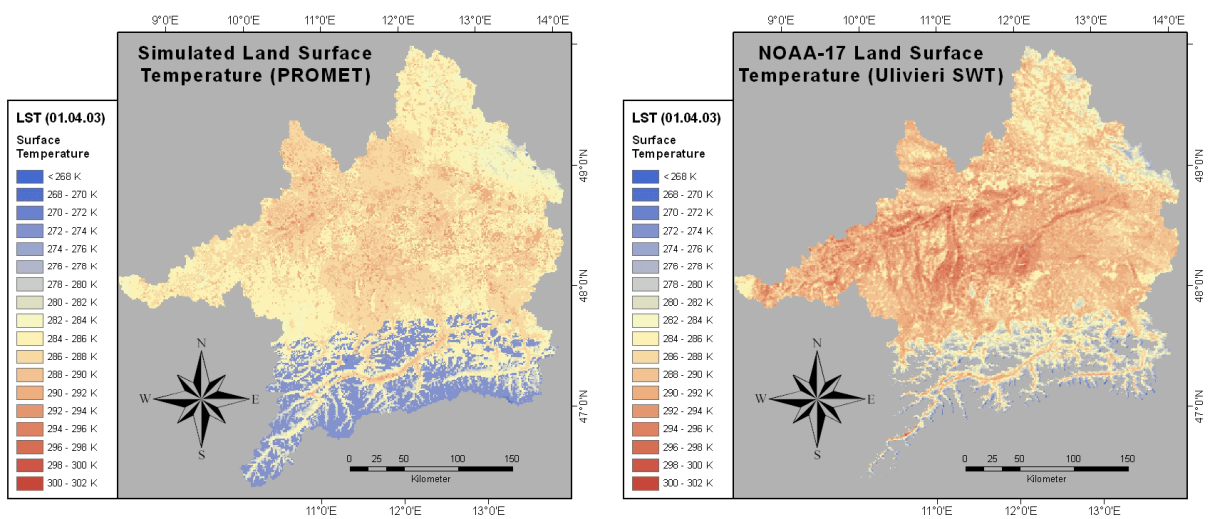
Fig. 6-36: LST maps (01.04.2003, DOY 91) simulated with PROMET (left) and derived from NOAA-AVHRR with the Ulivieri SWT (right).
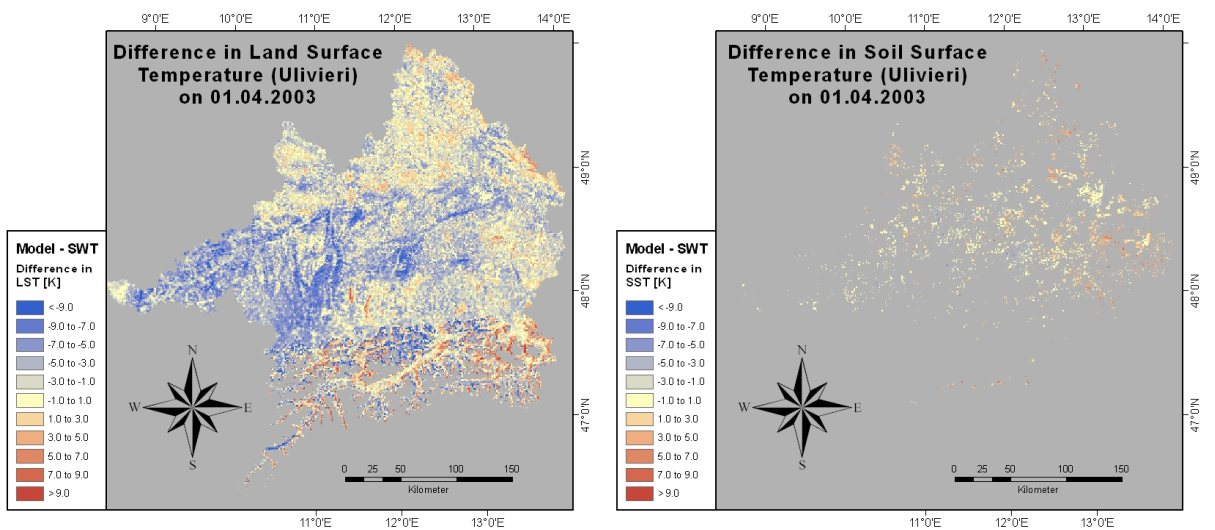
Fig. 6-37: Difference maps of simulated to Ulivieri SWT derived LSTs (left) and SSTs (right) for the Upper Danube catchment on 01.04.2003 (DOY 91).

Contrary to the analysis of PROMET results versus the AVHRR scene taken in 2005, the variation in surface temperature derived from AVHRR data with the *Ulivieri* SWT on the 1st of April 2003 (Fig. 6-36) is not equally reproduced by the PROMET simulation. As a consequence, the LST difference map in Fig. 6-37 depicts stronger regional variations than the maps in Fig. 6-34. Therefore, the average LST bias (-2.37 K) between simulation and Ulivieri SWT, as well as the average RMSD (4.19 K) are greater for the spring scene, than for the autumn scene (Fig. 6-39), even though most of the alpine part of the catchment is masked by snow and clouds. Despite the average deviation between simulation and *Kerr*-LST is lower (-0.32 K), the RMSD is also high (3.48 K). The bias between simulation and *Yang&Yang*-LST is even worse than for the September scene (-3.85 K), leading to a RMSD of 5.16 K. The standard deviation of all three LST difference frequency distributions (Fig. 6-38) is equally high with 3.43 K, showing that the relative variation of the LST values within a NOAA scene is the same for all three SWTs. The simulated air temperatures are on average 2.7 K lower than the simulated LSTs and their frequency distributions of temperature differences spread even stronger (standard deviation of 3.7 K). This is contrary to the September scene analysis, where the standard deviations of the air temperature differences were lower than ones of the LST differences. All in all, the stronger spatial heterogenity of the surface temperatures recognisable in the NOAA-AVHRR scene is not reproduced in the same manner by the PROMET surface temperature map. Possibly, the sparse canopies in early spring lead to the fact, that a higher fraction of longwave radiation emitted from the soil surface reaches the satellite's sensor. The transmittance of a canopy for longwave radiation is related to LAI in the model, but potentially the chosen dependency has to be reanalysed in the future.

About 6% of all proxels are considered bare soil surfaces until mid of April and therefore their surface temperatures are assumed to be soil surface temperatures in the analysis. But due to the cloud and snow cover in the alpine part of the catchment ~7% of the available AVHRR pixels are considered bare soil in the following.

Like in the autumn scene analysis, the absolute mean deviation between remote sensing data and model is lowest (1.07 K) and the RMSD best (2.60 K), when comparing PROMET output with the SSTs derived with the *Ulivieri*-SWT (Fig. 6-38). Again, the deviation of simulated surface temperatures from *Kerr*-SSTs is highly positive for the spring scenes (3.19 K) with a very high RMSD (4.01 K) and the PROMET output is on average lower than the *Yang&Yang*-SSTs (-1.89 K) with a RMSD of 3.07 K. The standard deviations of the SST frequency distributions are roughly the same (~2.4 K) and notedly lower than the ones of the LST frequency distributions (~3.4 K). The shapes of the distribution curves in Fig. 6-38 make this clearly visible, because the vertical axes are scaled in relation to the total number of available proxels available for LST and SST analysis.

For comparison, the frequency distribution diagrams of the differences between simulated temperatures and surface temperatures derived with the Ulivieri et al (1994) SWT for all 12 processed NOAA-AVHRR scenes are found in Appendix C.
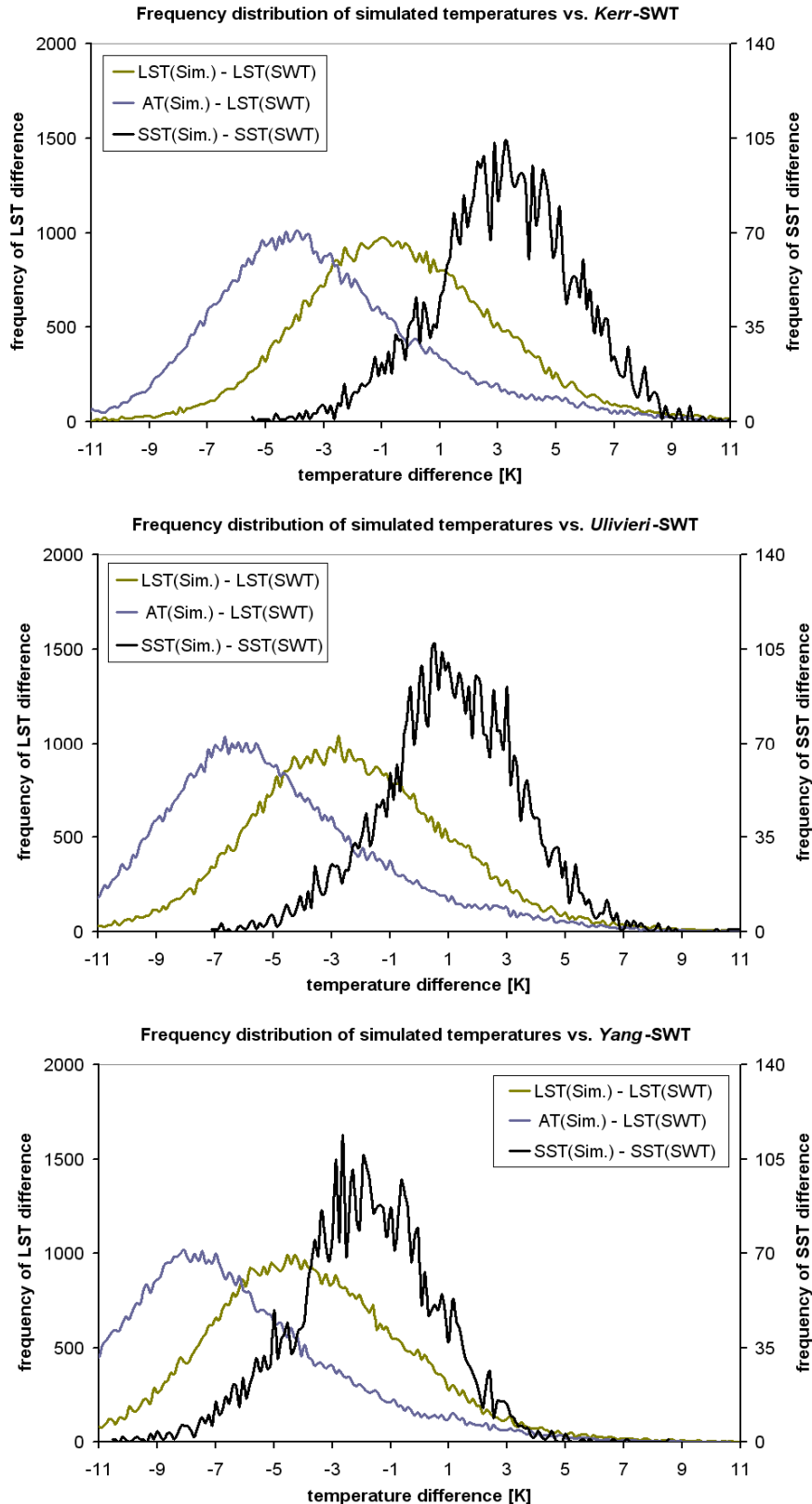
Fig. 6-38: Frequency distributions of the differences between simulated surface and air temperatures and the LSTs and SSTs derived from NOAA-AVHRR data with three different SWTs (KERR et al 1992, ULIVIERI et al 1994 and YANG & YANG 2006) for the 1ˢᵗ of April 2003, 10:57 CET.

As there is no "true" remotely sensed LST product, Fig. 6-39 presents the average values of mean deviation (MD) and RMSD of the simulated surface temperatures and air temperatures from the SWT derived LSTs and SSTs for all 12 NOAA-AVHR scenes.

PROMET simulates spatially distributed air temperature fields by interpolating DWD station data. For that reason, it is assumed, that the mean air temperature of the non-alpine part of the Upper Danube catchment is represented well by the simulation, if atmospheric conditions are similar throughout the investigated area. Since most of the catchment is cloud-free at the particular times of NOAA observations used, this should be true for the investigated dates.
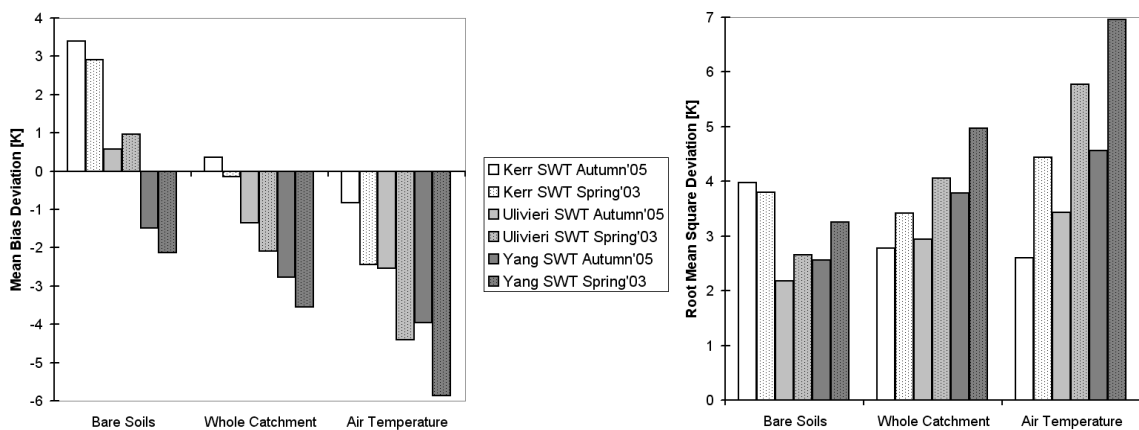
Fig. 6-39: Average MD (mean deviation) and RMSD values of SST, LST and air temperature simulated with PROMET compared to surface temperature derived from the three different split window techniques (SWT).
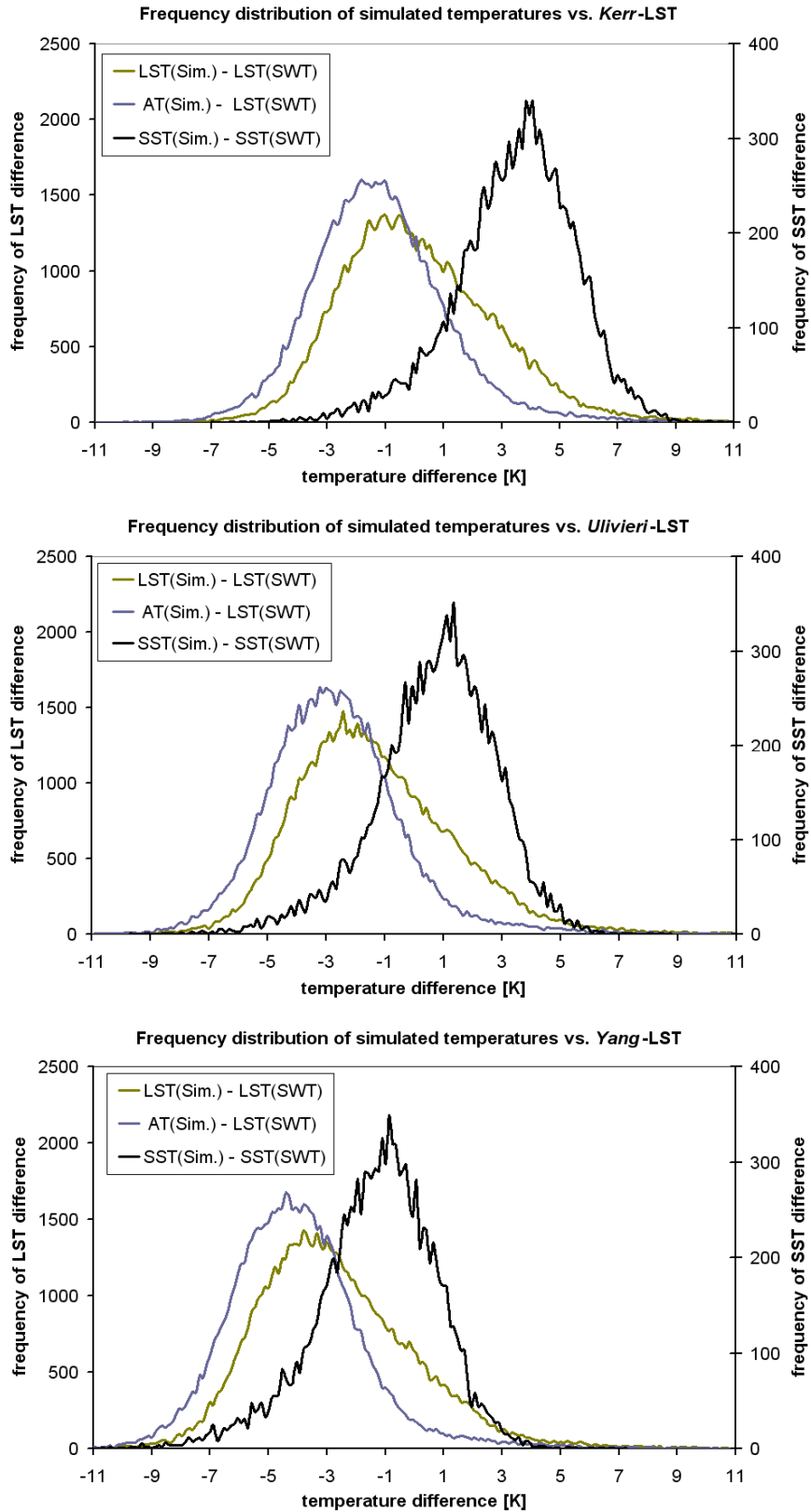
The mean difference between simulated surface and air temperatures is 2.3 K in spring 2003 and 1.2 K in autumn 2005. Average differences between remotely sensed LST and simulated air temperature range between 0.8 and 6.0 K (Fig. 6-39). The temperature of vegetated surfaces should be close to air temperature recorded at 2 m above canopy after Prihodko & Goward (1997) and the maximum difference between surface temperature and air temperature after noon is 5 to 10 K after Campbell & Norman (1998). This leads to the assumption, that the Yang & Yang (2006) SWT overestimates LSTs in this case. LSTs derived with the Kerr et al (1992) algorithm fit well with the simulated LSTs, but the extremely low soil surface temperatures calculated with this model seem to be a relict of the development of the original parameterisation in a semi-arid region.

Average SSTs simulated with PROMET including SHTM perform well, when compared to surface temperatures derived from NOAA-AVHRR data with the Ulivieri et al (1994) SWT. The average bias is 0.7 K and the RMSD is 2.3 K for all 12 points in time investigated. Additionally, this SWT is recommended by Vasquez et al (1997) and Yu et al (2008) for use in heterogeneous, large regions, where true thermal emissivities are not know.
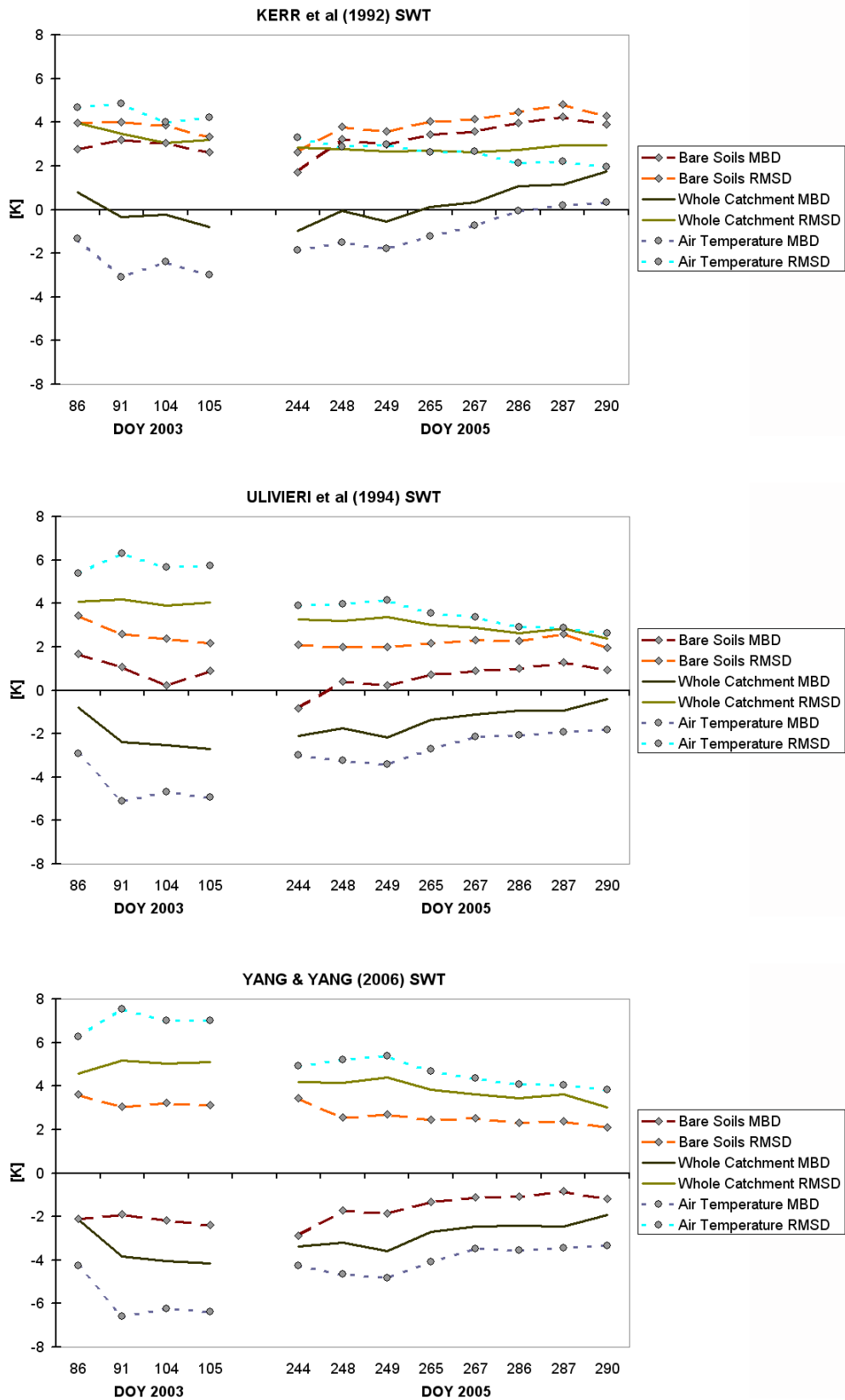
Fig. 6-40: Diagrams of mean deviation (MD) and root mean squared difference (RMSD) between surface temperatures simulated with PROMET and the ones derived from the three different SWTs for all investigated NOAA-AVHRR scenes.

7.Conclusions and Outlook

The Global Change decision support system DANUBIA has been under further development during the second project stage (2004 to 2007) in the integrative project GLOWA-Danube. The Landsurface component of DANUBIA was enhanced to close the water-related energy and nitrogen cycles in the soil-vegetation-atmosphere system of the land surface. It was the intent of this thesis to show, that the soil temperature and energy balance modules developed for the hydrological model PROMET are ready to bridge the gap between regional scale (up to 100,000 km^2) application and the demand for implementation of physical process models in predictive, coupled model frameworks like DANUBIA.

The modelling approach for the Soil Heat Transfer Module (SHTM) and the related soil water and surface balance modules is physical and process oriented, but also includes a variety of empirical simplifications and parameters, that were related to basic soil and vegetation properties.

A variety of validation runs showed that the chosen methods and parameterisations reproduce time series recorded on a multitude of locations in the catchment with satisfying accuracy without site-specific calibrations. Comparison of land surface temperature (LST) patterns derived from remote sensing data indicated, that the simulated soil surface temperatures are within the range of accuracy of the LST extraction methods. Yet, different LST retrieval methods exhibited serious differences in absolute surface temperatures.

The achievements presented in this thesis provide a basis for the interdisciplinary improvement of biochemical soil process models and of the coupling of land surface and atmosphere models. Additionally, first results with an empirical model of lateral runoff on frozen soils promise future improvements in winter high flow simulation.

Preparation of input data for the soil process models

The provision of spatially distributed input and validation data for soil process models run in mesoscale catchments still is an unsolved problem of environmental sciences. The high spatial heterogeneity of soil properties needed for soil process models and the continuous nature of these properties limit the availability of spatially accurate, quantitative soil maps. Even for parts of the investigated area that have been mapped in detail, the assignment of soil property values to map units and their aggregation to the desired scale is a scientific task on its own. Remote sensing techniques, for the most part based on microwave sensors, are still under development for use in densely vegetated, humid climates and are limited to top soil investigations. Therefore, the 1:1,000,000 Soil Overview Map (BÜK1000) of the German part of the Upper Danube basin was reclassified with regard to the vertical sequence of soil textural properties.

Because of the interactions between the soil water and soil energy modules, a set of *Pedotransfer Functions* for the estimation of the hydraulic parameters of the *Eagleson* soil water model was applied on the new soil type classes. The characteristic values of soil moisture content derived with the *Brooks & Corey* soil water retention equation compared well to those given for the chosen BÜK1000 soil classes with regard to the coarse resolution of the soil map. Together with the results of other authors on the spatial distribution of soil moisture (LÖW 2007) and the temporal course of river runoff (MAUSER & BACH 2008), this concluded that the prepared spatially distributed data set of soil properties appropriately reflects the true physical characteristics of the soils in the Upper Danube basin on a raster scale of 1 km^2. Both the regionalization of the static soil parameters and the realistic simulation of the dynamic soil water content were prerequisites for a successful representation of soil energy fluxes and storage.

Configuration of SHTM

Like in most SVAT schemes, the energy cycle of the land surface was described by vertical, one-dimensional process equations in PROMET. For the heat transport in soils, therefore the one-dimensional, conductive heat transfer equation was applied. The dynamic lower boundary condition controlled by the annual temperature cycle of the preceding year represented the interannual temperature differences. Changes in soil moisture content and the release of latent energy due to soil water freezing were integrated in the numerical solution.

A simulation run carried out with known boundary conditions identified the potential precision of SHTM in reproducing measured soil temperatures (RMSE < 1 °C), despite its coarse vertical resolution of just four soil layers. A second one, where all input variables except for soil moisture were provided, underlined the effect of soil moisture on temperature and the possible error due to convective heat fluxes in an extreme case of ground water influence.

Because the land surface model is intended for applications in mid-latitude regions, the implemented soil energy balance algorithms reflect soil-atmosphere, soil-snow and soil-vegetation energy fluxes. For three surface ground heat flux algorithms with differing complexity the impacts on simulated soil temperature time series were analysed. This highlighted the need for the separate computation of canopy and soil surface energy processes, if simulated temperatures are to be used as sensitive input variables for other process models.

Empirical estimates of the ground heat flux or analytical sine-wave soil temperature models performed poorly in predicting topsoil temperatures and definitely cannot be recommended in coupled modelling systems. Furthermore, the analysis exposed that future improvements in the canopy radiation transmission algorithm are possible. The sensitivity of the soil surface energy balance on simulated LAI values also showed that a biophysical plant growth model sensitive to climatic change should enhance the predictive accuracy of future soil conditions relevant for carbon and nitrogen transformation models.

Evaluation of SHTM results

Validation of a soil heat transfer and storage model applied on a regional scale catchment in a temperate, humid climate with spatially distributed measurements of absolute temperatures is nearly impossible. Dense vegetation, snow and anthropogenic structures cover the soil surface most of the year and in most parts of the investigated area. Even if bare soil surfaces are exposed to the field of view of airborne or space borne sensors, the discrepancy between the spatial resolution of land cover in the mesoscale raster-based model and the true land cover inhibits direct comparison of simulated and remotely sensed soil surface temperatures. Furthermore remote sensing techniques cannot quantify subsurface temperatures.

For that reason, measurements from field campaigns and observational networks were the only source of accurate soil temperature data at different depths. Even though these point scale data sets basically are of limited significance for the surrounding area, it was supposed that, if the process description in the model is correct, the differences between simulated and measured values originate from the disparity of the parameters and inputs of the model from the real conditions.

Since the model had shown its accuracy with known boundary conditions, the validation of SHTM at 43 different sites in the catchment could show that the predictive error due to model geometry, parameterisation and inaccuracy of input variables increased only moderately. The mean annual temperature was reproduced with an accuracy better than 1 K at 90% of all measurement sites and the average RMSE of the simulated temperatures in the upper two soil layers was lower than 2 K when daily values were compared with data from 15 DWD sites. The average RMSE of predicted soil temperatures increased to 1.75 K for the 20 cm depth and to 2.3 K for the 5 cm soil depth, when hourly value were evaluated. Further analysis of the data also highlighted that simulated daily temperature amplitudes correlated well with measured ones and that the model could explain > 97% of the annual variation in daily mean temperatures. All in all the model performance proved to be robust over different parts of the investigated area and the spatial distribution of soil parameters seemed to characterize the main physiographic regions well.

To include some measure of the energy exchange between soil surface and atmosphere, in a next step simulated surface temperature maps were compared to LST patterns derived from NOAA-AVHRR remote sensing data. 12 AVHRR nearly cloud-free records from early spring and autumn were selected to compare the surface temperature of areas with potentially sparse vegetation cover. Areas in the eastern part of the Upper Danube basin with intensive agricultural crop production were identifiable in both the simulated and remotely sensed LST maps.

Assuming that the land cover map utilised in the model represents the true land use, the (soil) surface temperatures of the simulated bare field proxels were compared with the corresponding temperatures derived from AVHRR data. Since all three Split Window Techniques used to extract surface temperatures from the AVHRR data provided unequal results, the absolute deviation between model and satellite data

could not be identified. The lowest average Root Mean Square Deviation of 2.3 K and the lowest mean bias deviation were achieved when the simulated soil surface temperatures were compared to the ones derived with the ULIVIERI et al (1994) technique. Nonetheless, this comparative analysis gave important insights into the spatial variability of simulated surface temperatures to be due, even though the application of thermal infrared remote sensing data is still a complex issue.

Outlook

Further integrative investigations will show, to which extent the application of SHTM, instead of approximative algorithms, improves the performance of biochemical soil process representations, especially of the Soil Nitrogen Transformation (SNT) model developed within the GLOWA-Danube project. Furthermore, the ongoing analysis of soil moisture and soil temperature trends in climate change scenario runs with DANUBIA, will provide a universal basis for the further assessment of the state of the soils in the Upper Danube catchment in the next 50 years.

The upcoming bidirectional coupling of the *Landsurface* component of DANUBIA with the RCMs available in the project, will show to which extent the energy fluxes computed by the PROMET energy balance algorithms comply with the energy fluxes that are expected by the individual RCMs. It is assumed that both the energy flux densities computed by PROMET and the ones computed by the internal land surface algorithms of the RCMs have their own characteristics. The adjustment of the individual models of land surface and atmosphere processes for a seamless bidirectional coupling is one of the great challenges of the development of integrated simulation models for Climate Change impact assessment.

From a hydrological point of view, the influence of frozen soil water on lateral runoff generation, especially during snow melt events, is an interesting topic. So far, only few regional scale hydrological models incorporated the effect that under some circumstances frozen soil water blocks infiltrating melt water or precipitation and therefore increases surface runoff, or more often interflow runoff below the soil surface. If PROMET is run with SHTM, the amount of frozen water in the upper soil layers can be simulated with reasonable vertical resolution. Therefore, an empirical model for lateral runoff was implented in PROMET (Appendix D) and is under further evaluation. First results show that the simulated frequency of winter high flows can be improved by including this simple model even in mesoscale basins.

Three subcatchments in the Upper Danube region are now under investigation, that exhibit no significant influence from anthropogenic structures, like dams and reservoirs, on the annual course of gauged river runoff. These are the subcatchments of the *Ammer* at the northern edge of the Alps, the *Naab*, draining parts of the northern mountain region, and the *Vils* situated in the central-eastern lowland.

Just like some authors report (see Appendix D), only in specific situations lateral runoff on frozen soils contributes to winter high flows. PROMET simulates some runoff peaks more closely with the proposed empirical soil ice extension than without,

but the timing or quantity of many other high runoff events is not sufficiently reproduced. This is due to the preliminary model parameterisation now under further investigation, but just as much due to the inherent uncertainties of mesoscale predictions of precipitation or snow melt events.

But with respect to the assessment of long-term changes in runoff behaviour, the present version of the runoff on frozen soil extension already produces promising results. Analysis of the daily river runoff at the gauge *Heitzenhofen* (*Naab*) demonstrates that PROMET reproduces the frequency of high water runoffs in winter more closely with the proposed extension than without (Fig. 2-1). Similar results are achieved in the other two subcatchments, but further statistical appraisal of the results must be accomplished. In addition, the interrelationship of snow melt, frozen soil runoff and other influencing factors during winter high waters must be more deeply analysed.

As the regional warming trend in Europe will likely lead to shorter retention times of water as snow and ice and many models propose lower water levels in summer, the estimation of the effects of soil ice on runoff generation could be helpful to better quantify the future amounts of water recharging the aquifers or running off laterally in winter.
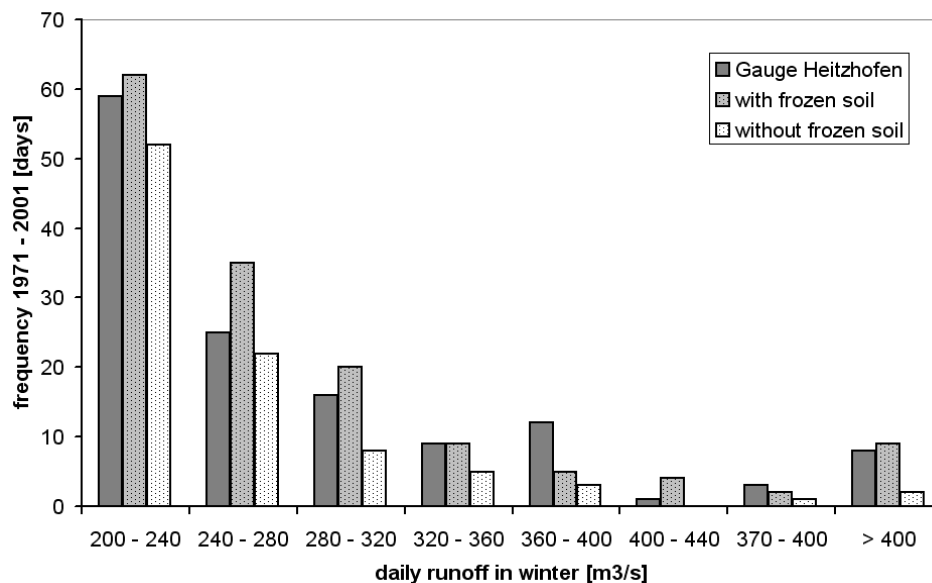
Fig. 7-1: Frequency distribution of simulated and measured daily high water runoff values during winter (November to April) at the gauge *Heitzenhofen* (*Naab*) for the period of 1971 to 2001.

8. ABSTRACT

The investigation of the impact of Global Change on the basic resources on which life, and man, depends, is the main objective of the environmental science community at the beginning of the 21st century. Advances in information technology, new methods of spatially distributed data retrieval and increased understanding of the physical, chemical and biological processes in the Earth system facilitate integrative models of the dynamic processes under change. Together with the integration of deep actors models from social and economical sciences into a common model framework, scenario runs based on inputs from Regional Climate Models (RCMs) and constrained by prognoses of the future developments in demography, economy and human behaviour are now possible.

The objective of the integrative project GLOWA-Danube is the development of such a modelling system and its application on the mesoscale catchment of the Upper Danube river with an area of about 77,000 km2. The decision support system DANUBIA is designed for plausible predictions of the impact of changes in climate, human behaviour and land use on the future of the water and related matter cycles. DANUBIA is able to assist knowledge-based management decisions, by predicting the effects of adaptation and mitigation strategies on the natural resources of the Upper Danube basin.

The closure of the water, energy, nitrogen and carbon cycles in the soil-vegetation-atmosphere system relies on the adequate representation of all processes involved and their interaction. To close the energy cycle in the soil-vegetation-atmosphere system and provide valuable input data for biochemical models of soil nitrogen and carbon transformation, this thesis presents the Soil Heat Transfer Module (SHTM) together with an energy balance algorithm of the soil surface for regional scale simulations.

SHTM combines simplified physical algorithms for the computation of the actual temperature in the upper soil layers and a dynamic lower boundary condition to represent Climate Change conditions. Changes in soil moisture and soil freezing are explicitly taken into account. The surface ground heat flux as the driving force of the model is provided by an explicit solution of the soil surface energy balance and a snow-soil coupling algorithm, respectively.

This thesis shows, that the soil temperature and energy balance modules developed as extensions of PROMET (PROcesses of Matter and Energy Transfer) are ready to bridge the gap between regional scale (up to 100,000 km^2) application and the requirement of physical process models in predictive, coupled modelling systems like DANUBIA.

9. References

Abu-Hamdeh, N.H. (2003): Thermal properties of soils as affected by density and water content. *Biosystems Engineering* 86(1), p. 97-102.

Ács, F., Mihailovic, D.T. & Rajkovic, B. (1991): A coupled soil moisture and surface temperature prediction model. *Journal of Applied Meteorology* 30, p. 812-822.

Ad-hoc-AG Boden (2005): *Bodenkundliche Kartieranleitung.* 5th Edition, Hannover, Germany, 438 p.

Anderson, S.P., Hinton, A. & Weller, R.A. (1998): Moored observations of precipitation temperature. *Journal of Atmospheric & Oceanic Technology* 15, p. 979-986.

Bahrenberg, G., Giese, E. & Nipper, J (1999): *Statistische Methoden in der Geographie - Band 1: Univariate und bivariate Statistik.* 4th Edition, Teubner Stuttgart - Leipzig, 234 p.

Baldocchi, D.D., Hicks, B.B. & Camara, P. (1987): A canopy stomatal resistance model for gaseous depositions to vegetated surfaces. *Atmospheric Environment* 21, p. 91-101.

Barthel, R., Rojanschi, V., Wolf, J. & Braun, J. (2005): Large-scale water resources management within the framework of GLOWA-Danube - Part A: The groundwater model. *Physics and Chemistry of the Earth*, Volume 30 (6-7), p. 372-382.

Bayard, D., Stähli, M., Parriaux, A. & Flühler, H. (2005): The influence of seasonally frozen soil on the snowmelt runoff at two Alpine sites in southern Switzerland. *Journal of Hydrology 3*09, p. 66-84.

Becker, A. & Braun, P. (1999): Disaggregation, aggregation and spatial scaling in hydrological modelling. *Journal of Hydrology* 217 (3-4), p. 239-252.

Becker, F. & Li, Z.L., (1990): Towards a local split window method over land surface. *International Journal of Remote Sensing* 11, p. 369–393.

Beltrami, H. (2001): On the relationship between ground temperature histories and meteorological records: a report on the Pomquet station. *Global and Planetary Change* 29, p. 327-348.

Best, M.J., Cox, P.M. & Warrilow, D. (2005): Determining the optimal soil temperature scheme for atmospheric modelling applications. *Boundary Layer Meteorology* 114, p. 111-142.

BGR (1998): Bodenübersichtskarte von Deutschland 1:1,000,000. Bundesanstalt für Geowissenschaften und Rohstoffe, Hannover, Germany.

Boegh, E., Soegaard, H. & Thomsen, A. (2002): Evaluating evapotranspiration rates and surface conditions using Landsat TM to estimate atmospheric resistance and surface resistance. *Remote Sensing of Environment* 79, p. 329–343.

Bohrmann, H. (2007): Analysis of the suitability of the German soil texture classification for the regional scale application of a physical based hydrological model. *Advances in Geosciences* 11, p. 7-13.

Boone, A., Masson, V., Meyers, T. & Noilhan, J. (2000): The influence of the inclusion of soil freezing on simulations by a soil-vegetation-atmosphere transfer scheme. *Journal of Applied Meteorology* 39, p. 1544-1568.

Braden, H. (1995): The Model AMBETI - A detailed description of a Soil-Plant-Atmosphere Model. *Berichte des Deutschen Wetterdienstes* 195.

Brakensiek, D.L., Rawls, W.J. & Stephenson, G.R. (1984): Modifying SCS hydrologic soil groups and curve numbers for rangeland soils. ASAE Paper No. PNR-84-203, St. Joseph, MI.

Brooks, R.H. & Corey, A.T. (1964): Hydraulic properties of porous media. *Hydrology Paper* 3, Colorado State Univ., Fort Collins, CO.

Buntebarth, B. (2002): Temperature measurements below the Earth's surface - a history of records. *Earth Sciences History* 21(2), p. 190-198.

Campbell, G.S. (1985): *Soil physics with BASIC: transport models for soil-plant systems*. Amsterdam.

Campbell, G. & Norman, J. (1998): *An Introduction to Environmental Biophysics*. 2nd Edition, Springer, New York, 312 p.

Carslaw, H.S. & Jaeger, J.C. (1959): *Conduction of heat in solids*. Oxford University Press, UK.

Chen, F., & Dudhia, J. (2001): Coupling an Advanced Land Surface–Hydrology Model with the Penn State–NCAR MM5 Modeling System. Part I: Model Implementation and Sensitivity. *Monthly Weather Review* 129, p. 569-585.

Choudhury, B.J., Reginato, R.J. & Idso, S.B. (1986): An analysis of infrared temperature observations over wheat and calculation of latent heat flux. *Agricultural & Forest Meteorology* 37, p. 75-88.

Choudhury, B.J., Idso, S.B. & Reginato, R.J. (1987): Analysis of an empirical model for soil heat flux under a growing wheat crop for estimating evaporation by an infrared-temperature based energy balance equation. *Agricultural & Forest Meteorology* 39, p. 283-297.

CLC 2000 (2004): Corine Land Cover 2000 – Mapping a decade of change, Brochure No 4/2004, http://www.eea.europa.eu/documents/brochure/CLC2000brochure.pdf, visited 21-01-2008, also see: http://terrestrial.eionet.europa.eu/CLC2000, visited 21-01-2008.

Cornelis, W.M., Ronsyn, J., van Meirvenne, M. & Hartmann, R. (2001): Evaluation of pedotransfer functions for predicting the soil moisture retention curve. *Soil Science Society of America Journal* 65, p. 638-648.

Cosby, B.J., Hornberger, G.M., Clapp, R.B. & Ginn, T.R. (1984): A statistical exploration of the relationship of soil moisture characteristics to the physical properties of soils. *Water Resources Research* 20 (6), p. 682–690.

Cosenza, P., Guérin, R. & Tabbagh, A. (2003): Relationship between thermal conductivity and water content of soils using numerical modelling. *European Journal of Soil Science* 54, p.581–587

Crank, J. (1956): *The Mathematics of Diffusion*. Oxford University Press, New York.

Dabberdt, W.F., Lenschow, D.H., Horst, T.W., Zimmerman, P.R., Oncley, S.P. & Delany, A.C., (1993): Atmosphere-surface exchange measurements. *Science* 260, p. 1472–1481.

Dash, P., Göttsche, F.M., Olesen, F.S. & Fischer H. (2002): Land surface temperature and emissivity estimation from passive sensor data: theory and practice – current trends. *International Journal of Remote Sensing* 23(13), p. 2563-2594.

de Vries, D.A. (1963) : Thermal properties of soils. In: van Wjik, W.R. (Ed.): *Physics of Plant Environment*. Amsterdam, p. 210-235.

Deardorff, J. (1978): Efficient prediction of ground surface temperatureand moisture with inclusion of a layer of vegetation. *Journal of Geophysical Research* 83, p. 183-203.

Dedecek, P., Safanda, J., Heidinger, P., Kukkonen, I. & Rajver, D. (2008): Anthropogenic component of the subsurface temperature field: observed and synthetic examples. *Geophysical Research Abstracts* 10, EGU2008-A-03818.

Dingman, S.L. (2002): *Physical Hydrology*. 2nd Edition, Prentice Hall, Upper Saddle River, NJ.

Eagleson, P.S. (1978): Climate, Soil, and Vegetation, 3. A simplified model of soil water movement in the liquid phase. *Water Resources Research* 14, p. 722-730.

Farquhar, G.D., von Caemmerer, S. & Berry, J.A. (1980): A biochemical model of photosynthetic CO2 assimilation in leaves of C3 species. *Planta* 149, p. 78–90.

Forbes, J.D. (1846): Account of experiments on the temperature of the earth at differnt depths, and in different soils, near Edinburgh. *Transactions of the Royal Society of Edinburgh* 16, p. 189-236.

Fourier, J.B.J. (1822): *Théorie analytique de la chaleur*. Firmion Didot, Paris.

Frödin, J. (1913): Beobachtungen über den Einfluss der Pflanzendecke auf die Bodentemperatur. *Lunds Universitets Årsskrift N.F.* 8(9), p. 1-15.

Fröhlich, G. (2001): *Modellierung, Realisierung und Validierung eines offenen Managementsystems für agrarmeteorologische Messdaten.* PhD thesis. Center of Life and Food Sciences Weihenstephan, Technical University Munich, 228 p.

Gardner, W.R. (1958): Some steady-state solutions of the unsaturated moisture flow equation with application to evaporation from a water table. *Soil Science* 85, p. 228-232.

Geiger, R. (1961): *Das Klima der bodennahen Luftschicht.* Braunschweig.

Hagemann, S., Botzet, M., Dümenil, L. & Machenhauer, B. (1999): Derivation of global GCM boundary conditions from 1 km land use satellite data. *Max-Planck-Institute for Meteorology Report* 289. Hamburg, Germany. (Report available electronically from: http://www.mpimet.mpg.de/en/web/science/a_reports.php)

Hagemann, S. & Jacob, D. (2007): Gradient in the climate change signal of European discharge predicted by a multi-model ensemble. *Climatic Change* 81, p. 309-327.

Hammel, K. & Kennel, M. (2001): Charakterisierung und Analyse der Wasser-verfügbarkeit und des Wasserhaushalts von Waldstandorten in Bayern mit dem Simulationsmodell BROOK90. *Forstliche Forschungsberichte München* 185.

Hank, T. (2008): *A biophysically based coupled model approach for the assessment of canopy processes under climate change conditions.* PhD thesis. Department of Geography, Ludwig-Maximilians University, Munich.

Hansen, S. (2002): *DAISY, a flexible soil-plant-atmosphere system model.* Model Description, 47 p.

Hansson, K., Simunek, J., Mizoguchi, M., Lundin, L. & van Genuchten, M. (2004): Water flow and heat transport in frozen soils: Numerical solution and freeze-thaw applications. *Vadose Zone Journal* 3, p. 693-704.

Hatfield, J.L., Perrier, A. & Jackson, R.D. (1983): Estimation of evapotranspiration at one time-of-day using remotely sensed surface temperatures. *Agricultural Water Management* 7, p. 341-350.

Hodges, G.B. & Smith, E.A. (1997): Intercalibration, objective analysis, intercomparison and synthesis of BOREAS surface net radiation measurements. *Journal of Geophysical Research* 102, Issue D24, p. 28885-28900.

Huwe, B. (1999): *SOHE: A numerical model for the simulation of heat flux in soils.* Software documentation. Department of Soil Physics, University of Bayreuth.

IPCC (2007): Summary for Policymakers. In: *Climate Change 2007: The Physical Science Basis.* Contribution of Working Group I to the Fourth Assessment Report of the Intergovernmental Panel on Climate Change [Solomon, S., D. Qin, M. Manning, Z. Chen, M. Marquis, K.B. Averyt, M.Tignor and H.L. Miller (Eds.)]. Cambridge University Press, Cambridge, United Kingdom and New York, NY, USA.

Janssen, H., Blocken, B. & Carmeliet, J. (2007): Conservative modelling of the moisture and heat transfer in building components under atmospheric excitation. *International Journal of Heat and Mass Transfer* 50, p.1128–1140.

Johnsson, H. & Lundin, L.C. (1990): Surface runoff and soil water percolation as affected by snow and soil frost. *Journal of Hydrology* 122, p. 141-159.

Kang, S., Kim, S., Oh, S. & Lee, D. (2000): Predicting spatial and temporal patterns of soil temperature based on topography, surface cover and air temperature. *Forest Ecology & Management* 136, p. 173-184.

Kerr, Y.H., Lagouarde, J.P. & Imbernon, J. (1992): Accurate land surface temperature retrieval from AVHRR data with use of an improved split window algorithm. *Remote Sensing of the Environment* 41, p. 197-209.

Kluender, R.A., Thompson, L.C. & Steigerwald, D.M. (1993): A conceptual model for predicting soil temperatures. *Soil Science* 156, p. 10-19.

Kondo, J. & Ishida, S. (1997): Sensible heat flux from the earth's surface under natural convective conditions. *Journal of Atmospheric Sciences* 54, p. 498-509.

Kuchment, L.S., Gelfan, A.N. & Demidov, V.N. (2000): A distributed model of runoff generation in the permafrost regions *Journal of Hydrology* 240, p. 1-22.

Kustas, W.P. & Daughtry, C.S.T. (1990): Estimation of the soil heat flux/net radiation ratio from spectral data. *Agricultural & Forest Meteorology* 49, p. 205-223.

Kustas, W.P. & Norman, J.P. (1999): Evaluation of soil and vegetation heat flux predictions using a simple two-source model with radiometric temperatures for partial canopy cover. *Agricultural & Forest Meteorology* 94, p. 13-29.

Legates, D.R. & McCabe, G.J. (1999): Evaluating the use of "goodness-of-fit" measures in hydrologic and hydroclimatic model validation. *Water Resources Research* 35(1), p. 233-241.

Lenz, V.I.S., (2007): *A process-based crop growth model for assessing Global Change effects on biomass production and water demand - A component of the integrative Global Change decision support system DANUBIA.* PhD thesis, University of Cologne, 180 pp.

Liang, X., Wood, E.F. & Lettenmaier, D.P. (1999): Modeling ground heat flux in land surface parameterization schemes. *Journal of Geophysical Research* 104/D8, p. 9581-9600.

Li, Q. & Sun, S. (2008): Development of the universal and simplified soil model coupling heat and water transport. *Science in China Series D: Earth Sciences* 51, p. 88-102.

Liu, S., Lu, L., Mao, D. & Jia, L. (2007): Evaluating parameterizations of aerodynamic resistance to heat transfer using field measurements. *Hydrology & Earth System Sciences* 11, p. 769–783.

Löpmeier, F.A. (2006): Die agrarmeteorologische Situation im Jahr 2006. In: Deutscher Wetterdienst (eds.): *Klimastatusbericht 2006*, http://www.ksb.dwd.de, p. 29-39.

Loew, A., Bach, H. & Mauser, W. (2007): 5 years of ENVISAT ASAR soil moisture observations in Southern Germany. *Proceedings of the ENVISAT Symposium* 23-27.04.2007, Montreux, Switzerland. ESA-SP636.

Löw, A. (2007): Assimilation of surface soil moisture information for improved land surface modelling – requirements for satellite observations. *Advances in Water Resources Research*, (submitted).

Ludwig, J., Meixner, F.X., Vogel, B. & Förstner. J. (2001): Soil-air exchange of nitric-oxide: An overview of processes, environmental factors, and modeling studies. *Biogeochemistry* 52, p. 225-257.

Ludwig, R., Mauser, W., Niemeyer, S., Colgan, A., Stolz, R., Escher-Vetter, H., Kuhn, M., Reichstein, M., Tenhunen, J., Kraus, A., Ludwig, M., Barth, M. & Hennicker, R. (2003a): Web-based modeling of water, energy and matter fluxes to support decision making in mesoscale catchments – the integrative perspective of GLOWA-Danube. *Physics & Chemistry of the Earth* 28, p. 621-634.

Ludwig, R., Probeck, M. & Mauser, W. (2003b): Mesoscale water balance modelling in the Upper Danube watershed using sub-scale land cover information derived from NOAA-AVHRR imagery and GIS-techniques. *Physics & Chemistry of the Earth* 28, p. 1351-1364.

Lundin, L.C. (1990): Hydraulic properties in an operational model of frozen soil. *Journal of Hydrology* 118, p. 289-310.

Marke, T. (2004): *Parametrisierung eines Verdunstungsmodells für Winterraps aus Eddy-Flux-Daten*. Diploma Thesis, unpublished. Department of Geography, Ludwig-Maximilians University, Munich, 107 p.

Marke, T. (2008): *A coupled land atmosphere model approach for climate change impact assessment in the Upper Danube river catchment*. PhD thesis. Department of Geography, Ludwig-Maximilians University, Munich.

Marks, D., Domingo, J., Susong, D., Link, T. & Garen, D. (1999): A spatially distributed energy balance snowmelt model for application in mountain basins. *Hydrological Processes* 13, p. 1935-1959.

Mauser, W. & Schädlich, S. (1997): Modelling the spatial distribution of evapotranspiration using remote sensing data and PROMET. *Journal of Hydrology* 212-213, p. 250-267

Mauser, W. & Ludwig, R. (2002): A research concept to develop integrative techniques, scenarios and strategies regarding global changes of the water cycle. In: Beniston, M. (Ed.) (2002): Climatic Change: Implications for the hydrological

cycle and for water management. *Advances in Global Change Research* 10, p. 171-188.

Mauser, W. (2003): Integrative hydrologische Modellentwicklung zur Entscheidungsunterstützung beim Einzugsgebietsmanagement. *Petermanns Geographische Mitteilungen* 147 (6), p. 68-75.

Mauser, W. & Muerth, M. (2007): GLOWA-Danube: Climate Change and the Future of Water in the Upper Danube Basin. *Proceedings of the 'Managing Alpine Future' Conference*, 2007, Innsbruck, Austria. (accepted)

Mauser, W., Prasch, M. & Strasser, U. (2007): Physically based modelling of Climate Change impact on snow cover dynamics in alpine regions using a stochastic weather generator. *Proceedings of the International Congress on Modelling and Simulation MODSIM07*, Christchurch, New Zealand.

Mauser, W. & Bach, H. (2008): PROMET – a Physical Hydrological Model to Study the Impact of Climate Change on the Water Flows of Medium Sized, Complex Watersheds. *Journal of Hydrology* (submitted).

Mayocchi, C.L. & Bristow, K.L. (1995): Soil surface heat flux: some general questions and comments on measurements. *Agricultural & Forest Meteorology* 75, p. 43-50.

McBratney, A.B., Minasny, B., Cattle, S.R. & Vervoort, R.W. (2002): From pedotransfer functions to soil inference systems. *Geoderma* 109, p. 43-71.

McBratney, A.B., Mendonca Santos, M.L. & Minasny, B. (2003): On digital soil mapping. *Geoderma* 117, p. 3-52.

Miao, J.-F., Chen, D. & Borne, K. (2007): Evaluation and Comparison of Noah and Pleim–Xiu Land Surface Models in MM5 Using GÖTE2001 Data: Spatial and Temporal Variations in Near-Surface Air Temperature. *Journal of Applied Meteorology & Climatology* 46, p. 1587-1605.

Minasny, B., McBratney, A.B. & Bristow, K.L. (1999): Comparison of different approaches to the development of pedotransfer functions for water-retention curves. *Geoderma* 93, p. 225-253.

Minnis, P. & Khaiyer, M. (2000): Anisotropy of land surface skin temperature derived from satellite data. *Journal of Applied Meteorology* 39, p. 1117-1129.

Moberg, A. & Jones, P.D. (2004): Regional climate model simulations of daily maximum and minimum near-surface temperatures across Europe compared with observed station data 1961–1990. *Climate Dynamics* 23, p. 695-715.

Møberg, J.P., Petersen, L. & Rasmussen, K. (1988): Constituents of some widely distributed soils in Denmark. *Geoderma* 42, p. 295-316.

Monteith, J.L (1965): Evaporation and the environment. *Symposiuim of the Society of Explanatory Biology* 19, p. 205-234

Monteith, J.L. (1973): *Principles of environmental physics.* Arnold, Paris.

Monteith, J.L. & Unsworth, M.H. (2008): *Principles of environmental physics.* 3rd Edition, Elsevier, Oxford, 418 p.

Nash, J.E. & Sutcliffe, J.V. (1970): River flow forecasting through conceptual models. Part I – A discussion of principles. *Journal of Hydrology* 10, p. 282-290.

Nemes, A., Schaap, M.G., Leij, F.J. & Wösten, J.H.M. (2001): Description of the unsaturated soil hydraulic database UNSODA version 2.0. *Journal of Hydrology* 251, p. 151-162.

Neuhaus, P. & Klar, C.W. (2007): An object-oriented framework for a process-based soil nitrogen model component. Poster at the EGU General Assembly Vienna, 14.-20. April 2007.

Niemeyer, S. (2000): *Modelling the surface energy balance on the regional scale with remote sensing and meteorological data – A case study in Sicily.* EC-JRC, Space Applications Institute: Natural Hazards Project, EUR 19523 EN. 239 p.

Norman, J.M., Kustas, W.P. & Humes, K.S. (1995): Source approach for estimating soil and vegetation energy fluxes in observations of directional radiometric surface temperature. *Agricultural & Forest Meteorology* 77, p. 263-293.

Nyberg, L., Stähli, M., Mellander, P. & Bishop, K. (2001): Soil frost effects on soil water on runoff dynamics along a boreal forest transect: 1. Field investigations. *Hydrological Processes* 15, p. 909-926.

Ochsner, T.E., Horton, R. & Ren T. (2001): A new perspective on soil thermal properties. *Soil Science Society of America Journal* 65, p. 1641-1647.

Ogée, J., Lamaud, E., Brunet, Y., Berbigier, P. & Bonnefond, J.M. (2001): A long-term study of soil heat flux under a forest canopy. *Agricultural & Forest Meteorology* 106, p. 173-186.

Ogée, J. & Brunet, Y. (2002): A forest floor model for heat and moisture including a litter layer. *Journal of Hydrology* 255, p. 212-233.

Oke, T.R. (1987): *Boundary layer climates.* 2nd edition, Routledge, London, 450 p.

Philip, J.R. (1957): The theory of infiltration: 1. The infiltration equation and its solution. *Soil Science* 83, p. 345-357.

Philip, J.R. (1969): The theory of infiltration. In: Chow, V.T. (Edt.): *Advances in Hydroscience* 5, Academic, New York, p. 215-296.

Pitman, A. (2003): Review: The evolution of, and revolution in, land surface schemes designed for climate models. *International Journal of Climatology* 23, p. 479-510.

Prasch, M., Strasser, U., Bernhard, M., Weber, M. & Mauser, W. (2007): Physically based modelling of snow cover dynamics in Alpine regions. *Proceedings of the 'Managing Alpine Future' Conference*, 2007, Innsbruck, Austria. (accepted)

Prasch, M., Strasser, U. & Mauser, W. (2008): Validation of a physically based snow model for the simulation of the accumulation and ablation of snow (ESCIMO).

Proceedings of the Alpine*Snow*Workshop 2006 Munich, Germany. *Berchtesgaden National Park Research Report* 53 (in press).

Prihodko, L & Goward, S.N. (1997): Estimation of Air Temperature from Remotely Sensed Surface Observations. *Remote Sensing of Environment* 60(3), p. 335-346.

Qin, Z. & Karnieli, A. (1999): Progress in the remote sensing of land surface temperature and ground emissivity using NOAA-AVHRR data. *International Journal of Remote Sensing* 20(12), p. 2367-2393.

Raich, J.W. & Schlesinger, W.H. (1992): The global carbon dioxide flux in soil respiration and its relationship to vegetation and climate. Tellus 44B, p. 81-99.

Rawls, W.J. & Brakensiek, D.L. (1985): Prediction of soil water properties for hydrologic modelling. *Proceedings of the American Society of Civil Engineers Watershed Management Symposium*, New York, S. 293-299.

Sauer, T.J. & Norman, J.M. (1995): Simulated canopy microclimate using below-canopy soil surface transfer coefficients. *Agricultural & Forest Meteorology* 75, p. 135-160.

Sauer, T.J., Norman, J.M., Tanner, C.B. & Wilson, T.B. (1995): Measurement of heat and vapour transfer coefficents at the soil surface beneath a maize canopy using source plates. *Agricultural & Forest Meteorology* 75, p. 161-189.

Saxton, K.E., Rawls, W.J., Romberger, J.S. & Papendick, R.I. (1986): Estimating generalized soil water characteristics from texture. *Soil Science Society of America Journal* 50, p. 1031–1036.

Schaap, M.G., Leij, F.J. & van Genuchten, Th. (2001): Rosetta - A computer program for estimating soil hydraulic parameters with hierarchical pedotransfer functions. *Journal of Hydrology* 251, p. 163-176.

Scheffer, F. & Schachtschabel, P. (2002): *Lehrbuch der Bodenkunde.* 15th Edition, Spektrum Akademischer Verlag, Heidelberg, Berlin, 593 p.

Scheinost, A.C., Sinowski, W. & Auerswald, K. (1997): Regionalization of soil water retention curves in a highly variable soilscape, I. Developing a new pedotransfer function. *Geoderma* 78, p. 129-143.

Scull, P., Franklin, J., Chadwick, O.A. & McArthur, D. (2003): Predictive soil mapping: a review. *Progress in Physical Geography* 27(2), p. 171-197.

Snyder, W.C., Wan, Z., Zhang, Y. & Feng, Y.Z. (1998): Classification-based emissivity for land surface temperature measurement from space. *International Journal of Remote Sensing* 19(14), p. 2753-2774.

Sobrino, J.A., Raissouni, N. & Li, Z.L. (2000): A comparative study of land surface emissivity retrieval from NOAA data. *Remote Sensing of the Environment* 75, p. 256-266.

Stähli, M. & Jansson, P.E. (1998): Test of two SVAT snow submodels during different winter conditions. *Agricultural & Forest Meteorology* 92, p. 31-43.

Stähli, M., Nyberg, L., Mellander, P.E., Jansson, P.E., Bishop, K.H. (2001): Soil frost effects on soil water and runoff dynamics along a boreal transect: 2. Simulations. *Hydrological Processes* 15, p. 927-941.

Strasser, U., Etchevers, P. & Lejeune, Y. (2002): Intercomparision of two Snow Models with Different Complexity Using Data from an Alpine Site. *Nordic Hydrology* 33 (1), p. 15-26.

Strasser, U., Bernhardt, M., Weber, M., Liston, G.E. & Mauser, W. (2007): Is snow sublimation important in the alpine water balance? *The Cryosphere Discussions* 1, p. 303-350.

Thom, A.S. (1975): Momentum, mass and heat exchange of plant comunities. In: Monteith, J.L. (Ed.): Vegetation and the atmosphere. Academic Press, London, p. 57-109.

Thorn, C., Schlyter, J., Darmody, R. & Dixon, J. (1999): Statistical relationships between daily and monthly air and shallow-ground temperatures in Kärkevagge, Swedish Lapland. *Permafrost and Periglacial Processes* 10, p. 317-330.

Thunholm, B. (1990): A comparison of measured and simulated soil temperature using air temperature and soil surface energy balance as boundary conditions. *Agricultural & Forest Meteorology* 53, p. 59-72.

Tietje, O. & Tapkenhinrichs, M. (1993): Evaluation of pedo-transfer functions. *Soil Science Society of America Journal* 57, p. 1088-1095.

Twine, T.E., Kustas, W.P., Norman, J.M., Cook, D.R., Houser, P.R., Meyers, T.P., Prueger, J.H., Starks, P.J. & Wesely, M.L. (2000): Correcting eddy-covariance flux underestimates over grassland. *Agricultural & Forest Meteorology* 103, p. 279-300.

Ulivieri, C., Castranuovo, M., Francioni, R. & Cardillo, A. (1994): A split window algorithm for estimating land surface temperature from satellites. *Advances in Space Research* 14(3), p. 59-65.

Van Genuchten, M.Th. (1980): A closed-form equation for predicting the hydraulic conductivity of unsaturated soils. *Soil Science Society of America Journal* 53, p. 987-996.

Vasquez, D.P., Reyes, F.J.O. & Arboledas, L.A. (1994): A comparative study of algorithms for estimating land surface temperature from AVHRR data. *Remote Sensing of the Environment* 62, p. 215-222.

Vereecken, H., Feyen, J., Maes, J. & Darius, P. (1989): Estimating the soil water retention characteristic from texture, bulk density and carbon content. *Soil Science* 148, p. 389-403.

Waldmann, D. & Mauser, W. (2007): Temporal disaggregation of precipitation data for modelling soil erosion in landuse change scenarios. *Proceedings of the 'Managing Alpine Future' Conference* 2007, Innsbruck, Austria. (accepted)

Wagner, B., Tarnawski, V.R., Hennings, V., Müller, U., Wessolek, G. & Plagge, R. (2001): Evaluation of pedo-transfer functions for unsaturated soil hydraulic conductivity using an independent data set. *Geoderma* 102, p. 275-297.

Wagner, B., Tarnawski, V.R. & Stöckl, M. (2004): Evaluation of pedotransfer functions predicting hydraulic properties of soils and deeper sediments. *Journal of Plant Nutrition & Soil Science* 167, p. 236-245.

Watanabe, K. & Mizoguchi, M. (2002): Amount of unfrozen water in frozen porous media saturated with solution. *Cold Regions Science & Technology* 34, p. 103-110.

Welpmann, M. (2003): *Bodentemperaturmessungen und –simulationen im Lötschental (Schweizer Alpen)*. PhD thesis. Friedrich-Wilhelms University, Bonn.

Wösten, J.H.M. (1997): Pedotransfer functions to evaluate soil quality. In: Gregorich, E.G., Carter, M.R. (Eds.): Soil Quality for Crop Production and Ecosystem Health. *Developments in Soils Science* 25, Elsevier, Amsterdam, p. 221–245.

Wösten, J.H.M., Lilly, A., Nemes, A. & Le Bas, C. (1999): Development and use of hydraulic properties of European soils. *Geoderma* 90, p. 169-185.

Wösten, J.H.M., Pachepsky, Y.A. & Rawls, W.J. (2001): Pedotransfer functions: bridging the gap between available basic soil data and missing soil hydraulic characteristics. *Journal of Hydrology* 251, p. 123-150.

Yang, H. & Yang Z. (2006): A modified land surface temperature split window retrieval algorithm and its applications over China. *Global and Planetary Change* 52, p. 207-215.

Yu, Y., Privette, J.L. & Pinheiro, A.C. (2008): Evaluation of split-window land surface temperature algorithms for generating climate data records. *IEEE Transactions on Geoscience and Remote Sensing* 46(1), p. 179-192.

Zheng, D., Hunt Jr., E.R. & Running, S.W. (1993): A daily soil temperature model based on air temperature and precipitation for continental applications. *Climate Research* 2, p. 183-191.

APPENDIX

Appendix A: Soil Hydraulic Properties

Appendix A 1: Hydraulic parameters for the soil type classes used in DANUBIA and PROMET, derived from basic soil property data with the Pedotransfer Functions of Rawls & Brakensiek (1985) and Wösten et al (1999).

soil type class	soil layer	texture	bulk density [g/cm3]	residual water content [m3/m3]	pore size distribution index	bubbling pressure head [hPa]	effective porosity [m3/m3]	saturated hydraulic conductivity [cm/s]
1	1	mS	1.285	0.1443	0.4836	6.57	0.2948	0.001939
1	2	mS	1.444	0.0422	0.5012	6.86	0.3458	0.001412
1	3	mS	1.444	0.0422	0.5012	6.86	0.3458	0.000617
1	4	mS	1.744	0.0051	0.5740	9.68	0.2869	0.000301
2	1	gS	1.580	0.0515	0.5271	7.69	0.2930	0.000667
2	2	gS*	1.728	0.0226	0.5686	9.43	0.2150	0.000683
2	3	gS*	1.763	0.0087	0.5808	10.02	0.2199	0.000364
2	4	gS*	1.636	0.0041	0.5412	8.23	0.2571	0.000343
3	1	Sl4	1.391	0.1043	0.3501	10.27	0.3189	0.000583
3	2	Sl3	1.529	0.0603	0.4029	12.38	0.3121	0.000579
3	3	Ls4	1.735	0.0909	0.3207	22.06	0.1647	0.000071
3	4	Ls4	1.735	0.0816	0.3207	22.06	0.1740	0.000071
4	1	Slu	1.060	0.1438	0.3478	12.95	0.3792	0.000363
4	2	Sl4*	1.243	0.0890	0.3400	8.13	0.2878	0.000757
4	3	Sl4*	1.545	0.0552	0.3623	14.01	0.1692	0.000120
4	4	Sl3*	1.545	0.0306	0.4029	15.58	0.1899	0.000142
5	1	Sl4	1.391	0.1229	0.3501	10.27	0.3004	0.000370
5	2	Sl4	1.391	0.1043	0.3501	10.27	0.3189	0.000583
5	3	Lt2	1.717	0.1623	0.2160	96.34	0.1759	0.000051
5	4	Ls2	1.630	0.1020	0.3187	49.99	0.2513	0.000109
6	1	Sl4	1.199	0.1662	0.3231	9.95	0.2248	0.000321
6	2	Sl4	1.198	0.1013	0.3231	9.95	0.2897	0.000709
6	3	Sl4	1.524	0.0827	0.3370	18.55	0.2250	0.000149
6	4	gS*	1.696	0.0102	0.5007	7.81	0.1148	0.001641
7	1	Ut3	1.259	0.1136	0.3328	45.64	0.3521	0.000440
7	2	Ut4	1.259	0.0951	0.3328	45.64	0.3707	0.000121
7	3	Ut4	1.471	0.1113	0.3060	71.49	0.2930	0.000133
7	4	Ut4	1.550	0.1020	0.3007	85.52	0.2768	0.000103
8	1	Lu	1.418	0.1484	0.3158	48.96	0.2729	0.000231
8	2	Lu	1.418	0.1113	0.3158	48.96	0.3100	0.000185
8	3	Tu3	1.603	0.1878	0.1882	137.65	0.1943	0.000052
8	4	Lu	1.602	0.0918	0.3083	75.57	0.2342	0.000082

soil type class	soil layer	texture	bulk density [g/cm3]	residual water content [m3/m3]	pore size distribution index	bubbling pressure head [hPa]	effective porosity [m3/m3]	saturated hydraulic conductivity [cm/s]
9	1	Lt2	1.405	0.1808	0.2617	38.21	0.2577	0.000327
9	2	Lt2	1.405	0.1623	0.2617	38.21	0.2762	0.000327
9	3	Lt2	1.444	0.1623	0.2547	70.34	0.2635	0.000117
9	4	Lt2	1.537	0.1785	0.2025	114.21	0.2240	0.000066
10	1	Tl	0.928	0.3988	0.1833	24.74	0.2317	0.000404
10	2	Tl	1.206	0.3338	0.1520	61.68	0.2074	0.000457
10	3	Tl	1.299	0.3153	0.1288	83.55	0.1947	0.000037
10	4	Tl	1.299	0.3060	0.1288	83.55	0.2040	0.000037
12	1	Lts	1.012	0.3177	0.2479	8.43	0.2531	0.000255
12	2	Lts	1.428	0.2643	0.1902	29.70	0.1795	0.000182
12	3	Tl	1.444	0.1113	0.1338	65.48	0.0694	0.000088
12	4	Lts*	1.397	0.0344	0.1701	38.87	0.0366	0.000110
13	1	Ls4	1.154	0.2208	0.3081	6.21	0.1840	0.000121
13	2	Ls4	1.285	0.1456	0.3122	7.48	0.1792	0.000240
13	3	Ls4	1.602	0.0705	0.3191	14.95	0.1468	0.000085
13	4	Sl4*	1.630	0.0408	0.3195	16.13	0.1005	0.000059
14	1	Lt2	1.057	0.2152	0.2811	18.10	0.2249	0.000195
14	2	Slu	1.312	0.0405	0.3343	21.27	0.0497	0.000169
14	3	Slu	1.670	0.0195	0.4256	16.61	0.0460	0.000124
14	4	Slu	1.670	0.0195	0.4256	16.61	0.0460	0.000124
15	1	Lt3	0.967	0.2875	0.2536	23.26	0.3042	0.000345
15	2	Tl	1.142	0.2411	0.1967	26.68	0.1976	0.000566
15	3	Tt	1.089	0.1471	0.1423	62.25	0.0629	0.000759
15	4	Tt*	1.124	0.1471	0.1423	62.25	0.0629	0.000966

Appendix B: Individual Statistical Values of the Validation Runs at AgMet Sites

Appendix B 1: Statistical values derived from the comparison of the SHTM w/ EEB simulation with measured time series of the year 2003 from 25 agrometeorological stations.

AgMet Station (Year 2003)	deviation of mean soil temperature [K] in layer 2	RMSE [K] of soil layer 2	CME of soil layer 2	deviation of mean soil temperature [K] in layer 1	RMSE [K] of soil layer 1	CME of soil layer 1
Burgheim (Nr. 35)	-0.46	1.68	0.94	0.00	1.94	0.94
Edelshausen (Nr. 11)	0.03	2.49	0.85	0.50	3.17	0.78
Ehekirch (Nr. 101)	1.34	3.29	0.72	1.62	3.88	0.68
Eschenhart (Nr. 15)	-0.27	1.35	0.98	0.06	1.55	0.97
Frankendorf (Nr.45)	-0.15	1.50	0.96	0.62	2.42	0.93
Freising (Nr. 08)	0.13	1.31	0.97	0.27	1.67	0.97
Großberghofen (Nr. 68)	0.18	1.69	0.95	0.64	2.23	0.93
Gut Hüll (Nr. 72)	n/a	n/a	n/a	n/a	n/a	n/a
Häringhof (Nr. 10)	0.08	1.08	0.98	0.33	1.55	0.96
Hüll (Nr. 40)	-0.43	1.33	0.97	-0.05	1.57	0.97
Karolinenfeld (Nr.125)	n/a	n/a	n/a	n/a	n/a	n/a
Köfering (Nr. 17)	0.08	1.72	0.95	0.46	2.34	0.93
Konnersreuth (Nr. 67)	0.41	1.82	0.92	1.08	2.63	0.87
Kringell (Nr. 122)	0.10	1.52	0.95	-0.17	2.23	0.91
Lochheim (Nr. 74)	0.22	2.37	0.89	0.86	2.55	0.89
Mittelstetten (Nr. 54)	1.52	2.78	0.81	1.78	2.94	0.84
Neuhof (Nr. 99)	-0.68	1.44	0.96	-0.23	2.01	0.94
Pösing (Nr. 120)	-1.18	2.29	0.93	-1.50	2.60	0.92
Reith (Nr. 50)	-0.03	1.99	0.92	0.76	2.72	0.87
Reschenberg (Nr. 62)	-0.56	1.47	0.96	-0.31	1.87	0.94
Sarching (Nr. 18)	0.22	1.96	0.94	0.68	3.40	0.86
Schönbrunn (Nr. 48)	n/a	n/a	n/a	n/a	n/a	n/a
Sommersthof (Nr.19)	-0.17	1.56	0.95	0.55	2.16	0.91
Spitalhof (Nr. 38)	-0.17	1.17	0.98	-0.20	2.28	0.94
Steinach (Nr. 42)	-0.97	1.60	0.96	-0.62	1.60	0.97
Uttenkofen (Nr. 03)	-0.65	3.06	0.89	-0.46	2.43	0.94
Wallerstein (Nr. 60)	0.59	1.85	0.93	0.68	2.12	0.93
Windsfeld (Nr. 52)	n/a	n/a	n/a	1.28	2.79	0.89

Appendix B 2: Statistical values derived from the comparison of the SHTM w/ EEB simulation with measured time series of the year 2004 from 28 agrometeorological stations.

| AgMet Station (Year 2004)	deviation of mean soil temperature [K] in layer 2	RMSE [K] of soil layer 2	CME of soil layer 2	deviation of mean soil temperature [K] in layer 1	RMSE [K] of soil layer 1	CME of soil layer 1
Burgheim (Nr. 35)	-0.56	1.87	0.91	0.00	2.16	0.90
Edelshausen (Nr. 11)	-0.09	2.29	0.83	0.24	2.71	0.79
Ehekirch (Nr. 101)	0.90	1.97	0.88	0.98	2.23	0.88
Eschenhart (Nr. 15)	-0.12	1.17	0.97	-0.03	1.47	0.96
Frankendorf (Nr.45)	0.25	1.37	0.96	0.65	2.21	0.92
Freising (Nr. 08)	0.29	1.26	0.97	0.23	1.68	0.96
Großberghofen (Nr. 68)	0.21	1.54	0.94	0.58	1.78	0.94
Gut Hüll (Nr. 72)	-0.35	1.38	0.96	-0.17	1.67	0.95
Häringhof (Nr. 10)	0.13	1.30	0.95	0.18	1.66	0.94
Hüll (Nr. 40)	-0.57	1.56	0.95	-0.38	1.78	0.94
Karolinenfeld (Nr.125)	-0.45	1.92	0.97	-0.18	3.13	0.82
Köfering (Nr. 17)	0.54	2.21	0.89	0.76	2.80	0.84
Konnersreuth (Nr. 67)	0.08	1.75	0.91	0.68	2.35	0.86
Kringell (Nr. 122)	0.09	1.47	0.95	-0.30	2.14	0.90
Lochheim (Nr. 74)	0.34	2.31	0.86	0.91	2.60	0.84
Mittelstetten (Nr. 54)	1.00	2.01	0.88	1.14	2.18	0.89
Neuhof (Nr. 99)	-0.18	1.34	0.96	0.04	1.96	0.92
Pösing (Nr. 120)	-1.20	1.75	0.94	-1.45	2.10	0.93
Reith (Nr. 50)	0.10	1.95	0.90	0.50	2.14	0.91
Reschenberg (Nr. 62)	-0.63	2.00	0.91	-0.52	2.32	0.89
Sarching (Nr. 18)	-0.02	2.07	0.92	0.28	3.39	0.81
Schönbrunn (Nr. 48)	0.21	1.27	0.99	0.63	1.73	0.95
Sommersthof (Nr.19)	-0.24	1.17	0.97	-0.05	2.88	0.87
Spitalhof (Nr. 38)	0.27	1.58	0.94	0.17	2.44	0.90
Steinach (Nr. 42)	-0.42	1.22	0.97	-0.34	1.50	0.96
Uttenkofen (Nr. 03)	-0.37	1.47	0.97	-0.10	2.21	0.94
Wallerstein (Nr. 60)	0.17	1.47	0.95	-0.12	1.76	0.94
Windsfeld (Nr. 52)	n/a	n/a	n/a	1.14	2.44	0.86

Appendix B 3: Statistical values derived from the comparison of the SHTM w/ PME simulation with measured time series of the year 2003 from 25 agrometeorological stations.

| AgMet Station (Year 2003)	deviation of mean soil temperature [K] in layer 2	RMSE [K] of soil layer 2	CME of soil layer 2	deviation of mean soil temperature [K] in layer 1	RMSE [K] of soil layer 1	CME of soil layer 1
Burgheim (Nr. 35)	-1.15	2.23	0.90	-0.72	2.85	0.88
Edelshausen (Nr. 11)	-0.83	2.87	0.80	-0.34	3.97	0.66
Ehekirch (Nr. 101)	0.60	3.44	0.69	0.89	4.26	0.61
Eschenhart (Nr. 15)	-1.14	1.70	0.96	-0.89	2.19	0.94
Frankendorf (Nr.45)	-0.79	1.59	0.96	-0.03	1.99	0.95
Freising (Nr. 08)	-0.71	1.53	0.96	-0.58	1.84	0.96
Großberghofen (Nr. 68)	-0.60	1.90	0.93	-0.12	2.23	0.93
Gut Hüll (Nr. 72)	n/a	n/a	n/a	n/a	n/a	n/a
Häringhof (Nr. 10)	-0.45	1.59	0.95	-0.27	2.30	0.91
Hüll (Nr. 40)	-1.34	2.06	0.93	-1.03	2.52	0.91
Karolinenfeld (Nr.125)	n/a	n/a	n/a	n/a	n/a	n/a
Köfering (Nr. 17)	-0.60	1.25	0.98	-0.16	2.23	0.93
Konnersreuth (Nr. 67)	-0.12	2.21	0.89	0.56	3.31	0.79
Kringell (Nr. 122)	-0.50	1.82	0.93	-0.77	3.21	0.82
Lochheim (Nr. 74)	-0.57	2.55	0.87	0.18	3.10	0.84
Mittelstetten (Nr. 54)	0.70	2.56	0.84	0.91	2.71	0.86
Neuhof (Nr. 99)	-1.29	1.78	0.95	-0.91	2.45	0.91
Pösing (Nr. 120)	-1.84	2.57	0.91	-2.18	2.93	0.90
Reith (Nr. 50)	-0.70	2.38	0.88	-0.03	3.26	0.82
Reschenberg (Nr. 62)	-1.30	2.25	0.91	-1.03	3.10	0.84
Sarching (Nr. 18)	-0.29	2.16	0.93	0.21	4.06	0.80
Schönbrunn (Nr. 48)	n/a	n/a	n/a	n/a	n/a	n/a
Sommersthof (Nr.19)	-0.75	1.73	0.94	-0.07	2.68	0.86
Spitalhof (Nr. 38)	-0.74	1.36	0.97	-0.72	1.94	0.95
Steinach (Nr. 42)	-1.72	2.13	0.94	-1.40	2.51	0.93
Uttenkofen (Nr. 03)	-1.42	3.30	0.88	-1.17	2.89	0.92
Wallerstein (Nr. 60)	-0.20	1.88	0.93	-0.04	2.95	0.86
Windsfeld (Nr. 52)	n/a	n/a	n/a	0.44	2.26	0.93

Appendix B 4: Statistical values derived from the comparison of the SHTM w/ PME simulation with measured time series of the year 2004 from 28 agrometeorological stations.

| AgMet Station (Year 2004)	deviation of mean soil temperature [K] in layer 2	RMSE [K] of soil layer 2	CME of soil layer 2	deviation of mean soil temperature [K] in layer 1	RMSE [K] of soil layer 1	CME of soil layer 1
Burgheim (Nr. 35)	-1.22	2.24	0.87	-0.66	2.58	0.86
Edelshausen (Nr. 11)	-0.84	2.52	0.80	-0.52	3.40	0.67
Ehekirch (Nr. 101)	0.20	1.99	0.88	0.28	2.62	0.84
Eschenhart (Nr. 15)	-1.06	1.59	0.95	-0.99	2.03	0.93
Frankendorf (Nr.45)	-0.51	1.30	0.97	-0.11	1.69	0.96
Freising (Nr. 08)	-0.59	1.47	0.96	-0.66	1.71	0.95
Großberghofen (Nr. 68)	-0.65	1.70	0.93	-0.31	1.80	0.94
Gut Hüll (Nr. 72)	-1.62	2.23	0.90	-1.47	2.63	0.88
Häringhof (Nr. 10)	-0.46	1.42	0.94	-0.45	2.21	0.88
Hüll (Nr. 40)	-1.53	2.17	0.91	-1.35	2.50	0.89
Karolinenfeld (Nr.125)	-1.15	2.14	0.97	-0.90	2.68	0.87
Köfering (Nr. 17)	0.00	1.55	0.94	0.24	2.33	0.89
Konnersreuth (Nr. 67)	-0.43	1.85	0.90	0.14	2.64	0.82
Kringell (Nr. 122)	-0.46	1.76	0.93	-0.87	3.01	0.81
Lochheim (Nr. 74)	-0.36	2.48	0.84	0.21	3.00	0.79
Mittelstetten (Nr. 54)	0.24	1.64	0.92	0.36	1.83	0.93
Neuhof (Nr. 99)	-0.81	1.25	0.96	-0.61	1.93	0.92
Pösing (Nr. 120)	-1.78	2.10	0.92	-2.04	2.75	0.87
Reith (Nr. 50)	-0.55	1.99	0.90	-0.18	2.41	0.88
Reschenberg (Nr. 62)	-1.33	2.49	0.86	-1.25	3.10	0.80
Sarching (Nr. 18)	-0.48	2.31	0.90	-0.16	4.02	0.73
Schönbrunn (Nr. 48)	-0.56	1.46	0.99	-0.09	1.58	0.96
Sommersthof (Nr.19)	-0.85	1.31	0.96	-0.70	2.62	0.90
Spitalhof (Nr. 38)	-0.47	1.23	0.97	-0.63	1.94	0.94
Steinach (Nr. 42)	-1.13	1.76	0.94	-1.05	2.29	0.91
Uttenkofen (Nr. 03)	-1.09	1.74	0.95	-0.84	2.12	0.94
Wallerstein (Nr. 60)	-0.56	1.67	0.93	-0.77	2.52	0.88
Windsfeld (Nr. 52)	n/a	n/a	n/a	0.32	2.38	0.86

Appendix C: Frequency Distributions of surface Temperature Differences between PROMET and the *Ulivieri* Split Window Technique (SWT)
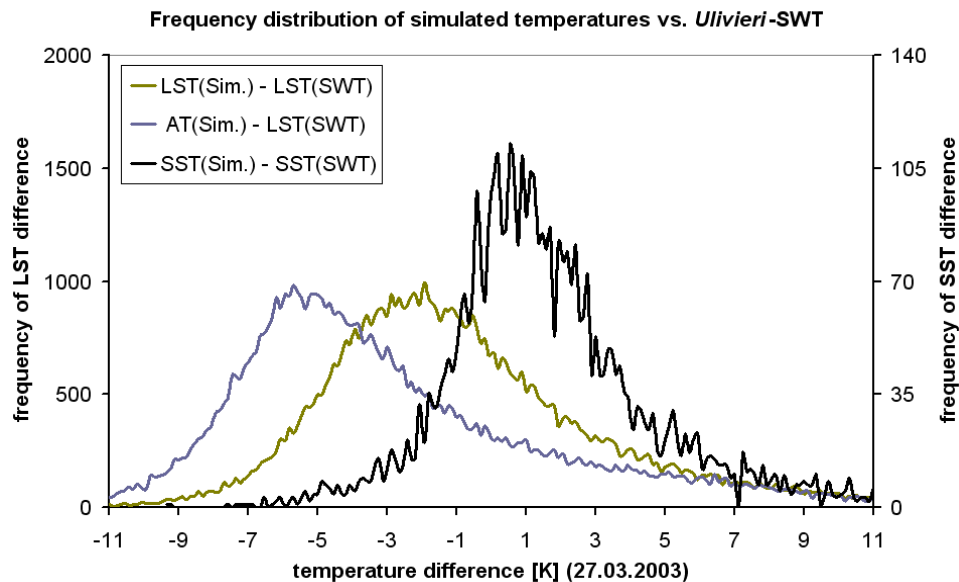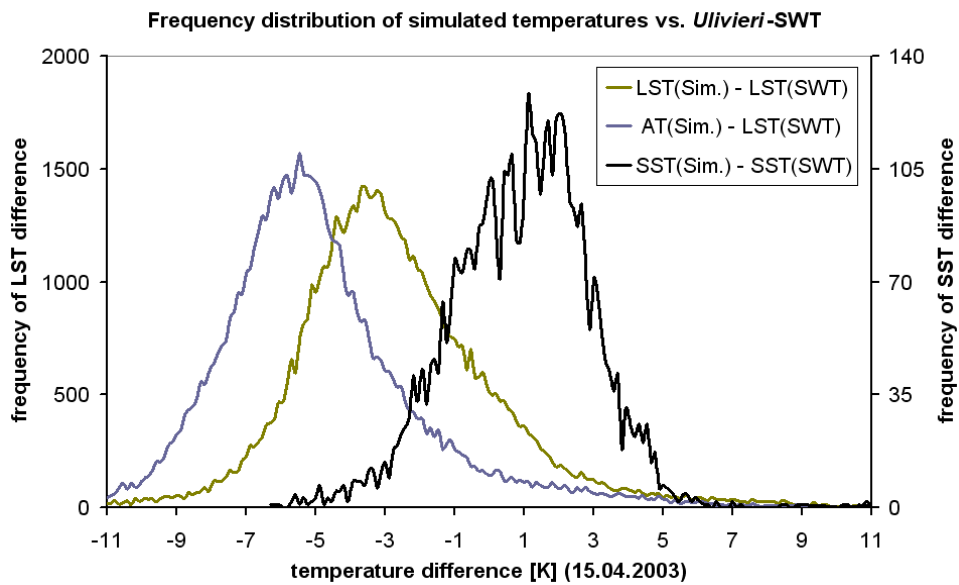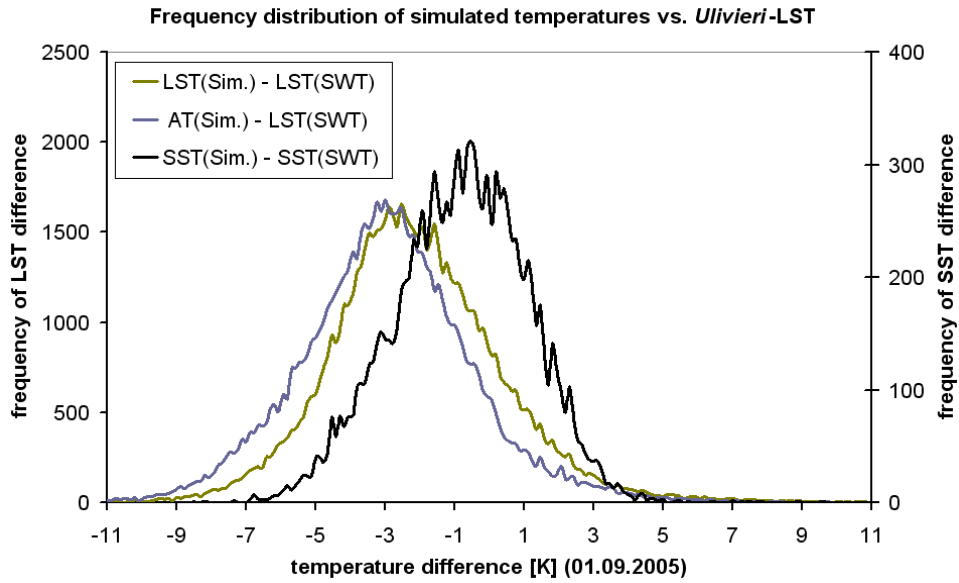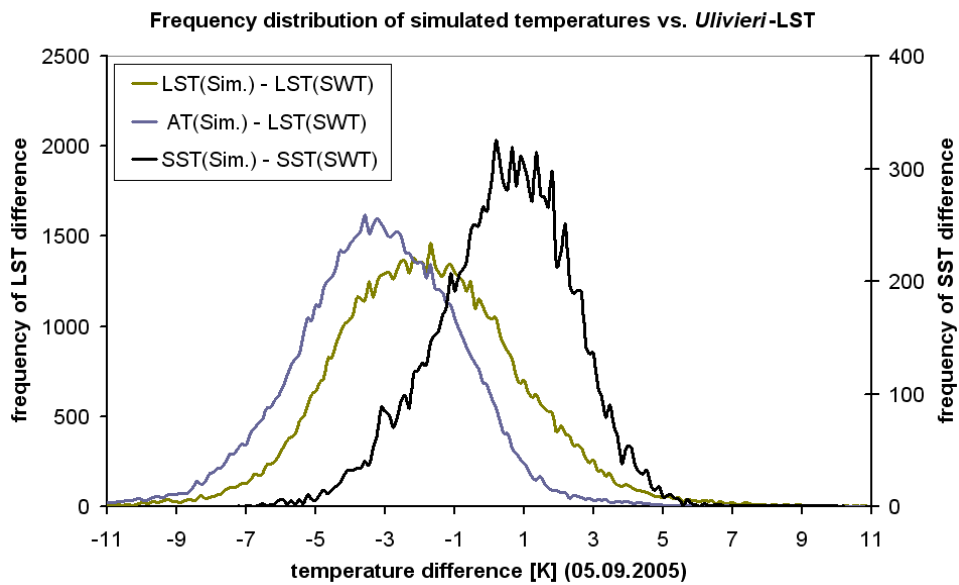

Appendix C 1: Frequency distributions of the differences between simulated surface and air temperatures and the LSTs and SSTs derived from NOAA-AVHRR data with the SWT of Ulivieri et al (1994) for the 27.03.2003, 11:09 CET.
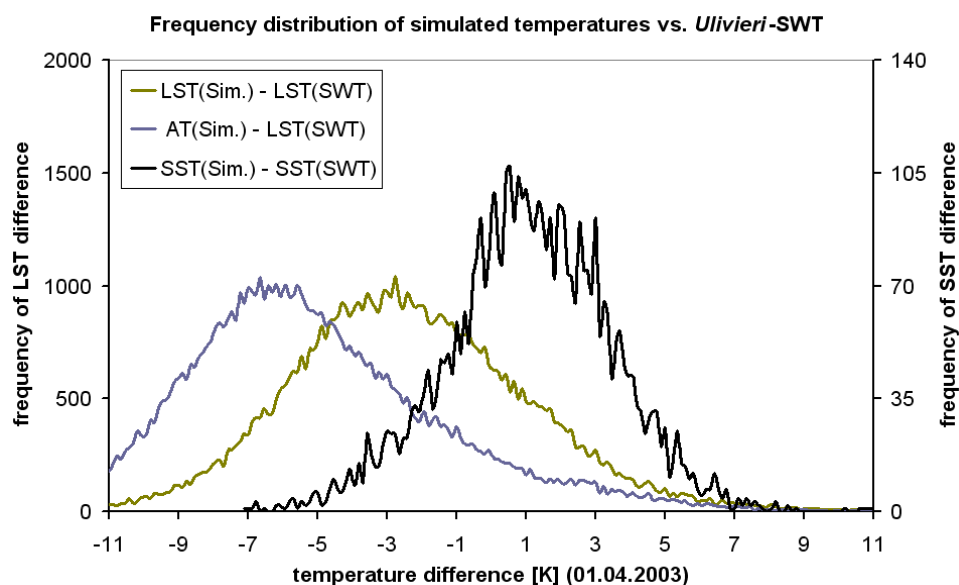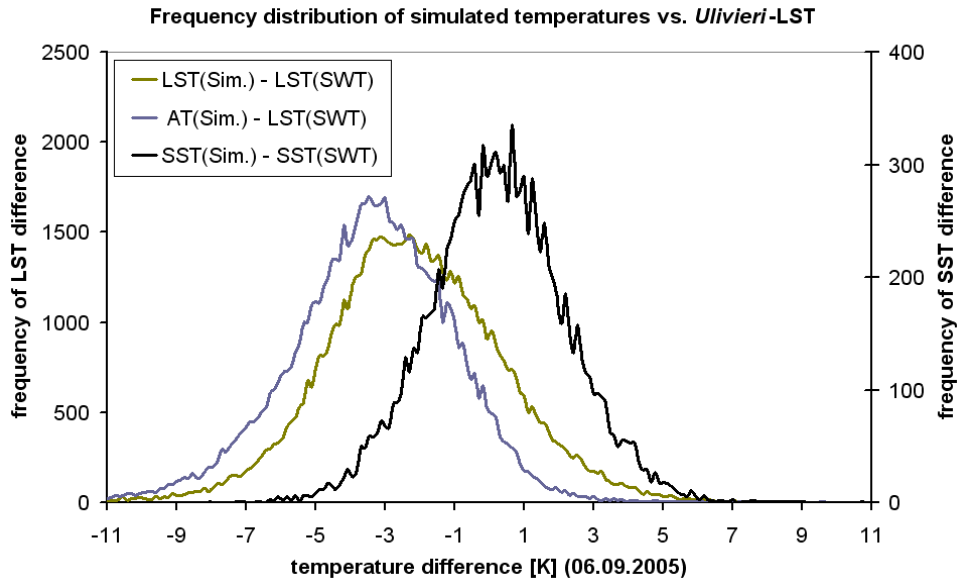

Appendix C 2: Frequency distributions of the differences between simulated surface and air temperatures and the LSTs and SSTs derived from NOAA-AVHRR data with the SWT of ULIVIERI et al (1994) for the 01.04.2003, 10:57 CET.
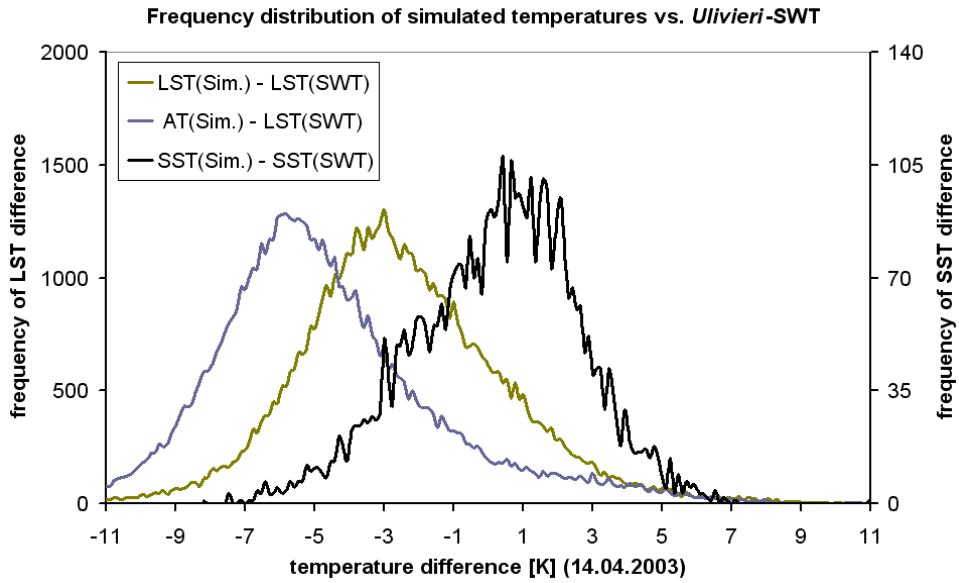
Appendix C 3: Frequency distributions of the differences between simulated surface and air temperatures and the LSTs and SSTs derived from NOAA-AVHRR data with the SWT of ULIVIERI et al (1994) for the 14.04.2003, 11:03 CET.

Appendix C 4: Frequency distributions of the differences between simulated surface and air temperatures and the LSTs and SSTs derived from NOAA-AVHRR data with the SWT of ULIVIERI et al (1994) for the 15.04.2003, 10:42 CET.
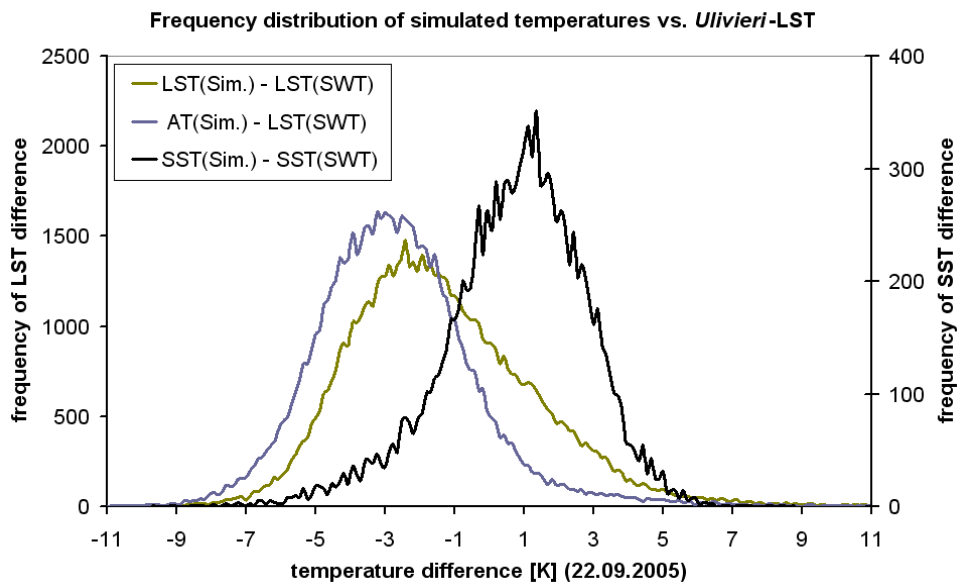
Appendix C 5: Frequency distributions of the differences between simulated surface and air temperatures and the LSTs and SSTs derived from NOAA-AVHRR data with the SWT of ULIVIERI et al (1994) for the 01.09.2005, 11:09 CET.
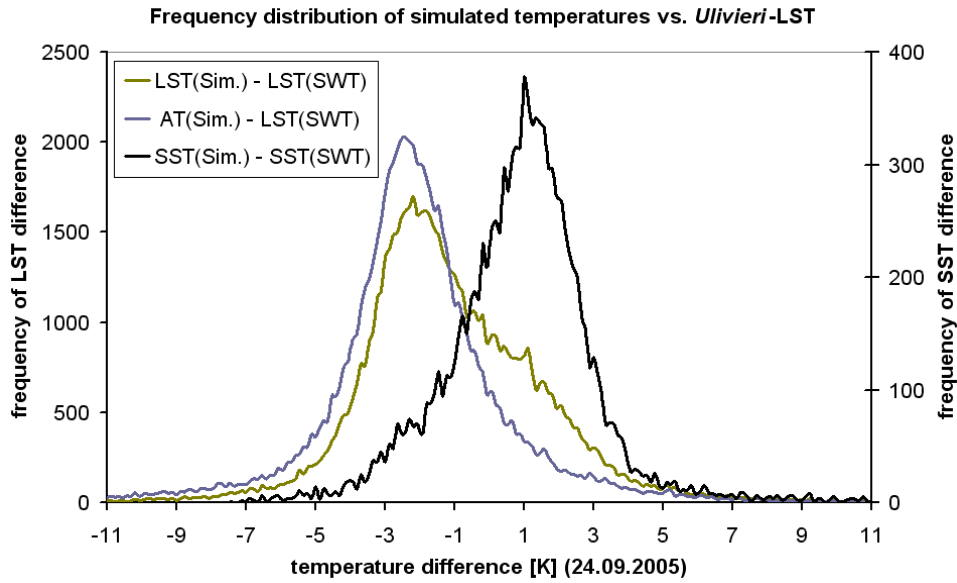

Appendix C 6: Frequency distributions of the differences between simulated surface and air temperatures and the LSTs and SSTs derived from NOAA-AVHRR data with the SWT of ULIVIERI et al (1994) for the 05.09.2005, 11:18 CET.
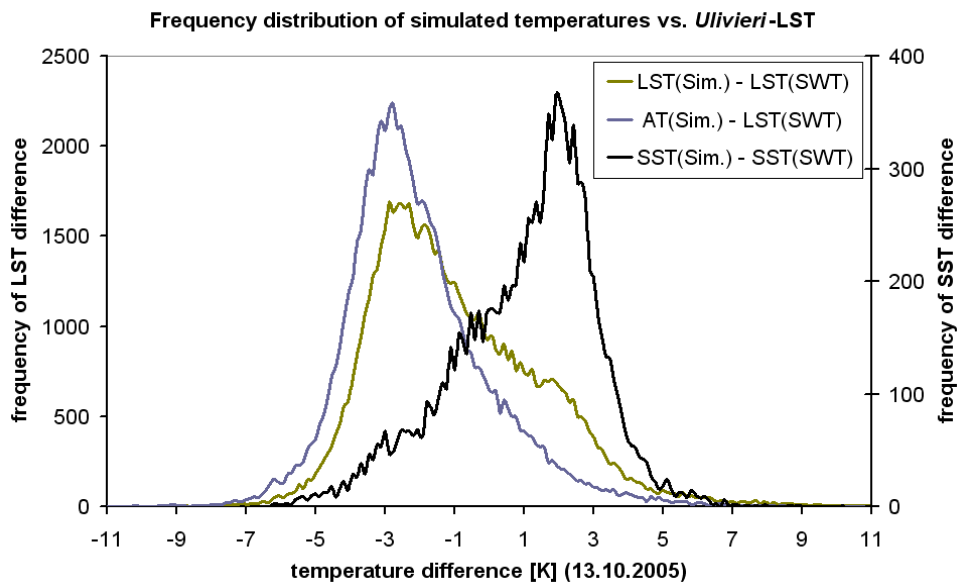
Appendix C 7: Frequency distributions of the differences between simulated surface and air temperatures and the LSTs and SSTs derived from NOAA-AVHRR data with the SWT of ULIVIERI et al (1994) for the 06.09.2005, 10:54 CET.

Appendix C 8: Frequency distributions of the differences between simulated surface and air temperatures and the LSTs and SSTs derived from NOAA-AVHRR data with the SWT of ULIVIERI et al (1994) for the 22.09.2005, 11:27 CET.
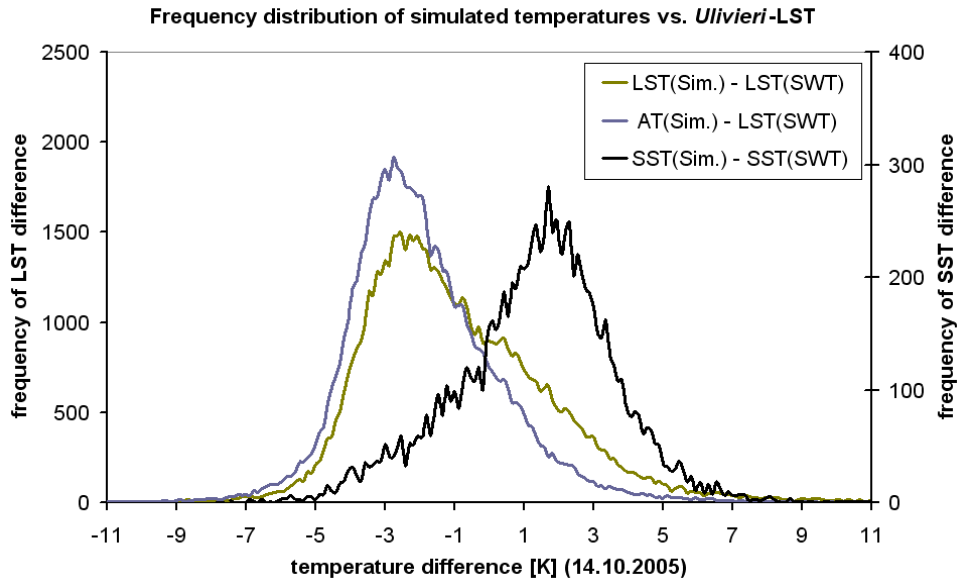
Appendix C 9: Frequency distributions of the differences between simulated surface and air temperatures and the LSTs and SSTs derived from NOAA-AVHRR data with the SWT of ULIVIERI et al (1994) for the 24.09.2005, 10:42 CET.
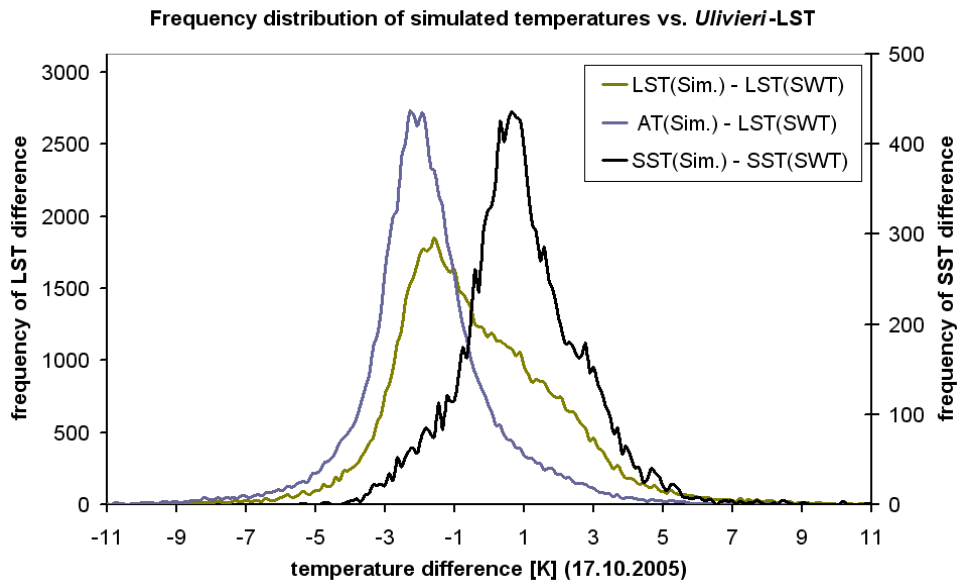

Appendix C 10: Frequency distributions of the differences between simulated surface and air temperatures and the LSTs and SSTs derived from NOAA-AVHRR data with the SWT of ULIVIERI et al (1994) for the 13.10.2005, 11:18 CET.

Frequency distribution of simulated temperatures vs. *Ulivieri*-LST

Appendix C 11: Frequency distributions of the differences between simulated surface and air temperatures and the LSTs and SSTs derived from NOAA-AVHRR data with the SWT of ULIVIERI et al (1994) for the 14.10.2005, 11:24 CET.

Frequency distribution of simulated temperatures vs. *Ulivieri*-LST

Appendix C 12: Frequency distributions of the differences between simulated surface and air temperatures and the LSTs and SSTs derived from NOAA-AVHRR data with the SWT of ULIVIERI et al (1994) for the 17.10.2005, 11:57 CET.

Appendix D: An Empirical Model of Soil Freezing Impact on Runoff Generation

The soil energy algorithm described in the model description calculates the amount of latent energy $LE_{act,j}$ stored as soil ice for each layer j. Therefore it is possible to compute the fractional content of frozen water for each soil layer and each time step by dividing $LE_{act,j}$ by the volumetric heat of fusion

$$\Theta_{ice,j} = LE_{act,j} \div \left[d_j \cdot 1m^2 \cdot 334000 \frac{J}{kg} \cdot 1000 \frac{kg}{m^3} \right] \qquad (4.82)$$

Substracting the amount of frozen soil water $\Theta_{ice,j}$ from the total soil water content Θ_j results in the liquid soil water content $\Theta_{liquid,j}$. Since water expands its volume by 8.9% during freezing, the air content of the soil decreases by an equal amount. From a modelers point of view, the freezing of soil water increases the content of solid particles of a soil layer and diminishes the effective porosity n_j of the layer j. Therefore, the freezing algorithm computes the new soil porosity $n_{act,j}$ of soil layer j by substracting the volumetric fraction of soil ice from n_j

$$n_{act,j} = n_j - \left(\Theta_{ice,j} \cdot 1.09 \right) \qquad (4.83)$$

Now the actual saturation of the remaining pore space decreases with freezing, because $n_{act,j}$ decreases, but the fraction of air-filled pores increases in relation to the pores filled with liquid water (see Fig. 0-1)

$$S_{act,j} = \frac{\Theta_{liquid,j}}{n_{act,j}} \leq \frac{\Theta_j}{n_j} = S_j \qquad (4.84)$$

If freezing in soil layers progresses, the volume of air-filled pores is further reduced, because water expands during the liquid to solid phase change. However, since water in bigger pores freezes first and adhesive water freezes last, the soil "dries" as the frozen phreatic water becomes part of the soil matrix (Fig. 0-2) as long as there is no infiltration and even if there is no exfiltration. Fig. 0-3 exemplifies that the soil suction increases with ice formation and therefore the total water content for a given suction. This leads to increased capillary rise into the frozen layer, if water is available from below, or additional retention of infiltrating water during snow melt or precipitation events. As this water freezes the model can simulate the build up of basal ice sheets when the air-filled pore fraction of the upper layer reaches a minimum and the reduced hydraulic conductivity by pore ice for the lower soil layers. This relates to theoretical and experimental findings of Johnsson & Lundin (1990), Bayard et al (2005) and others.
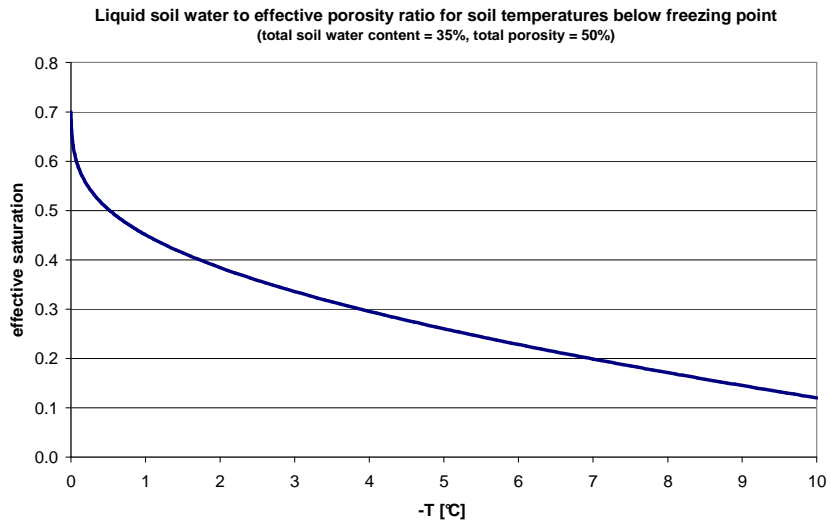
Fig. 0-1: Ratio of liquid water to effective porosity for temperatures below 0 °C.
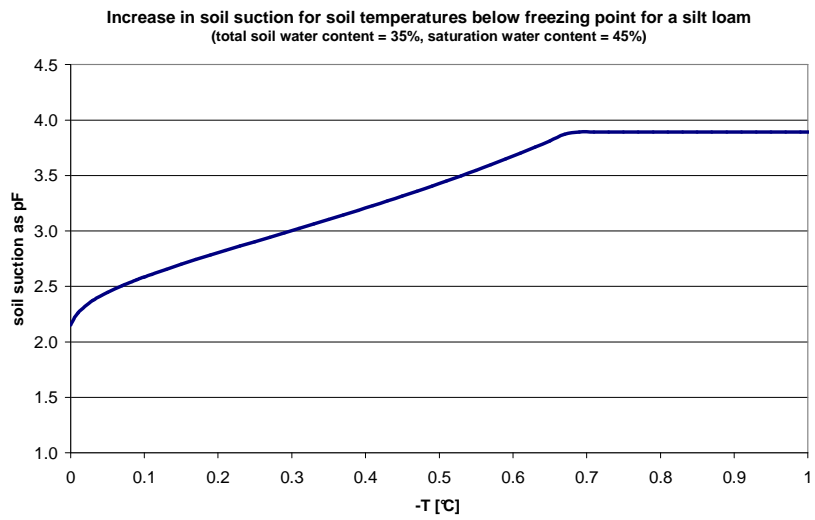

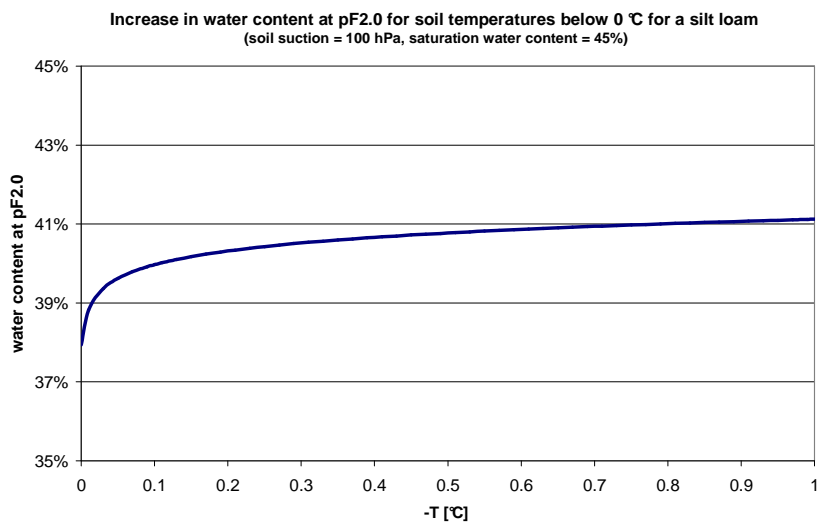**Fig. 0-2: "Drying" of a soil while freezing.**

Fig. 0-3: Virtual increase of soil water content at 100 hPa for temperatures < 0 °C.

To quantify the changes in runoff behaviour of frozen soil layers two complementary algorithms are implemented in PROMET. The first one is formulated similar to Lundin (1990), were the effect of frozen water on hydraulic conductivity K(s) is described with an impendence factor E_i and the soil ice coefficient C_{Ice}.

$$k(S)_{act} = 10^{-E_i C_{Ice}} \cdot k(S) \qquad (4.85)$$

According to Lundin (1990), the value of E_i has to be empirically determined and can have a value between 1 and 8. The typical value of E_i given by Johnsson & Lundin (1991) is 4, but to ensure numerical stability of the *Eagleson* type soil water model the impendance factor was set to 3.0. The soil ice coefficient C_{Ice} in the model of Lundin (1990) is the proportion of frozen to total soil water, called *thermal quality*. But this parameterisation leads to the same actual conductivities for dry and wet soils at a given temperature, because the *thermal quality* is the same for all soils at a given temperature in our model using the equation after Watanabe & Mizoguchi (2002). Therefore we substituted the total soil water content by the effective porosity of the soil layer to take different soil moisture values into account. Fig. 0-4 exemplifies the difference between the *thermal quality* and the soil ice coefficient C_{Ice}.
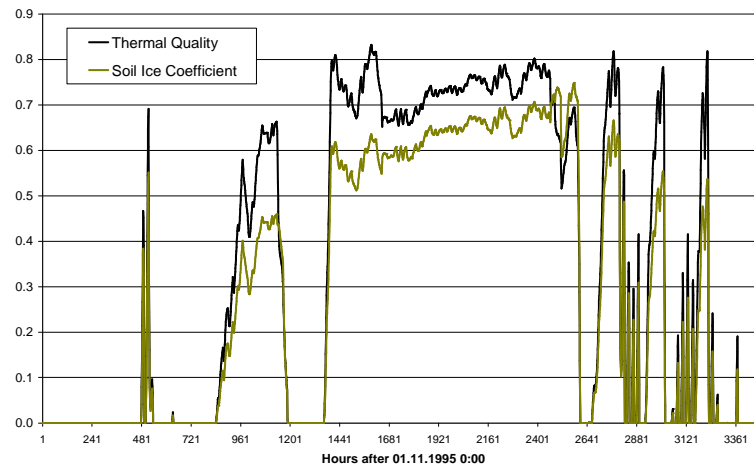

Fig. 0-4: Comparison of simulated thermal quality and soil ice coefficient of the upper soil layer of a lowland maize field.

But even with very low actual hydraulic conductivities lateral runoff from frozen soils are hard to simulate at hourly time steps and with relatively large soil layers in contrast to high resolution soil physics models at the field scale. Therefore, a second algorithm is implemented in PROMT that mimics ice blocking in case that most of the medium and large pores of a soil layer are filled with ice. The idea behind this approximate equation is that the soil water exposed to the lowest adhesive forces inside the soil matrix freezes first. Water held by strong forces will freeze last, but these water molecules also interact weakly with external water fluxes like infiltration. So if the soil moisture is near field capacity and most of the phreatic water is frozen, the soil matrix no longer interacts with infiltrating water, nor does capillary rise occur. If water tries to infiltrate into the frozen soil layer, some of it runs off laterally while

the other part passes through the macro pores to the next soil layer. The distribution of these two water fluxes is difficult to parameterize for mesoscale simulations, but field experiments published by other groups (JOHNSSON & LUNDIN 1991, STADLER et al 1997, KUCHMENT et al 2000, NYBERG et al 2001, BAYARD et al 2005) and analysis of recorded runoff peaks were used to identify the runoff splitting coefficient C_{split}.

If the actual effective soil porosity $n_{act,j}$ is smaller than a certain threshold value n_{ib}, the water infiltrating (Q_{inf}) into a soil layer is split into lateral ($Q_{lateral}$) and vertical (Q_{macro}) water fluxes according to the empirical C_{split} value, individually assigned to each soil layer by the following equations

$$Q_{lateral} = C_{split} * Q_{inf} \qquad\qquad (4.86)$$

$$Q_{macro} = (1 - C_{split}) * Q_{inf} \qquad\qquad (4.87)$$

The parameterisation of n_{ib} and C_{split} used in this work is mainly influenced by the findings of BAYARD et al (2005) for alpine terrain, that about 25 – 40% of snowmelt run off laterally on frozen ground with a frost depth greater 30 cm and up to 60 % run off on basal ice sheets. Despite the field scale nature of their investigation, it serves as an evidence for realistic C_{split} values. The splitting coefficients in this study are set to 0.15, 0.30, 0.50 and 1.00 for the soil model layers 1 to 4, so that the lateral flows depicted in Fig. 0-5 ensue. The threshold n_{ib} is set to 3 % to enable ice blocking only when a soil layer is nearly saturated with water and most of it has frozen. First results with the ice blocking algorithm show an improvement of simulated winter high flows compared to standard model runs. But further investigation on the regionalization of the C_{split} values has to be conducted.
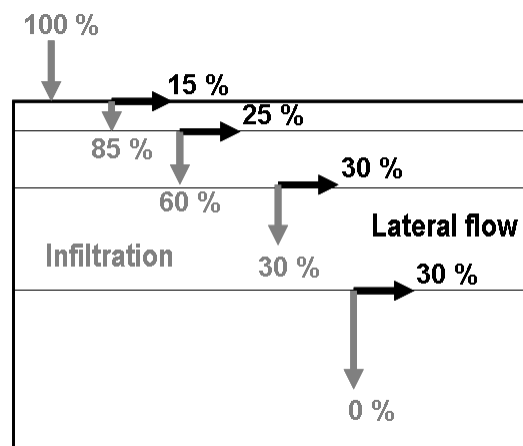

Fig. 0-5: Lateral runoff (relative to surface infiltration) modelled due to the chosen ice blocking parameterisation for frozen soil layers.

Curriculum Vitae

Personal

Name	Markus Josef Muerth
Date of Birth	26.06.1975
Place of Birth	Munich, Germany
Nationality	German

Education

1981 – 1985	Primary School, Landshut (Germany)
1985 - 1994	High School, Fürstenfeldbruck (Germany)
11/1994 – 10/1995	Studies of Political Sciences at the Ludwig-Maximilians University (LMU) Munich (Germany)
11/1995 – 10/1997	Undergraduate studies of Physics with Informatics at the LMU Munich
11/1997 – 03/2003	Graduate studies of Physical Geography with Physics and Meteorology at the LMU Munich
	Graduate Degree: *Diplom-Geograph (Univ.)*
	Diploma thesis: *Parametrisierung von Abflussbildung und Abflusskonzentration*

Scientific Career

09/2000 – 08/2002	Student research assistant at the Chair of Geography and Remote Sensing, LMU Munich (Germany)
Since 05/2003	Research associate at the Chair of Geography and Remote Sensing, LMU Munich
Since 05/2004	PhD student, Department of Geography, LMU Munich
Since 05/2004	Collaboration in the 'Hydrology and Remote Sensing' working group of the BMBF funded GLOWA-Danube project
Since 04/2007	Lecturer at the Department of Geography, LMU Munich